# EXPERIMENTAL AND COMPUTATIONAL INVESTIGATIONS OF KINETICALLY STABLE SELENIDES SYNTHESIZED BY THE MODULATED ELEMENTAL REACTANTS METHOD

by

MARCO MICHAEL ESTERS

A DISSERTATION

Presented to the Department of Chemistry and Biochemistry
and the Graduate School of the University of Oregon
in partial fulfillment of the requirements
for the degree of
Doctor of Philosophy

December 2017

DISSERTATION APPROVAL PAGE

Student: Marco Michael Esters
Title: Experimental and Computational Investigations of Kinetically Stable Selenides Synthesized by the Modulated Elemental Reactants Method

This dissertation has been accepted and approved in partial fulfillment of the requirements for the Doctor of Philosophy degree in the Department of Chemistry and Biochemistry by:

| | |
|---|---|
| Shannon W. Boettcher | Chairperson |
| David C. Johnson | Advisor |
| Mark C. Lonergan | Core Member |
| Gregory D. Bothun | Institutional Representative |

and

| | |
|---|---|
| Sara D. Hodges | Interim Vice Provost and Dean of the Graduate School |

Original approval signatures are on file with the University of Oregon Graduate School.

Degree awarded December 2017

DISSERTATION ABSTRACT

Marco Michael Esters

Doctor of Philosophy

Department of Chemistry and Biochemistry

December 2017

Title: Experimental and Computational Investigations of Kinetically Stable Selenides Synthesized by the Modulated Elemental Reactants Method

The controlled and targeted synthesis of new solid materials is still a challenge difficult to overcome. Slow diffusion rates and long diffusion lengths require long reaction times and high synthesis temperatures, resulting in limited control over the reaction pathway. The Modulated Elemental Reactants (MER) method uses compositionally modulated precursors with atomically thin elemental layers that form amorphous alloys upon annealing while maintaining composition modulation. In this amorphous intermediate, nucleation, not diffusion, control the formation of the product, enabling kinetic control of the reaction, and the synthesis of new metastable compounds, heterostructures with designed nanoarchitecture, and thin films with a high degree of texturing.

This dissertation uses experimental and computational methods to investigate compounds synthesized by the MER method. Firth, the MER method is used to synthesize ferromagnetic $CuCr_2Se_4$ films that show a large degree of crystallographic alignment and interesting magnetic properties such as temperature-dependent easy axes and negative magnetoresistivity.

The second part investigates ferecrystals, rotationally disordered members of the misfit layer compounds family. The MER method's ability to control the nanoarchitecture of the products is used to synthesize a new type of structural isomers, allowing for the synthesis of thousands of ternary compounds using the same elements. Experimental methods are also used to monitor the formation of ferecrystalline compounds using $[(SnSe)_{1+\delta}][VSe_2]$ as a model system.

Despite the vast number of compounds available, however, explaining the properties and stability of ferecrystals is still in its infancy. In the last part of this dissertation, *ab initio* methods are employed to investigate the components in our ferecrystals. Specifically, isolated layers of $VSe_2$ with its structural distortions due to a charge density wave, SnSe with its thickness-dependent structures, and BiSe with its flexible lattice and anti-phase boundaries are investigated to complement experimental results. Some properties, such as the structural distortion in $VSe_2$ and the different stabilities of BiSe layers, can be explained very well using this simplified model, but others, such as the structure of SnSe layers, are not exclusively determined by their dimensionality, underlining the complex nature of the interactions in ferecrystals.

This dissertation includes previously published and unpublished co-authored material.

# CURRICULUM VITAE

NAME OF AUTHOR: Marco Michael Esters

GRADUATE AND UNDERGRADUATE SCHOOLS ATTENDED:

University of Oregon, Eugene
RWTH Aachen University, Aachen, Germany

DEGREES AWARDED:

Doctor of Philosophy, Chemistry, 2017, University of Oregon
Master of Science, Chemistry, 2012, RWTH Aachen University
Bachelor of Science, Chemistry, 2010, RWTH Aachen University

AREAS OF SPECIAL INTEREST:

Solid State Chemistry and Physics: Thin Films, Magnetic Properties
Density Functional Theory: 2D Materials

PROFESSIONAL EXPERIENCE:

Graduate Research Assistant/Graduate Teaching Fellow, University of Oregon, 09/2012 – present

Teaching Assistant, RWTH Aachen University, 10/2008 – 07/2012

GRANTS, AWARDS, AND HONORS:

Springorium Commemorative Coin, RWTH Aachen University, 2013

Schöneborn Award, proRWTH, 2011

International Research Experiences for Undergraduates (IREU), American Chemical Society and Deutscher Akademischer Austauschdienst, 2010

PUBLICATIONS:

Hamann, D.; Lygo, A. C.; **Esters, M.**; Merrill, D. R.; Ditto, J.; Sutherland, D. R.; Bauers, S. R.; Johnson, D. C. "Structural Changes as a Function of Thickness in $[(SnSe)_{1+\delta}]_mTiSe_2$ Heterostructures". Submitted to *ACS Nano*

**Esters, M.**; Hennig, R. G.; Johnson, D. C. "Dynamic Instabilities in $VSe_2$ Monolayers and Bilayers". Submitted to *Phys. Rev. B*

**Esters, M.**; Johnson D. C. Johnson "Targeted Synthesis of Metastable Compounds and Intergrowths: The Modulated Elemental Reactants Method". In *Crystal Growth: Concepts, Mechanisms, Applications*; Li, J.; Li, J.; Chi, Y., Eds.; Nova Science Publishers: New York, 2017; p. 35 – 118

Edelman, I.; **Esters, M.**; Johnson, D. C.; Yurkin, G.; Tarasov A.; Rautsky, M.; Volochaev, M.; Lyashchenko, S.; Ivantsov, R.; Petrov, D.; Solovyov, L. A. "The Competition Between Magnetocrystalline and Shape Anisotropy on the Magnetic and Magneto-transport Properties of Crystallographically Aligned $CuCr_2Se_4$ Thin Films" *J. Magn. Magn. Mater.* **2017**, *443*, 107 – 115

Falmbigl, M.; **Esters, M.**; Johnson, D. C. "Formation of a Selenide-Based Heterostructure From a Designed Precursor" *Cryst. Res. Technol.*, **2017**, *52* (10), 1700067

Hite, O. K.; Falmbigl, M.; Alemayehu, M. B.; **Esters, M.**; Wood, S. R.; Johnson, D. C. "Charge density wave transition in $(PbSe)_{1+\delta}(VSe_2)_n$ compounds with $n$ = 1, 2, and 3" *Chem. Mater.*, **2017**, *29* (13), 5646 – 5653

Mitchson, G.; Hadland, E.; Göhler, F.; Wanke, M.; **Esters, M.**; Ditto, J.; Bigwood, E.; Ta, K.; Hennig, R. G.; Seyller, T.; Johnson, D. C. "Structural Changes in 2-D BiSe Bilayers as $n$ Increases in $(BiSe)_{1+\delta}(NbSe_2)_n$ ($n$ = 1 - 4) Heterostructures" *ACS Nano*, **2016**, *10* (10), 9489 – 9499

**Esters, M.**; Liebig, A.; Ditto, J. J.; Falmbigl, M.; Albrecht, M.; Johnson, D. C. "Synthesis, Structure, and Magnetic Properties of Crystallographically Aligned $CuCr_2Se_4$ Thin Films" *J. Alloy. Compd.* **2016**, *671*, 220 – 225

Wood, S. R.; Merrill, D. R.; Falmbigl, M.; Moore, D. B.; Ditto, J.; **Esters, M.**; Johnson D. C. "Tuning Electrical Properties through Control of $TiSe_2$ Thickness in $(BiSe)_{1+\delta}(TiSe_2)_n$ Compounds" *Chem. Mater.*, **2015**, *27* (17), 6067 – 6076

Falmbigl, M.; Putzky, D.; Ditto, J.; **Esters, M.**; Bauers, S. R.; Ronning, F.; Johnson, D. C. "Influence of Defects on the Charge Density Wave of $([SnSe]_{1+\delta})_1(VSe_2)_1$ Ferecrystals" *ACS Nano*, **2015**, *9* (8), 8440 – 8448

**Esters, M.**; Alemayehu, M. B.; Jones, Z.; Nguyen, N. T.; Anderson, M. D.; Grosse, C.; Fischer, S. F.; Johnson, D. C. "Synthesis of Inorganic Structural Isomers By Diffusion-Constrained Self-Assembly of Designed Precursors: A Novel Type of Isomerism" *Angew. Chem. Int. Ed.* **2015**, *127* (4), 1146 – 1150

Pecher, O.; **Esters, M.**; Görne, A.; Mausolf, B.; Ormeci, A.; Haarmann, F. "The Zintl Phase $Cs_7NaSi_8$ – From NMR Signal Line Shape Analysis and Quantum Mechanical Calculations to Chemical Bonding" *Z. Anorg. Allgem. Chem.*, **2014**, *640*, 2169 – 2176

Deringer, V. L.; Goerens, C.; **Esters, M.**; Dronskowski, R.; Fokwa, B. P. T. "Chemical Modeling of Mixed Occupations and Site Preferences in Anisotropic Crystal Structures: Case of Complex Intermetallic Borides" *Inorg. Chem.* **2012**, *51* (10), 5677 – 5685

# ACKNOWLEDGMENTS

Science is never done as a one-person project, so there is a very long list of people and organizations I would like to thank. First and foremost, of course, to my advisor, David C. Johnson, for letting me do my summer internship in 2010 and creating a pleasant first stay in the United States for me during that time, and for inviting me back to join his group for my PhD. I appreciated his guidance, patience, encouragement, and his support in my rather unconventional path to do theory in his experimental group. I cannot understate how grateful I am that I got this opportunity.

I would also like to thank my department members of my thesis committee, Shannon Boettcher and Mark Lonergan, whose support, feedback, and encouragement helped me immensely. Special thanks go to my outside committee member Gregory Bothun from the Department of Physics for graciously stepping in for Roger Haydock last minute.

I had tremendous support in my research endeavors, especially by my co-workers, past and present, including Matti Alemayehu, Sage Bauers, Jeff Ditto, Matthias Falmbigl, Danielle Hamann, Alex Lygo, Gavin Mitchson, Dan Moore, Devin Merrill, Duncan Sutherland, and my undergraduate researcher Nika Jin. I would like to especially thank Dan Moore for being an invaluable resource for the deposition system, and Matthias Falmbigl for always taking the time to explain or to help with pretty much anything. I would also like to thank my collaborators in Krasnodar, especially Irina Edelman – it was a pleasure working with them.

Special thanks go out to my collaborators at the University of Florida in Gainesville, FL, especially to Richard Hennig for his expertise and mentorship for my theory work, and for letting me work in his group in February 2016. His group, especially Joshua Gabriel, Joshua Paul, Kiran Matthew, Biswas Rijal, and Michael Ashton, went above and beyond to make me feel welcome and part of the team, even though I was only there for three weeks.

Thank you also to the fantastic team at the Center for Advenced Materials Characterization in Oregon (CAMCOR), especially to Julie Chouinard, for their assistance. Furthermore, I would like to thank Carlo Segre and Joshua Wright at the

Advanced Photon Source (APS) at Argonne National Lab (ANL) for their assistance with XAFS measurements.

Science is not cheap, so I would like to acknowledge the National Science Foundation for funding (DMR-1266217), the Department of Chemistry for their support, the University of Oregon ACISS cluster (National Science Foundation OCI-0960354) and the University of Florida Research Computing System for providing computational resources, and my union, the Graduate Teaching Fellowship Federation (GTFF).

There are a lot of people outside of our labs that I would like to acknowledge whose contributions have helped me with all my work. The contributions of our Machine Shop, the Technical Science Administration, and our Facilities Management cannot be overstated. Thank you especially to Kris Johnson and Cliff Dax who time and time again came to save our deposition system. I would also like to thank all of our administrative staff, especially Jeanne Basom, Melodi Jayne, Diane Lachenmeyer, Janet Macha, Christi Mabinouri, Heathre Prehodra, Jim Rasmussen, and Kiran Varani-Edwards.

I have had the privilege to have a lot of people to support me throughout my life. I would like to thank my family, especially my parents and my uncle, for fostering my talents and encouraging me to pursue my passions. I would also like to thank my friends in Germany and the United States who were there for me when I needed them and who've been a steady source of joy in my life. I would especially like to thank Rebecca Engel for her friendship in Germany and beyond, Melissa Hale for the always amazing pizza and cider nights, and Caitlin Corona for whose friendship I will be forever grateful.

I would also like to thank everyone at the Cascades Raptor Center for allowing me to have what can only be described as the most amazing volunteer experiences I have ever had – it has contributed more to this work than I can describe.

At last, I would like to thank my wonderful wife, Lena Trotochaud, whose words, love, support, and encouragement have carried me further than I thought I could go. I could not have done this without you, and I'm looking forward to seeing what the future has in stock for us.

Dedicated to the loving memory of my great grandparents

Piotr “Dziadek” Sudol (11/07/1922 – 12/17/2012)

Anastasia “Babka” Sudol (11/02/1923 – 12/03/2014)

TABLE OF CONTENTS

Chapter Page

Chapter Page

LIST OF FIGURES

Figure Page

Figure Page

Figure Page

Figure Page

Figure Page

Figure Page

Figure Page

LIST OF TABLES

Table Page

# LIST OF SCHEMES

Scheme Page

# CHAPTER I

# INTRODUCTION: THE MODULATED ELEMENTAL REACTANTS METHOD

Portions of this chapter were previously published as Esters, M.; Johnson, D.C. "Targeted Synthesis of Metastable Compounds and Intergrowths: The Modulated Elemental Reactants Method". In *Crystal Growth: Concepts, Mechanisms, and Applications*; Li, J., Li, J., Chi, Y., Eds.; Nova Science Publishers: New York, **2017**; pp. 35–118. M.E. wrote the book chapter and made the figures. D.C.J. was the principal investigator and provided editorial assistance.

## I.1. Rethinking Solid State Synthesis

Throughout history, the search for and discovery of new materials and compounds has been an important driving force for innovation and transformation of human society. From early metallurgy to complex nanomaterials, and from the extraction of herbal medical ingredients to the targeted synthesis of potent drugs, the emergence of new materials and compounds has continuously changed the way humans lived. While many materials have already been discovered, it is predicted that they still make up only the tip of the iceberg.[1] Using a purely combinatorial approach, the total number of possible systems *N*, i.e., without taking different compositions and polymorphs into account, increases exponentially:

$$N = \sum_{k=1}^{n} \frac{n!}{k!\,(n-k)!} = 2^n - 1 \qquad (1.1)$$

where $k$ is the number of elements in a compound and $n$ is the number of elements that can form a compound. Using $n = 95$ (the number of elements of which compounds are known), the maximum number of combinations is approximately $4 \times 10^{28}$. The numbers of element combinations for each individual $k$ are displayed in Figure 1.1a. Including different possible compositions and structures, this number easily increases to $10^{90}$, making this parameter space impossible to explore in an unrestricted manner.[1] The number of known structures is significantly smaller as it is more challenging to include an increasing number of elements (Figure 1.1b).

For solids, significant effort has been expended to develop computational algorithms dedicated to finding stable structures. Notable examples are genetic algorithms and explorations of energy landscapes.[2,3] However, even when a material is predicted to be thermodynamically stable, i.e., it lies in the global minimum in the parameter space, finding the synthesis route to obtain it, ideally while using as little energy and time as possible, is one of the biggest challenges in chemical synthesis. Such a synthesis should ideally have a controllable reaction pathway that yields exactly the

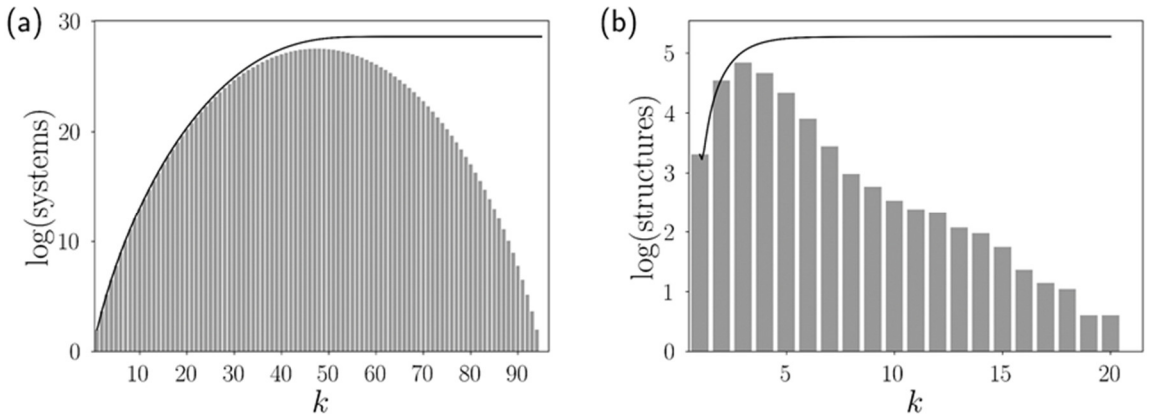


**Figure 1.1.** (a) Number of possible element combinations as a function of components in the system $k$. (b) Number of entries for structures in the International Crystal Structure Database (ICSD) as a function of elements in the structure $k$ as of January 2017. The lines represent the cumulative sums.

desired product and nothing but the desired product. The difficulty to meet these goals is even further amplified when trying to synthesize compounds that lie in local minima of the parameter space.

Significant strides to control this reaction pathway have been made in the synthesis of organic compounds where different pathways with different activation energies can be accessed to end in a local minimum instead of a global minimum (Figure 1.2a). The simplest way is reducing the temperature below the activation energy required to synthesize the thermodynamic product, but high enough to overcome the activation energy to another reaction pathway that leads to a kinetic product. Other methods to open new reaction pathways are to change the energy landscape by functionalizing molecules with electron donating and electron withdrawing groups as it is done in electrophilic substitutions, or by stabilizing a byproduct/leaving group. A different approach is to block certain reaction pathways by employing protective groups. These protective groups can also be used to limit diffusion access to certain sites of the molecule through steric hindrance.

Moreover, many reaction mechanisms and many reactions that manipulate specific functional groups or sites are well known for organic reactions. As a result, design principles could be established that allowed the development of viable synthesis routes based on the target molecule alone. An example of such an analysis is shown in Figure 1.2b. This retrosynthetic approach proved to be so impactful that it earned Elias J. Corey the Nobel prize in chemistry in 1990, and nowadays, even software to perform retrosynthetic analysis exists.[4,5]

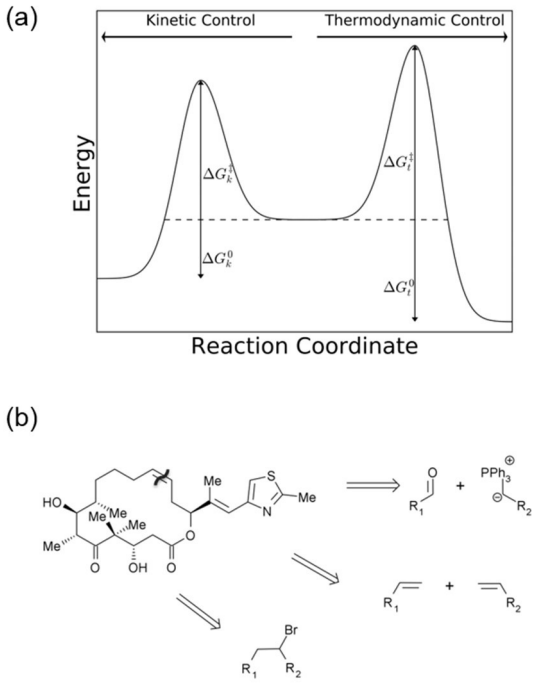


**Figure 1.2.** (a) Schematic reaction pathway for kinetically and thermodynamically controlled reactions. $\Delta G_k^{\ddagger}$and $\Delta G_t^{\ddagger}$are the activation energies, and $\Delta G_k^0$ and $\Delta G_0^t$ are the Gibbs free enthalpies for the kinetically and thermodynamically controlled reactions, respectively. (b) Retrosynthesis of Epothilone C with three possible reactions to form the double bond.

For the synthesis of solids, however, kinetic control and systematic synthesis approaches have not been realized yet to the degree that exists in organic chemistry. Solid state reactions can only occur at interfaces, which adds significant challenges that do not exist in the reactions of discrete molecules in a homogeneous solution.

Since powders are inherently inhomogeneous, the ratio of interface to bulk is very low. This makes observing the processes at the interfaces, and thus determining the reaction mechanisms, extremely challenging because not only is the volume of interest very small, but it also needs to be selectively probed. Moreover, the reaction is limited by diffusion, which follows the Arrhenius equation in solids:

$$D = D_0 e^{-\frac{E_A}{kT}} \tag{1.2}$$

where $D$ is the diffusion coefficient, $D_0$ is the diffusion coefficient at infinite temperature, $E_A$ is the activation energy for diffusion, $T$ the temperature, and $k$ the Boltzmann constant. $D$ is extremely small for solids, so very high temperatures and long reaction times are typically required for solid state syntheses. Consequently, many reaction pathways that could lead to local minima are either not available, or the product does not remain inside these minima and instead converges to the most stable product or products.

Further complications arise when compounds with three or more different elements are being synthesized from three or more reactants. Since it is very unlikely that all three reactants meet at the same interface, intermediates need to form. These intermediates may be thermodynamically more stable than the desired product, leading to a dead end. Kinetic control in solid state synthesis is thus extremely challenging and in many cases not possible yet.

Many approaches have been devised to overcome these drawbacks. Most of them are focused on increasing diffusion rates by introducing a fluid phase. One method, hydrothermal synthesis, uses aqueous solutions at high temperatures and high vapor pressures, so crystals that are unstable at high temperatures can be grown. While this method gave access to a wide variety of metastable aluminosilicates (zeolites) and phosphates, controlling and observing the reaction is very difficult.[6] Similar approaches using liquid metals, low temperature eutectic mixtures or polychalcogenide fluxes provide access to new compounds, but the reaction mechanisms are not known.

Another common approach is to use starting materials that are structurally similar to the desired product, which can even be applied to traditional solid state synthesis. One

example of such a reaction is the synthesis of the Zintl phases $Rb_7NaSi_8$ and $Cs_7NaSi_8$ from $Na_4Si_4$, and $Rb_4Si_4$ and $Cs_4Si_4$, respectively.[7,8] Various *chimie douce* methods also use precursors that undergo low-temperature reactions such as intercalation/deintercalation, ion exchanges, dehydration, etc. Sol-gel methods and co-precipitation reactions use solutions as the starting materials instead of solids.[9,10] All of these methods have the disadvantage that the selection of precursors is limited either due to a lack of structurally similar materials or because there are no soluble precursors available.

This chapter will introduce another precursor-based approach, the Modulated Elemental Reactants method (MER).[11] MER uses compositionally modulated, atomically thin, elemental precursors prepared with physical vapor deposition to control the starting local composition and structure to increase the total interfacial area and significantly reduce diffusion lengths. As a result, synthesis times and temperatures are greatly reduced, resulting in kinetically controlled reactions.

## I.2. The Modulated Elemental Reactants Method

*Precursor Synthesis and Analysis*

Solid state synthesis is challenged by low diffusion rates, long diffusion paths, and small interfacial areas, requiring high temperatures and long reaction times, which makes kinetic control of the reaction pathway very difficult. The Modulated Elemental Reactants (MER) method addresses two of these drawbacks, long diffusion paths and small interfacial areas, by using compositionally modulated, layered thin film precursors with individual layers being only a few Ångström thick. The individual layers are repeated a set number of times to achieve a desired total film thickness. The repeated set

of atomic layers will be referred to as the *repeating unit* and its thickness, the modulation wavelength of the precursor, as the *repeat unit thickness* $t_{\text{repeat}}$.

A representation of such a precursor is shown in Figure 1.3. As the figure demonstrates, the number of atoms that are not close to an interface is very low, which greatly reduces the need for atoms to diffuse through the solid. Moreover, the distances an atom needs to travel to reach an interface are only a few Ångström, which is a very short diffusion length. Both factors do not require a large diffusion coefficient, which should greatly reduce reaction temperatures and reaction times, since the atoms that need to diffuse only need to travel very short distances.

Precursors are synthesized using physical vapor deposition (PVD) in a custom-built vacuum chamber.[12] Chalcogens and antimony are evaporated using an effusion cell with resistive heaters whereas metals with very low vapor pressures are evaporated using electron beam guns. Deposition rates (typically less than 1 Å $s^{-1}$) are controlled using quartz crystal microbalances (QCMs). Shutters are used to control the elements deposited

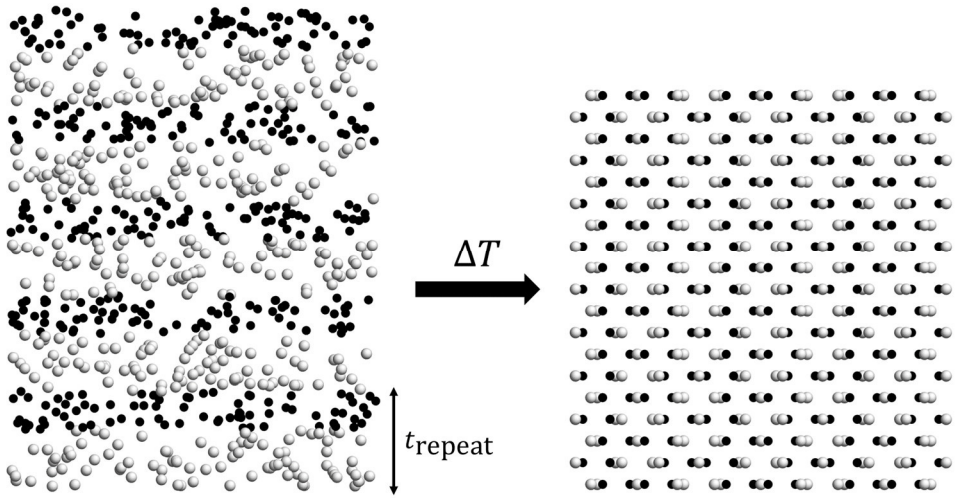


**Figure 1.3.** Schematic representation of an MER precursor of alternating atomic layers of Nb and Se that reacts to form $Nb_5Se_4$. $t_{repeat}$ is the repeat unit thickness of the Nb-Se repeating unit. Nb atoms are gray, Se atoms are black.

onto the substrate. To control the thickness of the individual layers, the shutters can be opened for a specified time or the shutters can be controlled by the QCMs that close the shutters at a specified thickness is achieved.

Since the microbalances are typically situated below the substrate, neither the product of the time the shutters are opened times the deposition rate nor the thickness measured with the QCMs directly corresponds to the thickness of the layer on the substrate. The deposition parameters thus need to be calibrated for composition and thickness. For this, the parameters of one element will be held constant while the parameters of the other element are systematically varied.

The composition of the precursors can be determined using electron probe microanalysis (EPMA) and x-ray fluorescence spectroscopy (XRF).[13,14] The repeat unit thickness of the precursor can be determined using x-ray diffraction (XRD) and Bragg's law of diffraction. X-ray reflectivity (XRR) can be used to determine the total thickness of the precursor using a modified version of Bragg's law:

$$\left(n + \frac{1}{2}\right)\lambda = 2d(\sin\theta - \sin\theta_c)^2 \qquad (1.3)$$

where $n$ is a positive integer, $\lambda$ the wavelength, $d$ is the total thickness of the layer, $\theta$ the angle between the x-ray source and the sample, and $\theta_c$ is the critical angle of reflection.

Figure 1.4 shows representative XRR patterns of a precursor with 42 Ti-Se bilayers. The thickness read on the QCM for the Se layers was kept constant while the thickness of the Ti layer, $t_{\mathrm{Ti}}$, was systematically increased to create the different samples.

The maxima of the oscillations in the XRR pattern, the Kiessig fringes, shift systematically to lower 2θ with increasing $t_{\mathrm{Ti}}$ because of an increased total film

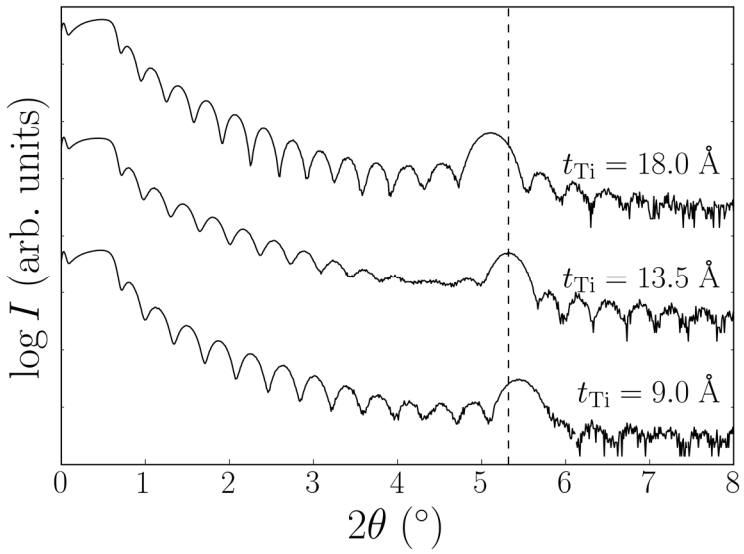


**Figure 1.4.** XRR patterns for Ti-Se precursors. The Se thickness read by the QCM was kept constant at 54.9 Å, and the thickness of Ti ($t_{Ti}$) was varied. The vertical line corresponds to the Bragg reflection maximum for $t_{Ti}$ = 13.5 Å. Offset added for clarity.

thickness. Above 5° 2θ, a broad maximum with higher intensity than the Kiessig fringes can be observed, which can be described with Bragg's law of diffraction. The repeating electron density that is responsible for diffraction comes from the modulated nature of the precursors, and the *d*-spacing corresponds to its repeat unit thickness $t_{\mathrm{repeat}}$.

If the sticking coefficients of the elements are constant and if depositions are consistent, a linear increase in $t_{\mathrm{Ti}}$ should result in a linear increase in the Ti:Se ratio and in $t_{\mathrm{repeat}}$. Systematically varying $t_{Ti}$ can then be used as a calibration procedure to find the parameters for the desired $t_{\mathrm{repeat}}$ and the desired precursor composition. Figure 1.5 shows such calibration curves. The slopes show the change in the Ti:Se ratio and the repeat unit thickness per Ångström of Ti read by the QCM. The intercept in Figure 1.5b, 15.25 Å, is the actual thickness of the Se layer in the film. The thickness read by the QCM was 59.4 Å, so only 25% of the Se deposited onto the QCM is actually deposited onto the substrate, emphasizing the importance of this calibration procedure. Assuming

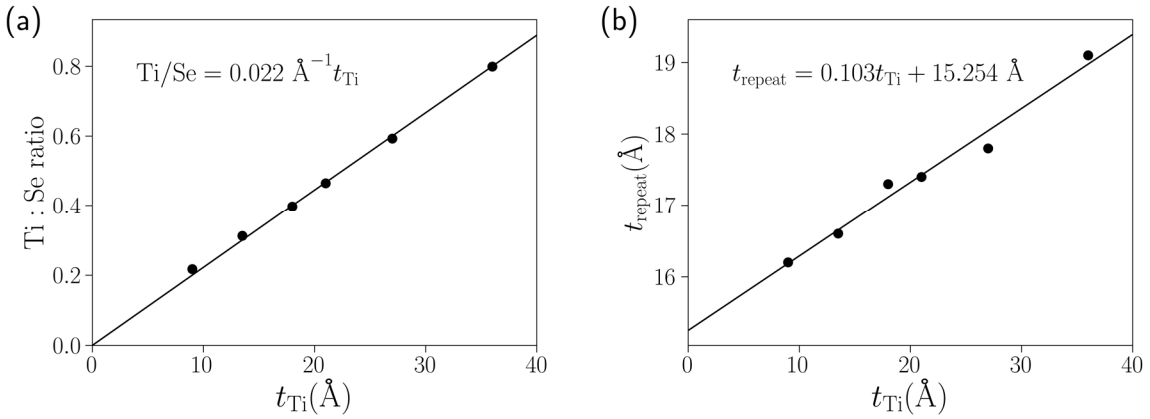


**Figure 1.5.** Calibration data for a Ti-Se precursor. The Se thickness read by the quartz crystal microbalance was kept constant at 54.9 Å, and the thickness of Ti ($t_{Ti}$) was varied. (a) Composition calibration. (b) Repeat unit thickness ($t_{\text{repeat}}$) calibration. The insets show the results of the linear fits through the data.

that no excess Se is added to the precursor, $t_{\text{Ti}}$ for a precursor for $TiSe_2$ should have a value of:

$$t_{Ti} = \frac{1}{2} \cdot \frac{1}{0.022} \text{Å} = 22.7 \text{ Å} \tag{1.4}$$

This would result in a repeat unit thickness of:

$$t_{\text{repeat}} = 0.103 \cdot 22.7 \text{ Å} + 15.254 \text{ Å} = 17.6 \text{ Å} \tag{1.5}$$

*Kinetic and Thermodynamic Control in Solid State Reactions*

The thickness of the repeating unit in the precursor plays an important role in the MER synthesis method. $Nb_5Se_4$, a thermodynamically stable compound, will be used to illustrate this phenomenon.[15] Figure 1.6a and b show the differential scanning calorimetry (DSC) scans of precursors with a repeat unit thickness of (a) above and (b) below 90 Å. Samples for DSC can be obtained by depositing the precursor onto silicon wafers that are coated with poly(methyl)methacrylate (PMMA), which is then dissolved in acetone, lifting off the precursor as a powder. The powder can be collected by filtration and transferred into the DSC sample container.

The DSC data shows two exothermal signals for both precursor types, but they appear at different temperatures. For the precursor with thick atomic layers, the exotherms appear at 125°C and 200°C. X-ray diffraction, however, shows that at these temperatures, the precursor structure is mostly preserved and the sample needs to be annealed further to crystallize completely into $Nb_5Se_4$. The grain sizes are rather small with 40 nm or less. All of this is consistent with nucleation and growth along the Nb-Se interfaces. For the precursor with thin atomic layers, the DSC data look significantly different: instead of two prominent exotherms at low temperatures, a very broad exotherm starts at approximately 100°C and lasts until about 400°C, and a sharp exotherm is present between 550°C and 600°C. The x-ray diffraction pattern (Figure

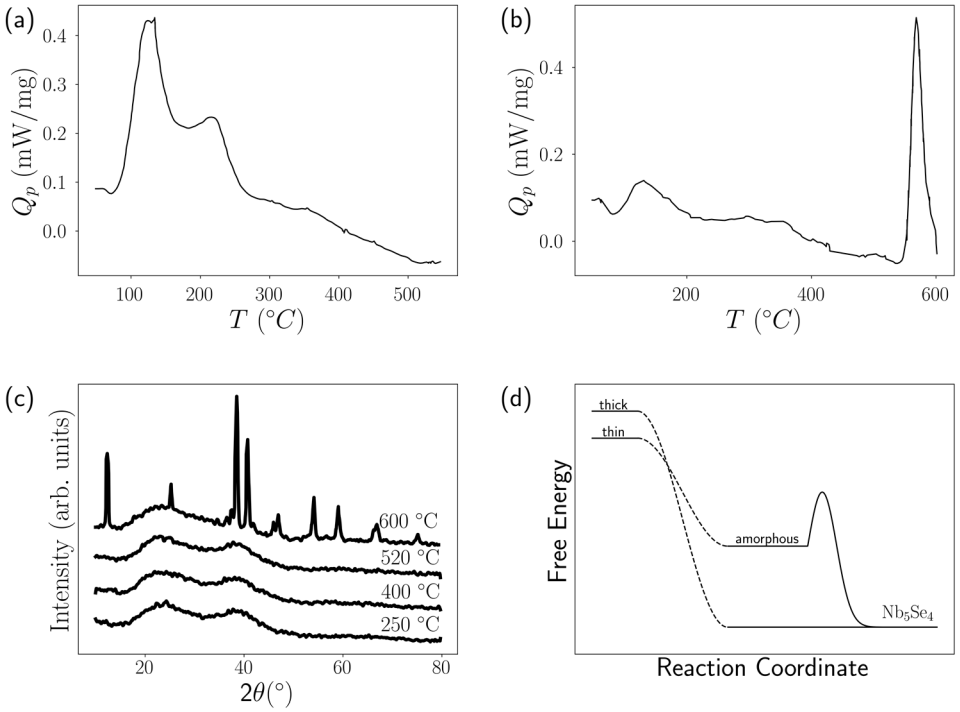


**Figure 1.6.** Differential scanning calorimetry data of a $Nb_5Se_4$ precursor with (a) thick and (b) thin atomic layers. (c) X-ray diffraction pattern of a $Nb_5Se_4$ precursor with thin atomic layers. (d) Schematic free energy vs. reaction coordinate plot for a $Nb_5Se_4$ precursor with different thicknesses of atomic layers.[15]

1.6c) of this precursor annealed at different temperatures shows that below 600°C, the sample is amorphous, and that it is fully crystalline at 600°C.

This indicates two different reaction pathways: for precursors with atomic layers above a certain thickness, the *critical thickness*,[16] the crystallites that nucleate first form at the interface and by diffusion of the elements around them, they grow heterogeneously. Below the critical thickness, the precursor becomes completely amorphous first and needs to overcome a considerable nucleation barrier to homogeneously nucleate and grow into $Nb_5Se_4$. Figure 1.6d shows a schematic of the free energy of these different reaction pathways.

Figure 1.7 provides an illustration on how the structures evolve during that process. Using thin atomic layers, the product of the reaction thus depends on the crystal phase that nucleates first, which is a kinetic parameter. Thus, if nucleation can be controlled, kinetic control of the reaction can be achieved.

The different reaction pathways have profound consequences for the phases that form. For thick atomic layers, the compound that forms at the interface can be determined by the "First Phase Rule" according to Walser and Bené: "The first compound nucleated in planar binary reaction couples is the most stable congruently melting compound adjacent to the lowest temperature eutectic on the bulk equilibrium phase diagram".[17] For the Nb-Se system, this would be $NbSe_2$ and corresponds to the first exothermal peak in the DSC data. Due to the composition of the precursor, $NbSe_2$ then reacts to $Nb_5Se_4$.

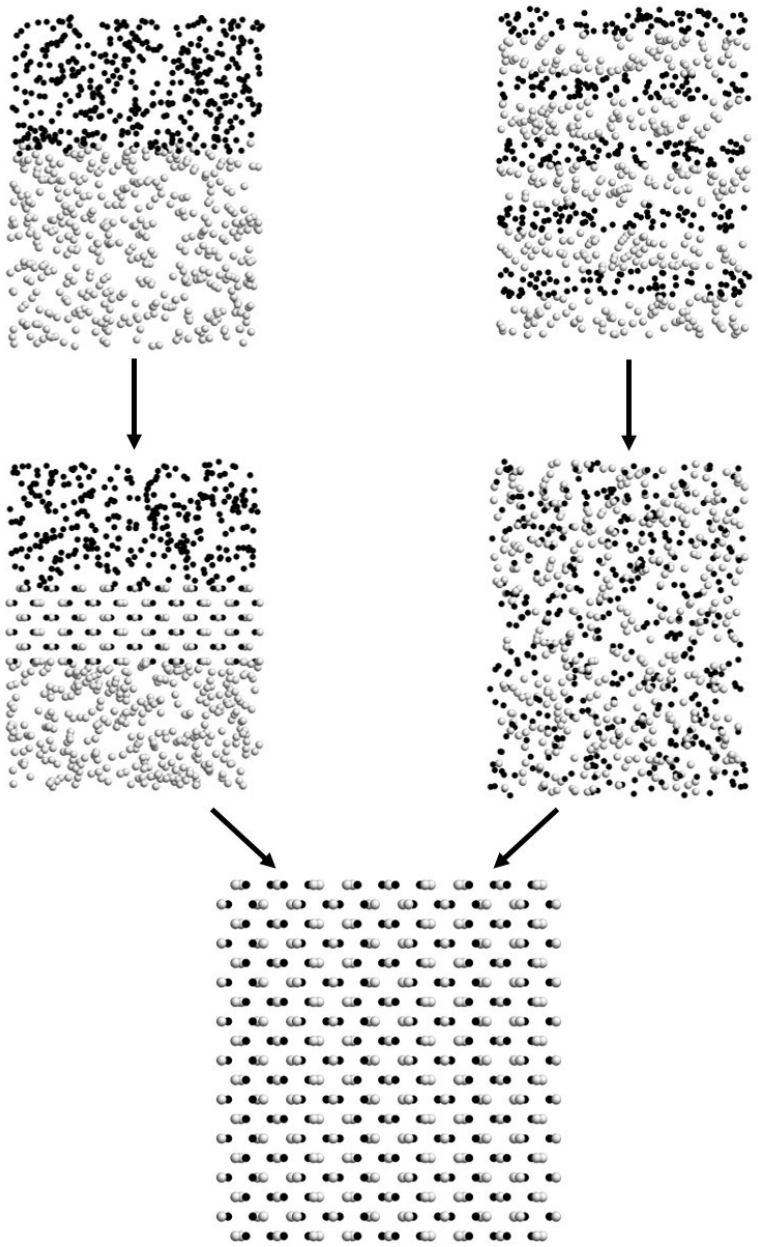

**Figure 1.7.** Reaction pathway for a $Nb_5Se_4$ precursor with thick and thin atomic layers.

However, this can only be successful when the compounds are thermodynamically stable at the reaction temperatures.

The Fe-Si system provides an example for a system that contains a compound that is only stable at high temperatures, $Fe_5Si_3$ (see schematic phase diagram in Figure 1.8).[18]

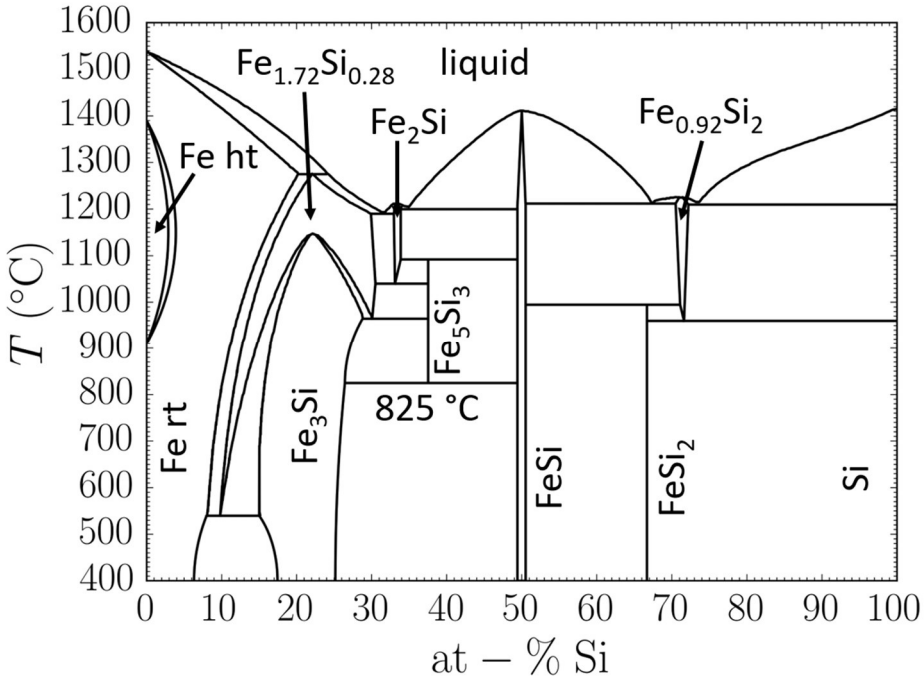


**Figure 1.8.** Schematic phase diagram of the Fe-Si system.[18]

The "First Phase Rule" predicts that the compound that forms first is FeSi, and the product(s) of the reaction depend on the overall stoichiometry of the precursor film and the reaction temperature. If the precursor contains Fe and Si in a 1:1 ratio, phase pure FeSi will form. If the precursor contains excess Si, the Si will react with FeSi to form $FeSi_2$ until one of the components is depleted. If the precursor contains excess Fe and if the temperature of the reaction is below 825°C, the excess Fe will react with FeSi to form $Fe_3Si$ until one of the components is depleted. Above 825°C, however, $Fe_5Si_3$ will form first until Fe is depleted and the reaction stops, or until FeSi is depleted, in which case the remaining Fe will react with $Fe_5Si_3$ to form $Fe_3Si$. These processes are illustrated schematically in Figure 1.9.

Thus, using thick elemental layers, synthesizing $Fe_5Si_3$ should only be possible with temperatures above 825°C. Thin layers, however, amorphize quicker than

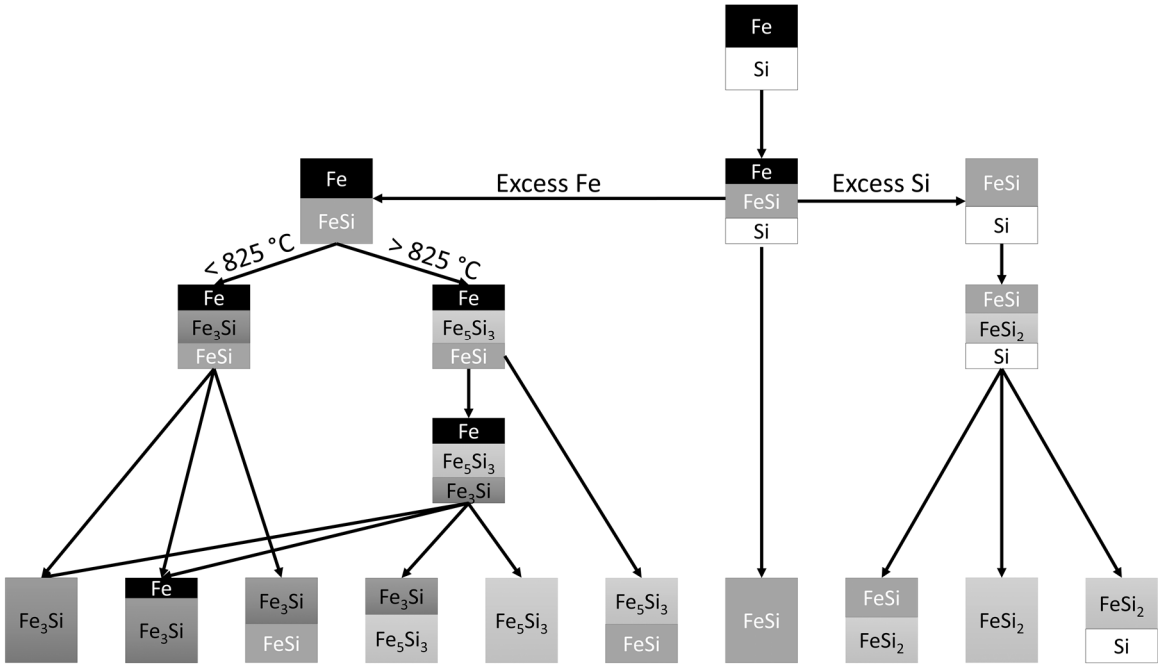


**Figure 1.9.** Schematic representation of the reaction pathways of a Fe-Si thin film diffusion couple for different Fe-Si ratios and temperatures.

components nucleate, so the first phase to crystallize cannot be predicted by the First Phase Rule anymore. In general, the nucleation energy depends on the change of free energy, the surface energy of the growing nucleus, internal stresses, and the energy required to rearrange the amorphous alloy to form the crystallite. While the first three terms are guided by the First Phase Rule, the rearrangement energy depends on the local structure of the amorphous alloy. It is reasonable to assume that the crystallite with a composition closest to the composition of the amorphous alloy has the lowest rearrangement energy, so it should be possible to control which phase nucleates by controlling the composition of the precursor.

A systematic test of this hypothesis was conducted by Novet and Johnson by conducting a DSC analysis on multi-layer precursors with different Fe:Si ratios.[19,20] The main results of these experiments are displayed in Table 1.1. For every composition, a

**Table 1.1.** Thermodynamic data of the annealing of different Fe-Si multilayers from DSC.[19] $\Delta H_{formation}$ is taken from the literature.[21–23] No crystallization event occurs for multilayers with an Fe:Si ratio of 2:1 beneath 600°C

| Fe:Si ratio | $\Delta H_{mixing}$ (kJ/mol/atom) | $\Delta H_{crystallization}$ (kJ/mol/atom) | $\Delta H_{total}$ (kJ/mol/atom) | $\Delta H_{formation}$ (kJ/mol/atom) | $T^{onset}_{crystallization}$ (°C) |
|---|---|---|---|---|---|
| 1:2 | -20(4) | -8(1) | 28(4) | 30.6[21] | 485 |
| 1:1 | -22(4) | -4(0.5) | 26(4) | 39.3[22] | 290 |
| 5:3 | -30(4) | -1(0.3) | 31(4) | — | 455 |
| 2:1 | -37(4) | — | 37(4) | — | — |
| 3:1 | -15(4) | -1(0.3) | 16(4) | 25.8[23] | 540 |

broad exotherm could be observed at 80°C, followed by a sharp exotherm at different temperatures for different compositions, except for precursors with a Fe:Si ratio of 2:1, which did not show an exothermal peak. The broad exotherm corresponds to the formation of an amorphous alloy, which shows that the amorphization reaction is independent of the sample composition and only depends on whether the layers are below or above the critical thickness. The mixing enthalpies, $\Delta H_{mixing}$, however, do depend on the composition of the precursor with a minimum observed at a Fe:Si ratio of 2:1. X-ray diffraction of samples annealed above the amorphization temperature confirms that the samples are amorphous even when annealed for more than 12 hours.

The exotherm corresponds to the crystallization of the crystalline phases. X-ray diffraction shows that the phases are $FeSi_2$, FeSi, $Fe_5Si_3$ and $Fe_3Si$ for Fe:Si ratios of 1:2, 1:1, 5:3 and 3:1, respectively. For a precursor with an Fe:Si ratio of 2:1, no crystallization was observed below 600°C. The crystallization enthalpies, $\Delta H_{crystallization}$, are all very small, suggesting that only little rearrangement is required to transition from the amorphous alloy to the crystalline phase. The extensive intermixing during annealing for

these very thin layers results in a total change of heat, $\Delta H_{total}$, that is lower than the formation energies found for bulk reactions.[21–23] The onset crystallization temperatures also depend on the composition of the precursor and increase with increasing deviation from an equimolar Fe:Si ratio, and are a measure for the energy required to nucleate the crystalline phase.

The data show that the rate limiting step in the formation of compounds with the MER method is nucleation, not diffusion, since the amorphization reaction occurs spontaneously. They also confirm that the composition of the precursor determines the phase that nucleates, and that the nucleated phase determines the final structure. This is especially notable for the precursors with Fe:Si ratios of 2:1 and 5:3. The former does not crystallize at all below 600°C because the energy barrier to form a $Fe_2Si$ nucleus is too high. However, the phases that are the closest in composition, $Fe_3Si$ and $Fe_5Si_3$, do not crystallize either, even though they have lower crystallization temperatures, because the energy required to rearrange the local structure to form a nucleus of either compound is too large due to low diffusion rates in solids. In other words, the farther the composition of the precursor deviates from the composition of a stable nucleus, the larger is the nucleation energy. This relationship has also been shown for InSe MER precursors.[24]

The precursor with an Fe:Si ratio of 5:3 crystallizes into $Fe_5Si_3$ at 455°C, which, according to the phase diagram in Figure 1.8, is far below its decomposition temperature of 825°C. In an Fe-Si diffusion couple, $Fe_5Si_3$ should not form at these temperatures, but since the precursor has a Fe:Si ratio of 5:3, the nucleation energy of $Fe_5Si_3$ is lower than for the other silicides. The MER method is thus able to synthesize metastable compounds

if the energy required to nucleate them is lower than the energy required to rearrange the precursor and to nucleate thermodynamically more stable compounds.

*Synthesis of Ternary Compounds with the MER Method*

In this chapter, the MER method has so far only been demonstrated on the synthesis of binary compounds. Ternary compounds pose additional challenges, which will be demonstrated with the synthesis of $Cu_xMo_6Se_8$. In traditional solid state synthesis, $Cu_xMo_6Se_8$ is synthesized from the elements or from Mo, Se, and CuSe at 1200°C.[25,26] As Figure 1.10 demonstrates, interfaces predominantly consist of only two components. Each interface will behave like diffusion couples and crystallize in a similar scheme as in Figure 1.9, so the first phases to form are the binary phases $MoSe_2$ and $Cu_{2-x}Se$. Over time, $MoSe_2$ and $Cu_{2-x}Se$ will react at newly formed interfaces and nucleate $Cu_xMo_6Se_8$, but $MoSe_2$ also reacts with the remaining Mo to form $Mo_3Se_4$. For a complete reaction to $Cu_2Mo_6Se_8$, $Mo_3Se_4$ must react with other Cu-containing intermediates to finally form $Cu_2Mo_6Se_8$. Since the interfacial area compared to the bulk volume is small and diffusion is slow, the entire synthesis takes multiple days. Another drawback is that this reaction only works if the final product is thermodynamically more stable than the mixture of

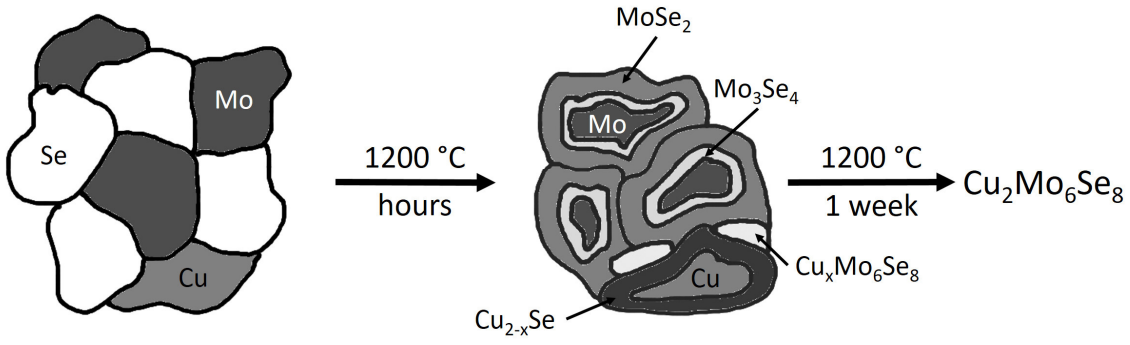


**Figure 1.10.** Cartoon of the processes during synthesis of $Cu_2Mo_6Se_8$ from the elements using classic solid state synthesis techniques.

binary intermediates. If an intermediate mixture is more stable, the ternary compound will not form.

The repeating unit of an MER precursor would consist of a Mo-Cu-Se multilayer. In this case, however, the high diffusion rates of copper in selenium leads to copper diffusing into the Se layer at room temperature so that the precursor actually consists of multilayers of molybdenum and an amorphous copper-selenium alloy.[27]

Depending on the chosen Mo layer thickness, two different behaviors can be found. Above 12 Å, $MoSe_2$ forms at the interface first. These $MoSe_2$ layers are crystallographically aligned along the *c*-axis so that in specular diffraction patterns, only 00*l* reflections can be found. This intermediate reacts with the remaining copper, molybdenum and selenium at 1200°C to $Cu_xMo_6Se_8$. The precursor forms an amorphous ternary alloy at low temperatures, however, when the thickness of the Mo layer is kept at 12 Å or below. Small reflections can already be found below 170°C that grow in intensity and become sharper with higher temperatures. $Cu_xMo_6Se_8$ fully crystallizes at 912°C without forming $MoSe_2$ as a binary intermediate.[27]

Interdiffusion plays an important role in the formation of the amorphous intermediate since $MoSe_2$ interfacially nucleates at temperatures as low as 200°C.[28] Forming a ternary molybdenum selenide would thus require rapid interdiffusion of the third component with the selenium layer. Elements that only poorly diffuse through selenium such as nickel cannot prevent the formation of interfacial $MoSe_2$, and thus will not form an amorphous alloy. Instead, $MoSe_2$ will nucleate and nickel will then diffuse into the dichalcogenide to form $Ni_xMoSe_2$.[29]

Investigations on MER precursors of the composition $M_xMo_{0.75}Se_1$ (M = Cu, In, Zn) showed very different behaviors for different metals and concentrations of the third component.[29] Samples with copper, which has a higher diffusion rate through selenium than the other metals, crystallized $MoSe_2$ for $x < 0.31$ and nanocrystalline $Cu_xMo_6Se_8$ for higher concentrations above 250°C. At higher temperatures, $MoSe_2$ forms which then reacts to the Chevrel phase at 850°C. The higher the copper concentration is the more depressed is the formation of the dichalcogenide. Indium also diffuses rapidly through selenium and can prevent $MoSe_2$ from crystallizing when $x > 0.36$ to form an amorphous intermediate instead. Annealing the intermediate between 600 and 700°C results in the formation of $In_{3.3}Mo_{15}Se_{19}$. Zinc was only tested for $x > 0.37$, but could prevent the formation of $MoSe_2$ in all cases. It forms a Chevrel phase at 800°C, but $MoSe_2$ forms simultaneously as a second phase.

The general trend is that the higher the concentration of the ternary metal is the higher is the nucleation temperature of interfacial $MoSe_2$. In order to form $MoSe_2$, the precursor needs to rearrange in a way that expels the third component from the $MoSe_2$ nucleus. The higher the concentration of the ternary component, the more energy needs to be expended for this rearrangement. Once the local concentration of the third component is below a critical composition, $MoSe_2$ can form interfacially. This also explains why in some cases, such as in the zinc system, the formation of $MoSe_2$ cannot be prevented: as the Chevrel phase forms, the precursor will become increasingly Zn-poor until it reaches the critical composition. When the zinc concentration decreases further, $MoSe_2$ crystallites can form. In some cases, the nucleation barrier to form the ternary compound

is too high and $MoSe_2$ forms regardless such as for Sn-Mo-Se precursors, which only form the Chevrel phase at 1250°C in a thermodynamically controlled reaction.[29]

The challenge in the MER synthesis has thus shifted from preventing the binary compound that is thermodynamically more stable to form to preventing the binary compound that nucleates more easily to form. One way to achieve this is to use components that need higher nucleation temperatures to form binary compounds or that interdiffuse at temperatures lower than the crystallization temperature of the binary compounds. The $FeSb_3$ skutterudite system is such a system where interdiffusion occurs more rapidly than crystallization. Many metastable filled $FeSb_3$ skutterudites have been synthesized with the MER method, many of which have not been accessible with classic solid state synthesis routes.[30–32]

Another strategy to change the crystallization behavior is to change the layering sequence of the three constituents to avoid interfaces that could crystallize undesired phases. $CuCr_2Se_4$ is a ferromagnetic spinel that can be synthesized with the MER technique, but the precursor structure is important to avoid the formation of binary compounds.[33] As discussed earlier, copper diffuses into selenium layers at room temperature, so an MER precursor with the sequence Cr-Se-Cu-Cr-Se will rapidly nucleate $Cu_{2-x}Se$ ($0 < x \leq 1$). Upon annealing at higher temperatures, more Cu-Se binaries form before reacting with the remaining chromium and selenium to $CuCr_2Se_4$ at 600°C. Chromium obviously diffuses much slower through selenium than copper, which prevents the formation of a homogeneous amorphous intermediate. However, using the layering sequence Se-Cr-Cu-Cr-Se leads to the formation of an amorphous intermediate that crystallizes to $CuCr_2Se_4$ at 400°C in Se vapor without binary compounds as

intermediates. The chromium layers act as a diffusion barrier for copper and can thus prevent the formation of amorphous Cu-Se layers that crystallize to $Cu_{2-x}Se$ at room temperature.

## I.3. Summary and Bridge

The Modulated Elemental Reactants (MER) method was presented as a technique to achieve kinetic control in solid state reactions. It uses a compositionally modulated precursor that consists of atomically thin elemental layers which are synthesized using physical vapor deposition. The deposition parameters need to be calibrated for composition and repeat unit thickness.

Below a critical thickness, these layers interdiffuse rapidly to form an amorphous alloy, which changes the reaction kinetics from being diffusion-limited to being nucleation-limited. The final product is thus controlled by the phase that nucleates quicker and not by the phase that is thermodynamically more stable, i.e., the final product can be controlled with the composition of the precursor.

The synthesis of ternary compounds is more complex and depends on the diffusivity of all three elements. If one element diffuses slower than a binary compound can interfacially nucleate, the amorphous intermediate cannot form. The amorphous intermediate can be formed with elements that diffuse rapidly into Se such as Cu or In, or by using the slower elements as diffusion barriers. The latter will be used in Chapter II to synthesize crystallographically aligned $CuCr_2Se_4$ films.

This dissertation will explore the synthesis, structures, and properties of compounds synthesized with the MER method. The first part, spanning over Chapters I – III, will use the MER rationale and experimental methods to synthesize

crystallographically aligned $CuCr_2Se_4$ thin films and explain their magnetic properties. Chapters IV – VI will introduce ferecrystals, rotationally disordered members of the misfit layer compounds, their isomers and use experimental methods to elucidate the processes involved in the formation of these compounds. The third and last part uses computational methods to explain the behavior of ferecrystals two-dimensional materials.

This chapter and chapters II – VI and VIII – XI of this dissertation contain previously published and/or unpublished co-authored material. The co-authors are, in order of first appearance, David C. Johnson (Chapters II – VI and VIII – XI), Andreas Liebig, Manfred Albrecht (both Chapter II), Jeffrey Ditto (Chapters II, X, and XI), Matthias Falmbigl (Chapters II, VI, and VIII), Irina Edelman (Ирина Эдельман), Gleb Yurkin (Глеб Юркин), Anton Tarasov (Антон Тарасов), Mikhail Rautsky (Михаил Раутский), Mihail Volochaev (Михаил Волочаев), Sergei Lyashchenko (Сергеий Лященко), Ruslan Ivantsov (Руслан Иванцов), Dmitrii Petrov (Дмитрий Петров), Leonid A. Solovyov (Леонид А. Соловьёв, all Chapter III), Zachary Jones, Ngoc T. Nguyen, Michael D. Anderson, Corinna Gosse, Saskia F. Fischer (all Chapter VI), Matti B. Alemayehu (Chapters VI and VIII), Omar K. Hite, Suzannah R. Wood (both Chapter VIII), Richard G. Hennig (Chapters IX and XI), Danielle M. Hamann, Alex C. Lygo, Devin R. Merrill, Duncan R. Sutherland, Sage R. Bauers (all Chapter X), Gavin Mitchson, Erik Hadland, Fabian Göhler, Martina Wanke, Erik Bigwood, Kim Ta, and Thomas Seyller (all Chapter XI). Details regarding the contributions of each author and the bibliographic citation information for these publications can be found at the beginning of each chapter, directly after the chapter title.

# CHAPTER II

# SYNTHESIS, STRUCTURE AND MAGNETIC PROPERTIES OF CRYSTALLOGRAPHICALLY ALIGNED $CuCr_2Se_4$ THIN FILMS

Portions of this chapter was previously published as Esters, M.; Liebig, A.; Ditto, J.J.; Falmbigl, M.; Albrecht, M.; Johnson, D.C. "Synthesis, structure and magnetic properties of crystallographically aligned $CuCr_2Se_4$ thin films" *Journal of Alloys and Compounds*, **2016**, *671*, 220 – 225. M.E. synthesized the samples, did the structural analysis, analyzed the precession electron diffraction (PED) images, performed some magnetic calculations, made all figures except Figure 2.3 and wrote the paper. A.L. performed the magnetic measurements and calculations. J.J.D. performed the PED measurements and assisted with the analysis of the PED images. M.F. performed the Rietveld refinement and made Figure 2.3. M.A. was the principal investigator of A.L., and D.C.J. was the principal investigator of M.E., J.J.D. and M.F. and provided editorial assistance.

## II.1. Introduction

Information technology can be considered one of the key drivers of modern society. With its increasing penetration of modern life comes an ever increasing demand for higher storage capacities, faster data processing and data transmission speeds, and increased information storage lifetimes.[1] Spin-based electronic applications, spintronics, are a promising technology to supply these demands, making research on spin-polarized thin films an important area of research.[1,2] Ideally, spintronic materials exhibit a Curie

temperature considerably above room temperature and strong spin polarizability.[1,2] Because of their relatively high Curie temperatures and good spin polarizability, many oxide materials have been investigated for their magnetic properties and their potential application in spintronic materials.[3,4] Other chalcogenides, however, have only received limited attention as potential spintronic materials.

Chalcogenide chromium spinel materials, $ACr_2X_4$ (A = Cd, Co, Cu, Fe, Hg, Zn; X = S, Se, Te), are especially interesting due to their relatively high Curie temperatures and the capability to accommodate a large variety of atoms in the structure, which has resulted in a large versatility in magnetic, magnetoresistive and electrical properties.[5-26] $CuCr_2Se_4$ is a ferromagnetic compound at room temperature ($T_C > 430$ K[11,13]) and has the highest Curie temperature among non-oxide chalcospinels. It also exhibits metallic transport properties, which makes it an interesting candidate for spin-polarized electronics applications.

Most of the research on $CuCr_2Se_4$ was conducted on bulk or nanocrystalline compounds, but in order to be technologically relevant approaches to prepare thin films of these compounds need to be developed.[11,13,24,27,28] Thin films of $CuCr_2Se_4$, however, have proven to be difficult to synthesize. The first to report films with the composition close to $CuCr_2Se_4$ were Berzhansky *et al.*, yet without structural characterization.[29] Bettinger *et al.* successfully prepared $CuCr_2Se_4$ films with $Cr_2Se_3$ as a secondary phase.[30] Recently, Anderson *et al.* published a method to synthesize highly textured $CuCr_2Se_4$ films by depositing Se-Cr-Cu-Cr-Se multi-layer precursors, but with limited structural characterization and without properties reported.[31]

Here, we report the synthesis of $CuCr_2Se_4$ films using multilayer precursors, the structural characterization of the resulting highly textured films and the correlation of the observed ferromagnetic behavior with the structure. The $CuCr_2Se_4$ films were synthesized using the method employed by Anderson *et al.*[31] Rietveld refinement of specular X-ray diffraction scans shows that the compound crystallizes in a regular spinel structure similar to the bulk material. Specular X-ray diffraction and precession electron diffraction reveal strong crystallographic alignment with the <111> direction perpendicular to the substrate. Random orientation of the crystallites about the <111> axes was observed in the plane of the film. The magnetic properties of the films show anisotropy with an easy axis out of plane. The saturation magnetization is higher than in other $CuCr_2Se_4$ films and the bulk compound.

## II.2. Experimental

Multi-layer precursors were prepared using a custom-built physical vapor deposition chamber modeled after a similar chamber described previously.[32] Cr and Cu were evaporated using an electron beam source, and Se was deposited using an effusion cell under a vacuum of less than $5 \times 10^{-7}$mbar. Relative thicknesses of the elements were calibrated to yield compositions close to that of the desired $CuCr_2Se_4$ stoichiometry. (100)-oriented Si was used as substrate material. The total film thickness of the precursors according to X-ray reflectivity were approximately 50 nm. The unit thickness of the repeated Se-Cr-Cu-Cr-Se layers was approximately 1.6 nm.

The precursors annealed on a custom-made hot plate under a nitrogen atmosphere (< 0.6 ppm) at temperatures ranging from 400 °C to 600 °C yielded samples of poor quality due to Se loss. Samples were therefore annealed in a sealed fused silica

tube ($p \approx 10^{-5}$ mbar) at 400 °C for 24 h, 48 h, and 96 h. CuSe powder (99.5%, *Alfa Aesar*) was added to generate a positive Se vapor pressure in order to prevent the evaporation of Se off the film.

The structure of the films was probed using X-ray diffraction (XRD) and electron microscopy techniques. XRD patterns were collected under specular and off specular conditions using a Rigaku Smartlab. Off specular scans were done in grazing incidence (GIXRD) and grazing incidence in-plane geometry (in-plane XRD). The lattice parameters of the samples were determined from the specular XRD pattern with a least square refinement method using WinCSD software suite.[33] The structure of the sample annealed for 24 h was also refined using the Rietveld method and the FullPROF software suite.[34,35] In order to determine a map of the crystallographic alignment of the crystallites in the film, precession electron diffraction measurements were performed at the Pacific Northwest National Laboratory using a JEOL JEM-3000SFF.

Magnetic properties were measured using a Quantum Design MPMS3. Temperature-dependent magnetization measurements were carried out for the sample annealed for 24 h from 4.2 K to 400 K. The sample annealed for 24 h was additionally measured from 300 K to 450 K. Magnetization hysteresis curves were recorded as a function of external field strength at 300 K.

## II.3. Results and Discussion

*Structural Characterization*

Representative diffraction patterns for the synthesized compounds are shown in Figures 2.1 and 2.2. The specular XRD scans, shown in Figure 2.1, contain three reflections that can be indexed with (*hhh*) (*h* = 1, 2, 4) indices of the spinel structure,

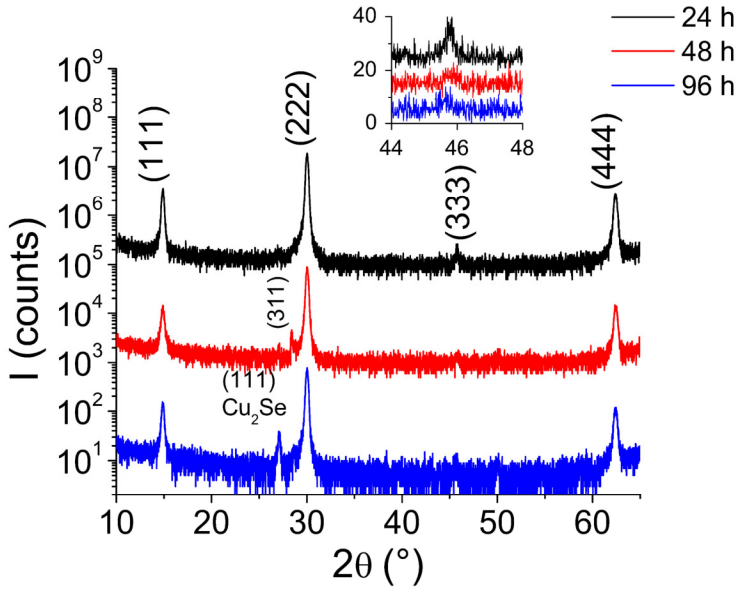


**Figure 2.1.** Specular diffraction patterns of $CuCr_2Se_4$ samples annealed for 24 h, 48 h, and 96 h. The inset shows the intensity of the (333) reflection. Offsets added for clarity.

**Figure 2.2.** In-plane XRD (a) and GIXRD (b) patterns of $CuCr_2Se_4$ films annealed for 24 h, 48 h, and. 96 h. Reflections denoted by an asterisk are reflections from the substrate. The inset shows the intensity of the (222) reflection in the in-plane XRD scan.

suggesting a crystallographically aligned structure. The samples annealed for 24 hours are the most crystallographically aligned. Rocking curves around the (222) reflection show an increase of the FWHM as annealing time is increased from 24 h (5.3°) to 48 and 96 h (5.6°). The FWHM of all samples are slightly smaller than the thin films synthesized

by Anderson *et al.*, indicating stronger crystallographic alignment.[31] The specular scan for the sample annealed for 24 hours has the highest intensity with a weak reflection with $h = 3$. In the diffraction patterns for the samples annealed for 24 h and 48 h, only reflections of normal spinel $CuCr_2Se_4$ ($Fd\bar{3}m$) are observed. Thus, according to x-ray diffraction, the films are pure $CuCr_2Se_4$. The sample annealed for 96 h also shows an additional reflection, which is consistent with the (111) reflection of cubic $Cu_2Se$. The in-plane XRD and GIXRD patterns (Figure 2.2) can all be indexed to the regular spinel structure ($MgAl_2O_4$-type, $Fd\bar{3}m$).

The diffraction patterns show small changes as the samples are annealed for longer times. There is a small shift in the lattice parameters when the sample is annealed, changing from 10.315(3) Å to 10.306(1) Å to 10.309(1) Å for the samples annealed for 24 h, 48 h, and 96 h respectively. These values are all smaller than the reported value for single crystalline $CuCr_2Se_4$ (10.337(6) Å).[36] The decrease in intensity of the (*hhh*) reflections in conjunction with the wider rocking curve widths with increasing annealing time suggests a loss of crystallographic alignment over time. The in-plane XRD patterns (Figure 2.2a) confirm the loss of crystallographic alignment. The in-plane diffraction pattern of the sample annealed for 24 h does not show (*hhh*) reflections. The (440) reflection on the other hand is very intense, showing that the {440} planes, which are perpendicular to the {*hhh*} planes, are strongly aligned perpendicular to the substrate surface. The strong intensity of the (222) reflection and the absence of the (440) reflection in the specular XRD pattern and vice versa in the in-plane XRD show that the sample is crystallographically aligned along the <111> axes. The in-plane XRD pattern of the sample annealed for 48 h contains the (222) reflection and the intensity of

the (440) reflection is decreased. The specular diffraction pattern also contains the (311) reflection, even though only visible in a logarithmic scale. This suggests that the sample is less crystallographically aligned than the sample annealed for 24 h, which correlates well with the decreased intensities in the specular XRD patterns (Figure 2.1) and the overall increased intensities in the GIXRD pattern (Figure 2.2b). The absence of the (440) reflection in the specular XRD pattern suggests that the sample is still strongly aligned. The sample annealed at 96 h, however, has lower intensities than the sample annealed at 48 h, along with an additional reflection in the specular XRD consistent with the (022) reflection of $Cu_2Se$. In the in-plane XRD, the (222) reflection is present, but less intense than for the sample annealed for 48 h. We attribute this decrease in intensity to a reduced degree in crystallinity.

Since the $CuCr_2Se_4$ film annealed for 24 h is layered along the [111] direction, and hence, only contains information on the distances between atomic planes along this direction, a simple one-dimensional model can be used to refine the specular diffraction scan. Figure 2.3 shows the Rietveld refinement of the specular scan of the sample annealed for 24 h. Considering instead of atomic positions only atomic planes, the length of the repeat unit along the [111] direction is $\frac{\sqrt{3}a}{3}$ and in addition contains a mirror plane as indicated in the structural scheme in Figure 2.3. Using the bulk crystal structure[36] as a model, the only refinable parameter is the position of the plane of the Se-atoms. The structure was modeled in the trigonal space group $P\bar{3}m1$as this space group has a mirror plane at 0.5 in the z-direction, and detailed results are provided in Table 2.1. The structural refinement resulted in low *R*-values ($R_F$=0.054 and $R_I$=0.015) and a reasonable position of the Se-plane (0.2446(2) compared to 0.2426 for the single crystal[36])

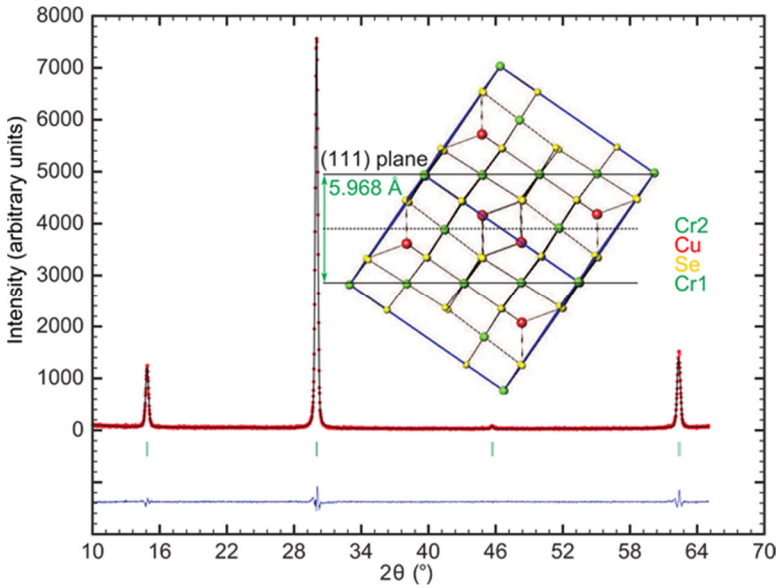


**Figure 2.1.** Rietveld refinement of the sample annealed for 24 h. The inset shows the layered model that was used for the refinement of the atomic planes along the [111] direction. The solid lines indicate the length of the repeat unit corresponding to $\frac{\sqrt{3}a}{3}$ and the dashed line displays the position of the mirror plane. The red, black and blue line show the measured intensity, the calculated intensity and the intensity difference, respectively.

confirming the presence of a $CuCr_2Se_4$ structure in the thin film. Converting the thickness of the repeat unit yields a lattice parameter of the 10.3159(7) Å compared to 10.337(6) Å for the single crystal. This is the first time that cell parameters for a $CuCr_2Se_4$ thin film sample have been reported.

Precession electron diffraction images were taken to qualitatively assess the degree of alignment of the crystallites in the film. The sample was aligned so that the z-direction is parallel to the surface normal of the film. A representative image is shown in Figure 2.4. The grains exhibit a variety of sizes, but are on average 80 nm across. The colors of the grains predominantly show light blue and purple shades, showing that the grains are mostly aligned along or close to the <111> axes. The pole figures show a homogeneous distribution of different crystallographic alignments along the x and y axis

**Table 2.1.** Rietveld refinement results for the $CuCr_2Se_4$ thin film annealed for 24h.

| | |
|---|---|
| Composition from refinement | $CuCr_2Se_4$ |
| Radiation | Rigaku Smartlab, Cu $K_\alpha$ |
| $2\theta$ range (degrees) | $10 \leq 2\theta \leq 65$ |
| Repeat unit thickness (Å) | 5.9559(4) |
| Reflections in refinement | 4 |
| Number of variables | 9 |
| $R_F = \Sigma \mid F_o - F_c \mid / \Sigma F_o$ | 0.015 |
| $R_I = \Sigma \mid I_o - I_c \mid / \Sigma I_o$ | 0.054 |
| $R_{wP} = [\Sigma w_i \mid y_{oi} - y_{ci} \mid^2 / \Sigma w_i \mid y_{oi} \mid^2]^{1/2}$ | 0.101 |
| $R_P = \Sigma \mid y_{oi} - y_{ci} \mid / \Sigma \mid y_{oi} \mid$ | 0.064 |
| $R_e = [(N-P+C)/(\Sigma w_i y^2_{oi})]^{1/2}$ | 0.0707 |
| $\chi^2 = (R_{wP}/R_e)^2$ | 5.5 |
| **Atom parameters** | |
| Cr1 in 1*a*(0) | |
| Occ. | 1.0 |
| Se1 in 2*c* (*z*), *z* | 0.2446(2) |
| Occ. | 4.0 |
| Cu in 2*c* (*z*), *z*=0.375 | |
| Occ. | 1.0 |
| Cr2 in 1*b* (0.5) | |
| Occ. | 1.0 |

(in plane) and a large concentration around the <111> directions along the z axis. The deviations from a pure alignment along the <111> axes are likely due to imperfect sample alignment during the TEM experiment.

The crystallographic alignment may be due to the surface energies in $CuCr_2Se_4$. The natural cleavage surface of single crystal $CuCr_2Se_4$ is the (111) plane, indicating that

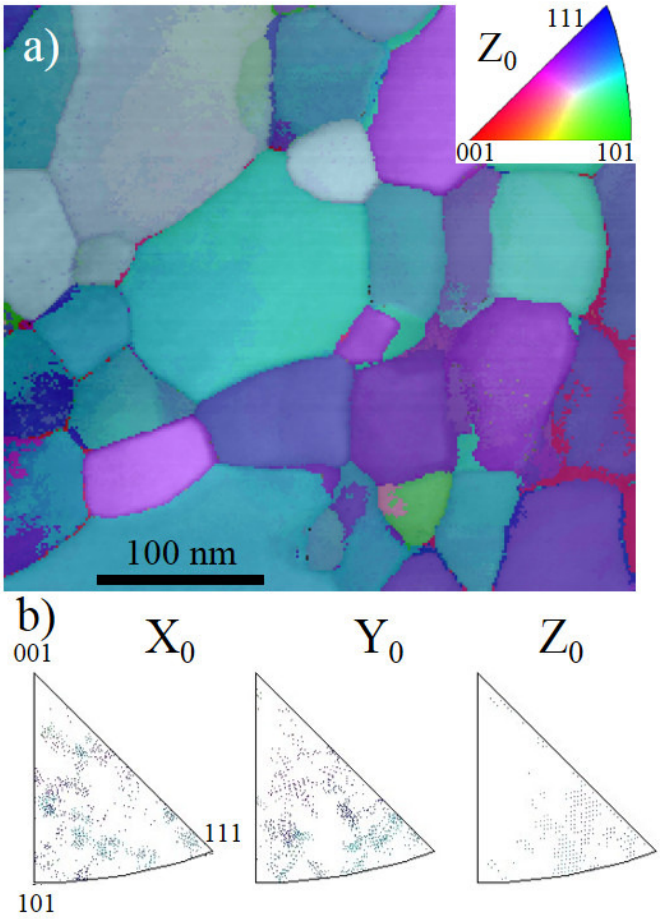


**Figure 2.2.** (a) Map of crystallographic orientations from precession electron diffraction. (b) Orientation distribution along the x, y, and z axis (z axis parallel to surface normal of the film).

this surface has the lowest surface energy.[37] Due to the mild reaction conditions, the main driving force of the $CuCr_2Se_4$ formation may be nucleation and Ostwald ripening. In order to minimize their surface energy, nuclei grow in a preferred orientation, forming crystallographically aligned films.

*Magnetic Properties*

Temperature-dependent magnetization curves (Figure 2.5) show Brillouin-type behavior. The Curie temperature of the sample annealed for 24 h is 406 K, which is comparable to Bettinger *et al.* ($T_c$ = 405 – 410 K), but lower than the Curie temperature

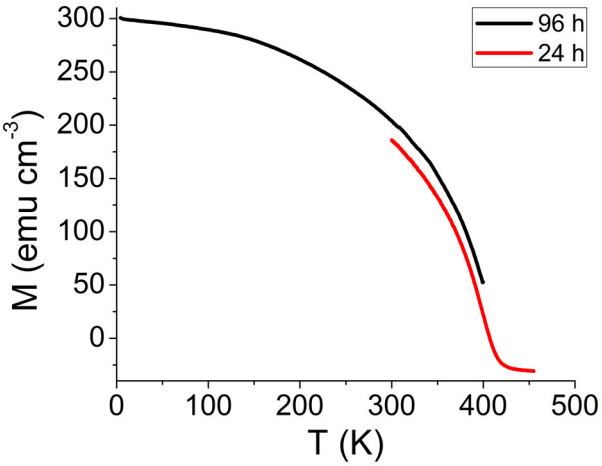


**Figure 2.3.** Representative temperature-dependent magnetization curves for samples annealed for 24 h, and 96 h.

found in bulk ($T_c$ > 430 K).[11,13,30] In-plane and out of plane magnetization curves of $CuCr_2Se_4$ films were measured at room temperature (Figure 2.6). They show the hysteresis behavior characteristic of a ferromagnetic compound.

The magnetization shows saturations at an external magnetic field of 2 kOe. At 4.2 K, the saturation magnetization of the samples annealed for 24 h and 48 h are 413 emu/cm$^3$ and 448 emu/cm$^3$, respectively, which corresponds to 6.1 $\mu_B$/f.u. and 6.6 $\mu_B$/f.u., respectively. These values are higher than in bulk and in the thin films found by Bettinger (4.5 – 5.0 $\mu_B$/f.u.).[11,13,30] Colminas predicted a moment of 6 $\mu_B$/f.u. under the assumption that Cr is present as $Cr^{3+}$ and Cu is present as $Cu^+$.[38] DFT calculations conducted by Bettinger *et al.* suggest that the increase in the magnetization may be due to Se deficits.[30] Doping experiments with $Br^-$ ions also showed that a decrease in the Se concentration correlates with stronger magnetization due to a decrease in $Cu^{2+}$ concentrations and thus an increase in the $Cu^+$ concentration.[37] Thus, our films may have a significant amount of $Cu^+$ ions and defects on Se sites. Another factor for this increased magnetization may be

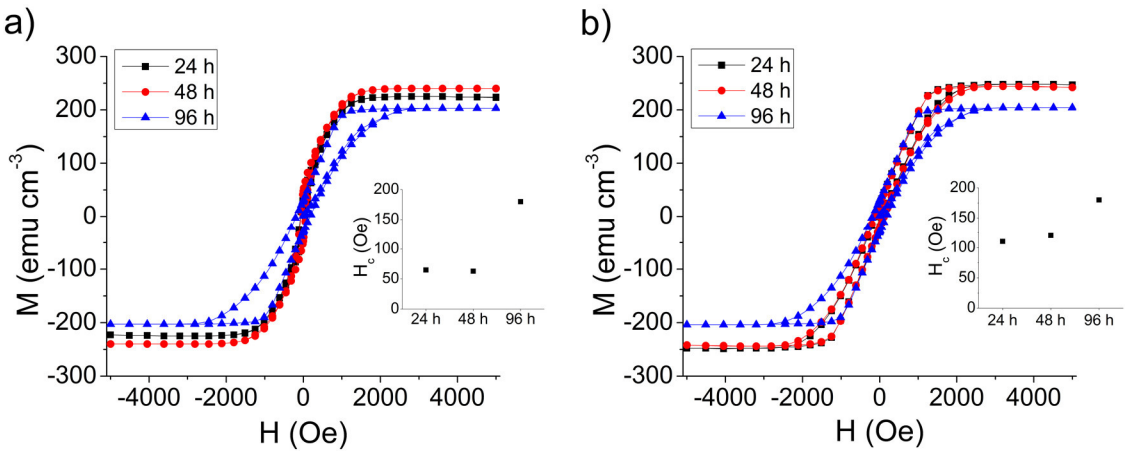


**Figure 2.4.** Room temperature magnetization hysteresis (a) in plane and (b) out of plane. The insets show the coercive forces $H_c$ as a function of annealing time.

the orbital momentum of the chromium ions. A not fully quenched orbital angular momentum, would increase the magnetization per formula unit compared to the spin-only magnetism. A stronger influence of the orbital angular momentum would also contribute to magnetic anisotropy. However, this effect is expected to be very small. The saturation magnetization is significantly lower for the sample annealed for 96 h (253 emu/cm$^3$ or 3.7 $\mu_B$/f.u.), which is probably due to the $Cu_2Se$ impurity or lower degree of crystallization.

The saturation moment, coercitivity and remanence are larger out of plane than in plane, suggesting anisotropy in the films. The effective anisotropy for the sample annealed for 24 h is $1.82\times10^6$ erg cm$^{-3}$ with the easy axis being out of plane, i.e. along the <111> axes. The sample annealed for 48 h shows a stronger effective anisotropy with $2.6\times10^6$ erg cm$^{-3}$. Due to higher magnetization, the shape anisotropy is also higher for the sample annealed at 48 than for 24 h with $1.26 \times 10^6$ erg cm$^{-3}$ and $1.07 \times 10^6$ erg cm$^{-3}$, respectively. The anisotropy shown is stronger than in the single crystals and may be due to strain inside the sample or a stronger influence of the orbital angular momentum,

which is typically stronger along the easy axis of magnetization.[13] This is the first time, magnetic anisotropies are published in $CuCr_2Se_4$ thin films, so no comparison with other films can be made.

Anisotropy is also observed in the coercive forces. The insets of Figure 2.6 show the coercive force $H_c$ as a function of annealing time and show an increase in the coercive force for the out-of-plane magnetization with increasing annealing time. While the difference between the sample annealed for 24 h and 48 h is rather small (10 Oe), there is a strong increase for the sample annealed for 96 h (60 Oe difference to 48 h). For the in-plane magnetization, $H_c$ is approximately the same for the samples annealed for 24 h and 48 h (65 Oe and 63 Oe, respectively), the sample annealed for 96 h has a much larger $H_c$ (180 Oe). For the samples annealed at 24 h and 48 h, $H_c$ is larger for the out-of-plane than for the in-plane magnetization. This phenomenon can be explained by the different degrees of crystallographic alignment and crystallinity. The coercive force increases with increasing defect and domain wall concentrations. X-ray diffraction has shown that the sample annealed for 96 h is less crystalline and less aligned than the other samples and thus has larger coercive forces than the samples annealed for 24 h and 48 h. The lack of anisotropy in the coercive force shows the reduced degree in crystallinity as there are more defects in the entire film. The in-plane coercive forces for the samples annealed at 24 h and 48 h are approximately the same, whereas they are higher in the out-of-plane magnetization for the sample annealed for 48 h. As shown by PED, the films are aligned along the [111] direction, but are rotationally disordered in the perpendicular plane. The consequence of this rotational disorder are abrupt interfaces between individual $CuCr_2Se_4$ slabs, which are not present within the plane. This and the easy axis of magnetization,

which is out-of-plane, elevate the out-of-plane $H_c$ compared to the in-plane $H_c$. The fact that the in-plane $H_c$ are approximately the same for the samples annealed for 24 h and 48 h and much smaller than for the sample annealed for 96 h shows that both have a similar defect concentrations and are well crystallized within the plane. Lower degree of crystallographic alignment, potentially stronger rotational disorder, and increased magnetization all contribute to a larger $H_c$, which explains why the out-of-plane $H_c$ for the sample annealed for 48 h is larger than $H_c$ for the sample annealed for 24 h.

## II.4. Conclusions and Bridge

This chapter showed the successful synthesis of $CuCr_2Se_4$ films aligned along the <111> axes at a relatively low temperature of 400 °C. The degree of crystallographic alignment decreases with time while annealing at elevated temperatures. These films are ferromagnetic up to a temperature of 406 K. Films exhibit anisotropic magnetism with the easy axis lying along the <111> axes. The saturation magnetization is higher than in bulk $CuCr_2Se_4$ and in other $CuCr_2Se_4$ films. The none-forced preferred orientation and the ability to deposit thin layers may open the pathway to magnetic intergrowth compounds with interesting magnetic properties.

The enhanced magnetic properties of these films raise interesting questions about the mechanism of magnetization in these films. Chapter III will include an in-depth discussion about the magnetization processes in these films and reveal a competition between two forms of magnetization that are dominant in different temperature ranges.

# CHAPTER III

# THE COMPETITION BETWEEN MAGNETOCRYSTALLINE AND SHAPE ANISOTROPY ON THE MAGNETIC AND MAGNETO-TRANSPORT PROPERTIES OF CRYSTALLOGRAPHICALLY ALIGNED $CuCr_2Se_4$ THIN FILMS

Portions of this chapter were previously published as Edelman, I.; Esters, M.; Johnson, D.C.; Yurkin, G.; Tarasov, A.; Rautsky, M.; Volochaev, M.; Lyashchenko, S.; Ivantsov, R.; Petrov, D.; Solovyov, L.A. "The competition between magnetocrystalline and shape anisotropy on the magnetic and magneto-transport properties of crystallographically aligned $CuCr_2Se_4$ thin films" *Journal of Magnetism and Magnetic Materials*, **2017**, *443*, 107 – 115. M.E. synthesized the samples, and co-wrote the paper with I.E. D.C.J. was the principal investigator of M.E. and provided editorial assistance. I.E. analyzed the magnetic measurement data and co-wrote the article with M.E. R.I. assisted with data analysis and D.P. calculated anisotropy data. The measurements were performed by G.Y. (magnetometry), A.T. (magneto-resistivity), M.R. (ferromagnetic resonance), M.V. (electron microscopy), S.L. (Kerr spectra), and L.A.S. (x-ray diffraction).

## III.1. Introduction

The development of spintronics based on the use of the electron spin degrees of freedom requires an effective search for new materials with high spin polarization.[1] Until recently, oxide compounds such as $Cr_2O_3$, $Fe_3O_4$, $La_{0.7}Sr_{0.3}MnO_3$, etc. were mainly considered as materials for spintronic devices.[2-4] In recent years, more and more attention

has been drawn to complex chalcogenides. It can be expected that the transition from ionic bonds in oxides to more covalent bonds in chalcogenides will result in transport properties similar to the properties of semiconductors or metals. One of the most promising groups of materials for this task are the chalcogenide chromium spinels of the general formula $MCr_2X_4$ (where M = Cd, Co, Cu, Fe, Hg, Zn, and X = S, Se, Te). Many of them have Curie temperatures above room temperature and possess the ability to include a wide variety of atoms into their structure, which leads to diverse magnetic, magneto-resistive and electrical properties.

$CuCr_2Se_4$ stands out from the whole series of chromium chalcogenides: It has the highest Curie temperature ($T_C \sim 430$ K) and metallic conductivity, which makes it a promising candidate for applications in spintronics. $CuCr_2Se_4$ is characterized by the highest value of the magneto-optical Kerr effect in the near infra-red (1.1° for 0.8 eV and 0.6° for 1.25 eV at 295 K[5]), and is found to undergo light-induced changes in the magnetization.[3] Studies of this compound were carried out mainly on bulk crystals[6-11] or nanocrystalline powders.[12-22] However, most suitable for spintronic applications are samples in the form of thin films that can be integrated into silicon based structures.

Only few articles in the literature are devoted to $CuCr_2Se_4$ films. The first attempt to synthesize polycrystalline $CuCr_2Se_4$ films was undertaken in 1990 by Berzhanski *et al.*[23] In 2007, Bettinger *et al.* synthesized $CuCr_2Se_4$ films by pulsed laser deposition on isostructural $MgAl_2O_4$ substrates. X-ray diffraction confirmed the structure of $CuCr_2Se_4$ along with secondary phases of $Cr_2Se_3$, $CuCrSe_2$, and $Cr_{2.8}Se_4$.[24] Anderson with co-authors suggested the modulated elemental reactants (MER) method[25,26] to fabricate single-phase films of the ternary chalcogenide compounds. This method was applied

successfully to synthesize crystallographically aligned $CuCr_2Se_4$ thin films consisting of large enough crystallites (several hundred nanometers in lateral dimension) with the (111) planes oriented parallel to the film plane.[27] The almost homogeneous orientation of the (111) planes of the crystallites in combination with a large negative magneto-crystalline anisotropy that depends strongly on temperature[12] creates conditions where this anisotropy competes with the easy-plane anisotropy characteristics of thin films, which raises promises new interesting effects in the aligned films.

In this paper, we present the magnetic, magneto-optic, and magneto-transport properties of crystallographically aligned $CuCr_2Se_4$ thin films synthesized with MER technique.[27] X-ray diffraction and high-resolution electron microscopy study confirmed almost ideal orientation of the crystallite (111) planes inside the film plane. Magneto-optic transverse Kerr effect spectra appear to be close in shape to the polar Kerr effect spectra of bulk $CuCr_2Se_4$, suggesting identical electronic structures. Magnetic measurements carried out between 4.2 and 300 K revealed their magnetic properties to be governed by the competition between the magnetocrystalline and shape anisotropy, and that the predominant mechanism of magnetization depends on the temperature with a transition at around 155 K. The microwave and magneto-transport temperature changes correlate with that of the static magnetization. These results show that the $CuCr_2Se_4$ samples studied herein provide an unusual opportunity to probe the competition between anisotropies of different origin on the magnetic properties of a thin film.

## III.2. Experimental

Films were synthesized using the Modulated Elemental Reactants (MER) method as outlined in Ref. 27, using multi-layer precursors with the sequence Se-Cr-Cu-Cr-Se. The precursors were deposited onto (100)-oriented Si wafers in a custom-built physical vapor deposition chamber with pressures inside the vacuum chamber of less than $5 \times 10^{-7}$ mbar.[28] Se was evaporated using a resistive heater effusion cell, and Cr and Cu were deposited using electron beam guns. The total film thickness of the precursors was approximately 50 nm, and the thickness of the repeated Se-Cr-Cu-Cr-Se layers was approximately 1.6 nm. Relative thicknesses of the elements were calibrated to yield compositions close to that of the desired $CuCr_2Se_4$ stoichiometry. Samples were annealed in an evacuated ($p \approx 10^{-5}$ mbar), sealed fused silica tube at 400 °C for 1, 2, and 3 days (samples 1, 2, and 3, respectively). CuSe powder (99.5%, Alfa Aesar) was added to generate a positive Se vapor pressure in order to prevent the evaporation of Se off the film.

The structure of the films was determined using X-ray diffraction (XRD) and electron microscopy techniques. XRD patterns were collected using a PANalytical X'Pert PRO (Cu Kα) diffractometer in the angular range $2\theta = 10° - 65°$. The lattice parameters of the samples were refined using the full-profile derivative difference method.[29] Cross-sections of the samples were prepared by focus ion beam (FIB) using a FB2100 (40 kV accelerating voltage) with subsequent Ar+ polishing at 0.5 kV. Film cross-section images were obtained with Hitachi HT7700 (W-source) transmission electron microscope (TEM) at 110 kV accelerating voltage. Magnetization hysteresis loops were recorded with a

QUANTUM Design MPMS-XL system at temperatures between 4.2 and 300 K with magnetic fields applied parallel and perpendicular to the film plane.

Magneto-transport properties were studied using a homebuilt facility based on a helium cryostat, an electromagnet and a Keithley 2400 Source Meter.[30] Magnetoresistance (MR) was measured between 4.2 and 70 K using a standard four-probe technique. MR was defined as:

$$\mathrm{MR}(H) = 100\% \cdot \frac{R(H) - R_{\max}}{R_{\max}} \tag{3.1}$$

where $R(H)$ is the resistance at an external magnetic field strength $H$, and $R_{\max}$ is the maximum resistance. In the experiment, electric current flowed inside the film plane, and the magnetic field direction changed from $\theta = 0°$ to $\theta = 180°$ degrees relatively to the normal ($\vec{n}$) of the film plane.

Ferromagnetic resonance spectra were collected between 120 and 350 K with a Bruker Elexsys E580 spectrometer, operating at the X-band (9.7 GHz) and using 100 kHz as the modulation frequency.

Magneto-optical transverse Kerr effect (TKE) measurements were carried out in the region of 1.25 - 4.25 eV using an Ellips-891 high speed spectral ellipsometer in an experimental setup described elsewhere.[31] The relative changes of the intensity of the linearly polarized light reflected from the sample surface when changing the direction of the external magnetic field were used as the measured values:

$$\frac{\delta I}{I}(\theta_1, \theta_2) = 2\frac{I_\uparrow - I_\downarrow}{I_\uparrow + I_\downarrow} \tag{3.2}$$

where $I_\uparrow$ and $I_\downarrow$ are the intensities of the light incident on the photodetector at the sample during magnetization reversal, θ1 = –45° and θ2 = +45° are the angles of the

polarizer and analyzer rotation relative to the light incidence plane of the sample. The angle of the light incidence with respect to the normal of the film surface was 70°. The magnetic field strength parallel to the film surface changed from +3 to -3 kOe. To minimize the error in the determination of δI/I, the measurements of $I_{\uparrow}$ and $I_{\downarrow}$ were performed 10 times, followed by the calculation of the mean values $\langle I_{\uparrow} \rangle$ and $\langle I_{\downarrow} \rangle$, as well as mean-square deviations $\Delta I_{\uparrow}$ and $\Delta I_{\downarrow}$. The magnetic field dependence of δI/I of each sample were obtained for several wavelengths.

## III.3. Results and Discussion

*Structure of the $CuCr_2Se_4$ Films*

The X-ray diffraction patterns of three $CuCr_2Se_4$ films annealed for different periods are shown in Figure 3.1. The reflections of all samples match completely with $CuCr_2Se_4$ spinel structure ($Fd\bar{3}m$, no. 225, JCPDS 33-0452). The reflections can be indexed with the (*hhh*) (*h* = 1, 2, 4) indices of the spinel structure, suggesting a crystallographically aligned structure. Comparing the diffraction patterns shown in Figure 3.1 with the XRD patterns presented in Ref. 27 for the $CuCr_2Se_4$ films synthesized with the same method, one can note some minor differences. Intensities of all reflections for samples 1 and 2 are close to each other, while they are noticeably lower for sample 3. However, no additional reflections are seen for sample 3 compared to samples 1 and 2. The lattice parameters are also close for samples 1 and 2 with 10.310(1) Å and 10.311(1) Å, respectively. For sample 3, the lattice parameter is 10.307(1) Å. The lattice parameters shown for samples 1 and 2 in Ref. 27 were 10.315(3) Å and 10.306(1) Å. The minor differences in the characteristics of the samples synthesized here and presented in Refs. 26 and 27 fabricated with the same method are well within the experimental errors.

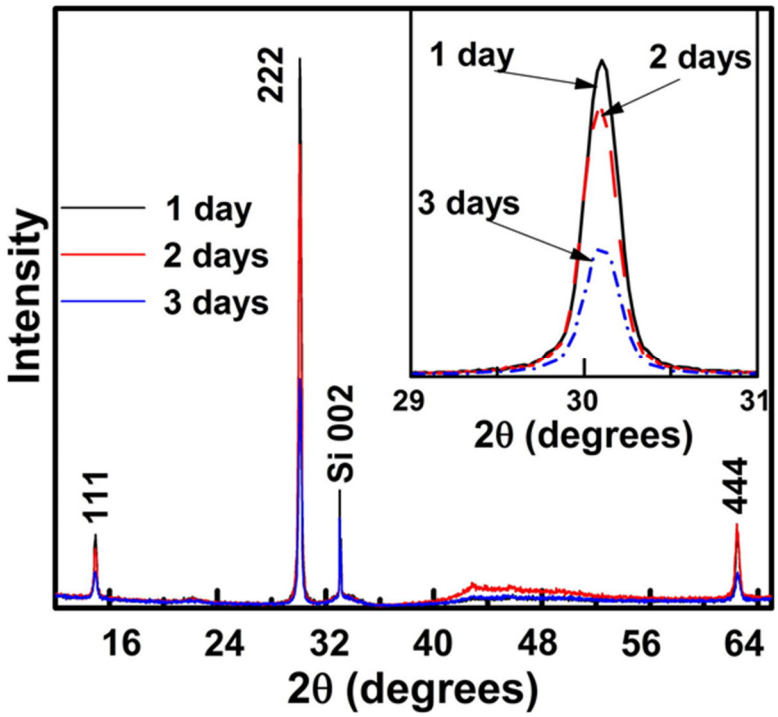


**Figure 3.1.** X-ray diffraction pattern of three $CuCr_2Se_4$ films annealed for 1, 2, and 3 days. Inset: enlarged region near 2θ = 30°.

TEM and High-resolution TEM (HRTEM) measurements show that the films consist of well-shaped rectangular nanocrystals with lateral dimensions of a few hundred nanometers and a thickness of 50 nm (Figures 3.2a and b). The space between two adjacent lattice planes in the direction perpendicular to the film surface is 2.68 Å, which is characteristic for the interplanar (111) distance in the face-centered cubic phase of

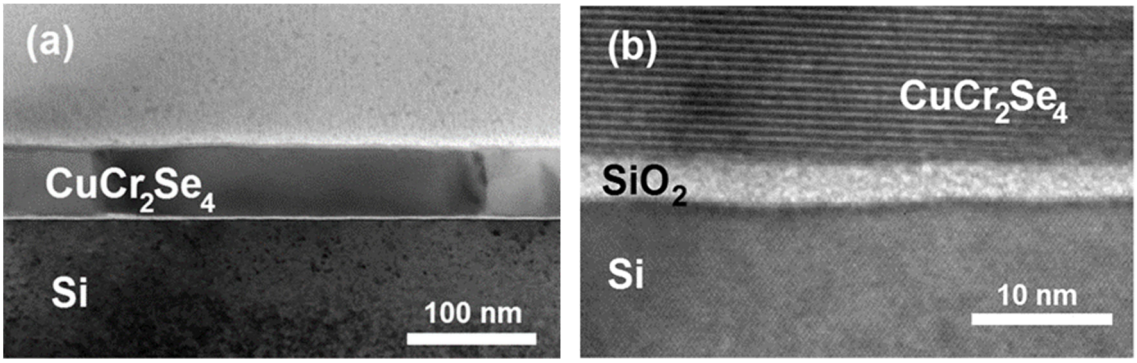


**Figure 3.2.** TEM (a) and HRTEM (b) images of the cross-section of sample 1.

$CuCr_2Se_4$. The X-ray diffraction and HRTEM data are consistent with the films consisting of pure $CuCr_2Se_4$ nanocrystals with the (111) planes oriented parallel to the film surface. Apart from the degree of crystallographic alignment, only insignificant differences are seen between the structural characteristics of films with different annealing times.

*Magnetic Hysteresis Loops*

Figure 3.3 shows the magnetization temperature dependence for sample 1 showing the Brillouin-type behavior. For the other two samples, the $M(T)$ curves are analogous. The Curie temperature is $T_C$ = 420 K, which is a little bit higher compared to those presented for thin films ($T_C$ = 405 – 410 K),[24,27] but lower than the $T_C$ found in bulk ($T_C$ > 430 K).[12]

The magnetization of the films parallel and perpendicular to the film plane as a function of the external magnetic field $H$ were identical for all samples, and representative data from sample 1 at different temperatures are shown in Figure 3.4. We will focus on the data for sample 1 because it has the highest degree of crystallographic

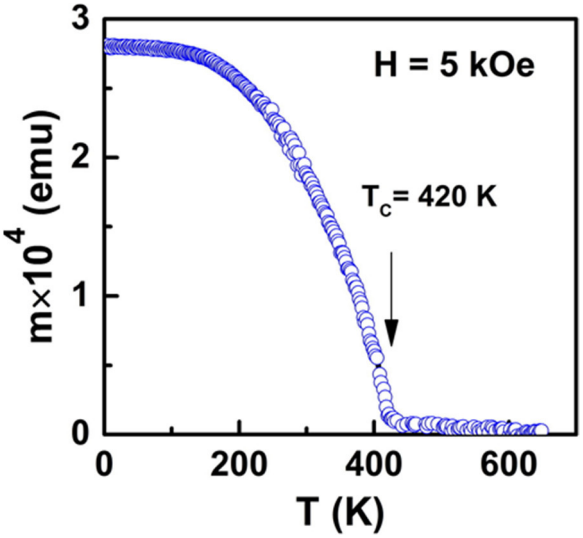


**Figure 3.3.** Temperature-dependent magnetization curve for sample 1.

alignment compared to the other samples. At room temperature, relatively narrow hysteresis loops close in shape to those presented in Ref. 27 are observed for both orientations of an external magnetic field, parallel and perpendicular to the films surface (curves 1 in Figures 3.4a and 3.4b). Room temperature coercive fields $H_c$ are of 140 Oe, 135 Oe, and 150 Oe (for samples 1, 2 and 3, respectively). The only noticeable difference between hysteresis loops recorded at the two magnetic field directions is the magnetization behavior in relatively high magnetic fields. While in the parallel geometry, magnetic saturation occurs at $H$ = 2.0 kOe, for the perpendicular geometry, saturation is not reached at $H$ = 5 kOe.

A decrease in temperature results in strong changes in the shape of the magnetization curves. For the parallel magnetic field direction, the coercive field decreases slightly and the magnetization does not reach saturation up to $H$ = 5 kOe (Figure 3.4a), while for the perpendicular magnetic field direction, the coercivity increases approximately an order of magnitude from 140 Oe to 1.6 kOe when

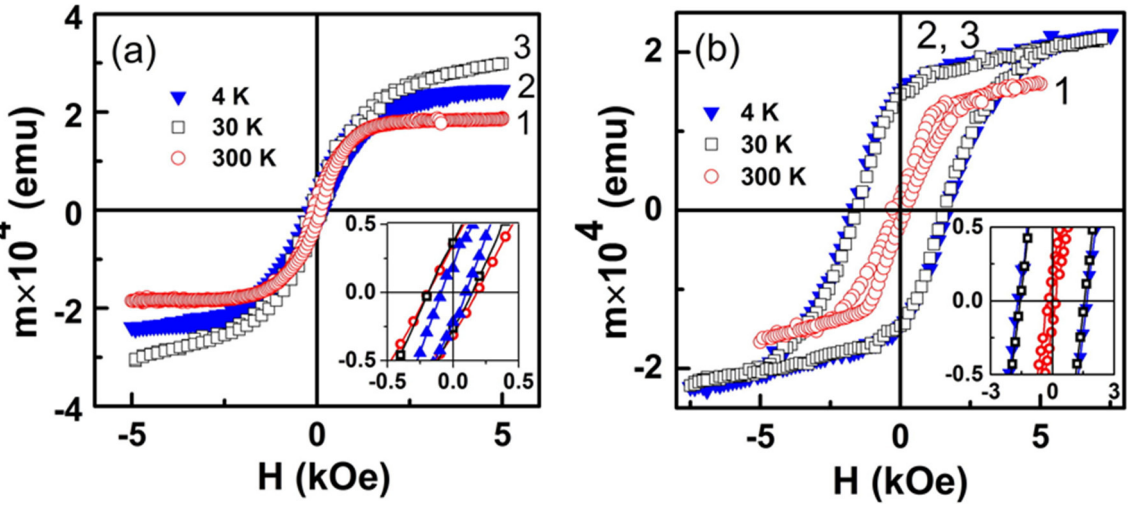


**Figure 3.4.** Magnetization curves of sample 1 recorded for the external magnetic field directions parallel (a) and perpendicular (b) to the film plane at 300, 30, and 4.2 K. Insets: enlarged regions of lower fields.

the temperature decreases from 300 to 4.2 K (Figure 3.4b). The area of the hysteresis loop increases from 7 emu Oe to 56 emu Oe for the perpendicular geometry and stays almost unchanged in the parallel geometry. These changes can be explained with the coexistence of two types of magnetic anisotropy in the $CuCr_2Se_4$ films: the shape anisotropy, which tends to orient the magnetic moment inside the film plane, and the magneto-crystalline anisotropy, which tends to orient the magnetic moment along one of the easy axes. These two types of anisotropy possess different temperature dependences. The field of the in-plane shape anisotropy $H_{sh}$ is described by the equation:

$$H_{\mathrm{sh}} = 4\pi M_s \tag{3.3}$$

where $M_s$ is the saturation magnetization, so its temperature dependence is determined by the temperature dependence of $M_s$. As it is shown in Ref. 27, the magnetization of the film increases strongly near the Curie temperature (420 K) and changes insignificantly with decreasing temperature below 300 K.

The magneto-crystalline anisotropy of $CuCr_2Se_4$ is characterized by easy magnetization axes oriented parallel to the <111> crystal axes and by a very strong temperature dependence of the anisotropy parameter. $K_1$, the first anisotropy constant, increases almost one order of magnitude with the temperature decreasing from 300 to 5 K ($K_1 = -6.9 \times 10^5$ erg/cm$^3$ at 5 K, and $K_1 = -0.9 \times 10^5$ erg/cm$^3$ at 290 K[12]). In cubic crystal lattices, there are four crystal axes of the <111> family, one with an angle of 90° and three oriented at an angle $\alpha = 19.5°$ relative to the (111) crystal plane, i.e. the film's plane. A schematic of these easy axes orientations is presented in Figure 3.5a. The crystal anisotropy field is given by

$$H_{\mathrm{K}} = \frac{2K_1}{M_s} \tag{3.4}$$

Both $M_s$ and $K_1$ are temperature dependent. Figure 3.5b illustrates the $H_{sh}$ and $H_K$ temperature dependences calculated for the $CuCr_2Se_4$ thin films using the temperature dependence of $M_s$ taken from Ref. 27 and the temperature dependence of $K_1$ taken from Ref. 12. While the temperature dependence of $K_1$ for these films may be different (magnetocrystalline anisotropy measurements are ongoing), Figure 3.5b can provide a good qualitative picture of the temperature dependence of $H_{sh}$ and $H_K$. The shape anisotropy is nearly temperature independent and $H_{sh}$ increases only slightly when the temperature decreases from 300 K to ~160 K, and plateaus at lower temperatures. The magnetocrystalline anisotropy field increases almost one order of magnitude when the temperature decreases from 300 to 4.2 K. At higher temperatures, $H_{sh}$ noticeably exceeds $H_K$ and becomes close to it at approximately 160 K. Below this temperature, $H_K$ starts to prevail and dominates at lower temperatures. This suggests that the magnetic anisotropy

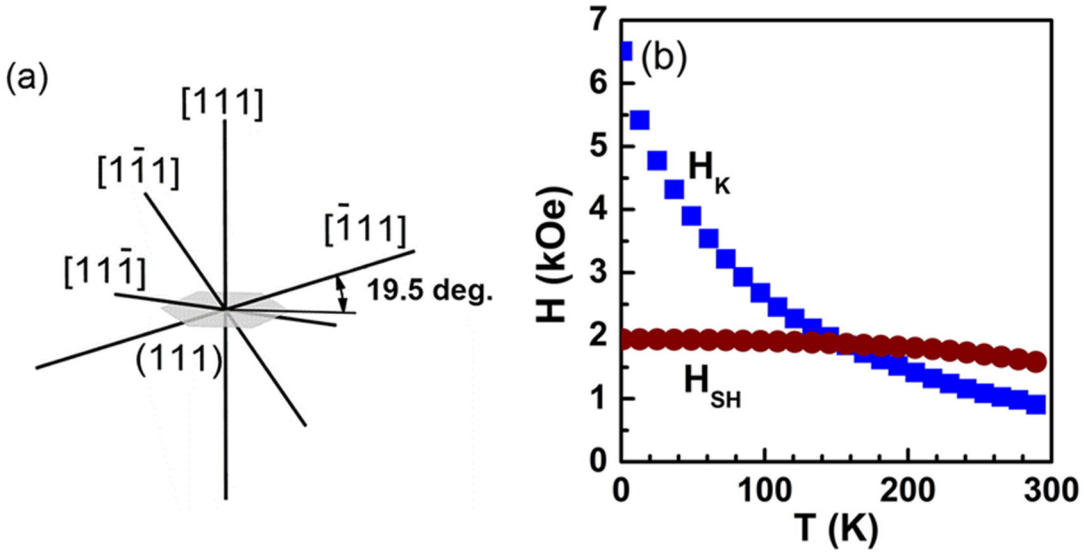


**Figure 3.5.** (a) Schematic of the magneto-crystalline anisotropy easy axes orientation relative to the film plane; (b) Temperature dependence of $H_{sh}$ and $H_K$ calculated according Equations 3.3 and 3.4 with the $M_s$ temperature dependence taken from Ref. 27 and the $K_1$ temperature dependence taken from Ref. 12.

can be characterized by an effective anisotropy axis with temperature-dependent orientation.

These findings are consistent with the magnetization measurements. In the parallel geometry of the experiment (magnetic field is parallel to the film plane), the film's magnetic moment remains in the plane or rather close to it, and magnetic saturation occurs at relatively low field (Figure 3.4a). Hysteresis with low coercive force may indicate an involvement of domain wall motion processes along with a rotation of the magnetic moment. Additionally, magnetic moments inside domains are oriented close to the film plane along the effective easy axis located between the external magnetic field direction and one of the magneto-crystalline easy axes $[\bar{1}11]$, $[1\bar{1}1]$, $[11\bar{1}]$ (Figure 3.5a). The magnetization process in this case ends with a rotation of the magnetic moment into the film plane. With decreasing temperature, the effective anisotropy axis rotates closer to the magneto-crystalline anisotropy axis, which leads to an increase of the saturated magnetic field.

In the case of the perpendicular geometry, the situation is more complex. The external magnetic field tends to direct the magnetic moment perpendicular to the film plane. However, at higher temperatures, this direction is not energetically favorable. Thus, in low external magnetic fields, magnetic moments locate along one or several of the $[\bar{1}11]$, $[1\bar{1}1]$, $[11\bar{1}]$ axes and the film magnetization process occurs identically to that in the parallel geometry. Further increase of the external magnetic field leads to the rotation of the magnetic moment to the field direction, i.e. to the direction perpendicular to the film plane (Figure 3.4b). When the magnetocrystalline anisotropy increases sufficiently at lower temperatures, orienting the magnetic moment along the $[111]$ easy

axis normal to the film plane becomes energetically preferable, and after turning off the external field, the magnetic moments tend to keep this orientation. The wide hysteresis loops at 4.2 K and 30 K (Figure 3.4b) confirm this explanation. Formation of magnetic domains and the motion of domain walls are also possible mechanisms. Magnetic moments inside domains are oriented perpendicular to the film plane, which reduces the energy of the demagnetizing fields. The relatively large remnant magnetization in this case suggests that in zero external field, a domain structure with domains magnetized predominantly along the previously applied field exists. Thus, the redistribution of the individual contributions of each different type of anisotropy to the magnetization processes can explain the observed magnetization curves. A more detailed study of the magnetization processes is in progress.

*Transverse Kerr Effect*

Transverse Kerr effect spectra of each sample are presented in Figure 3.6. For all three samples, the spectra are very similar to each other, and coincide with the polar Kerr effect spectra observed in several works for $CuCr_2Se_4$ single crystals,[5,8,33] and with the magnetic circular dichroism spectra observed in Ref. 22 for ensembles of $CuCr_2Se_4$ nanoparticles. As all three effects are due to electronic transitions between energy bands of a substance, it can be concluded that the band structures of the investigated films are identical to the band structure of $CuCr_2Se_4$ single crystals.

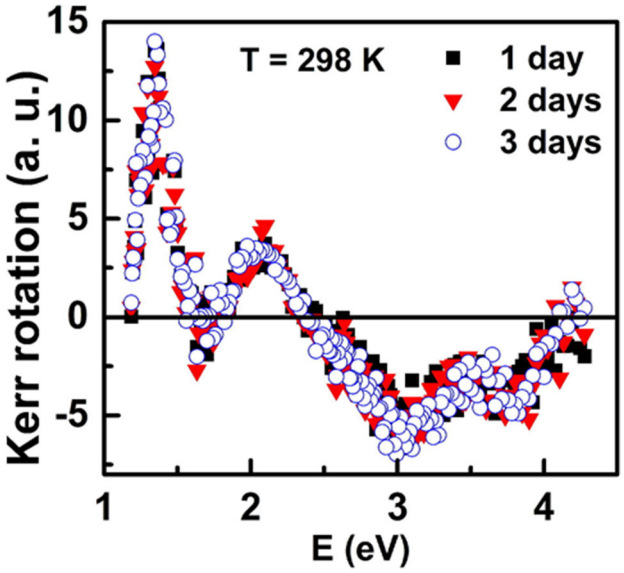


**Figure 3.6.** Room temperature transverse Kerr effect spectra of samples 1, 2, and 3 recorded in magnetic field $H$ = 3.0 kOe applied parallel to the films plane.

The Kerr effect hysteresis loops are shown in Figure 3.7a for sample 1 for the three incident light energies that correspond to the gravity centers of the Kerr spectral maxima (E = 2.8, 1.4, and 1.25 eV). Figure 3.7b presents the hysteresis loops of all three

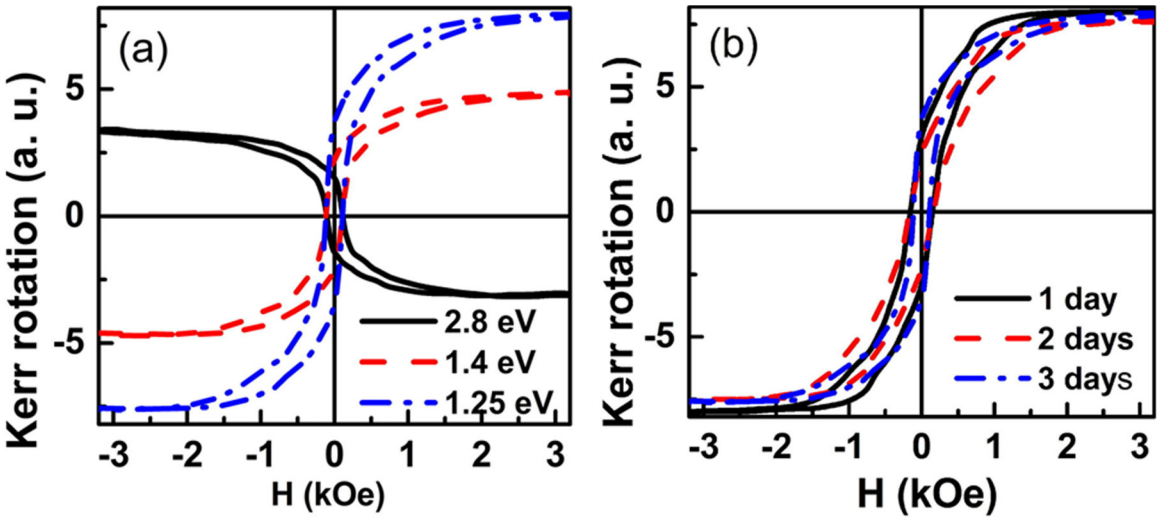


**Figure 3.7.** Room temperature transverse Kerr effect hysteresis loops recorded in magnetic fields parallel to the film plane (a) for sample 1 at three different values of the light wave energy $E$ = 2.8, 1.4, and 1.25 eV, and (b) for all three samples at 1.25 eV.

samples for $E$ = 1.25 eV. These loops correlate well with the magnetic hysteresis loops recorded with the magnetometer at 300 K for the magnetic field directed parallel to the film plane (Figure 3.4a), which was expected since the transverse Kerr effect is proportional to the magnetization projection in the film plane.

*Magnetotransport Properties*

The investigated $CuCr_2Se_4$ films show negative magnetoresistance (MR) with a maximum of -9% at 4.2 K. The MR dependence on the external magnetic field is shown in Figure 3.8a for 30 K. The shape of the curves suggests that the MR is mostly due to the film magnetization processes as inferred from the MR hysteresis. There are two mechanisms that are most likely responsible for MR: spin-dependent scattering of charge carriers on domain walls and spin-dependent tunneling between crystallites. The first mechanism is characteristic for all conductive ferromagnetic materials while the latter is characteristic for thin films.[34] Note that the in-plane and out-of-plane MR dependences have the same shape, differing only in width and position of the peaks. In other words, we do not see a difference between the cases where an electric current is applied parallel or perpendicular to the direction of the magnetic field, which indicates that the contribution to the MR associated with the Lorentz force is minimal. Considering that the MR value is only a few percent, one can conclude that spin-dependent tunneling between crystallites is the main mechanism responsible for the MR effect in the $CuCr_2Se_4$ thin films. Spin-dependent tunneling between metal (Ni) granules dispersed in $SiO_2$ films was considered in Ref. 34 where the MR dependence on an external magnetic field was shown to be:

$$MR = -\left(\frac{JP}{4kT}\right)[M^2(H,T) - M^2(0,T)] \tag{3.5}$$

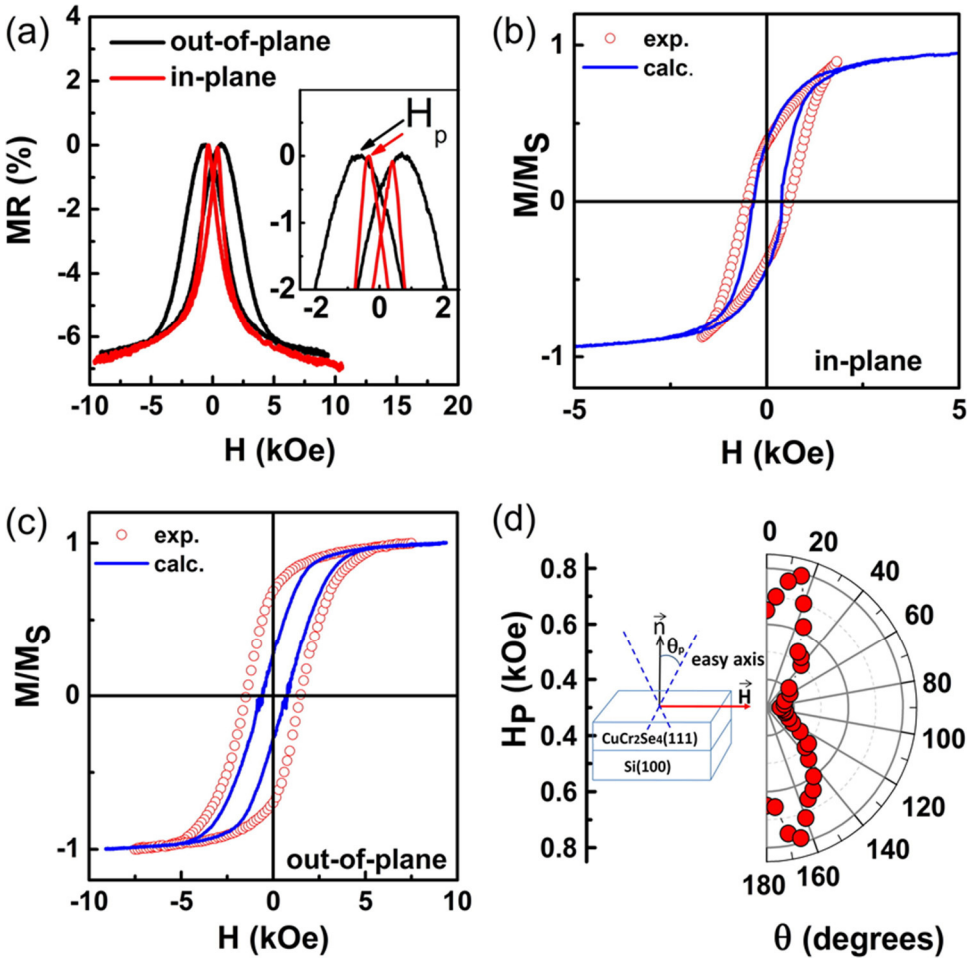


**Figure 3.8.** (a) In-plane and out-of-plane MR as a function of external magnetic field strength H of a $CuCr_2Se_4$ film at 30 K. Inset: the peak position $H_p$ in the MR dependence on H for the in-plane and out-of-plane geometries. (b, c) Magnetization hysteresis loops calculated from experimental MR($H$) with the help of Equation 3.6 for the in-plane and out-of-plane geometries, respectively, in comparison with the magnetization experimental hysteresis loops. (d) Polar dependence of the MR hysteresis peak position $H_p$ (right) along with a scheme of the experimental geometry and the directions of the two effective easy axes (left).

where $P$ is the polarization of the tunneling electrons, $J$ is the exchange coupling constant within the ferromagnetic metal grains, $M$ is the grain magnetic moment, $k$ is the Boltzmann constant, $H$ is an external magnetic field, $T$ is the temperature. Later, Li *et al.*[35] have shown that in low magnetic fields, the MR dependence on the external magnetic field can be described in good approximation as:

$$\mathrm{MR} \sim \left(\frac{M(H)}{M_s}\right)^2 \tag{3.6}$$

where $M(H)$ and $M_s$ are the magnetization in a given field and the saturation magnetization, respectively. We used this approach to calculate the in-plane and out-of-plane magnetization curves from the measured field dependences of the MR. The obtained curves (Figure 3.8b and Figure 3.8c) correlate well with the experimental magnetization curves (Figures 3.4a and b). In particular, the wide hysteresis loop appearing at lower temperatures when the external magnetic field $H$ was applied perpendicular to the film plane was very well reproduced. However, calculated coercive fields for both orientations are lower than experimental ones. This may be due to the fact that in addition to the main MR mechanism, other magnetization mechanisms such as magnetic domain motion and an anisotropic magnetoresistance may contribute to the magnetization. Moreover, in the magnetization processes, the competition of crystal and shape anisotropy played an important role, which makes fitting the hysteresis loops more challenging, especially for the perpendicular magnetic field. Nevertheless, according to the proposed mechanism, the maximum MR should occur near the coercive field because of the randomly oriented magnetic moments of the crystallites in the film plane. Consequently, the peak position $H_p$ in the MR vs. $H$ curves (inset in Figure 3.8a) can be interpreted as the coercive field $H_c$ in the magnetization curves. Using MR curves recorded at different angles $\theta$ to the film normal, we have obtained the polar dependence of $H_p(\theta)$ that should correspond approximately to $H_c(\theta)$. The results are shown in Figure 3.8d. Two distinct maxima at $\theta_p = 15°$ and 165° can be observed. As the maximal $H_c$ value should be observed when the magnetic field is directed along the easy axis, it is possible that two effective easy axes directed at the angles ± 15° relative to the film

normal occur at 30 K. This is consistent with the temperature dependence of the anisotropy parameters (Figure 3.5), which shows that the magnetization is primarily directed along the easy axis [111], i.e. the normal of the film plane. Note that the effective easy axis orientation at an angle to the film normal can explain the fact that the magnetization does not reach its saturation at low temperatures (Figure 3.4b).

*Ferromagnetic Resonance*

Figure 3.9 shows the differential ferromagnetic resonance (FMR) signal recorded at different temperatures of sample 1 with the dc magnetic field $H$ applied parallel (in-plane) and perpendicular (out-of-plane) to the film plane. For the other two films, the results are similar. The resonance signal is a single asymmetric line of Lorentzian shape. Such an asymmetric line shape is generally observed in metallic samples, which confirms the metallic character of the $CuCr_2Se_4$ films.

The resonance field $H_R$ is defined as the $H$ value where the derivative of $P$ with respect to $H$ is equal to zero:

$$H_R = H|_{\frac{dP}{dH}=0} \tag{3.7}$$

Here, $P$ is the absorbed microwave power. The temperature dependence of $H_R$ and the resonance line width $\Delta H_R$, which is defined as a distance between positive and negative maxima in the resonance curves, are presented in Figure 3.10a. The $H_R(T)$ curves are not typical for films with only in-plane shape anisotropy. For the in-plane and out-of-plane geometries of the experiment, $H_R$ is described by the expressions:

$$\frac{\omega}{\gamma} = H_{R_\perp} - 4\pi M_S \tag{3.8}$$

$$\left(\frac{\omega}{\gamma}\right)^2 = H_{R_\parallel}\left(H_{R_\parallel} + 4\pi M_S\right) \tag{3.9}$$

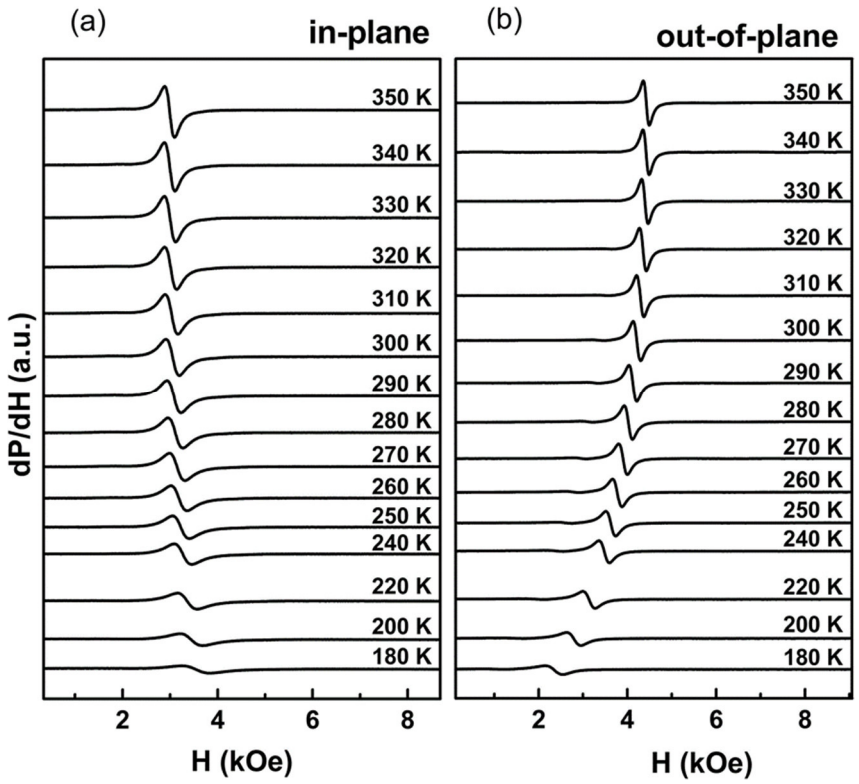


**Figure 3.9.** Differential FMR spectra (d*P*/d*H*) at different temperatures for sample 1 with *H* applied (a) parallel (in-plane) and (b) perpendicular (out-of-plane) to the (111) plane of the film.

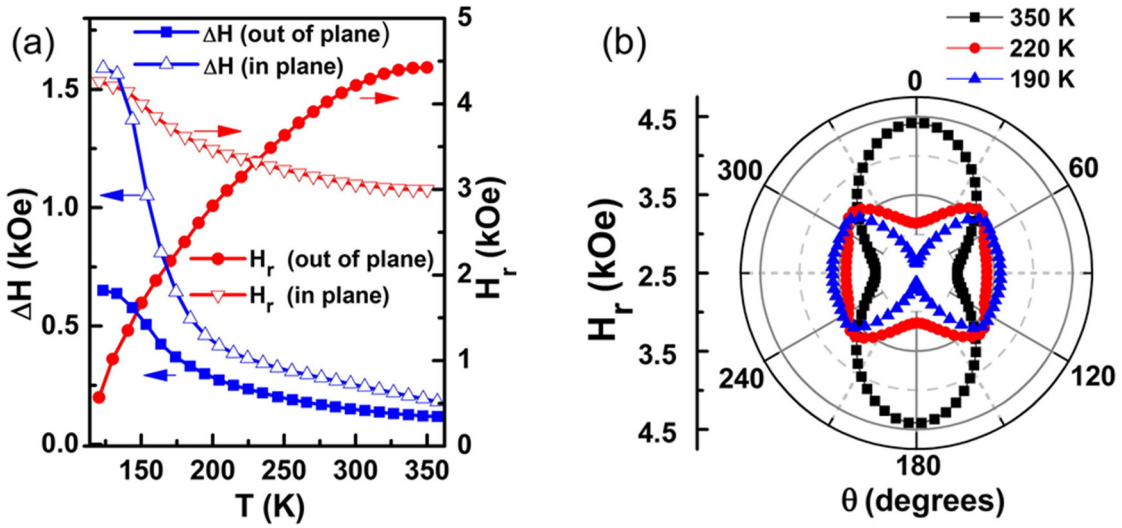


**Figure 3.10.** (a) Temperature dependences of $H_R$ and $\Delta H_R$ for sample 1 with *H* applied perpendicular (filled symbols) and parallel (empty symbols) to the film plane. (b) Polar angle $\theta$ dependence of $H_R$ for the same film at different temperatures. $\theta = 0°$ corresponds to the orientation of the [111] axis perpendicular to the film plane (see also Figure 3.4a).

where ω is the microwave frequency, γ is the gyromagnetic ratio, and $H_{R_\perp}$ and $H_{R_\parallel}$ are the out-of-plane and the in-plane resonance fields, respectively. The temperature dependence of $H_R$ is based on the temperature dependence of the saturation magnetization, $M_s$. As $M_s$ increases with decreasing temperature, $H_{R_\perp}$ should increase and $H_{R_\parallel}$ should decrease. However, the opposite is observed in the $CuCr_2Se_4$ as shown in Figure 3.9. In order to explain the temperature dependence of $H_R$ observed for our films, we need to take into account the magneto-crystalline anisotropy discussed above, which will lead to the equations:

$$\frac{\omega}{\gamma} = H_{R_\perp} - 4\pi M_S - \frac{2K_1}{M_S} \tag{3.10}$$

$$\left(\frac{\omega}{\gamma}\right)^2 = H_{R_\parallel}\left(H_{R_\parallel} + 4\pi M_S + \frac{2K_1}{M_S}\right) \tag{3.11}$$

Thus, the temperature dependences of $H_R$ shown in Figure 3.10a are determined by the temperature dependence of the magneto-crystalline anisotropy constant, $K_1$, to a greater extent than the temperature dependence of the shape anisotropy. To realize this scenario, the magneto-crystalline anisotropy field of a sample should be oriented at an angle to the shape anisotropy field and should increase with decreasing temperature, which is the case for the $CuCr_2Se_4$ films crystallographically aligned in the (111) plane (see Figure 3.5). As mentioned earlier, the magneto-crystalline anisotropy is dominated by the shape anisotropy at higher temperatures, and the magneto-crystalline anisotropy starts to prevail at lower temperatures (Figure 3.5b), i.e. the direction perpendicular to the film plane is the hard magnetization axis at higher temperatures and becomes the easy magnetization axis at lower temperatures. This is seen very well in the polar angular dependence of $H_R$ (Figure 3.10b), where the angle $\theta$ is the angle between

the direction of an external magnetic field and the normal to the film plane. At $T = 350$ K, the maximum of $H_R$ corresponds to the hard magnetization axis and is observed when the external magnetic field is normal to the film plane ($\theta = 0°$). The minimum of $H_R$ corresponds to the easy axis and is observed when the external magnetic field is directed within the film plane. This behavior indicates that at room temperature, the magnetic properties of the films are determined by the shape anisotropy. When the temperature decreases to 190 K, the situation is changing dramatically. The minimum of $H_R$ is observed when the external magnetic field is directed normal to the film surface, i.e. this direction becomes the easy direction of magnetization. These results are in good agreement with the results obtained with other techniques.

A predominant axis inside the film plane was not determined, which could be due to the random orientations of the crystallites within the film plane.[27] The random orientation of the crystallites inside the plane and the crystallographic alignment outside the plane are likely responsible for the stronger increase of the in-plane resonance line width with decreasing temperature compared to the out-of-plane line width.

### III.4. Conclusions and Bridge

Crystallographically aligned nanocrystalline films of ferromagnetic spinel $CuCr_2Se_4$ were successfully synthesized, and their structure and alignment were confirmed by X-ray diffraction and high-resolution transmission electron microscopy. The average size of the crystallites is of about 200 – 250 nm, and their (111) crystal plane is oriented parallel to the film plane. Transverse Kerr effect spectra of the films coincide with the polar Kerr effect spectra observed for $CuCr_2Se_4$ single crystals and with the magnetic circular dichroism spectra observed for ensembles of $CuCr_2Se_4$ nanocrystals,

suggesting that the band structure of the investigated films to be the same as in $CuCr_2Se_4$ crystals.

The combination of the almost ideal crystallite (111) planes alignment in the film plane, the orientation of the magneto-crystalline easy axes at an angle to this plane, and the in-plane shape anisotropy characteristic for thin films provides a rare opportunity to study the role of the competition between anisotropies of different origin on the magnetic properties of a thin film. The strong temperature dependence of the magneto-crystalline anisotropy along with an almost temperature-independent shape anisotropy below 300 K results in a switch of the easy axis from inside the film plane to perpendicular to the film plane below 160 K, which is responsible for a number of peculiarities of the static and dynamic magnetic properties as well the low temperature magneto-transport properties of the films. In particular, the changes of the hysteresis loop shapes with temperature are remarkably different for magnetic fields applied parallel and perpendicular to the film plane. In the first case, narrow loops with nearly the same coercivity are observed below 300 K, but in the latter case, the coercivity increases with decreasing temperature by almost an order of magnitude. Such a behavior is associated with different mechanisms involved in the films magnetization processes. Data on FMR and magnetoresistance correlate well with the features of the static magnetic properties. A moderately large low-temperature negative magnetoresistance in the $CuCr_2Se_4$ thin films is observed here for the first time.

In the previous chapters, the MER method has been used to synthesize strongly textured films of the thermodynamically stable compound $CuCr_2Se_4$. Chapter IV will introduce misfit layer compounds and ferecrystals, which will underline the versatility of the MER method.

# CHAPTER IV

# BRIDGE: FERECRYSTALLINE COMPOUNDS

Portions of this chapter were previously published as Esters, M.; Johnson, D.C. "Targeted Synthesis of Metastable Compounds and Intergrowths: The Modulated Elemental Reactants Method". In *Crystal Growth: Concepts, Mechanisms, and Applications*; Li, J., Li, J., Chi, Y., Eds.; Nova Science Publishers: New York, **2017**; pp. 35–118. M.E. wrote the book chapter and made the figures. D.C.J. was the principal investigator and provided editorial assistance.

## IV.1. Ferecrystals – Heterostructures with Designed Nanoarchitecture

Ferecrystals (from the Latin *fere*: "almost") are heterostructures that belong to the family of Misfit Layer Compounds (MLCs). MLCs are layered structures that are synthesized directly from the constituent elements, and crystals of them are grown using vapor transport methods. They consist of slabs of two subunits that are alternating along the *c*-axis as shown in Figure 4.1a. One subunit consists of an MX bilayer (M = Sn, Pb, Bi, Sb, rare earth; X = S, Se) in a pseudo-tetragonal structure. The atoms are ordered in a NaCl-like arrangement in the *ab*-plane, but the M atoms are distorted to the outside (Figure 4.1b). The other subunit is a trilayer that consists of a transition metal dichalcogenide $TX_2$ (Figure 4.1c). These subunits are aligned such that their *a*-lattice vectors are parallel to each other. To achieve this, the lattice vectors along the *b*-axes of the subunits distort, giving rise to a common *b*-lattice vector. The $TX_2$ lattice now needs to be described as an orthorhombic lattice with $a = a_{TX_2}$ and $b = \sqrt{3}a_{TX_2}$ where $a_{TX_2}$ is the lattice parameter of the hexagonal $TX_2$ lattice (Figure 4.1d).

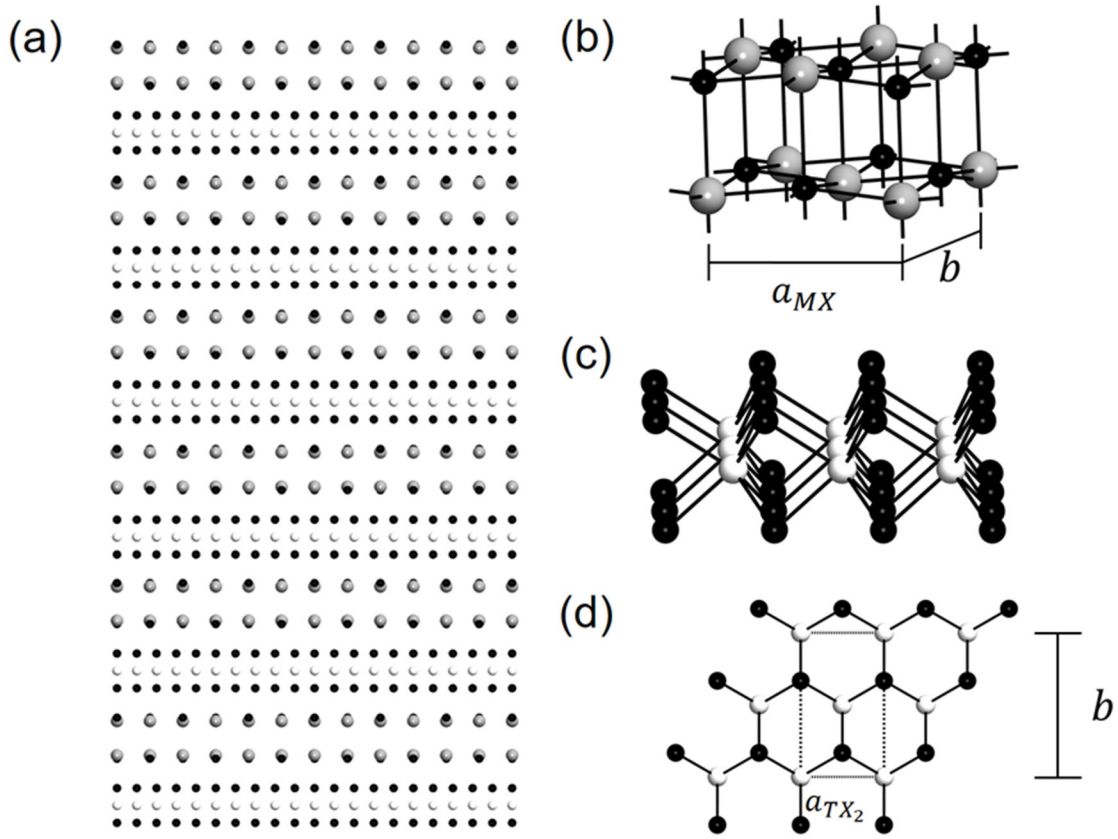


**Figure 4.1.** (a) A $(MX)_{1+\delta}TX_2$ misfit layered compound (MLC) viewed along the *b*-axis. (b) The unit cell of the MX subunit with its lattice parameters $a_{MX}$ and $b$. M atoms are gray, X atoms are black. (c) The structure of the $TX_2$ subunit. T atoms are white, X atoms are black. (d) The transformation of the $TX_2$ structure into the MLC unit cell with the lattice parameters $a_{TX_2}$ and $b = \sqrt{3}a_{TX_2}$.

Since $a_{MX}$, the *a*-axis lattice parameter of the MX subunit, and $a_{TX_2}$ are of different sizes, this alignment creates a lattice mismatch, which requires one subunit to be in excess, resulting in a general formula of $(MX)_{1+\delta}TX_2$. The parameter 1+δ, the misfit parameter, describes the excess of MX that is needed to accommodate this lattice mismatch. It can be calculated as:

$$1 + \delta = \frac{\frac{Z_{MX}}{V_{MX}}}{\frac{Z_{TX_2}}{V_{TX_2}}} = \frac{4a_{TX_2}bc}{2a_{MX}bc} = \frac{2a_{TX_2}}{a_{MX}} \tag{4.1}$$

where $Z_i$ represents the number of formula units in each subsystem, and $V_i$ represents the volumes of each subsystem in the crystal. $c$ represents the *c*-axis lattice parameter of the repeating unit of the MLC and *b* is lattice parameter of the common in-plane axis of both constituents. The misfit parameter thus describes the ratio of cation densities between both subsystems and typically assumes a value between 1.07 and 1.28.

MLCs have a variety of electrical, magnetic, and superconducting properties, depending on the metals that are used. The structures and properties have been extensively reviewed by Wiegers and the interested reader is referred to Ref. 1. In Figure 4.1a, the structure shows alternating MX bilayers and $TX_2$ layers. However, since $TX_2$ layers have no dangling bonds and MX bilayers are stable in MLCs, it is reasonable to assume that a repeating unit consisting of more than one $TX_2$ layer or MX bilayer might be stable, or at least be in a local minimum in free energy. The formula for a misfit layered compound would thus need to be rewritten as $[(MX)_{1+\delta}]_m[TX_2]_n$. For each integer *m* and *n*, the energy of such a misfit layered compound should lie inside a local minimum as shown in Figure 4.2. Using kinetic control, the synthesis of MLCs with arbitrary *m* and *n* should be possible. Since MLCs are synthesized using vapor transport methods, only the thermodynamically stable product is accessible, which in most cases is $m = n = 1$; only a few cases are known where $m = 2$, and $n = 2, 3$.

In Chapter I, it was demonstrated that by depositing a layered precursor with atomically thin elemental layers, the Modulated Elemental Reactants (MER) method can access local minima if the precursor composition is close to the composition of the desired phase. Figure 4.3 shows the rationale for MER precursors to form $[(MX)_{1+\delta}]_m[TX_2]_n$: M-X and T-X layers are deposited *m* and *n* times to form the repeating

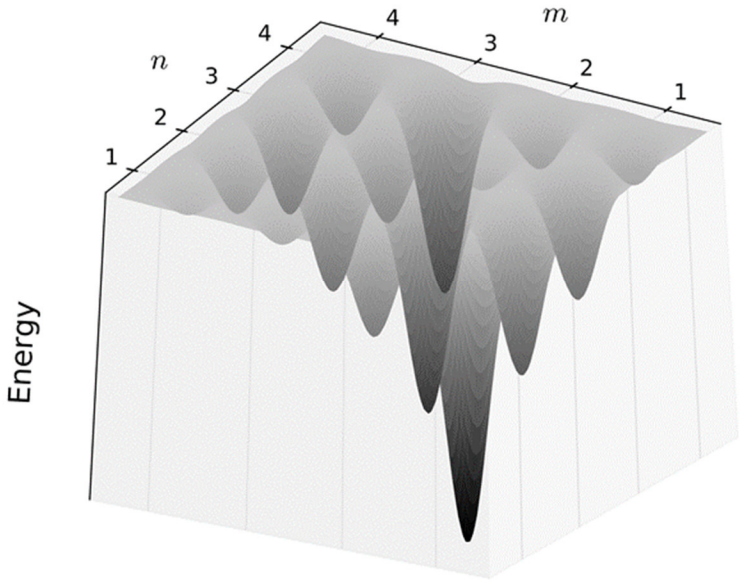


**Figure 4.2.** Hypothetical energy hypersurface as a function of the number of subunits in a MLC repeating unit *m* and *n*.

unit. To ensure that only the desired number of layers form in the final compound, the thicknesses of these layers need to be carefully controlled to contain approximately the number of atoms required to form the desired subunit, which typically corresponds to a thickness of around 6 Å.

The calibration procedure outlined for binary compounds is complicated by two factors. First, the repeat unit thickness is comprised of the thickness of both subunits, so x-ray diffraction on the precursor cannot resolve the individual thicknesses of the M-X and T-X layers. Second, determining the composition of the precursor cannot resolve the composition of the individual M-X and T-X layers. In order to determine the thickness and composition of individual layers, a more elaborate procedure needs to be developed.

The repeat unit thickness $d$ is comprised of $m$ layers of M-X and $n$ layers T-X with the corresponding thicknesses $d_{M-X}$ and $d_{T-X}$:

$$d = m \cdot d_{M-X} + n \cdot d_{T-X} \tag{4.2}$$

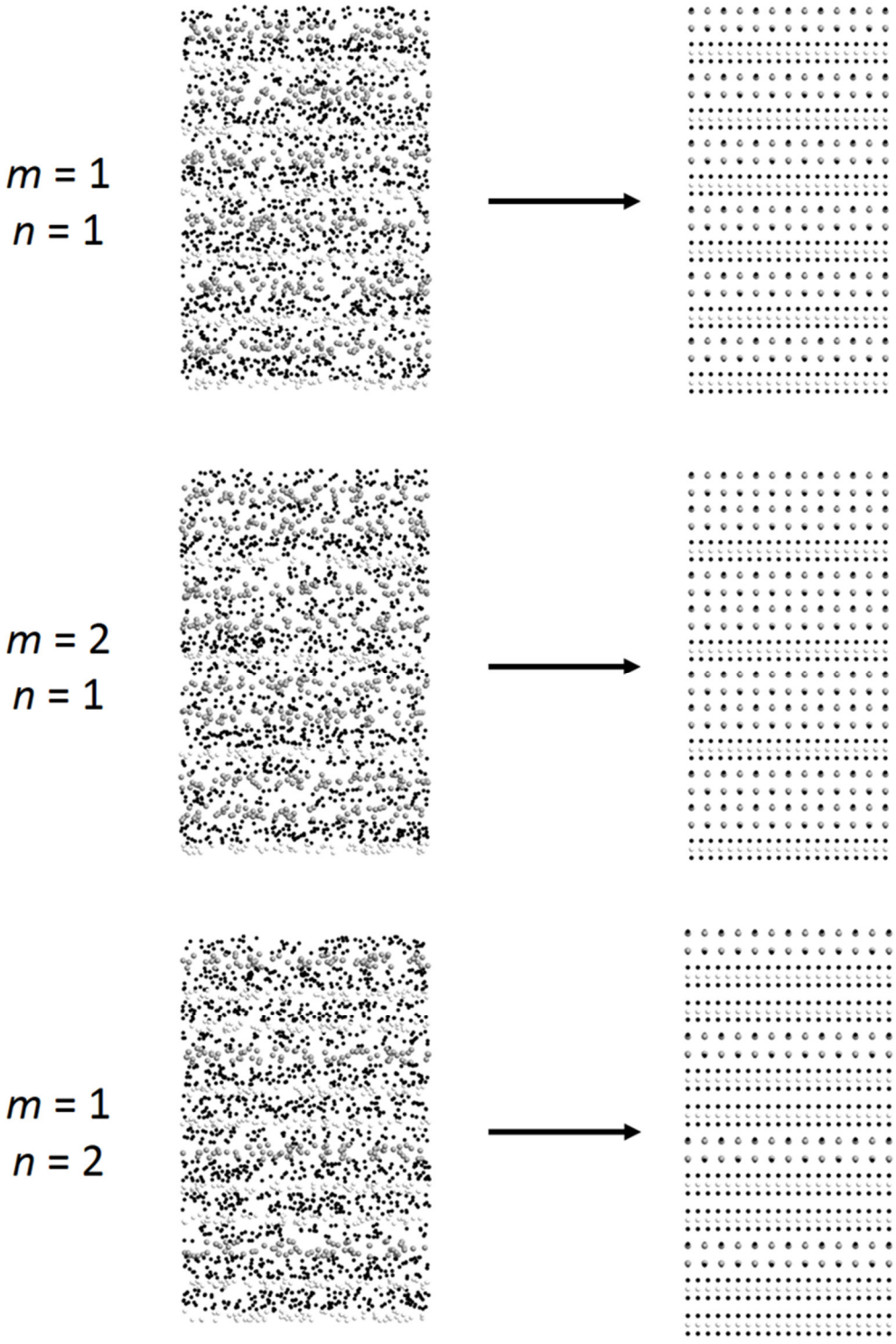


**Figure 4.3.** Schematic of MER precursors that react to $[(MX)_{1+\delta}]_m[TX_2]_n$ with $m = 1, 2$ and $n = 1, 2$.

This can be rearranged to:

$$\frac{d}{m} = d_{M-X} + \frac{n}{m} d_{T-X} \tag{4.3}$$

$$\frac{d}{n} = \frac{m}{n} d_{M-X} + d_{T-X} \tag{4.4}$$

To determine the thickness of the individual layers, a series of precursors with varying *m* and *n* needs to be deposited. Plotting *d*/*m* against *n*/*m* yields a straight line, and a linear fit provides $d_{T-X}$ from the slope and $d_{M-X}$ from the intercept, and vice versa for a plot of *d*/*n* against *m*/*n*. Ideally, the results extracted from the slopes should be within error of the results from the intercepts. Deviations from linearity or significant differences point to inconsistencies between depositions. Figure 4.4 shows an example for a V-Se-Sn-Se precursor. While the V-Se thickness is close to the desired thickness, the Sn-Se thickness is too large and needs to be scaled down.

Determining the composition also requires a series of samples because the chalcogen is present in both the T-X and M-X layer. The general formula of the precursor

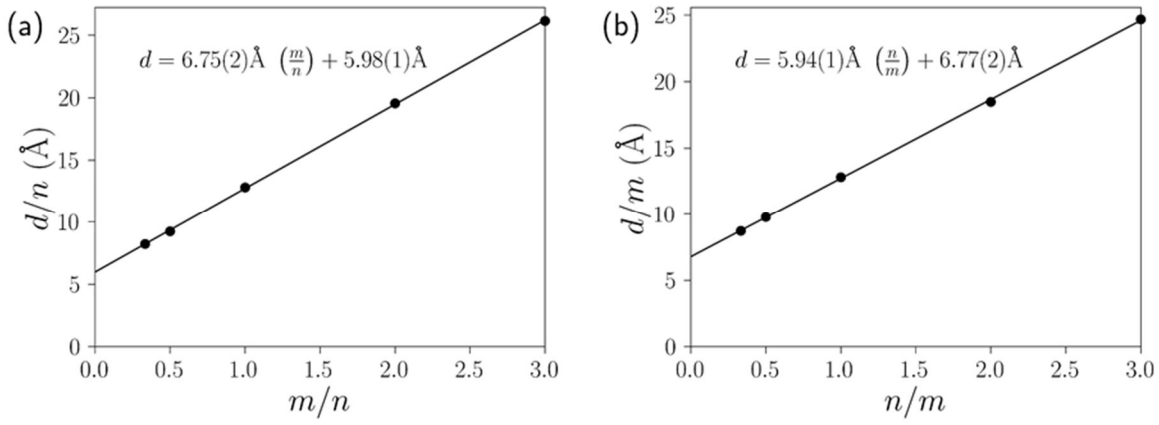


**Figure 4.4.** Thickness calibration for the M-X and T-X layers in an MLC MER precursor. A linear fit through (a) yields $d_{M-X} = 6.77 \pm 0.02$ Å and $d_{T-X} = 5.91 \pm 0.01$ Å and a linear fit through (b) yields $d_{M-X} = 6.75 \pm 0.02$ Å and $d_{T-X} = 5.98 \pm 0.01$ Å.

can be written as $[(MX_x)_y]_m[TX_z]_n$ or $M_{my}T_nX_{mxy+nz}$. The atomic ratios of each element are thus:

$$\frac{\text{at.-\% X}}{\text{at.\% M}} = \frac{mxy + nz}{my} = x + \frac{nz}{my} \tag{4.5}$$

$$\frac{\text{at.-\% M}}{\text{at.\% T}} = \frac{m}{n} \tag{4.6}$$

$$\frac{\text{at.-\% X}}{\text{at.\% T}} = \frac{mxy + nz}{n} = z + \frac{mxy}{n} \tag{4.7}$$

Equations 4.5 and 4.7 can be rearranged to:

$$\frac{m}{n}\,\frac{\text{at.-\% X}}{\text{at.\% M}} = \frac{m}{n}x + \frac{z}{y} \tag{4.8}$$

$$\frac{n}{m}\,\frac{\text{at.-\% X}}{\text{at.\% T}} = \frac{n}{m}z + xy \tag{4.9}$$

These equations allow the direct determination of *x*, *y*, and *z* from the slopes of linear plots resulting from Equations 4.6, 4.8, and 4.9 as is shown in Figure 4.6. Using *y* = 1.19(1) from Figure 4.6b, *x* and *z* can be additionally determined using the intercepts of the plots from Equations 4.8 and 4.9. In the case shown in Figure 4.6, *x* can be determined as 1.16(1) from the slope and 1.17(2) from the intercept, and *z* is found to 2.05(1) and 2.06(2), respectively. *x* and *z* should be 1 and 2, respectively, although some excess of the chalcogens is often added to account for evaporation loss during annealing. The determined values are thus close to the desired values. The ideal value for *y* is unknown, but can be estimated by calculating the misfit parameter using the in-plane lattice parameters of the bulk forms of $TX_2$ and rock salt MX. For $VSe_2$ and SnSe, $a_{VSe_2} = 3.35$ Å and $a_{SnSe} = 5.99$ Å, which results in an ideal *y* value of 1.12, suggesting that the determined *y* value is too high. This is consistent with the determined Sn-Se layer

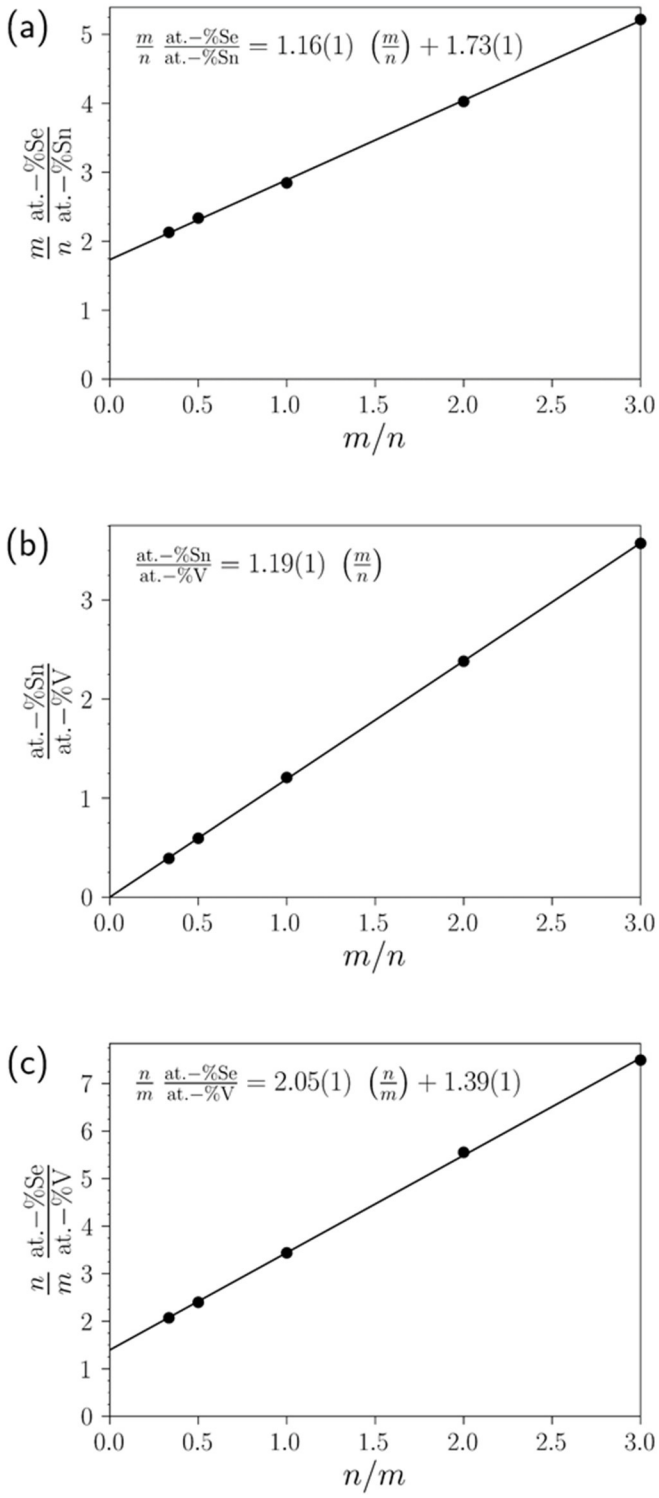


**Figure 4.5.** Composition calibration plots with linear fits. *x* can be determined from the slope of (a) and the intercept of (c), *y* can be determined from the slope of (b), and *z* can be determined from the slope of (a) and the intercept of (c). The insets show the results of the linear fits through the data.

thickness. For future depositions, the deposition parameters for the Sn and the Se layer deposited after the Sn layer both need to be decreased.

In contrast to MLCs synthesized using traditional solid state synthesis routes, MLCs synthesized with the MER method exhibit rotational disorder along the *c*-axis. This *turbostratic disorder* and the resulting short coherence lengths give rise to a new class of materials called ferecrystals ("almost crystals").

The turbostratic disorder also leads to the structure being incommensurate along the *b*-axis, i.e., there is no common *b*-lattice parameter compared to misfit layer compounds. For ferecrystals, a more general definition of the misfit parameter needs to be used:

$$1 + \delta = \frac{\frac{Z_{MX}}{V_{MX}}}{\frac{Z_{TX_2}}{V_{TX_2}}} = \frac{2\sqrt{3}a_{TX_2}^2}{a_{MX}b_{MX}} \tag{4.10}$$

Ferecrystals have been synthesized with numerous elements. Ti, V, Nb, Mo, Ta, and W have been successfully incorporated as the transition metals, and La, Ce, Sn, Pb, and Bi as the metal in the rock salt component (see periodic table in Figure 4.6).[2–19] To date, many more rare earth metals have been used for MLCs compared to ferecrystals because these metals oxidize rapidly and are thus difficult to deposit consistently. While MLCs are mostly sulfides with only few selenides, ferecrystals have been almost exclusively synthesized as selenides.[1,20,21] There are no ferecrystalline sulfides yet because the controlled physical vapor deposition of atomically thin sulfur layers is very challenging. With $[(PbTe)_{1.17}]_m[TiTe_2]_n$, ferecrystalline tellurides have been synthesized as well, which do not exist as MLCs yet.[16]

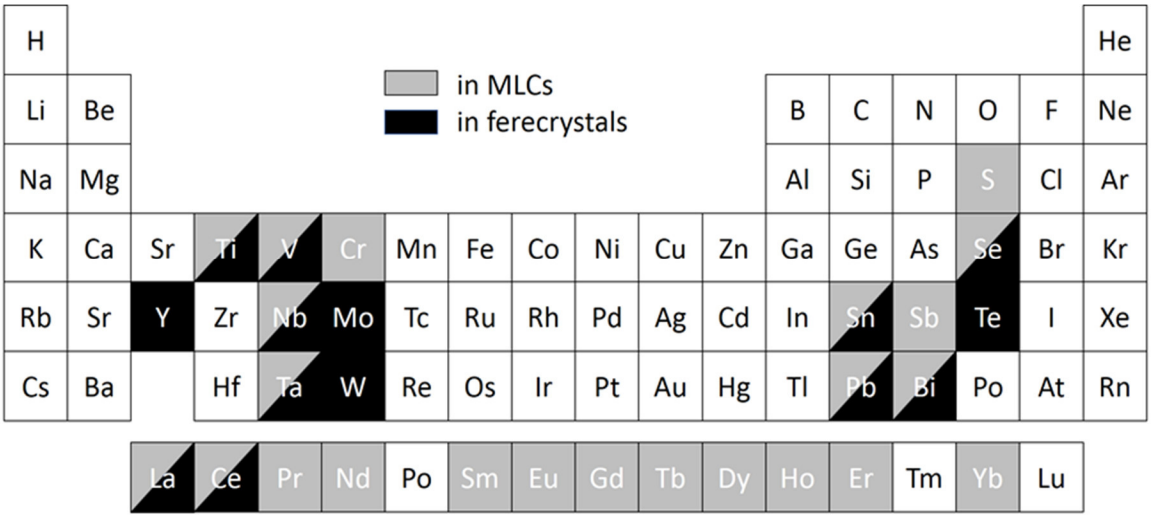


**Figure 4.6.** Elements in the periodic table that are found in misfit layer compounds and ferecrystals.

It was hypothesized earlier that any ferecrystal with integer *m* and *n* can be synthesized if the thicknesses and compositions of the individual layers are close to such a ferecrystal (see Figure 4.2 and Figure 4.3). The large number of existing ferecrystals with a diverse array of *m*-*n* combinations support this hypothesis, with values for *m* and *n* going as high as 32.[19]

## IV.2. Conclusions and Bridge

Ferecrystals are complex heterostructures of the misfit-layer-compound family. They consist of stacks of rock-salt like MX bilayers (M = Sn, Pb, Bi, La, Ce; X = Se, Te) and transition metal dichalcogenide trilayers, and have the general formula $[(MX)_{1+\delta}]_m[TX_2]_n$ where $1 + \delta$ is the misfit parameter, which accounts for the lattice mismatch of the two constituents. While misfit layer compounds have one commensurate axis, the *b*-axis, and typically can only access $m = n = 1$, ferecrystals show turbostratic disorder and can access nearly any integer *m* and *n*.

The complexity of ferecrystalline compounds goes beyond simple *m*-*n* combinations. Chapter V will explore that for many combinations of *m* and *n*, different stacking sequences with the same *c*-axis lattice parameter can be achieved, defining a new type of structural isomerism.

# CHAPTER V

# INORGANIC STRUCTURAL ISOMERS SYNTHESIZED BY DIFFUSION CONSTRAINED SELF-ASSEMBLY OF DESIGNED PRECURSORS – A NOVEL TYPE OF ISOMERISM

Portions of this chapter were previously published as Esters, M.; Alemayehu, M.; Jones, Z.; Nguyen, N.T.; Anderson, M.D.; Grosse, C.; Fischer, S.F.; Johnson, D.C. "Inorganic Structural Isomers Synthesized By Diffusion Constrained Self-Assembly of Designed Precursors – A Novel Type Of Isomerism" *Angewandte Chemie International Edition*, **2015**, *54(4)*, 1130 – 1134. M.E. helped develop the idea of ferecrystalline isomers, wrote programs to calculate all isomers, and co-wrote the paper with M.A. and D.C.J. M.A. and Z.J. synthesized and characterized all isomers. N.T.N. was the first to synthesize some of the isomers. M.D.A. took the transition electron microscopy images. C.G. performed the electrical property measurements. D.C.J. was the principal investigator.

## V.1. Isomers in Ferecrystals

In molecular chemistry, chemists utilize local bonding concepts to predict kinetically stable compounds. Molecules that contain all of their atoms in common coordination numbers and electron counts, for example carbon atoms that make four covalent bonds, are considered reasonable synthetic targets. These predictions allow for the development of targeted synthetic strategies and the isolation of increasingly complex molecules by controlling kinetics.[1] Conceptually, there are an infinite number of

kinetically stable molecules that satisfy these local bonding rules including isomers – compounds with the same molecular formula but a different connectivity of atoms. While the synthetic challenge scales with the number of atoms and the complexity of their interconnectivity, chemists have developed synthetic tools that enable the designed synthesis of increasingly complex targets. This ability to kinetically control the synthesis of specific compounds, however, does not extend to engineering the resulting crystal structure, consisting of an ordered array of ~$10^{23}$ molecules or atoms with a specific arrangement between them.[2,3]

Here, we ask if similar bonding concepts can be used to predict the structure of kinetically stable extended inorganic solids. We imagine new extended solids containing interwoven layers of known structures (A and B) with precise control of the number of structural units (*m* and *n*) in these new compounds $(A)_m(B)_n$. The known misfit layered compounds would be examples of this type of compound, where typically only the $m = n = 1$ compound is thermodynamically stable.[4] It is chemically reasonable to expect the presence of a local free energy minimum for any value of *m* or *n* in these $(A)_m(B)_n$ compounds, as only atoms at the interfaces would potentially not have their local bonding needs optimally satisfied. If this hypothesis is correct, then one could also imagine compounds with the same stoichiometry and the same total number of structural units, but with a different connectivity. For example, there are 6 potential combinations that contain 4 structural units of A and 4 structural units of B in the repeating unit: $(A)_4(B)_4$, $(A)_3(B)_1(A)_1(B)_3$, $(A)_3(B)_2(A)_1(B)_2$, $(A)_2(B)_3(A)_2(B)_1$, $(A)_2(B)_1(A)_1(B)_2(A)_1(B)_1$ and $(A)_2(B)_2(A)_1(B)_1(A)_1(B)_1$. (In the rest of this manuscript, the short hand notation 4:**4**, 3:**3:**1:**1**, 3:**2:**1:**2**, 2:**3:**2:**1**, 2:**2:**1:**1**:1:**1**, and 2:**1:**1:**2**:1:**1** will be used where the normal and

bold fonts represent the different structural units, the number is the number of consecutive structural units of each type, and the order is the order of the structural units in the unit cell.) Whereas the different connectivity in molecules such as $C_4H_8$ would lead to different molecular shapes (linear, branched and cyclic), the different connectivity in these compounds would lead to different numbers of interfaces (2 in 4:**4**, 4 in 3:**1**:1:**3**, 2:**3**:2:**1** and 3:**2**:1:**2**, and 6 in 2:**2**:1:**1**:1:**1** and 2:**1**:1:**2**:1:**1**), which would represent a novel type of structural isomerism. The experimental challenge is finding a synthetic technique to control the self-assembly of $\sim 10^{23}$ atoms to obtain the targeted structure of a particular isomer.[3]

In order to obtain the specific isomers, our idea was to prepare elemental precursors with enough structural similarities to the targeted product that, on low temperature annealing, the self-assembly of the desired compound would be trapped in the local free energy minima defined by the precursor structure (Figure 5.1). This exploits the enthalpy released during the formation of the constituents of the targeted compounds to direct the self-assembly but uses small solid-state interdiffusion rates at low temperatures to prevent the system from evolving into the global free energy minima.[5,6] We used the $[(PbSe)_{1.14}]_m(NbSe_2)_n$ system to test this concept. In this family of compounds, the n = 1, 2 or 3 and m = 1 compounds can be prepared using traditional high temperature reaction of the elements by varying the composition of the initial mixture.[7-9] These compounds and several others in this family of compounds have been made as disordered polytypes or ferecrystals by using designed precursors.[10,11] These compounds consist of interleaved layers of PbSe and $NbSe_2$. Each $NbSe_2$ layer consists of a hexagonal layer of niobium between hexagonal layers of selenium with the niobium

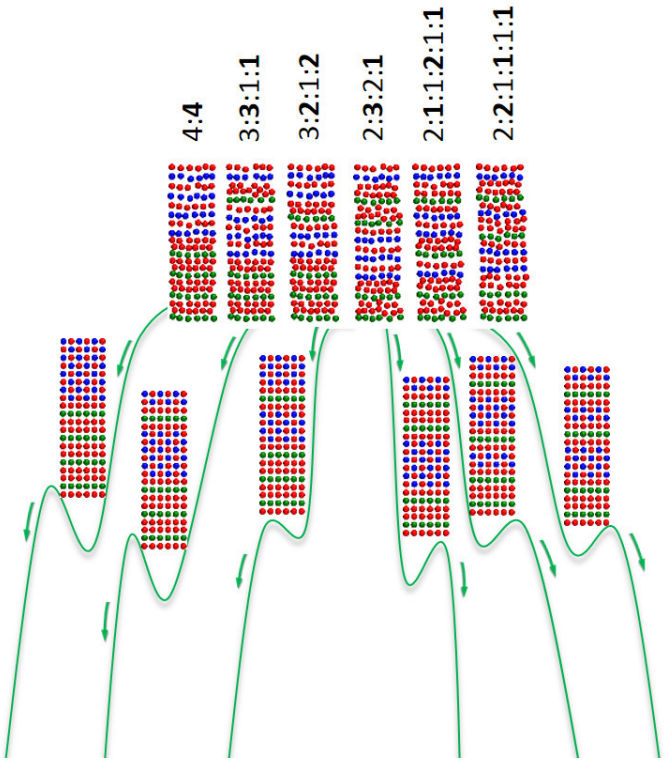


**Figure 5.1.** This figure contains a schematic of the free energy landscape for the formation of the six isomers of $[(PbSe)_{1.14}]_4(NbSe_2)_4$. The top images are a schematic structure of the structure of the initial reactants. The images in the middle of the image are idealized atomic structures of the 6 $[(PbSe)_{1.14}]_4(NbSe_2)_4$ isomers formed on annealing. The six different green lines show the energy pathway for the six different reactants going to the six different targeted compounds.

atoms in trigonal prisms or octahedra of Se. Each PbSe layer contains two distorted (001) planes of the rock salt structure. The rock salt structured layers contain equal amounts of Pb and Se atoms and are incommensurate with the close packed Se planes of the selenium layers of $NbSe_2$. The non-integer (1.14) PbSe stoichiometry reflects the difference between the area per cation in the respective layers.

## V.2. Synthesis and Structure of the Ferecrystalline Isomers

We prepared the designed precursors by physical evaporation from elemental sources. We determined the deposition conditions required to deposit a pair of elemental layers for each constituent where the ratio of the elements corresponds to the

stoichiometric ratio found in each of the constituents.[12] The thickness of the pair of elemental layers was made to correspond to the absolute amount of material required to make a single layer of each constituent. We then deposited 6 different sequences of layer pairs corresponding to the nanoarchitectures of the 6 potential structural isomers of $[(PbSe)_{1.14}]_4(NbSe_2)_4$.

We followed the evolution of the diffraction patterns of these precursors as a function of annealing time and temperature. The as-deposited diffraction scans of each sample contain Bragg diffraction maxima at low angle from the layering of the precursor. Additional diffraction peaks, all of which can be indexed as (00*l*) reflections from the initial precursor period, grow in intensity with increased annealing time and temperature. By 450 °C, the diffraction patterns are well developed and rocking scans indicate a very strongly preferred (00*l*) orientation.

Figure 5.2 contains the diffraction patterns of the six isomers of $[(PbSe)_{1.14}]_4(NbSe_2)_4$ annealed at 450 °C. All of the diffraction peaks are located in the same position, indicating identical unit cell sizes of all six compounds. As expected, the relative intensities of the different Bragg diffraction maxima vary considerably, reflecting the different positions of atomic planes in each of the isomers.

Above the diffraction patterns in Figure 5.2 are cross sectional high-angle annular dark-field scanning transmission electron microscope (HAADF- STEM) images of four of the six isomers. The different layer sequences are clearly distinguishable in the images and are consistent with that expected from the precursor. The *c*-axis lattice parameters from the images agree with the values obtained from our x-ray diffraction study. The atomic planes are highly ordered along the *c*-axis of the compounds, but rotational

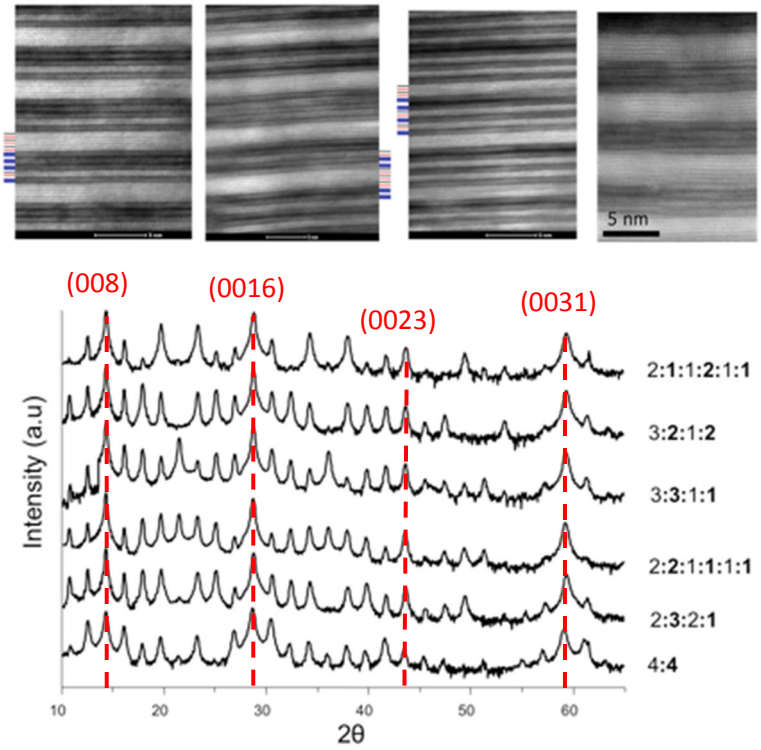


**Figure 5.2.** Top: HAADF STEM images of the 3:**3**:1:**1** (left), 2:**3**:2:**1** (middle left), and 2:**2**:1:**1**:1:**1** (middle right) and 4:**4** (right) $[(PbSe)_{1.14}]_4(NbSe_2)_4$ isomers. Bottom: The high angle x-ray diffraction pattern of the six $[(PbSe)_{1.14}]_4(NbSe_2)_4$ isomers annealed at 450 °C. Dashed vertical lines were added to select reflections to emphasize the identical position of Bragg reflections, showing that all isomers have the same *c*-axis lattice parameter.

orientation of the layers varies. This is the first report of the targeted synthesis of structural isomers of an extended inorganic solid via a non-epitaxial growth technique that we are aware of.

## V.3. Electrical Properties of $[(PbSe)_{1.14}]_4(NbSe_2)_4$ Isomers

The temperature dependence of the electrical resistivity of the six $[(PbSe)_{1.14}]_4(NbSe_2)_4$ isomers is shown in Figure 5.3. The magnitude of the resistivity is similar to that reported for $[(PbSe)_{1.14}]_1(NbSe_2)_n$ compounds, where $n$ = 1 - 3.[7-9] The temperature dependencies of all of the isomers are similar, suggesting similar electron-phonon scattering mechanisms. The resistivity and the residual resistivity ratio do not

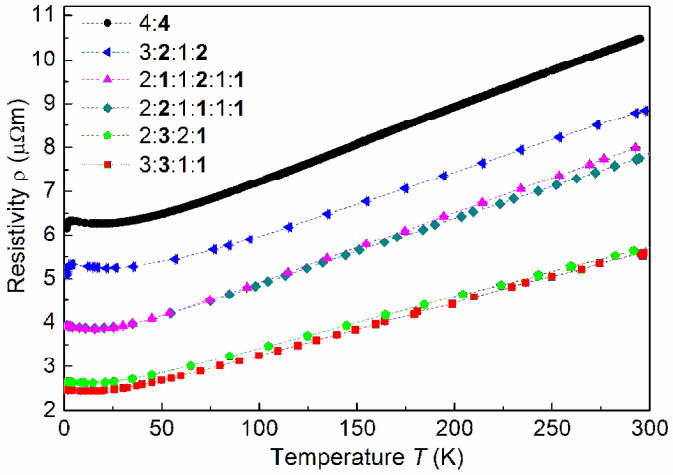


**Figure 5.3.** In-plane electrical resistivity data obtained for the 6 isomers of $[(PbSe)_{1.14}]_4(NbSe_2)_4$ for temperatures between 1.4 K and 300 K.

show a systematic trend as the number of interfaces is decreased, perhaps reflecting changes in the structure of the PbSe layers with thickness that change scattering at the interfaces between PbSe and $NbSe_2$ layers.[13,14] Hall measurements using the van der Pauw[15] method of the 4:**4** isomer revealed a positive Hall coefficient $R_H$ and a hole density $p$ at room temperature of $p = 3.16 \pm 0.06 \times 10^{21}$ cm$^{-3}$, calculated assuming a single-band model. As seen in Figure 5.4, the carrier density $p$ increases with increasing temperature, reflecting the limitations of using the single band model or suggesting that thermally activated charge carriers also contribute to the transport. The mobility $\mu$ of the charge carriers decreases with increasing temperature, which can be attributed to increasing electron-phonon scattering with increasing temperatures. Finally, we note that while there is a slight increase in resistivity with decreasing temperatures below about 50 K for all samples, there is a reduction in resistivity at the lowest temperatures measured for the 4:**4** and 3:**2**:1:**2** isomers, suggesting that these samples become superconducting, which has also been reported previously for the misfit layered compounds $[(PbSe)_{1.14}]_1(NbSe_2)_1$, $[(PbSe)_{1.14}]_1(NbSe_2)_2$, and $[(PbSe)_{1.14}]_1(NbSe_2)_3$.[7-9]

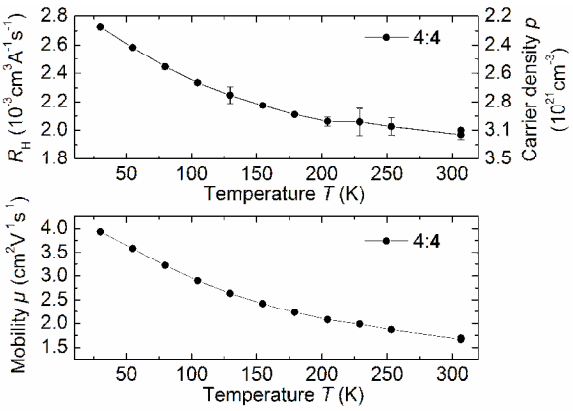


**Figure 5.4.** Hall coefficient $R_H$ and mobility μ for the 4:**4** isomer of $[(PbSe)_{1.14}]_4(NbSe_2)_4$.

While electrical data on additional samples with different nanoarchitectures needs to be obtained to understand the observed dependence of electrical properties on structure, this data shows that compounds with different nanoarchitectures have different properties. By using bonding motifs found in thermodynamically stable compounds, it is possible to predict a large number of families of new materials containing interleaved layers where physical properties would be dependent on the nanoarchitecture of the compound.[16]

## V.4. Conclusions and Bridge

As shown herein, the use of designed precursors with a nanoarchitecture similar to that of the desired product enables the templated self-assembly of targeted products with predicted structures. Figure 5.5 contains the calculated number of potential isomers for a given *n* and *m* value. The number of different possible arrangements increases rapidly as *n* and *m* increase, leading to over 20,000 distinct compounds for *n* and *m* less than or equal to 10. The large number of potential new compounds, each of which can be altered through traditional alloying or doping approaches, fundamentally changes the approach taken to optimize materials properties. Ideally, theoretical approaches will be

| m\n | 1 | 2 | 3 | 4 | 5 | 6 | 7 | 8 | 9 | 10 |
|---|---|---|---|---|---|---|---|---|---|---|
| 1 | 1 | 1 | 1 | 1 | 1 | 1 | 1 | 1 | 1 | 1 |
| 2 | 1 | 1 | 2 | 2 | 3 | 3 | 4 | 4 | 5 | 5 |
| 3 | 1 | 2 | 2 | 4 | 5 | 6 | 8 | 10 | 11 | 14 |
| 4 | 1 | 2 | 4 | 6 | 10 | 14 | 20 | 26 | 35 | 44 |
| 5 | 1 | 3 | 5 | 10 | 15 | 26 | 38 | 57 | 79 | 110 |
| 6 | 1 | 3 | 6 | 14 | 26 | 46 | 76 | 122 | 183 | 275 |
| 7 | 1 | 4 | 8 | 20 | 38 | 76 | 132 | 232 | 375 | 600 |
| 8 | 1 | 4 | 10 | 26 | 57 | 122 | 232 | 432 | 750 | 1272 |
| 9 | 1 | 5 | 11 | 35 | 79 | 183 | 375 | 750 | 1384 | 2494 |
| 10 | 1 | 5 | 14 | 44 | 110 | 275 | 600 | 1272 | 2494 | 4735 |

**Figure 5.5.** The number of possible structural isomers for a given $A_mB_n$ stoichiometry are given in each of the boxes. The colors of the boxes reflect the rapid increase in the number of isomers as *m* and *n* increase.

developed that use measurements on only a couple of family members to successfully predict the properties of the rest of the family of compounds, hastening the discovery process of materials with optimized properties. Using necklace combinatorics, this principle can be expanded to ferecrystals with more than two constituents. A python module was developed to calculate all isomers for ferecrystals with multiple constituents. The results can be filtered by desired thicknesses or interfaces. The code can be found in Appendix A and on https://github.com/marcoesters/ferecrystal_isomers.

This chapter introduced a new type of structural isomerism in solids by stacking constituents of a ferecrystal in different ways to receive structures with the same unit cell size, but different layering sequences. It demonstrated the complexity ferecrystalline structures can achieve and that the nanoarchitecture can be tailored by controlling the precursor structure. The pathway from the designed precursor to the desired ferecrystal is a key question in designing new ferecrystalline materials. Chapter VI will investigate the formation of a ferecrystal using $[(SnSe)_{1+\delta}]_1[VSe_2]_1$ as an example.

# CHAPTER VI

# FORMATION OF A SELENIDE-BASED HETEROSTRUCTURE FROM A DESIGNED PRECURSOR

Portions of this chapter were published previously as Falmbigl, M.; Esters, M.; Johnson, D.C. "Formation of a Selenide-based Heterostructure from a Designed Precursor" *Crystal Research and Technology*, **2017**, *52* (10), 1700067. M.E. and M.F. co-wrote the paper. M.F. synthesized the samples, and performed x-ray diffraction and the transition electron microscopy analysis. M.E. performed electron probe microanalysis, differential scanning calorimetry measurements, and x-ray absorption spectroscopy analysis. D.C.J. was the principal investigator and provided editorial assistance.

## VI.1. Introduction

Ferecrystals are heterostructures with the general formula $([MX]_{1+\delta})_m(TX_2)_n$ (M = rare earth metal, Bi, Pb, Sn; T = transition metal, Ti, V, Nb, Ta, Mo, W; X = Se, Te; *m*, *n* are integer numbers, and δ accounts for the misfit between the two structural units). The two constituents MX, a rocksalt-like double layer, and $TX_2$, a transition metal dichalcogenide X-T-X trilayer, are stacked in the sequence (*m*,*n*) along the *c*-axis. Ferecrystals are kinetically trapped metastable structural analogs of the misfit layered compounds,[1] structurally differing from them in having no commensurate crystallographic axes and exhibiting extensive rotational disorder between the MX and $TX_2$ layers. While thermodynamically stable misfit layer compounds can be prepared typically only when $n = m = 1$,[1] ferecrystals can be synthesized with a wide range of *m*

and *n* values.[2–4] One can even prepare ferecrystals that are structural isomers, only distinguishable from one another by the number of interfaces between the different building blocks.[5–7]

Ferecrystalline thin films are synthesized via the modulated elemental reactant method (MER), which utilizes ultra-thin layers of the elemental constituents as a precursor with a structure similar to that of the targeted compound.[8,9] Annealing at low temperatures self-assembles the ferecrystalline compound while minimizing the extent of diffusion to prevent the formation of more stable products.[2] The short diffusion lengths result directly from the layered structure of the precursors and the resulting high interface-to-bulk ratio. This causes ferecrystals to form much faster and at lower temperatures and that processes at the interfaces happen in a much higher quantity than in a traditional reaction of powdered elemental precursors. In terms of an energy landscape, ferecrystals can be visualized as local energy minima, which are made accessible by controlling the structure of the precursor and minimizing the extent of diffusion by using low temperatures. Recent results have shown, however, that higher temperature annealing transforms $m = n$ compounds in the $([SnSe]_{1+\delta})_m(NbSe_2)_n$ family ($m,n > 1$) into $([SnSe]_{1+\delta})_1(NbSe_2)_1$ with a surprisingly low amount of stacking defects.[2] The diffusion and self-assembly of the precursors into ferecrystals during annealing and the energy landscape around the different local minima in free energy space are not well understood.

It is hypothesized that each distinct $([MX]_{1+\delta})_m(TX_2)_n$ ferecrystal lies inside a local minimum in the free energy landscape. Experimentally, these local minima are accessed by defining the structure of the precursor. The ratio of the elements in the M|Se and T|Se layer pairs deposited, the absolute number of atoms in each of the M|Se and

T|Se pairs, and the pattern of these layer pairs deposited controls *m*, *n* and the stacking sequence in the final product. The reaction pathway from the as deposited precursor to the final product, however, has not been investigated in much detail and many open questions remain, including (i) does one constituent crystallize first and therefore govern/restrict the formation process of the remaining constituent(s)?, and (ii) are different local minima accessible as the metal/selenium ratios or annealing temperatures are varied?

To address these questions, we have conducted a detailed study on the formation of the superlattice structure of the charge density wave compound $(SnSe)_{1.15}VSe_2$.[3,10,11] Specular and grazing incident in-plane X-ray diffraction scans collected after annealing at different temperatures revealed that in this particular case three constituents are involved during the formation, namely, $CdI_2$-structured $VSe_2$ and $SnSe_2$, and NaCl-like structured SnSe. All constituents crystallize simultaneously although the ratios between them change. Superlattice reflections are observed, however, even at low annealing temperatures where all three constituents coexist.

## VI.2. Experimental

Physical vapor deposition was utilized to form the thin film precursors used in this study in a vacuum deposition chamber evacuated to a base pressure of $10^{-7}$ mbar.[12] An effusion cell was used to evaporate Se (Alfa Aesar, 99.999 at% purity) and Thermionics electron beam guns were used to evaporate Sn (Alfa Aesar, 99.98 at% purity), and V (Alfa Aesar, 99.7 at% purity). Substrates, <100> oriented silicon wafers with native oxide layer, were positioned approximately 25 cm above the sources on a motorized carousel. Pneumatically powered shutters positioned before the substrates were

utilized to control the amount of each element deposited. Quartz crystal microbalances were used to control the deposition rates of each element. Se, V, and Sn were deposited at 0.5 $Å s^{-1}$, 0.4 $Å s^{-1}$, and 0.4 $Å s^{-1}$, respectively. The deposition for each sample was carried out in layers by repeatedly depositing a sequence of Se|Sn|Se|V until a thickness of 1000 Å was reached. The precursors were annealed on a hot plate inside a glove box ($N_2$, <0.5 ppm of $O_2$) at 100, 200, 300, and 400 °C for 20 min. For each annealing condition a separate piece of the as deposited sample was used. Electron probe microanalysis (EPMA) using a CAMECA SX-100 with wavelength dispersive (WDS) spectrometers was used to determine the composition of the thin films before and after annealing, utilizing a special thin film technique.[13] Both X-ray reflection (XRR) and X-ray diffraction (XRD) data were collected on a Bruker D8 Discover diffractometer using Cu-Kα radiation (λ = 1.54185 Å). Grazing incidence in-plane X-ray diffraction was conducted at the Advanced Photon Source (APS), Argonne National Laboratories, at Beamline 33BM, using an incident X-ray beam with λ = 1.22653 Å. High resolution scanning transmission electron microscopy (HRSTEM) was carried out on an aberration-corrected FEI Titan (300 kV incident beam). The preparation of selected samples for HRSTEM was performed utilizing an FEI Helios Nanolab D600 DualBeam focused ion beam (FIB).

To investigate changes to the oxidation state of the elements, X-ray absorption spectroscopy (XAS) measurements were performed on beamline 10-BM-B at APS. XAS measurements were performed on the K-edges of V, Se, and Sn in fluorescence mode. To maximize intensity of the fluorescent beam, the samples were tilted by approximately 45° with respect to the incoming X-ray beam. The samples were rotated at an angle of 54.7°

to the incident beam for the Se and Sn K-edges to eliminate diffraction caused by the layered nature of the samples and the horizontal polarization of the incoming beam. The edge energies were determined using the inflection point and the measured energy ranges were 5250-6250 eV for V, 12450-13450 eV for Se, and 29000-30000 eV for Sn, respectively.

For thermal analysis, precursors with a total thickness of approximately 2000 Å were deposited onto Si wafers coated with a thin layer of poly(methyl methacrylate) (PMMA). Acetone was used to dissolve the PMMA and lift the film off the substrate. Differential scanning calorimetry (DSC) scans were performed on the lifted-off film flakes with a total mass of 1.5 mg using a Netzsch DSC 200 PC. DSC curves were acquired in a $N_2$ atmosphere (< 0.5 ppm $O_2$) between 50 °C and 400 °C with a heating rate of 10 K $min^{-1}$.

## VI.3. Results and Discussion

The synthesis of the precursors is based on an extensive calibration procedure, which was already described in depth for $(SnSe)_{1.15}VSe_2$.[3,10] This method utilizes the MER technique to form layered precursors that mimic the desired ferecrystalline superlattice.[8,9] This process involves an initial adjustment of the atomic ratio to form Sn|Se and V|Se (| is used, as this is the composition in the as deposited state and not a chemical compound) at 1 to 1 and 1 to 2 ratios respectively, followed by optimizing the thickness close to the targeted c-axis length of the corresponding crystalline layers for each constituent individually. In a last calibration step, alternating layers of Sn|Se and V|Se are deposited in a manner that the cation ratio (Sn/V) is close to 1.15:1 corresponding to the anticipated in-plane mismatch between the two constituents.[14] The

precursors are always targeted to contain a slight excess of Se (in this case 9 %) to compensate for evaporation losses during annealing. Finally, precursors with a layering sequence of Se|Sn|Se|V were deposited onto Si-substrates and subsequently exposed to a 20 minutes annealing treatment in $N_2$ atmosphere at 100, 200, 300, and 400 °C.

The specular X-ray diffraction scans at different annealing temperatures permit following the evolution of the ferecrystalline $(SnSe)_{1.15}VSe_2$ superlattice from the initial precursor (Figure 6.1). In the as deposited state two sharp superlattice reflections (*), (001) and (002), arising from the modulated nature of the precursor with a repeat unit thickness of 13.9(1) Å are present. In addition, there are broad reflections (# in Figure 6.6.1) attributed to the (00*l*) reflections of a $CdI_2$-structure. However, due to the very broad appearance of the reflections and the very close c-axis lattice parameters of the two potential constituent compounds, 6.104(2) Å for $VSe_2$ and 6.137(4) Å for $SnSe_2$,[15,16] it is unclear to which constituent they belong. After annealing at 100 °C, the intensities of the precursor reflections are significantly decreased, whereas the reflections corresponding to $VSe_2$ and $SnSe_2$ increase in intensity and first weak superlattice reflections are observed. Upon increasing the annealing temperature to 200 °C the higher order superlattice reflections grow significantly in intensity and exhibit already a small peak width, implying that a superstructure with a narrowly defined repeat unit thickness of 12.33(1) Å is present in the film. However, the reflections appear asymmetric and at 300 °C these peaks become weaker and broader although the superlattice repeat unit remains almost constant at 12.31(1) Å. This might indicate the presence of considerable strain and/or disorder between the individual layers. This might also arise from the transition of one predominant layer sequence into another as the annealing temperature increases from

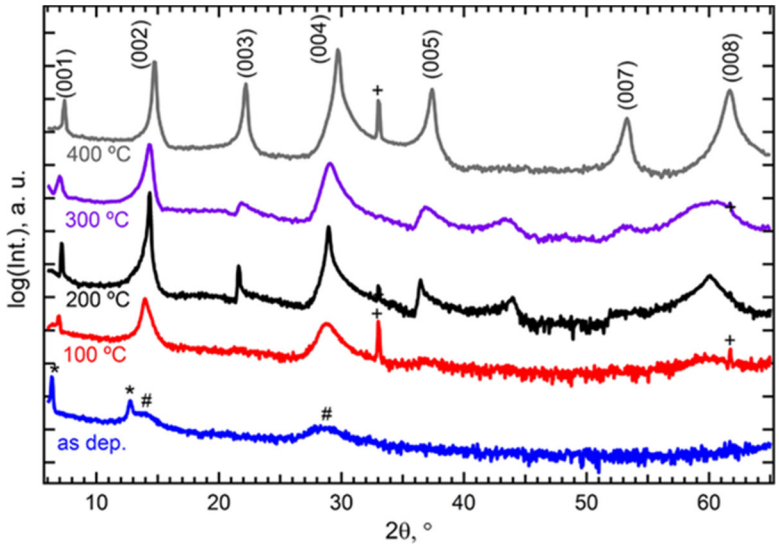


**Figure 6.1.** Specular X-ray diffraction as a function of annealing temperature. The (00l) indices along the superlattice direction are provided. + marks reflections from the (100)-Si substrate. For the as deposited sample the superlattice peaks (*) and the peaks corresponding to transition metal dichalcogenides (#) are indicated.

200 °C to 400 °C. Indeed, at 400 °C, a diffraction pattern typical for $(SnSe)_{1.15}VSe_2$ is observed and the superlattice thickness is significantly decreased to 12.01(1) Å. This value is within the range previously reported for $(SnSe)_{1.15}VSe_2$ ferecrystals with varying cation ratios.[11] The increased background between the (004) and (005) peak can be attributed to a surplus of Sn within the superlattice, which results in the formation of consecutive SnSe-layers causing a broad peak of the (400) SnSe reflection.[11]

In ferecrystalline compounds a superlattice only forms perpendicular to the substrate surface, but the layers keep their individual structures without sharing commensurate axes with the other layers. The individual layers also exhibit extensive rotational disorder between each other within the basal plane. These structural characteristics allow monitoring the crystallization process of each constituent separated from the others utilizing in-plane diffraction. Grazing incidence in-plane diffraction scans

collected after deposition and after annealing at 100, 200, 300, and 400 °C are depicted in Figure 6.2.

The observed reflections can all be indexed to $SnSe_2$ and $VSe_2$ in their trigonal bulk structure ($CdI_2$ type)[15,16] and SnSe in a distorted NaCl structure. For SnSe it was previously shown that the in-plane structure distorts from an initial square plane to a rectangular symmetry similar to the bulk structure (GeS-type)[17,18] as the layer thickness is increased.[14,19] In the as deposited sample only very weak and broad reflections are present and their positions roughly coincide with the *d*-spacings of (*hk*0) planes for $SnSe_2$ and $VSe_2$. At 100 °C reflections corresponding to three different structures, namely SnSe, $SnSe_2$, and $VSe_2$, can be distinguished unambiguously. In particular the (110) reflection of $SnSe_2$ is at a distinct angle and also sharper than reflections from the other constituents. The $SnSe_2$ reflections dominate until 300 °C, although the intensities of all other reflections increase and their widths become increasingly narrow as the annealing

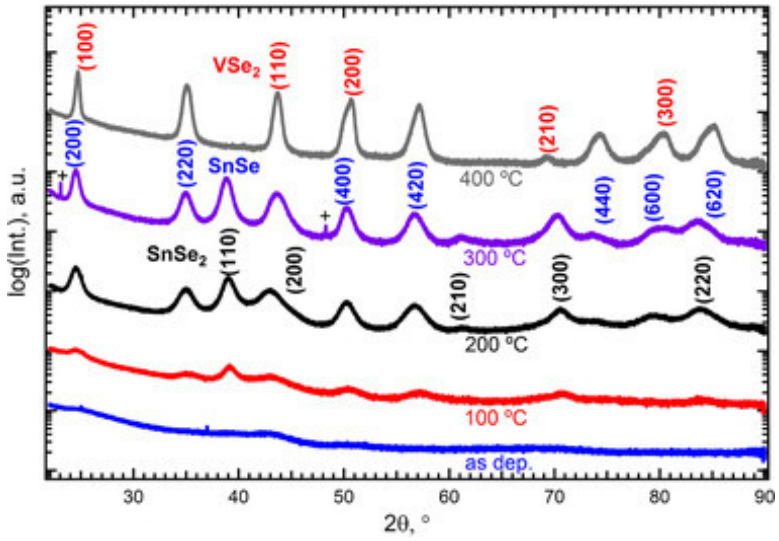


**Figure 6.2.** Grazing incidence X-ray diffraction scans as a function of annealing temperature. The (*hk*0) indices for each constituent, $SnSe_2$ and $VSe_2$ in $CdI_2$ structure type and SnSe in NaCl structure type, are provided. + marks reflections arising from the stage or substrate.

temperature is increased, implying a joint crystallization and crystal growth parallel to the substrate plane for all three constituents in this temperature regime. This scenario changes dramatically between 300 and 400 °C as only narrow reflections of SnSe and $VSe_2$ are observed, while all reflections corresponding to $SnSe_2$ vanish completely, indicating that the tin dichalcogenide layers become unstable under these annealing conditions. This is not unexpected, as $SnSe_2$ decomposes to SnSe and Se(g) at 340 °C,[20] and, even with a constant partial pressure of selenium, $SnSe_2$ is only stable below 470 °C, and at 530 °C, formation of phase-pure SnSe occurs.[21]

Differential scanning calorimetry (DSC) measurements were performed on powdered precursors of the ferecrystal and show only a single event, a broad exothermal signal at approximately 145 °C (Figure 6.3). This behavior corroborates the change observed in the diffraction patterns between 100 and 200 °C as the temperature of the exothermal event correlates well with the appearance of additional superlattice peaks in the specular diffraction scans (see Figure 6.1) and the transformation of the precursor into

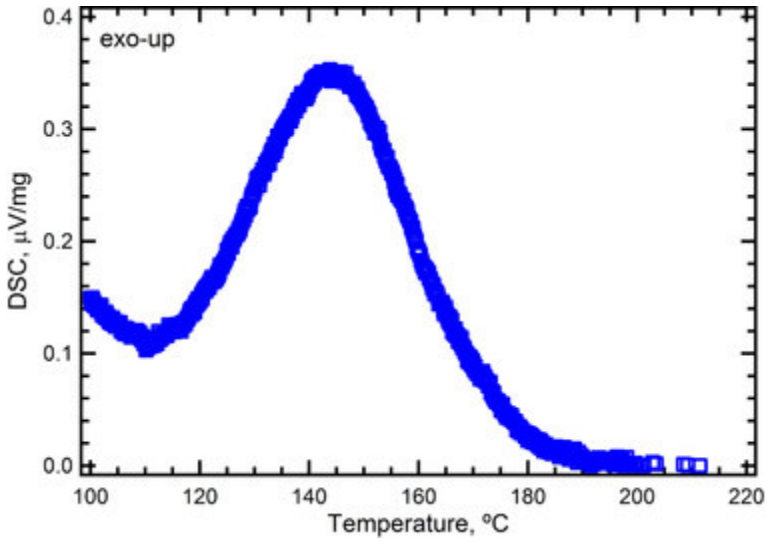


**Figure 6.3.** DSC scan of a powdered precursor for $(SnSe)_{1.15}VSe_2$. A broad exothermal peak around 145°C is clearly visible. Temperatures above 220°C were omitted because no signal was observed.

the crystalline $VSe_2$, SnSe and $SnSe_2$ layers (see Figure 6.2). However, the DSC data do not resolve the individual crystallization events of the three constituents $VSe_2$, $SnSe_2$, and SnSe. This is not surprising considering that although the nucleation barriers for each constituent should be slightly different, XRD experiments reveal a joint crystallization event. The crystallization temperatures are probably too close to be resolved as individual exotherms. The DSC is featureless above 250 °C, even though XRD shows a dramatic change in the diffraction patterns between 300 °C and 400 °C. We expected to see an endothermic signal from the decomposition of $SnSe_2$ and the evaporation of Se as well as an exothermic signal from the transformation into the $(SnSe)_{1.15}VSe_2$ ferecrystal. Since part of the superlattice has already formed at 300 °C and the amount of Se to evaporate is very small, the energy changes due to these processes are too small to be detected by DSC. These two events may also compensate each other, resulting in a total heat flow close to zero. In previous DSC experiments on MER-synthesized Fe-Si thin films it was demonstrated that the enthalpy of mixing is much larger than the crystallization enthalpy and usually results in a broad exothermal feature stretched over a large temperature range.[22]

In order to gain detailed insight into the layered structure at an intermediate stage, HAADF-STEM images of the film cross section after annealing at 300 °C were collected. A representative image is shown in Figure 6.4. Individual layers of all three constituents can be identified within the superlattice. A close inspection of the images reveals the presence of layering sequences such as $SnSe_2$-$VSe_2$-$SnSe_2$ (Figure 6.4a), where three consecutive $CdI_2$ trilayers are present. Interestingly, the three layers show similar crystallographic orientation resulting in a 1T-stacking sequence, typical for both bulk

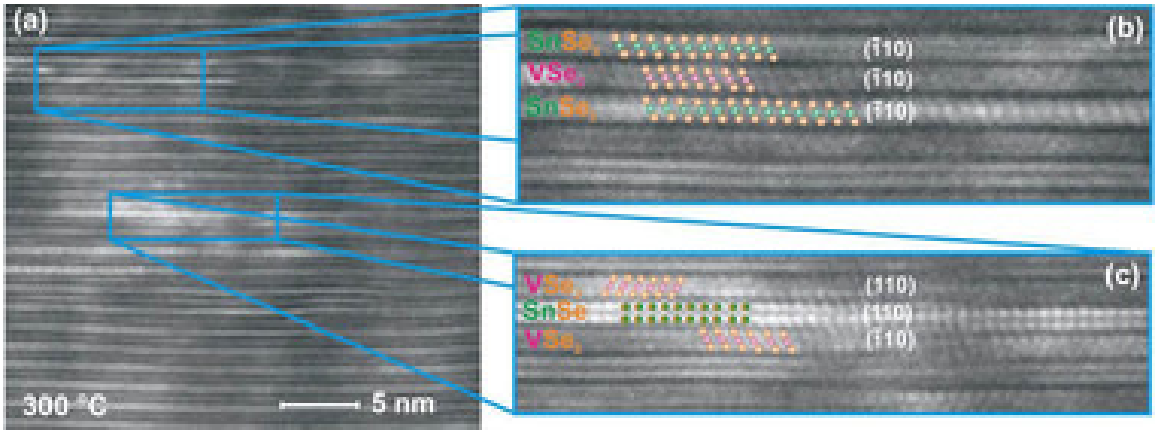


**Figure 6.4.** (a) HAADF-STEM image of the film annealed at 300°C. The magnified areas clearly reveal the presence of different stacking sequences, (b) $SnSe_2$-$VSe_2$-$SnSe_2$, and (c) $VSe_2$-SnSe-$VSe_2$.

structures.[15,16] This indicates that a templated growth of $SnSe_2$ and $VSe_2$ occurs in these regions of the superlattice similar to the $VSe_2$ blocks in $(SnSe)_{1.15}(VSe_2)_n$ with $n > 1$.[3] The insertion of a SnSe layer, which does not have the same structure, results in a random orientation of adjacent $VSe_2$ layers (Figure 6.4b). The presence of both layer sequences in adjacent regions of the same film clearly demonstrates that the preference of forming one or the other layer sandwiched between two $VSe_2$ trilayers is most likely dictated by local composition rather than energetically favoring one of the two configurations. Indeed, both stacking sequences readily form and coexist after annealing for 20 minutes at 300 °C.

Comparing the TEM images collected after annealing at 300 °C to a fully assembled $(SnSe)_{1.15}VSe_2$ ferecrystal after annealing at 400 °C reveals differences in the appearance of the interfaces (Figure 6.5). At 300 °C (Figure 6.5a) some areas exhibit significant distortions/bending of layers, which is most likely induced by the thickness mismatch between the two stacking sequences of SnSe-$VSe_2$ and $SnSe_2$-$VSe_2$. If the structure changes within a layer from $SnSe_2$ to SnSe, a strain of up to 3% can be

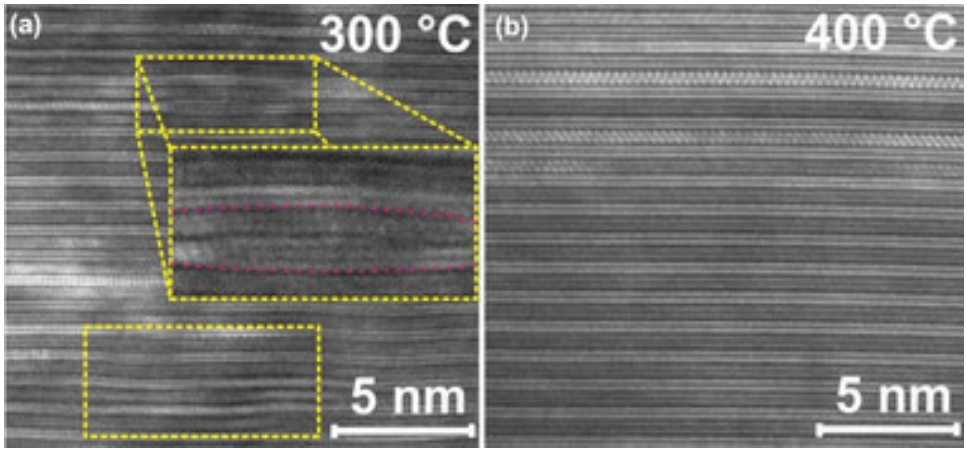


**Figure 6.5.** (a) HAADF-STEM image of a film annealed at 300°C highlighting areas with significant distortions and bending of individual layers, and (b) HAADF-STEM image of a film annealed at 400°C revealing an ideal stacking sequence with smooth, abrupt interfaces.

introduced, which can account for the asymmetry of the superlattice peaks and the broadening/weakening of the reflections observed below 400 °C (Figure 6.1).

A careful analysis using all information presented in section 3 along with changes in the composition allows to shed some light onto the formation mechanism of the ferecrystalline compound $(SnSe)_{1.15}VSe_2$ from the thin film precursor. The data is summarized in Table 6.1. The change in film thickness as a function of temperature exhibits two major decreases between the as deposited film and annealing at 100 °C as well as between 300 and 400 °C (Figure 6.6a). At the same time there is only one the initial decrease of film thickness can be attributed to densification due to a partial crystallization of all layers. This is supported by the observation of reflections of the individual constituents emerging in the in-plane diffraction data (Figure 6.2). The Se/(Sn+V)-ratio remains nearly constant with annealing temperature and exhibits a steep drop between 300 and 400 °C similar to the change in film thickness. At the same time the Sn/V ratio remains essentially unchanged indicating that only Se evaporates from the

**Table 6.1.** Film thickness, *c*-axis lattice parameter along the superlattice direction, composition in at.%, and in-plane lattice parameters of the individual constituents after annealing at different temperatures.

| condition | film thickness (Å) | *c* (Å) | Sn at.% | V at.% | Se at.% | $a_{SnSe}$ (Å) | $a_{SnSe_2}$ (Å) | $a_{VSe_2}$ (Å) |
|---|---|---|---|---|---|---|---|---|
| as dep. | 1245(5) | 13.9(1)<br>6.3(1)* | 20.5(1) | 17.8(1) | 61.7(1) | *n.a.* | *n.a.* | *n.a.* |
| 100 °C | 1154(5) | 12.4(1) | 20.7(1) | 18.0(1) | 61.3(1) | 5.92(2) | 3.78(2) | 3.46(2) |
| 200 °C | 1145(5) | 12.33(5) | 21.1(1) | 17.9(1) | 61.0(1) | 5.94(2) | 3.78(2) | 3.46(2) |
| 300 °C | 1142(5) | 12.31(5) | 21.0(1) | 18.1(1) | 60.9(1) | 5.95(1) | 3.79(1) | 3.40(1) |
| 400 °C | 1078(5) | 12.01(3) | 23.5(1) | 19.7(1) | 56.8(1) | 5.93(1) | *n.a.* | 3.39(1) |

* The first value corresponds to the superlattice period, and the second value to the *c*-lattice parameter of the transition metal dichalcogenides $VSe_2$ and $SnSe_2$; *n.a.* not applicable.

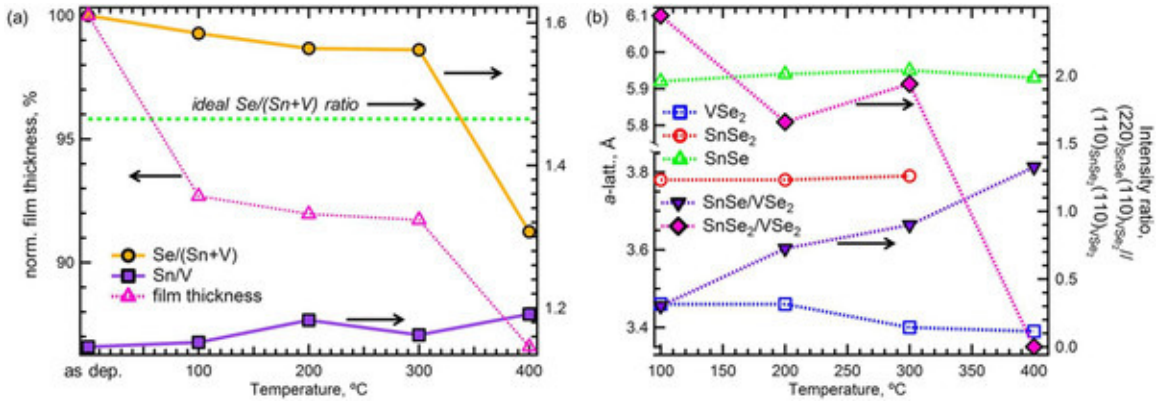


**Figure 6.6.** (a) Film thickness calculated from XRR normalized to the as deposited film thickness, and Se/(Sn+V) and Sn/V ratios extracted from EPMA as a function of annealing temperature (the green dashed line corresponds to the Se/(Sn+V) ratio for $(SnSe)_{1.15}VSe_2$, (b) In-plane lattice parameters of all three constituents as a function of temperature, and intensity ratios of $(220)_{SnSe}/(110)_{VSe_2}$ and $(110)_{SnSe_2}/(110)_{VSe_2}$.

film surface at 400 °C. A comparison to the ideal Se/(Sn+V)-ratio of 1.47 expected for stoichiometric $(SnSe)_{1.15}VSe_2$ (green dashed line in Figure 6.6a) reveals that initially there is a surplus of Se explaining the presence of $SnSe_2$ within the superlattice. However, after annealing at 400 °C the ratio drops below this value, which can be explained considering two scenarios: (i) at the same time as the Se content decreases there is a significant increase of oxygen from 6 to 18 %, which can partially account for the off-stoichiometry, (ii) Se-vacancies in SnSe and/or $VSe_2$. Considering the binary phase diagram, a significant phase width of SnSe can be ruled out,[23] and it is highly unlikely that the Sn cations get fully reduced to metallic Sn in the annealing environment. However, the binary V-Se phase diagram exhibits a large solubility range from $VSe_2$ to VSe at elevated temperatures,[24] which allows the presence of a Se deficient dichalcogenide. In the open annealing environment both, oxide formation and substoichiometric $VSe_2$, are most likely contributing to the observed change in composition. Neglecting the oxide formation and assuming stoichiometry for all SnSe layers, the average composition of the V-Se layers would be $VSe_{1.68}$ after annealing at 400 °C.

Further evidence for a change in the composition of the $VSe_2$ layers is provided by an evaluation of the in plane lattice parameters of all constituents (Figure 6.6b). Whereas the lattice parameters of SnSe and $SnSe_2$ remain essentially constant over the whole temperature range investigated, the in plane lattice parameter of $VSe_2$ decreases slightly between 200 and 300 °C. This points toward a change within the $VSe_2$ structure, most likely due to a decrease in the Se-content. The intensity ratios of the two tin selenides compared to vanadium diselenide, calculated from the peak heights, allow an

estimation of the change in relative content of the constituents. As depicted in Figure 6.6b the $(110)_{SnSe_2}/(110)_{VSe_2}$ ratio decreases first, remains constant between 200 and 300 °C with a sharp drop to 0 at 400 °C, whereas the $(220)_{SnSe}/(110)_{VSe_2}$ ratio constantly increases with temperature. This trend points toward a constant increase of SnSe on the expense of $SnSe_2$ based on the following reaction:

$$SnSe_2\ (s) \rightarrow SnSe\ (s) + Se\ (g) \qquad (6.1)$$

This reaction seems to happen at an extremely slow rate above 100 °C and shifts rapidly and completely to the reaction products at higher temperatures, driven in part by the open system annealing conditions, which allows Se to evaporate freely. Similar observations were also made in selenization studies of tin thin films, where in the presence of Se-vapor $SnSe_2$ only forms below 470 °C.[21]

This reaction also involves a change in the nominal oxidation state of Sn from 4+ to 2+. The evaluation of the absorption edge energy from XAS experiments performed on the K-edges of Sn, V, and Se provide a measure of the change in oxidation state for each element at a given temperature relative to the initial precursor (Figure 6.7).

The edge energy of Se decreases until 300 °C, consistent with a decrease in the oxidation number as Se is incorporated as anion in all three constituents and should be in all cases $Se^{2-}$. On the other hand, V and Sn increase in edge energy, which is consistent with an increasing oxidation state. Interestingly, the V edge energy remains constant between 200 and 400 °C. The total shift of +0.6 eV compared to the as deposited state is roughly half of the difference in edge energy between VO and $V_2O_4$ and can therefore be estimated to correspond to an increase in oxidation state by +1.[25] In contrast to that the edge energy of Sn first increases indicating an increase in the oxidation state before it

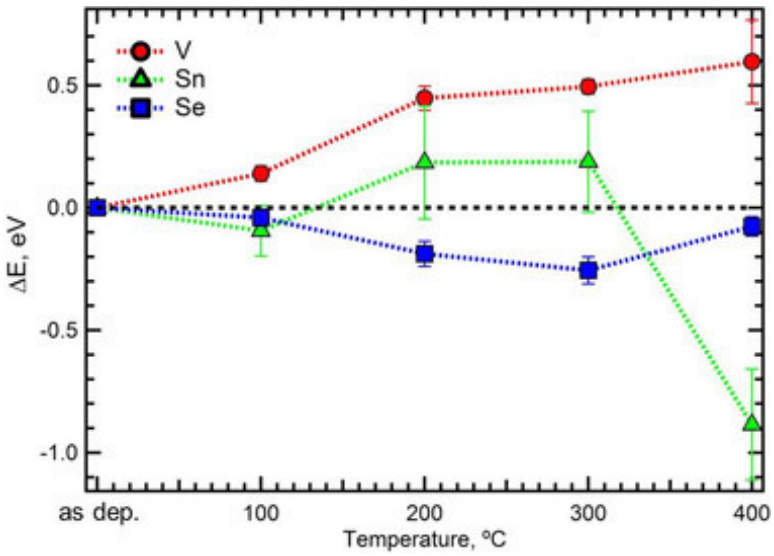


**Figure 6.7.** Energy shift ΔE of the K-absorption edge shift for Sn, V, and Se as a function of annealing temperature relative to the as deposited precursor.

decreases significantly at 400 °C. This decrease can be explained by the transformation of all $SnSe_2$ to SnSe and the accompanying decrease in the average oxidation state of Sn.[26] It is interesting to note that the change of the absorption edge energy between the as deposited sample and the one annealed at 300 °C is much smaller than the change between 300 °C and 400 °C. This observation indicates that Sn is already oxidized in the as deposited film.

## VI.4. Conclusions and Bridge

In summary we have investigated the formation of the ferecrystalline compound $(SnSe)_{1.15}VSe_2$ from a modulated thin film precursor. Diffraction data indicate that only a small fraction of the as deposited film is crystalline and that these crystallites are very disordered and/or have small coherent domains. Annealing initiates the simultaneous growth of three crystalline constituents, SnSe, $SnSe_2$, and $VSe_2$. By 200 °C, superlattice reflections are clearly visible. At 300 °C, different layering sequences involving all three constituents coexist pointing toward the existence of different minima in an energy

landscape, which can be readily accessed depending on the local composition. The $SnSe/SnSe_2$ ratio decreases with increasing temperature. At 400 °C, Se evaporation causes a complete transformation of $SnSe_2$ into SnSe and Se vapor, resulting in the formation of ferecrystalline $(SnSe)_{1.15}VSe_2$. Overall, this investigation showcases that metastable ferecrystalline compounds bear a high potential to produce a plethora of different heterostructures by controlling the reaction pathway via precursor composition and annealing conditions.

So far, experimental methods have been used to probe the formation, structure and properties of thin films synthesized by the modulated elemental reactants method. However, not all properties can be explained using experimental methods, and electronic structure calculations are needed to provide insights into the behavior of materials. Chapter VII will introduce important methods and concepts for electronic structure calculations, which will be used in the remainder of this work.

CHAPTER VII

BRIDGE: ELECTRONIC STRUCTURE CALCULATIONS

## VII.1. The Hartree-Fock Method

One fundamental goal of scientific inquiry is the explanation and discovery of the fundamental properties and processes that shape the universe around us. For atoms and sub-atomic particles, the discovery that properties do not exhibit a continuous spectrum, but instead adopt discreet (quantized) values, has led to the development of quantum mechanics with the time-dependent Schrödinger equation as its central tenet:[1,2]

$$\hat{H}\Psi(\vec{r},t) = i\frac{\partial}{\partial t}\Psi(\vec{r},t) \tag{7.1}$$

Where $\hat{H}$ is the Hamilton operator, $\Psi(\vec{r},t)$ is the wave function of the particle, which depends on the particle's position $\vec{r}$ and the time *t*, *i* is the imaginary number. This equation has the very important implication that wave functions can form stationary states in the form of standing waves, which are the atomic and molecular orbitals. The Schrödinger equation then becomes a time-independent eigenvalue problem with the energy *E* as the eigenvalue and the wave function as the eigenvector:

$$\hat{H}\Psi(\vec{r},t) = E\Psi(\vec{r},t) \tag{7.2}$$

The eigenvalues and wave functions can be found using the variational theorem. A trial function is used and the expectation value *E* is calculated using:

$$E = \frac{\langle\Psi|\hat{H}|\Psi\rangle}{\langle\Psi|\Psi\rangle} \tag{7.3}$$

These wave functions are subsequently varied to minimize the energy. When the energy does not lower within a set threshold, the calculation is considered converged. For

the time-independent Schrödinger equation, the expectation value is always greater than or equal to the ground state energy (Hartree-Fock limit).[3]

A major challenge is to find the correct Hamilton operator and the correct wave functions for the problem that is to be solved. The Hamilton operator in its most general form is:

$$\hat{H} = \hat{T}_e + \hat{T}_N + \hat{V}_{ee}(\vec{r}) + \hat{V}_{eN}(\vec{r}, \vec{R}) + \hat{V}_{NN}(\vec{R}) \tag{7.4}$$

With the kinetic energy operators $\hat{T}_e$ and $\hat{T}_N$ for the electrons and nuclei, respectively, and the operators $\hat{V}$ for the interactions between electrons (*ee*), electrons and nuclei (*eN*), and between nuclei (*NN*). $\vec{r}$ denotes the position of the electrons and $\vec{R}$ the position of the nuclei. Since the motion of electrons and nuclei happen on different time scales, i.e. electrons are much faster than nuclei, the wave function can be described as the product of electron and nucleus wave functions. Another consequence of this approximation, which is called the Born-Oppenheimer approximation,[4] is that the kinetic energy of the nuclei can be set to zero and the *NN* interactions become a constant term that can be calculated using Coulomb's law. The energy of a system then becomes:

$$E = \varepsilon(\vec{r}) + E_{nuc} = \varepsilon(\vec{r}) + \sum_{A>B} \frac{Z_A Z_B}{R_{AB}} \tag{7.5}$$

Where $\varepsilon(\vec{r})$ is the energy of the electrons, $E_{nuc}$ is the energy of the nuclei, and $Z_A$ and $Z_B$ are the charges of the nuclei *A* and *B*. Using the operator expression for the kinetic energy $\hat{T} = -\frac{1}{2}\nabla^2$ and Coulomb's law for the *ee* and *eN* interactions, the resulting electronic Schrödinger equation for a many-body system takes the form:

$$\left[-\frac{1}{2}\sum_i \nabla_i^2 - \sum_{i,A} \frac{Z_A}{r_{iA}} + \sum_{i>j} \frac{1}{r_{ij}}\right] \psi(\vec{r}, \vec{R}) = \left[\sum_i \hat{h}_i + \sum_{i>j} \frac{1}{r_{ij}}\right] \psi(\vec{r}, \vec{R}) = \varepsilon(\vec{r}) \psi(\vec{r}, \vec{R}) \tag{7.6}$$

Where $\psi(\vec{r},\vec{R})$ is the electronic wave function. The first sum of the operator represents the kinetic energy of all electrons *i*, the second sum the interaction between all electrons *i* all nuclei *A*, and the third sum the interaction between all electron pairs *ij*. $\hat{h}_i$ is a so-called one-electron operator:

$$\hat{h}_i = -\frac{1}{2}\nabla_i^2 - \sum_A \frac{Z_A}{r_{iA}} \tag{7.7}$$

For a system with *n* electrons and orbitals $\chi(x)$ at the space-spin coordinate $x = \{\vec{r}, s\}$, this wave function is typically expressed using a Slater determinant,[5] which satisfies the anti-symmetry requirements of fermions:

$$\psi(\vec{r},\vec{R}) = |1\ 2\ \cdots N\rangle = \frac{1}{\sqrt{n!}}\begin{vmatrix} \chi_1(x_1) & \chi_2(x_1) & \cdots & \chi_n(x_1) \\ \chi_1(x_2) & \chi_2(x_2) & \cdots & \chi_n(x_2) \\ \vdots & \vdots & \ddots & \vdots \\ \chi_1(x_n) & \chi_2(x_n) & \cdots & \chi_n(x_n) \end{vmatrix} \tag{7.8}$$

The expectation value for such a wave function is:

$$E_{HF} = \sum_i \langle i|\hat{h}_i|j\rangle + \frac{1}{2}\sum_{i,j}\left[\left\langle ij\left|\frac{1}{r_{ij}}\right|ij\right\rangle - \left\langle ji\left|\frac{1}{r_{ij}}\right|ij\right\rangle\right] \tag{7.9}$$

The first term in the second sum is the *Coulomb energy*, and the second term is the *exchange energy*, which is an artifact of using a Slater determinant and is only non-zero for orbitals with the same spin. The energy this expectation value represents is the *total Hartree-Fock energy* $E_{HF}$, and can be decomposed into four components (not including the Coulomb repulsion of the nuclei):

$$E_{HF} = T_e + E_{eN} + E_{Coul} + E_X \tag{7.10}$$

Where $T_e$ is the kinetic energy of the electrons, $E_{eN}$ is the electron-nucleus attraction energy, $E_{Coul}$ is the Coulomb energy and $E_X$ is the exchange energy.

## VII.2. Density Functional Theory

*The Hohenberg-Kohn Theorems*

The Hartree-Fock method assumes that the wave function of the system can be described using a single Slater determinant. The consequence of this is an incomplete description of electron correlation, which describes the influence of the presence of electrons on the movement of another electron. There are two forms of electron correlation: The Fermi correlation, which describes the correlation due to the repulsion of electrons with the same spin, and the Coulomb correlation, which describes the correlation due to Coulomb repulsion. The Hartree-Fock method includes Fermi correlation through the exchange energy, but the Coulomb correlation cannot be described using a single Slater determinant.

Density Functional Theory (DFT) is a computational method that includes both forms of correlation, and is based on the *Hohenberg-Kohn theorems*.[6] Pierre Hohenberg and Walter Kohn have shown that (i) the external potential is a unique functional of the electron density $\rho$, and that (ii) a universal functional for the energy $E[\rho]$ can be defined in terms of this density.

Like the Hartree-Fock method, DFT uses the Born-Oppenheimer approximation and treats the Coulomb potential from the nuclei as an external potential $V_{ext}(\vec{r})$, which results in the following Hamilton operator:

$$\hat{H} = \hat{T} + \hat{U} + \hat{V}_{ext} \tag{7.11}$$

Where $\hat{T}$ and $\hat{U}$ are the kinetic energy and the electron-electron interaction operators, respectively. $\hat{T}$ and $\hat{U}$ only depend on the number of electrons *N* and are often called *universal operators*. $\hat{V}_{ext}$ is the operator that describes the external potential. The

ground state $\Psi_0$ thus only depends on the number of electrons and the external potential. Associated with this ground state is a ground state electron density $n_0(\vec{r})$:

$$\rho_0(\vec{r}) = \langle \Psi_0 | \hat{\rho} | \Psi_0 \rangle = N \int |\Psi_0(\vec{r}, \vec{r}_2, \vec{r}_3, \dots, \vec{r}_N)|^2 d\vec{r}_2 d\vec{r}_3 \dots d\vec{r}_N \tag{7.12}$$

From the Hohenberg-Kohn theorems, it follows that the ground state energy is the energy at the ground state electron density $\rho_0(\vec{r})$:

$$E_0 = E[\rho_0(\vec{r})] \tag{7.13}$$

The ground state energy can thus be found by minimizing the energy with respect to the electron density using the variational principle. Using the Hamilton operators in Equation 7.11, the energy can be expressed as a density functional:

$$E[\rho] = T[\rho] + U[\rho] + V_{ext}[\rho] \tag{7.14}$$

*Kohn-Sham DFT*

The challenge is to find the appropriate functional for each interaction. $V_{ext}[\rho]$ can be explicitly written in terms of the electron density:

$$V_{ext}[\rho] = \int V_{ext}(\vec{r}) \rho(\vec{r}) d\vec{r} \tag{7.15}$$

For the kinetic energy, on the other hand, functionals using only the electron density are difficult to find and result in large errors. Instead of using the electron density, the approach by Walter Kohn and Lu Jeu Sham uses a fictitious system of non-interacting electrons that have the same electron density as the real system.[7] Using non-interacting electrons allows the system to be described as a single Slater determinant using one-electron orbitals $\psi_i$. The resulting Kohn-Sham (KS) equation is:

$$\left( -\frac{1}{2} \nabla^2 + \hat{V}_{eff}(\vec{r}) \right) \psi_i(\vec{r}) = \varepsilon_i \psi_i(\vec{r}) \tag{7.16}$$

Where $\hat{V}_{eff}$ is an effective potential consisting of the external potential and the electron-electron interactions. $\varepsilon_i$ is the eigenenergy of the KS orbitals. The KS equation can be solved by finding the set of orbitals that yields the lowest energy. The principle is demonstrated in Figure 7.1.

Using these one-electron orbitals, the kinetic energy functional can now be calculated exactly:

$$T[\rho] = -\frac{1}{2}\sum_i \langle i|\nabla^2|i\rangle \tag{7.17}$$

Even though this kinetic energy is not the kinetic energy of the real system, the error arising from using this kinetic energy functional is much lower than the error from approximating the kinetic energy of the electrons in the real system.

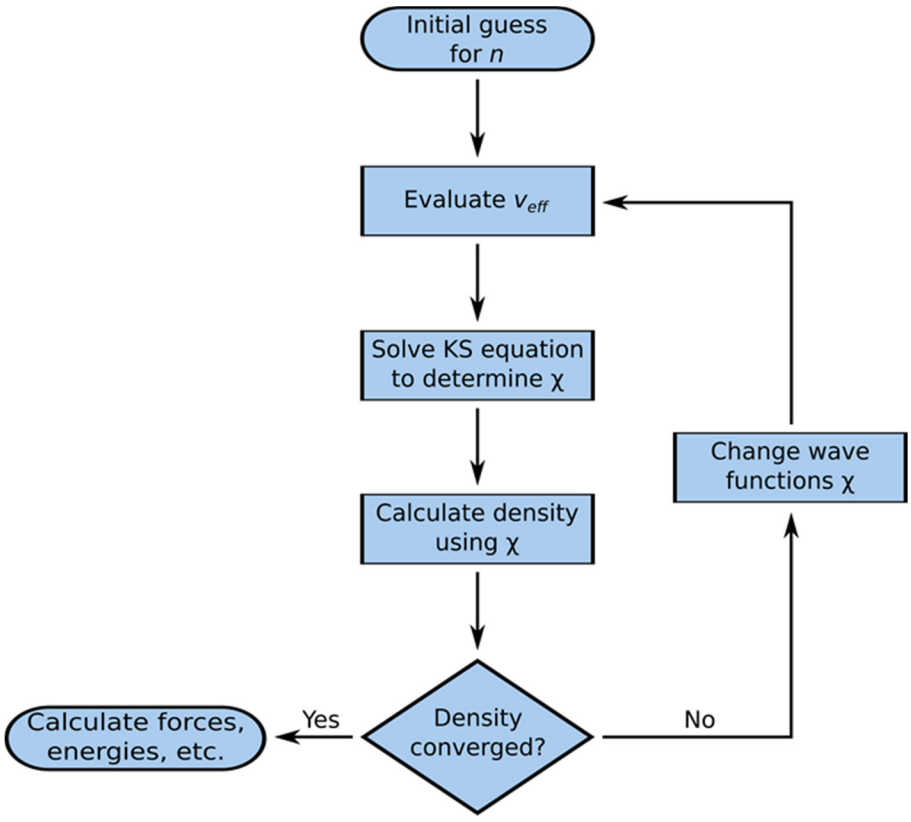


**Figure 7.1.** Flow chart for the self-consistency loop in Kohn-Sham DFT.

*Exchange-Correlation Functionals*

The electron-electron interaction functional $U[\rho]$ (see Equation 7.14) is composed of the classical Coulomb repulsion term $E_{Coul}[\rho]$ and the non-classical correlation term $E_{XC}[\rho]$, which includes Fermi (exchange) and Coulomb correlation. The Coulomb term can be written in terms of the electron density:

$$E_{coul}[\rho] = \frac{1}{2}\int\int \frac{\rho(\vec{r}_1)\rho(\vec{r}_2)}{r_{12}} d\vec{r}_1 d\vec{r}_2 \tag{7.18}$$

$E_{XC}[\rho]$, called the exchange-correlation (XC) functional, on the other hand, is unknown analytically and needs to be approximated. In the *local density approximation* (LDA), the functional depends only on the density where the functional is evaluated:

$$E_{XC}^{LDA}[\rho] = \int \varepsilon_{XC}(\rho)\rho(\vec{r})d\vec{r} \tag{7.19}$$

Where $\varepsilon_{XC}(\rho)$ is the XC functional of the homogeneous electron gas (HEG) with density $\rho$. For the HEG, the exchange part is known analytically. The correlation part is known for low and high densities and can be parametrized using quantum Monte Carlo methods – in this dissertation, the parametrization of Perdew and Zunger is used.[8]

Structural, elastic, and vibrational properties are relatively accurate using LDA, but the relative energies (cohesive energies, phase stabilities) can be very unreliable. An improvement over LDA is the *generalized gradient approximation* (GGA), which also takes the gradient of the electron density into account:

$$E_{XC}^{GGA}[\rho] = \int \varepsilon_{XC}(\rho, \nabla\rho)\rho(\vec{r})d\vec{r} \tag{7.20}$$

There are many different GGA functionals with the most common functional being the functional by Perdew, Burke and Ernzerhof (PBE), which uses the HEG exchange with an enhancement factor for exchange and correlation.[9]

*Strongly Correlated Electrons and the DFT+U Method*

Another consequence of using approximate XC functionals is the so-called self-interaction error (SIE). The self-interaction term arises from the Coulomb interactions:

$$J_c = \left\langle ij \left| \frac{1}{r_{ij}} \right| ij \right\rangle \tag{7.21}$$

This term does not vanish for $i = j$, which is unphysical because an electron does not interact with itself. This term exists in the Hartree-Fock method as well, but gets cancelled out by the exact exchange term (see Equation 7.9). Since the exchange energy in LDA and GGA are approximate, however, this term does not cancel out in DFT.

For materials with strongly correlated, i.e. less delocalized, electrons, this error can become fairly large. NiO, an antiferromagnetic charge transfer insulator, is one such example. GGA predicts NiO to be a semiconductor with a small band gap, and LDA even predicts NiO to be metallic.[10–13] Both GGA and LDA predict that electronic transitions are of $d \rightarrow d$ character, but it is experimentally known that they are of $p \rightarrow d$ character.[14–16] This is a direct consequence of the SIE.

The LDA and GGA exchange functionals, by virtue of being mean-field approaches, average the self-exchange term *U* and the exchange term between different orbitals *J*. However, *U* is an order of magnitude larger than *J* in real systems, so this averaging artificially increases the orbital energies, which is especially prominent with *d* and *f* orbitals and the reason why the highest occupied states are Ni *d* states and not O *p* states.

One way to correct this overestimation is to use the Hubbard model to add a screened intraatomic interaction. The Hubbard Hamilton operator is:

$$\hat{H} = -\sum_{ij\sigma}\left(t_{ij}c_j^{\dagger}c_i + t_{ij}^{*}c_i^{\dagger}c_j\right) + U(\hat{n}_{\uparrow}\hat{n}_{\downarrow}) \tag{7.22}$$

$t_{ij}$ is the hopping integral between sites *i* and *j*, σ is the spin, and *U* is a Coulomb repulsion term.[17] This repulsion term, along with the *J* term mentioned earlier, is added to the KS Hamiltonian. The method is called *LDA+U* or *GGA+U*. This dissertation uses the Dudarev method,[18] which only depends on an effective *U* term:

$$U_{eff} = U - J \tag{7.23}$$

The total energy with the Dudarev approach becomes:

$$E_{DFT+U} = E_{DFT} + \frac{U_{eff}}{2}\sum_{\sigma}\left[\sum_{i}\hat{n}_i^{\sigma} + \sum_{ij}\hat{n}_{ij}^{\sigma}\hat{n}_{ji}^{\sigma}\right] \tag{7.24}$$

Where $\hat{n}$ are atomic orbital occupation matrices. This means that a penalty functional is added that is driving the system away from partially occupied orbitals, i.e. towards an insulating state. It also means that energies cannot be compared unless $U_{eff}$ is the same. The choice of $U_{eff}$ needs to be carefully checked against experimental benchmarks.

*Hybrid Functionals*

Another approach to reduce the SIE are so-called *hybrid functionals*, which are more accurate in reproducing band gaps without the need to calibrate a value for *U*, but can be extremely expensive to compute and also introduce additional parameters.

The HSE (Heyd-Scuseria-Ernzerhof) functionals are examples of such hybrid functionals, which calculate the exchange energy using a mix of DFT functionals and the exact exchange from the Hartree-Fock method.[19] The exchange energy for HSE functionals is calculated using:

$$E_X^{HSE} = \alpha E_x^{HF,SR}(\omega) + (1-\alpha)E_x^{PBE,SR}(\omega) + E_x^{PBE,LR}(\omega) \quad (7.25)$$

*SR* and *LR* denote short-range and long-range exchange interactions. $\alpha$ is the weighting factor for the short-range exchange, which is 0.25 for HSE functionals. ω is a parameter used to screen the Coulomb potential using error functions $\mathrm{erf}(\omega r)$ and is 0.2 Å for HSE06 and 0.3 Å for HSE03. For the long-range exchange, a screened PBE exchange is used because the Fock exchange decays too slowly.

*The Projector Augmented Wave Method*

For a solid with periodic boundary conditions, the wave function is typically expressed as a Bloch function:

$$\left|\vec{k}\right\rangle = u_{\vec{k}}(\vec{r}) \cdot e^{i\vec{k}\vec{r}} \quad (7.26)$$

Where $u_{\vec{k}}(\vec{r})$ is a periodic function with the periodicity of the crystal, for example a periodic arrangement of atomic orbitals.[20] This function is also periodic in reciprocal space when $u_{\vec{k}}(\vec{r})$ is described as a Fourier series:

$$\left|\vec{k}\right\rangle = e^{i\vec{k}\vec{r}} \sum_{\vec{G}} c_{\vec{k}+\vec{G}} e^{i\vec{G}\vec{r}} \quad (7.27)$$

The advantage of using Bloch functions is that calculations can be limited to the unit cell and the first Brillouin zone. There remains a significant challenge, however: while the wave function is easy to calculate between atoms and in the valence region, the wave function undergoes strong oscillations near the core (see Figure 7.2), which are expensive to compute.

It would be computationally more efficient to transform this wave function into a smooth wave function in the near-core region, the *augmentation region*, and replace the oscillating potential with a smooth effective potential, the *pseudopotential*. To achieve

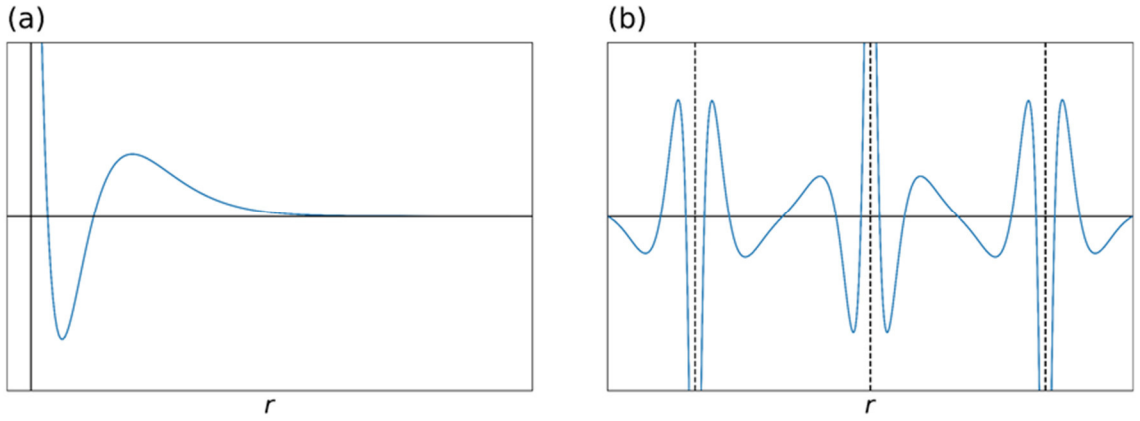


**Figure 7.2.** (a) Sketch of the radial part of the wave function of a Mg 3s orbital. (b) Sketch of the Bloch function of a 1-dimentional chain of Mg 3s orbitals at the *X* point.

this, the Kohn-Sham orbital $|\psi\rangle$ is transformed using a linear transformation operator $\hat{\mathcal{T}}_A$ that is only non-zero within the augmentation region:

$$|\psi\rangle = \left(1 + \sum_A \hat{\mathcal{T}}_A\right)|\tilde{\psi}\rangle \tag{7.28}$$

This method is called the *projector augmented wave* (PAW) method.[21] The pseudo wavefunction $|\tilde{\psi}\rangle$ can be decomposed into pseudo partial waves $|\tilde{\phi}_i\rangle$:

$$|\tilde{\psi}\rangle = \sum_i c_i|\tilde{\phi}_i\rangle \tag{7.29}$$

$$c_i = \langle p_i|\tilde{\psi}_i\rangle \tag{7.30}$$

$|p_i\rangle$ is a projection operator where $\langle p_i|\tilde{\phi}_i\rangle = \delta_{ij}$. The pseudo partial functions are related to all-electron partial waves $|\phi_i\rangle$, which are typically solutions to the Kohn-Sham equation for isolated atoms, via the same transformation operator.

The transformation operator can be written as:

$$\hat{\mathcal{T}} = 1 + \sum_i \left(|\phi_i\rangle - |\tilde{\phi}_i\rangle\right)\langle p_i| \tag{7.31}$$

Expectation values of an operator $\hat{O}$ transform accordingly:

$$O = \langle\tilde{\psi}|\mathcal{T}^{\dagger}\hat{O}\mathcal{T}|\tilde{\psi}\rangle = \langle\tilde{\psi}|\tilde{O}|\tilde{\psi}\rangle \tag{7.32}$$

Where the pseudo operator $\tilde{O}$ can be written explicitly as:

$$\tilde{O} = \hat{O} + \sum_{i,j} |p_i\rangle(\langle\phi_i|\hat{O}|\phi_j\rangle - \langle\tilde{\phi}_i|\hat{O}|\tilde{\phi}_j\rangle)\langle p_j| \tag{7.33}$$

Figure 7.3 depicts the partial all-electron and pseudo function, and projector function of the Mg 3s orbital using the PBE XC functional. The projector function is only non-zero inside the augmentation region, which is 1.7 Bohr radii in this case. The pseudo partial function is much smoother than the all-electron function as it oscillates much less inside the augmentation region, but is otherwise identical to the all-electron function. This ensures an accurate description of the valence (i.e. bonding regions) while making the computation of the near-core regions much simpler.

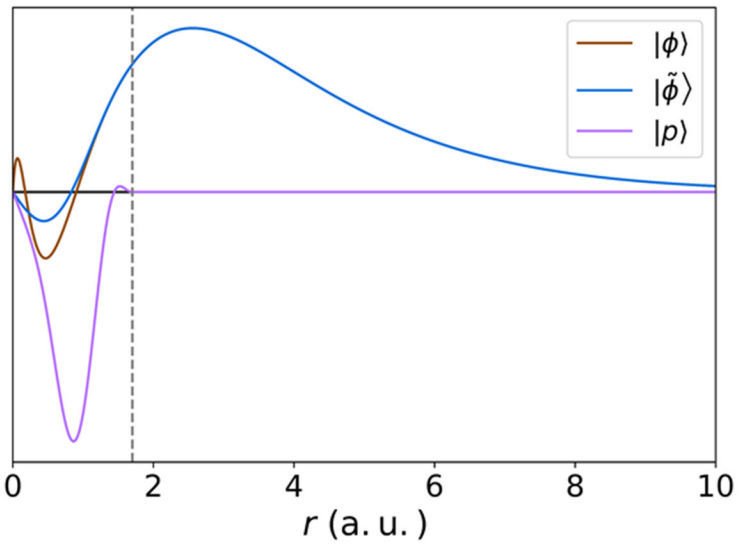


**Figure 7.3.** PAW partial and projector functions of the Mg 3s orbital. The augmentation region cut-off is depicted by the gray dashed line. *r* is given in atomic units.

*Van der Waals Forces in DFT*

DFT does not include spontaneous fluctuations in electron densities, which are the source of van der Waals interactions. This leads to inaccurate results for materials with large van der Waals forces such as transition metal dichalcogenides.

There are corrections that specifically introduce London dispersion forces. The energy resulting from these forces between atoms *A* and *B* is:

$$E_{AB}^{disp} \approx -\frac{3}{2} \cdot \frac{I_A I_B}{I_A + I_B} \cdot \frac{\alpha_A \alpha_B}{R^6} \tag{7.34}$$

Where *I* and α are the ionization potentials and the dipole polarizabilities of atoms *A* and *B*, respectively, and *R* is the distance between these atoms.

Multiple approaches exist to introduce these dispersions. This chapter will only briefly describe the methods used in this dissertation, which are Grimme's *DFT-D2* and *DFT-D3* methods,[22,23] the dispersion method by Tkatchenko and Scheffler,[24,25] which all add a dispersion term $E_{disp}$ to the Kohn-Sham energy, and methods based on Dion's *DFT-DF* method,[26–28] which change the XC functional to account for dispersions. Each method has different levels of accuracy and efficiency, which also depend on the system that is investigated. Benchmarking against experimental parameters is essential to find the best correction method.

Grimme's *DFT-D2* method uses a simple dispersion coefficient to add dispersion forces.[22] The energy $E_{disp}^{DFT-D2}$ added to the total Kohn-Sham energy is:

$$E_{disp}^{DFT-D2} = -\frac{1}{2} \sum_i \sum_{j>i} \frac{C_6^{ij}}{R_{ij}^6} f_{d,6}(R_{ij}) \tag{7.35}$$

The sum goes over all atoms and all translations of the unit cell until a cut-off radius (50 Å in VASP). The parameter $C_6^{ij}$ is the dispersion coefficient for the atom pair *ij*. The dispersion coefficients are parametrized for $i = j$ and can otherwise be calculated as:

$$C_6^{ij} = \sqrt{C_6^{ii} C_6^{ij}} \tag{7.36}$$

For the damping function $f_{d,6}(r_{ij})$, Fermi-type damping is used:

$$f_{d,6}(R_{ij}) = \frac{s_6}{1 + \exp\left[-d\left(\frac{R_{ij}}{s_R R_0^{ij}}\right) - 1\right]} \tag{7.37}$$

The parameter $s_6$ is a global scaling factor and depends on the XC functional (0.75 for PBE). $s_R$ and *d* are constant scaling and damping factors (defaults are 1.0 and 20 in VASP). $R_0^{ij}$ is tabulated for $i = j$ and can otherwise be calculated as:

$$R_0^{ij} = R_0^{ii} + R_0^{jj} \tag{7.38}$$

A correction to this method, the *DFT-D3* method,[23] has a similar form:

$$E_{disp}^{DFT-D3} = -\frac{1}{2} \sum_i \sum_j \left[ f_{d,6}(R_{ij}) \frac{C_6^{ij}}{R_{ij}^6} + f_{d,8}(R_{ij}) \frac{C_8^{ij}}{R_{ij}^8} \right] \tag{7.39}$$

The *C* parameters depend on the local geometry around the atom. With the following damping functions:

$$f_{d,n}(R_{ij}) = \frac{s_n}{1 + 6\left(\frac{R_{ij}}{s_R R_0^{ij}}\right)^{-\alpha_n}} \tag{7.40}$$

The parameters α are 14 ($n = 6$) and 16 ($n = 8$), and $s_n$ depend on the XC functional. The parameter $R_0^{ij}$ is calculated differently than in the DFT-D2 method:

$$R_0^{ij} = \sqrt{\frac{C_8^{ij}}{C_6^{ij}}} \tag{7.41}$$

Grimme's methods use damping functions and dispersion coefficients that are independent of the charge density. The method developed by Tkatchenko and Scheffler (*DFT-TS*) method is formally identical to *DFT-D2*,[24,25] but uses the charge-density dependent effective atomic volume $v_i$:

$$C_6^{ii,TS} = v_i^2 C_6^{ii} \tag{7.42}$$

$$R_0^{ii,TS} = \sqrt[3]{v_i} R_0^{ii} \tag{7.43}$$

The *C* parameters for $i \neq j$ are calculated using the polarizability of the atoms scaled by the effective atomic volume $\alpha^{TS}$:

$$C_6^{ij,TS} = \frac{2C_6^{ii,TS} C_6^{jj,TS}}{\frac{\alpha_j^{TS}}{\alpha_i^{TS}} C_6^{ii,TS} + \frac{\alpha_i^{TS}}{\alpha_j^{TS}} C_6^{jj,TS}} \tag{7.44}$$

A different approach is taken by the vdW-DF functionals by Dion *et al.*[26] Instead of adding a dispersion term to the total Kohn-Sham energy, these functionals add a non-local term $E_C^{nl}$ to the LDA correlation functional using a response function:

$$E_{XC}[\rho] = E_x^{GGA}[\rho] + E_C^{LDA}[\rho] + E_C^{nl}[\rho] \tag{7.45}$$

$$E_c^{nl}[\rho] = \frac{1}{2} \int \int \rho(\vec{r}_i) \Phi(\vec{r}_i, \vec{r}_j) \rho(\vec{r}_j) d\vec{r}_i d\vec{r}_j \tag{7.46}$$

The response function $\Phi(\vec{r}_i, \vec{r}_j)$ depends on the electron densities and gradients at $\vec{r}_i$ and $\vec{r}_j$, and on the distance between points $\vec{r}_i$ and $\vec{r}_j$.

It was also found that the choice of the exchange functional is critical to accurately describe dispersion forces, and PBE is often not suitable for this task.[26–28] In general, the GGA exchange energy is calculated using:

$$E_X^{GGA}[\rho] = \int \rho(\vec{r}) \varepsilon_X^{HEG}(\rho) F_x(s) d\vec{r} \tag{7.47}$$

Where $F_x(s)$ is the exchange enhancement factor with the reduced density gradient *s* as its argument:

$$s = \frac{|\nabla\rho|}{2(3\pi^2)^{\frac{1}{3}}\rho^{\frac{4}{3}}} \tag{7.48}$$

The functional forms of $F_x(s)$ are specific to the functional used and are summarized in Table 7.1. The vdW-DF method by Dion *et al.* uses revPBE.[26,29] Klimeš *et al.* later introduced optimized versions of the PBE,[9] B86b,[30] and B88[31] functionals called optPBE, optB86b, and optB88, respectively.[27,28]

**Table 7.1.** Functional forms of the exchange enhancement factor $F_x(s)$ and values of the parameters for different GGA functionals. PBE, revPBE and optPBE have the same functional form.

| Functional | $F_x(s)$ | Parameters |
|---|---|---|
| PBE | $1 + \kappa - \frac{\kappa}{1 + \frac{\mu s^2}{\kappa}}$ | $\kappa = 0.804$<br>$\mu = 0.2195$ |
| revPBE | | $\kappa = 1.245$<br>$\mu = 0.2195$ |
| optPBE | | $\kappa = 1.04804$<br>$\mu = 0.175519$ |
| optB86b | $1 + \frac{\mu s^2}{(1 + \mu s^2)^{0.8}}$ | $\mu = 0.1234$ |
| optB88 | $1 + \frac{\mu s^2}{1 + \beta \mathrm{arcsinh}(cs)}$ | $\mu = 0.22$<br>$\beta = \frac{1.2}{\mu}$<br>$c = \sqrt[3]{48\pi^2}$ |

## VII.3. Tight Binding and Linear Muffin-Tin Orbitals

*Traditional Non-Self-Consistent Tight Binding*

The Tight Binding (TB) method takes a very different and more simplistic approach to solving the Schrödinger equation. It assumes that electrons can only stay on ("are tightly bound to") a lattice site. The wave function can then be constructed from the atomic orbitals (AOs) similar to the Linear Combination of Atomic Orbitals (LCAO) approach that is used to construct molecular orbitals:

$$\Psi_n(\vec{k},\vec{r}) = |n\rangle = \frac{1}{\sqrt{N}}\sum_{\vec{T}} e^{i\vec{k}\vec{T}} \sum_{A}\sum_{AO} c_A^{AO}\varphi_{AO}(\vec{r}-\vec{T}) \tag{7.49}$$

Where the sums go over all atoms *A* in the unit cell and over all unit cell translations $\vec{T}$. Only the valence orbitals are used for the atomic orbitals $\varphi_{AO}$. They will be abbreviated as $|i\rangle$ where *i* is an index over the orbital's position and quantum numbers. The wave function can then be compactly written as:

$$|n\rangle = \sum_i c_i^n |i\rangle \tag{7.50}$$

The Hamilton operator $\widehat{H}_0$ with eigenenergies $\varepsilon_m$ is assumed to be of a non-interacting one-electron system, i.e. it does not contain electron-electron interactions. The coefficients $c_i^n$ can be determined by solving the Schrödinger equation which contains the Hamilton integral $H_{ij}^0 = \langle i|\widehat{H}_0|j\rangle$ and the overlap integral $S_{ij} = \langle i|j\rangle$ as matrix elements.

Due to the strong electron localization, only on-site and nearest neighbor interactions are considered, which simplifies the problem even more. Despite these simplifications, TB can give very good qualitative results. For example, it correctly predicts that graphene is a zero-gap semiconductor with Dirac points at the *K* points.[32,33]

*Cellular Methods and Linear Muffin-Tin Orbitals*

The cellular method is an approach by Wigner and Seitz[34,35] that uses a one-atom cell (Figure 7.4a) and matches the atomic function inside the cell with the function of the neighboring cells, which is computationally demanding.[36] The *muffin tin* (MT) method uses a simpler approach by using spherically symmetric atomic potentials $V_{MT}$ inside a cut-off radius $r_{MT}$, and a constant potential outside of this radius.[37] The orbitals resulting from this spherical potential are called *muffin-tin orbitals* (MTOs) and are sketched in Figure 7.4b.

This approach is further simplified in the atomic sphere approximation (ASA).[38] Instead of an interstitial wave function, the MTOs are expanded until all interstitial space is filled without overlapping too much with each other (see Figure 7.4c). If this cannot be achieved, empty spheres are added to the crystal structure and are treated like MTOs without nuclei.

A serious drawback of using MTOs is that the radial part of the wave function is energy-dependent. Thus, the secular matrix that needs to be diagonalized depends on the

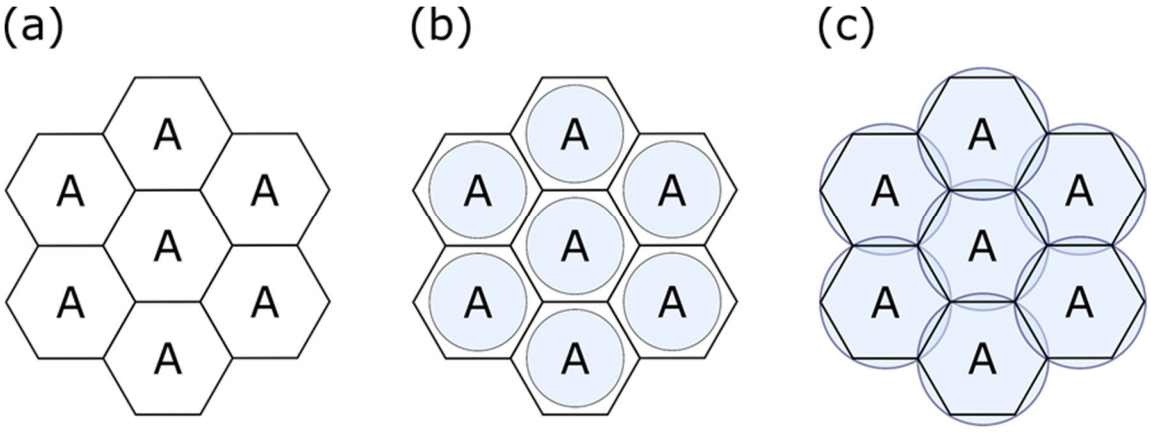


**Figure 7.4.** (a) Wigner-Seitz cells of a hexagonal array of atoms *A*. (b) Muffin tin orbitals (blue) around *A* with interstitial regions (white) inbetween. (c) Blown up muffin tin orbitals (blue circles) around *A* overlapping at the Wigner-Seitz cell boundaries.

energy that needs to be found, making the eigenvalue problem nonlinear and thus difficult to solve. The wave function can be linearized with a Taylor expansion:

$$\psi_l(E) = \psi_l(E_0) + \left.\frac{\partial \psi}{\partial E}\right|_{E_0} (E - E_0) + \mathcal{O}(E - E_0)^2 \tag{7.51}$$

In the vicinity of $E_0$ (which can, for example, be chosen as the Fermi energy), $\psi_l(E_0)$ and its derivative do not depend on the energy, and the secular matrix can easily be diagonalized. These linearized orbitals are called *linear muffin tin orbitals* (LMTOs).[38] Second generation LMTOs use more localized basis sets that can be used for TB calculations as realized in the Stuttgart TB-LMTO-ASA code.[39]

*Overlap and Hamilton Populations*

Population analyses are an important tool to gain chemical insights. In the LCAO approach, the total number of electrons in a molecule is:

$$N = \sum_A \sum_i \sum_m f_m c_{m,i}^2 + 2 \sum_A \sum_{B>A} \sum_{i,j} \sum_m f_m c_{m,i} c_{m,j} S_{ij} \tag{7.52}$$

Where the sum goes over all atoms $A$ and $B$, all atomic orbitals $i$ and $j$, and all molecular orbitals $m$. $f$ and $c$ are the occupation numbers and mixing coefficients, respectively. In solids, $c$ depends on $\vec{k}$ and must be integrated over reciprocal space. It is convenient to define a density matrix with the matrix elements:

$$P_{ij} = \int \sum_m f_m \, c_{m,i}^*(\vec{k}) c_{m,j}(\vec{k}) \, d\vec{k} \tag{7.53}$$

This allows one to write the total number of electrons for solids in a similar fashion as for molecules:

$$N = \sum_A \sum_i P_{ij} + 2 \sum_A \sum_{B>A} \sum_{i,j} \mathrm{Re}\left(P_{ij} S_{ij}\right) \tag{7.54}$$

The $\vec{k}$ dependence of the density matrix elements allows the number of electrons to be partitioned by energy:

$$P_{ij} = \int^{E_F} P_{ij}(E)dE \Leftrightarrow P_{ij}(E) = \sum_m f_m c^*_{m,i} c_{n,i} \delta(E - E_m) \tag{7.55}$$

The number of electrons can then be written as:

$$N = \int^{E_F} \sum_A \sum_i P_{ii}(E)\, dE + \int^{E_F} 2 \sum_A \sum_{B>A} \sum_{i,j} \mathrm{Re}\left[P_{ij}(E) S_{ij}\right] dE \tag{7.56}$$

This can be written in matrix form as:

$$\begin{pmatrix} P_{11}(E) & P_{12}(E)S_{12} & \cdots & & \cdots & P_{1j}(E)S_{1j} \\ P_{21}(E)S_{21} & P_{22}(E) & & & & \vdots \\ \vdots & & \ddots & & & \\ & & & P_{ii}(E) & & \\ \vdots & & & & \ddots & \vdots \\ P_{j1}(E)S_{j1} & \cdots & & & \cdots & P_{jj}(E) \end{pmatrix} \tag{7.57}$$

The sum of the elements of the lower triangle (including the diagonal elements) is the atom projected density of states (DOS).

The off-diagonal elements of this matrix provide interesting insights into bonding properties. Since the overlap integral $S_{ij}$ is positive for bonding and negative for antibonding overlap, the off-diagonal elements for a selected pair of atoms can indicate whether these atoms undergo a bonding or antibonding interaction. This overlap population-weighted DOS is called *crystal orbital overlap population* (COOP).[40] Positive COOPs denote bonding and negative COOPs antibonding interactions.

Using COOPs has the drawback that the shape may depend on the basis set. This issue can be avoided by partitioning the energy instead of the number of electrons using the Hamilton integrals $H_{ij}$:

$$E = \int^{E_F} \sum_A \sum_i P_{ii}(E) H_{ii}(E)\, dE + \int^{E_F} 2 \sum_A \sum_{B>A} \sum_{i,j} \mathrm{Re}\left[P_{ij}(E) H_{ij}(E)\right] dE \qquad (7.58)$$

These populations are called *crystal orbital Hamilton populations* (COHPs).[41] Compared to COOPs, the signs are reversed since $H_{ij}$ is negative for bonding and positive for antibonding interactions. To have bonding and antibonding interactions point into the same direction as with COOPs, –COHP is often plotted.

COHPs require a short-ranged orbital-based basis set to only include the interactions between the desired atoms. LMTOs are such a basis set and are able to execute TB calculations, which can easily determine $H_{ij}$. For that reason, TB-LMTO-ASA codes have been the tool of choice to calculate COHPs.However, the majority of DFT codes uses plane wave-based basis sets. To get COHP curves, the plane-wave functions $|\psi_i(\vec{k})\rangle$ need to be projected onto local orbitals $|\phi_\mu\rangle$ such as Slater-type orbitals using a transfer matrix $T_{i\mu}(\vec{k})$ with the matrix elements:[42,43]

$$T_{\mu i}(\vec{k}) = \langle \psi_i(\vec{k}) | \phi_\mu \rangle \qquad (7.59)$$

This transfer matrix can be used to obtain a projected density matrix $P_{\mu\nu i}^{proj}$ and projected Hamilton integrals $H_{\mu\nu}^{proj}$:

$$P_{\mu\nu i}^{proj}(\vec{k}) = \langle \phi_\mu | \phi_\nu \rangle = \langle \phi_\mu | \psi_i(\vec{k}) \rangle \langle \psi_i(\vec{k}) | \phi_\nu \rangle = T_{i\mu}^*(\vec{k}) T_{i\nu}(\vec{k}) \qquad (7.60)$$

$$H_{\mu\nu}^{proj} = \langle \phi_\mu | \hat{H}^{PW} | \phi_\nu \rangle = \sum_i \varepsilon_i \langle \phi_\mu | \phi_\nu \rangle = \sum_i \varepsilon_i(\vec{k}) T_{i\mu}^*(\vec{k}) T_{i\nu}(\vec{k}) \qquad (7.61)$$

Where $\widehat{H}^{PW}$ is the Hamilton operator of the plane waves. The projected COHP (pCOHP) can then be defined analogous to Equation 7.58:

$$\mathrm{pCOHP}_{\mu\nu}(E,\vec{k}) = \sum_i \mathrm{Re}\left[P_{\mu\nu i}^{proj}(\vec{k}) H_{\mu\nu}^{proj}(\vec{k})\right] \delta\left(\varepsilon_i(\vec{k}) - E\right) \qquad (7.62)$$

## VII.4. Conclusions and Bridge

In this chapter, three methods of electronic structure calculations, Hartree-Fock, Density Functional Theory (DFT), and Tight Binding, have been introduced. DFT is the standard method for solids, but corrections are necessary to properly describe van der Waals forces and strong electron correlation. Linearized muffin tin orbitals provide a local basis set that enables the calculation of overlap and Hamilton populations. These populations provide valuable information on the bonding character in solids.

DFT has not been used extensively to describe ferecrystalline compounds. In the following chapters, DFT calculations will be employed to describe low-dimensional materials and to help explain the behavior of these layers in ferecrystalline materials.

# CHAPTER VIII

# CHARGE DENSITY WAVE TRANSITION IN $(PbSe)_{1+\delta}(VSe_2)_n$ COMPOUNDS WITH *n* = 1, 2, AND 3

Portions of this chapter were published previously as Hite, O.K.; Falmbigl, M.; Alemayehu, M.B.; Esters, M.; Wood, S.R.; Johnson, D.C. "Charge density wave transition in $(PbSe)_{1+\delta}(VSe_2)_n$ compounds with *n* = 1, 2, and 3" *Chemistry of Materials* **2017**, *29* (13), 5646 – 5653. O.K.H. was the primary author of this work, synthesized the compounds and performed structural and electrical characterizations. M.B.A. and M.F. assisted with sample preparations. M.F. also contributed to the diffraction analysis. M.E. performed all density functional theory calculations and wrote the Supporting Information of the publication. S.R.W. assisted with figure generation. D.C.J. was the principal investigator and provided editorial assistance.

## VIII.1. Introduction

The isolation of graphene[1] and the discovery that its properties differ from those of bulk graphite has lead to a surge of research on single layer and very thin layers of quasi-two-dimensional systems such as h-boron nitride (h-BN)[2,3] and transition metal dichalcogenides[4] and their heterostructures[5] in a search for emergent properties not present in the bulk constituents. For $MoS_2$ a transition was observed from an indirect to a direct band gap semiconductor as the materials dimensions are reduced from bulk to a single sheet.[6] It has been shown computationally that SnS, SnSe, GeS, and GeSe have increased band gaps as the number of layers is reduced from the bulk to monolayer.[7] A

similar trend in band gaps is seen for h-BN, where the bulk 4.0 eV band gap increases to a 4.6 eV band gap in the monolayer.[8] Emergent properties have also been observed in heterostructures,[9–12] including ultrafast charge transfer in $MoS_2/WS_2$ consistent with a type II band alignment having spatially direct absorption, but spatially indirect emission.[13] Other examples include long-lived interlayer excitons in a $MoSe_2$-$WSe_2$ heterostructure with experimentally observed type II band alignment,[14] and epitaxial single-layers of $MoS_2$ on a Au(111) surface showing a dramatic change in their band structure around the center of the Brillouin zone.[15]

The majority of the systems being investigated are semiconducting because isolation of single sheets of metallic systems has been challenging as they are not stable in air.[11] There are a number of interesting properties in metallic systems, however, that are being explored as a function of thickness towards the 2D limit, including superconductivity, and charge density waves (CDW). It has been demonstrated that the onset temperature of superconductivity in 2H-$NbSe_2$ decreases as the number of $NbSe_2$ layers is decreased.[16–18] Studies on mechanically exfoliated $TiSe_2$ have shown that as thickness of the exfoliated film is decreased the onset temperature of the CDW is increased.[26] Others have shown that the onset temperature of the CDW in $TaSe_2$ is decreased as the thickness of the mechanically exfoliated film is decreased.[27] It was shown both computationally and experimentally, that the ferromagnetism of $VS_2$ is enhanced as the $VS_2$ approaches the monolayer limit.[19,20] $VSe_2$ exhibits a CDW transition in the bulk[21] but there is disagreement on how this CDW changes as the number of $VSe_2$ layers are reduced in this n-type metal.[22–25] The onset of the CDW in thin layers of $VSe_2$ prepared via liquid exfoliation transitions from 100 K[21] in the bulk single crystal to 135 K

as thickness is reduced to 4-8 trilayers of $VSe_2$.[22] An opposite trend has been reported for micromechanically exfoliated nanoflakes, however, where the onset temperature decreases to 81 K at the lowest thickness measured, 11.6 nm.[23] The thin nanoflakes are n-type conductors, as is bulk $VSe_2$, but the carrier concentration increases as the nanoflake thickness is decreased. These exfoliation techniques were not able to precisely control the thickness of the $VSe_2$ flakes nor were they able to reach the monolayer limit. Studies of $[(SnSe)_{1.15}]_m(VSe_2)_n$ prepared by annealing designed precursors have shown that compounds with a single layer of $VSe_2$ separated by *m* layers of SnSe are p-type metals with a CDW that depends on the thickness of SnSe and exhibit a dramatic change in electrical resistivity and charge carrier concentration at the CDW transition temperature.[28] In contrast, increasing the $VSe_2$ layer thickness to two or more layers results in low temperature n-type metals and the suppression of the pronounced effect in transport properties at the CDW transition temperature similar to bulk $VSe_2$.[25] These compounds grown at low temperatures from designed precursors have been called ferecrystals, from the Latin root *fere-* meaning "almost", due to their extensive turbostratic disorder. The influence of surface contaminations and/or the substrate on the charge density wave transition has not been explored or discussed in the literature.

In order to explore the impact of neighboring layers on the CDW of $VSe_2$ heterostructures, we replaced SnSe with the isovalent PbSe in a sequence of $(PbSe)_{1+\delta}(VSe_2)_n$ compounds. The compounds were prepared using modulated elemental reactant precursors and electrical properties were measured as a function of temperature. Diffraction data is consistent with *n* layers of $VSe_2$ separating a single rock salt structured PbSe layer. The $n = 1$ ferecrystal is metallic with a positive Hall coefficient indicative of

p-type conduction, while for the $n = 2$ and 3 compounds, the Hall coefficient switches sign, indicating a change of the majority carriers to electrons equivalent to bulk $VSe_2$.[21] Both the resistivity and Hall coefficient of the $n = 1$ compound increase as the temperature is lowered below 100 K, becoming a factor of 3.7 and 8 higher, respectively, by 20 K. This anomaly is very similar to the CDW transition observed in $([SnSe]_{1.15})_mVSe_2$ compounds. The temperature dependencies of the resistivity and Hall coefficient of the $n = 2$ and 3 compounds are very similar to bulk $VSe_2$. There is a change in the slope of the resistivity and the Hall coefficient as a function of temperature at 100 K, suggesting that a CDW similar to the bulk occurs if there is more than one $VSe_2$ layer. The different sign of the Hall coefficient and large changes in resistivity and Hall coefficient indicates, the electronic structure of $(PbSe)_{1+\delta}VSe_2$ with a single $VSe_2$ layer is distinctly different than heterostructures with thicker $VSe_2$ layers. The changes in properties when PbSe replaces SnSe, although only an isovalent substitution, indicates that the interactions between constituents can be used to tune the electrical properties of heterostructures.

## VIII.2. Experimental and Computational Methods

The ferecrystalline compounds, $(PbSe)_{1+\delta}(VSe_2)_n$ where $1 \leq n \leq 3$, were synthesized using the modulated elemental reactants (MER) technique.[29] Precursors were prepared by sequentially evaporating elemental sources of Pb (99.995%, Alfa Aesar), V (99.8%, Alfa Aesar), and Se (99.999%, Alfa Aesar) on (100) oriented Si wafers in specific sequences for each compound in a custom built high-vacuum physical vapor deposition chamber, details provided elsewhere.[29] Precursors were annealed at 250 °C for 1 hour in a $N_2$ glove box with a concentration of oxygen below 0.6 ppm. Methods used to

determine the optimal annealing temperatures for converting the precursors into the desired product are described in the literature.[24]

Specular X-ray diffraction (XRD) was performed to determine the *c*-axis lattice parameter of the $(PbSe)_{1+\delta}(VSe_2)_n$ compounds on a Bruker D8 Discover diffractometer equipped with Cu $K_\alpha$ radiation ($\lambda$ = 0.15418 nm), Göbel mirrors, and Bragg-Brentano $\theta$-$2\theta$ optics geometry. In-plane XRD of the $n$ = 1 and 3 compounds were taken at the Advanced Photon Source, Argonne National Laboratories (BM 33-C, $\lambda$ = 0.12653 nm). In-plane XRD of the $n$ = 2 compound was done on a Rigaku SmartLab diffractometer equipped with Cu $K_\alpha$ radiation.

Compositional analysis was performed with electron probe micro-analysis (EPMA) on a Cameca SX-100. Accelerating voltages of 7.5, 13, and 18 keV were used and overall composition was calculated as a function of the three accelerating voltages using the technique for thin films developed by Donovan *et al*.[30]

Samples were prepared for High-angle Annular Dark-field Scanning Transmission Electron Microscopy (HAADF-STEM) on a FEI Helios 600 dual-beam using a technique described by Schaffer *et al*.[31] HAADF-STEM was taken on a FEI Titan 80-300 FEG-TEM at the Center for Advanced Materials Characterization in Oregon (CAMCOR).

Electrical resistivity and Hall measurements were determined using the van der Pauw technique[32] in a temperature range of 20 - 295 K. Samples were prepared on fused Quartz crystal slides in a 1 cm × 1 cm cross geometry. Further details on how temperature-dependent resistivity and Hall measurements were conducted are described elsewhere.[33]

Density functional theory (DFT) calculations were performed using the Vienna *ab initio* simulation package (VASP).[34-37] The interactions of the electrons with the ionic core were described using the projector augmented wave (PAW) method.[38,39] To describe exchange and correlation, the functionals of Perdew-Burke-Ernzerhof (PBE) were used.[40] A cutoff energy of 500 eV was used to expand the wave functions. To reduce interactions between periodic images, vacuum of 25 Å was added between $VSe_2$ monolayers and bilayers. For structural relaxations, a Γ-centered 8×8×1 k-point mesh was used. Electronic properties were calculated using a 21×21×1 Γ-centered grid. Since interactions between $VSe_2$ layers are of van-der-Waals type, dispersion corrections were added using Dion's method in the vdW-DF corrected optPBE functionals.[41-44]

**VIII.3. Results and Discussion**

Precursors for each of the compounds $(PbSe)_{1+\delta}(VSe_2)_n$ with $n = 1 - 3$ were prepared by depositing sequences of elemental layers where the elemental Pb|Se and V|Se bilayers were calibrated to match the composition of the desired product such that each Pb|Se bilayer formed two (001) planes of rock salt structured PbSe and each V|Se bilayer formed a single Se-V-Se dichalcogenide structured trilayer. The calibration was a three-step process. The composition of the Pb|Se and V|Se bilayers were calibrated by preparing a set of samples with a fixed metal thickness and varying thicknesses of Se, and determining the composition with EPMA. The resulting graphs of Se:Pb and Se:V ratio versus Se layer thickness were interpolated to obtain the ratio of thicknesses that resulted in the respective desired compositions. To determine the thickness ratio between the Pb and V layers to obtain the targeted misfit parameter of 1.11, a set of samples were prepared by depositing Pb|Se|V|Se sequences where the thickness of the Pb|Se bilayer at

the previously determined Pb/Se thickness ratio was scaled while holding the thickness and thickness ratio of the V|Se bilayer constant. The change in composition as a function of the thickness of the Pb|Se bilayer was interpolated to find the thickness required to obtain the desired misfit parameter. The last step was to hold the Pb|Se, V|Se and Pb|Se/V|Se ratios constant while scaling the total thickness, using the quality of the resulting annealed sample diffraction patterns to determine the thickness such that each Pb|Se bilayer forms two (001) planes of rock salt structured PbSe and the V|Se layer forms a single Se-V-Se dichalcogenide structured trilayer. X-ray diffraction (XRD) scans were taken on the annealed precursors in order to determine the total thickness that yields maximum peak intensity and minimum peak FWHM in the resulting product, as described previously by Atkins *et al*.[45]

Sequences with the nanoarchitecture of the desired products, for example the sequence of layers Pb|Se-V|Se-V|Se for $(PbSe)_{1+\delta}(VSe_2)_2$, were repeatedly deposited until

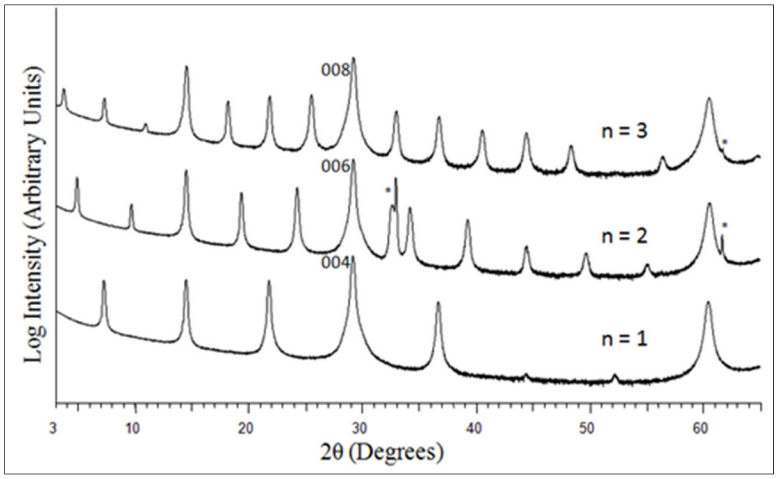


**Figure 8.1.** X-ray diffraction patterns of $(PbSe)_{1+\delta}(VSe_2)_n$ for $n = 1 – 3$ using Cu $K_\alpha$ radiation ($\lambda = 0.15418$ nm). Maxima can be indexed to 00*l* reflections of the respective compound, with the appropriate index given in the figure for the reflection at ~ 29° 2θ. Asterisks indicate substrate or stage reflections.

the desired total sample thickness of about 45 nm was reached. These precursors were annealed at 250 °C to self-assembly of the targeted products. This temperature was determined using the approach of Atkins *et al*.[45] Figure 8.1 shows the specular XRD patterns of the $n = 1 – 3$ compounds. Each peak can be indexed to a 00*l* reflection of the $(PbSe)_{1+\delta}(VSe_2)_n$ compounds indicating crystallographically aligned layers with the *c*-axis perpendicular to the substrate. Using Bragg's Law, the *c*-axis lattice parameters were determined to be 1.225(1) nm, 1.835(3) nm, and 2.445(4) nm for $n = 1$, 2, and 3, respectively. The change in thickness as *n* is increased yields the thickness of a $VSe_2$ layer from the slope and the thicknesses of the PbSe layer from the intercept. The PbSe bilayer thickness of 0.617(5) nm is slightly thicker than the 0.607-0.612 nm found in a series of $[(PbSe)_{1.14}]_m(NbSe_2)_n$ compounds[33] and the 0.61(1) nm found for the PbSe bilayer thickness in $(PbSe)_{1+\delta}(TiSe_2)_n$ ferecrystals.[46] The thickness of the $VSe_2$ trilayer is 0.610(2) nm, which is slightly thicker than the 0.596(1) nm reported for the $VSe_2$ sub-unit in $(SnSe)_{1.15}(VSe_2)_n$ compounds.[13] A Rietveld refinement of the $n = 1$ out-of-plane XRD was performed to determine relative positions of the atomic planes along the *c*-axis. Figure 8.2 contains the fitted intensities along with a schematic of the atomic plane positions compared to those previously determined for $(SnSe)_{1.15}VSe_2$.[14] The refinement revealed puckering of the PbSe layer, which separates the Pb and Se atomic planes from one another by 0.0367(2) nm. This puckering is typical for bilayers of rock salt structured constituents and has been seen previously in both SnSe and PbSe containing misfit layered compounds and ferecrystals.[25,47] The magnitude of this puckering is within the range reported previously, 0.020 nm to 0.065 nm, in the relatively few atomic level structures that have been previously determined.[48-54] It is larger than the puckering

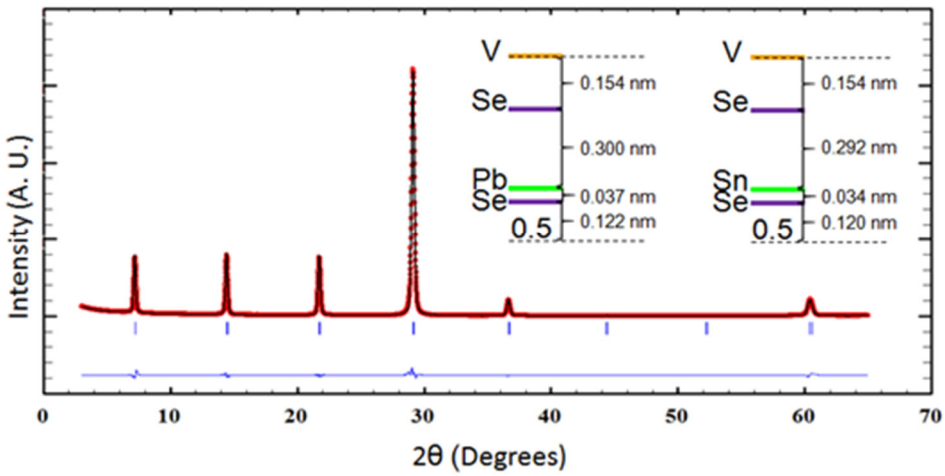


**Figure 8.2.** Experimental, calculated and difference patterns from Rietveld refinement of the positions of atomic planes along the *c*-axis of $(PbSe)_{1+\delta}VSe_2$. The inset figures contain the interplane distances obtained for $(PbSe)_{1+\delta}VSe_2$ and those for $(SnSe)_{1.15}VSe_2$ are presented for comparison.[25]

observed in $(PbSe)_{1.00}MoSe_2$ (0.025(1) nm) and $(PbSe)_{0.99}WSe_2$ (0.021(1) nm) ferecrystals[55] but smaller than the 0.062(5) nm found in the $(PbSe)_{1.18}(TiSe_2)_2$ ferecrystal.[56] The extent of the puckering may be related to the amount of charge transfer between the constituents, as a negatively charged environment in the dichalcogenide layer would attract the positive Pb and repel the negative Se ions. The gap between the PbSe and $VSe_2$ layers was found to be 0.300(5) nm which is very similar to the 0.306(5) nm observed in $(SnSe)_{1.15}VSe_2$.[25] The distance between V and Se planes along the *c*-axis in $VSe_2$ was found to be 0.153(2) nm, which is the same as the 0.154(2) nm reported for the $(SnSe)_{1.15}(VSe_2)$ compound.[25]

In-plane *hk*0 XRD scans were collected on all compounds (Figure 8.3), and the reflections in each scan can be indexed as either reflections from a hexagonal in-plane structure for $VSe_2$ or reflections from a square in-plane structure for PbSe. The reflections for each constituent can easily be distinguished as relative intensities of the $VSe_2$ peaks (for example the (110) reflection) proportionally increase relative to the PbSe

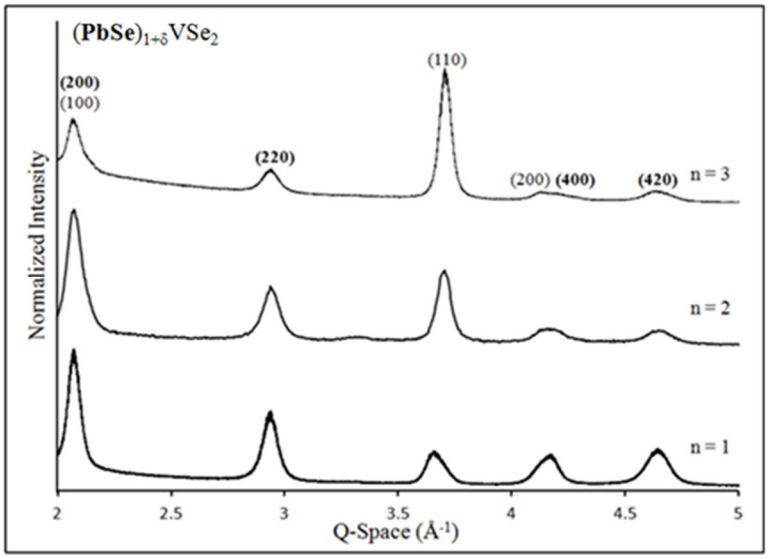


**Figure 8.3.** Normalized in-plane X-ray diffraction patterns of $(PbSe)_{1+\delta}(VSe_2)_n$ for $n$ = 1 – 3. Scans are individually normalized to the highest intensity reflection. The numbers above the $n$ = 3 scan reflections are the indices using hexagonal $VSe_2$ and square PbSe (bold font).

reflections (for example the (220) reflection) as the number of $VSe_2$ layers increase. The in-plane *a*-axis lattice parameter for the $VSe_2$ constituent remains the same within error and are 0.343(1) nm, 0.346(5) nm, and 0.339(1) nm for $n$ = 1, 2, and 3, respectively. These values are all within the uncertainty of the 0.334(8) nm[28] and 0.341(1) nm[24] previously reported for $(SnSe)_{1.15}VSe_2$. The square in-plane *a*-lattice parameter of the PbSe constituent additionally remains the same with values of 0.605(1) nm, 0.604(3) nm, and 0.607(1) nm for $n$ = 1, 2, and 3, respectively. All of these values are slightly smaller than the 0.6122(3) nm reported for $(PbSe)_{1.18}TiSe_2$[56] and the 0.618(2) nm reported for in $(PbSe)_{1.00}MoSe_2$ and $(PbSe)_{0.99}WSe_2$. The small changes in the in-plane lattice parameters of the constituents result in a misfit parameter that varies as the thickness of the $VSe_2$ constituent increases. The misfit parameter, (1+δ), was 1.11(1) for the $n$ = 1 compound, 1.14(2) for the $n$ = 2 compound and 1.08(1) for the $n$ = 3 compound. The

values for the misfit fall within the range of misfit values reported in the literature (0.99 to 1.29).[50-52,57-70]

HAADF-STEM images of $(PbSe)_{1.11}(VSe_2)$ show a regular repeating structure of a single plane of $VSe_2$ separated by single planes of PbSe. A representative image is shown in Figure 8.4. The visible areas aligned along a zone axis support the interpretation of the XRD data, as zone axes consistent with a distorted rocksalt structure are observed for PbSe layers and zone axis images of the $VSe_2$ layer are consistent with octahedral coordination of the vanadium atoms, which are situated between Se planes. The disorder in the orientation of the layers from layer to layer indicates that there is no long-range order. This is consistent with the XRD data, which show that there is long range order due to alternating $VSe_2$ and PbSe layers along (00*l*), that each layer is crystalline with distinct (*hk0*) diffraction from each of the constituents, and that there is no common in-plane axis between the constituents. The crystalline nature of each of the constituent

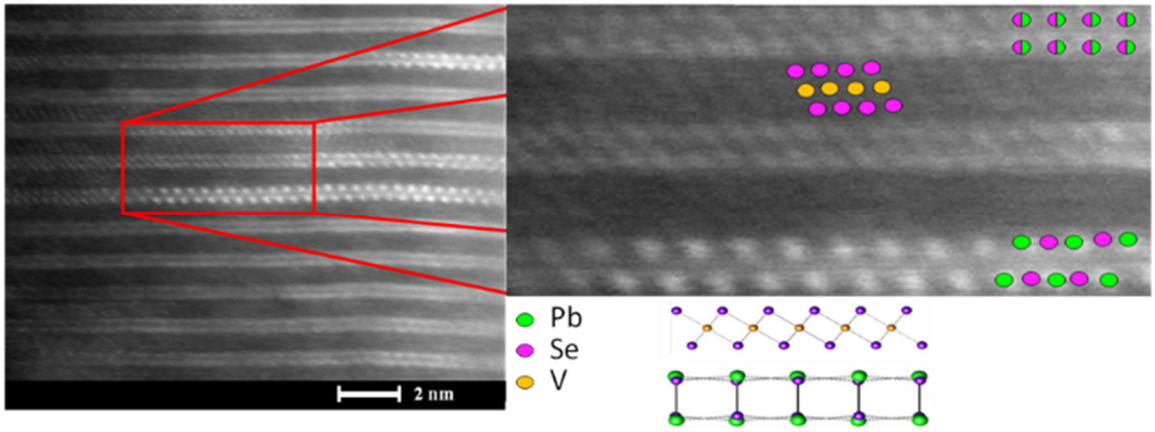


**Figure 8.4.** HAADF-STEM images of $(PbSe)_{1+\delta}VSe_2$ contain alternating PbSe bilayers and $VSe_2$ trilayers. The different crystallographic orientations of the PbSe layers are a result of turbostratic disorder. The expanded image shows a PbSe layer with a [100] crystallographic orientation (top) and a [110] crystallographic orientation (bottom). The $VSe_2$ layer is consistent with octahedral coordination of V.

layers with lack of long-range order between planes is a consequence of the mechanism of the self-assembly from the precursor.[71]

Temperature dependent resistivity measurements were conducted on all samples and the data is plotted in Figure 8.5 along with data previously reported for bulk $VSe_2$.[21] The absolute value of the room temperature resistivity and the temperature dependence of the resistivity above 150 K for all samples indicate that they are metallic. The magnitude of the resistivity systematically decreases as the percentage of the metallic constituent $VSe_2$ is increased, which is consistent with conduction occurring primarily through the $VSe_2$ layer as observed in the analogous $(PbSe)_{1.12}(NbSe_2)_n$ compounds.[33] The temperature dependence of the $n = 3$ sample is similar to that of bulk $VSe_2$, with a slightly decreased temperature dependence suggesting weaker electron-phonon scattering compared to bulk $VSe_2$. The temperature dependence of the $n = 2$ sample shows a further

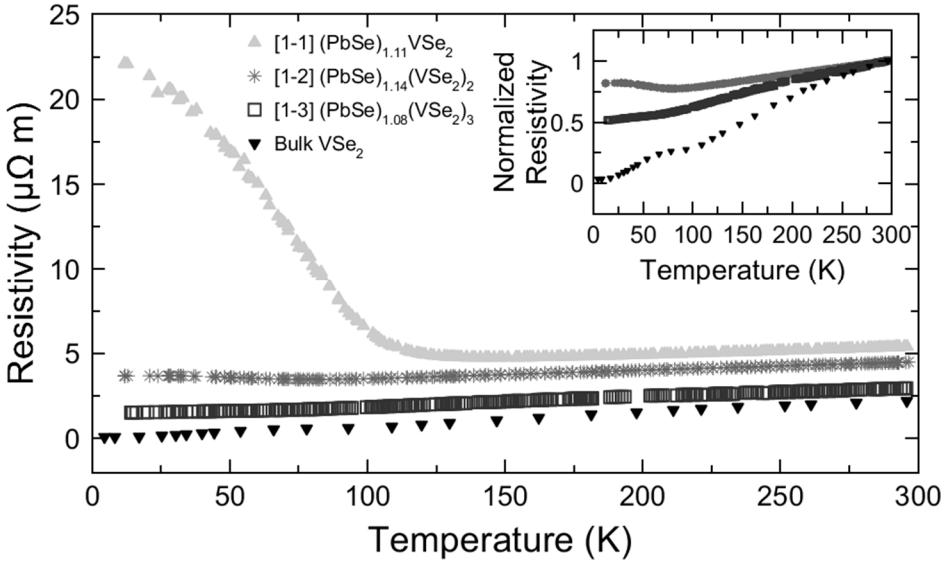


**Figure 8.5.** Temperature dependent resistivity of $(PbSe)_{1+\delta}(VSe_2)_n$ for $n = 1 – 3$ and bulk $VSe_2$.[21] Resistivity normalized to room temperature resistivity for the $n = 2$ and 3 heterostructures and bulk $VSe_2$ is displayed in the inset to highlight the anomalies observed in the CDW of bulk $VSe_2$.

decrease in the slope, suggesting even weaker electron-phonon scattering. The weaker electron-phonon scattering reflects the changes in phonon modes and phonon energies as the $VSe_2$ block is reduced in thickness. The $n = 2$ and 3 heterostructures both show a change in slope of the resistivity that is very similar to that seen as a result of a CDW in bulk $VSe_2$. The temperature dependence of the $n = 1$ sample is distinctly different than bulk $VSe_2$ and the $n = 2$ and 3 heterostructures, with the resistivity abruptly increasing at approximately 110 K as temperature is lowered. The resistivity ultimately reaches a value of more than 5 times higher at 20 K than would be extrapolated from the high temperature behavior. The change in resistivity of $(PbSe)_{1.11}VSe_2$ is very similar to that reported by Falmbigl *et al.* for $(SnSe)_{1.15}(VSe_2)$,[25] which has been attributed to a charge density wave (CDW) based on resistivity, Hall coefficient and heat capacity measurements.[72] The overall increase in resistivity in the $(PbSe)_{1.11}VSe_2$ compound is approximately double that of the analogous SnSe compound, indicating that a higher percentage of the charge carriers are localized and/or that there is a significant difference in the change of the carrier mobility below the CDW. This may reflect structural differences at the interface between the constituents (in $n = 1$ the $VSe_2$ and PbSe layers alternate and for the other compounds PbSe is separated by 2 or 3 $VSe_2$ layers) or a different Fermi level caused by a difference in charge transfer between the SnSe (bulk $E_g$, 1.38 eV[73]) or PbSe (bulk $E_g$, 0.23 eV[74]) layer and the $VSe_2$ layers. The difference in charge transfer could be a consequence of the different misfit parameters between the Sn and Pb compounds and/or due to different Fermi energies for the PbSe bilayer relative to the SnSe bilayer with respect to the monolayer of $VSe_2$.[75] A similar

increase in charge transfer was seen when substituting PbSe for SnSe in $NbSe_2$ containing heterostructures.[33]

Temperature dependent Hall measurements were conducted on all samples to provide further insight to the unusual resistivity behavior in $(PbSe)_{1.11}VSe_2$, and the data obtained is plotted in Figure 8.6 along with that measured for a single crystal of $VSe_2$.[21] The Hall coefficient for a single crystal of $VSe_2$ is negative along the entire temperature range, suggesting that electrons are the primary carrier, and has a change in slope at approximately 110 K that was attributed to a CDW.[21] The $n = 3$ sample also has a negative Hall coefficient that decreases as temperature is decreased and has a change in slope at approximately the same temperature as the bulk single crystal. The $n = 2$ sample has a small positive Hall coefficient at room temperature but decreases with decreasing temperature with a slope similar to the bulk single crystal, becoming negative at ~ 230 K. It also has a change of slope at about 100 K. The change in sign of the Hall coefficient suggests that at least two bands are contributing to the electrical transport, which suggests

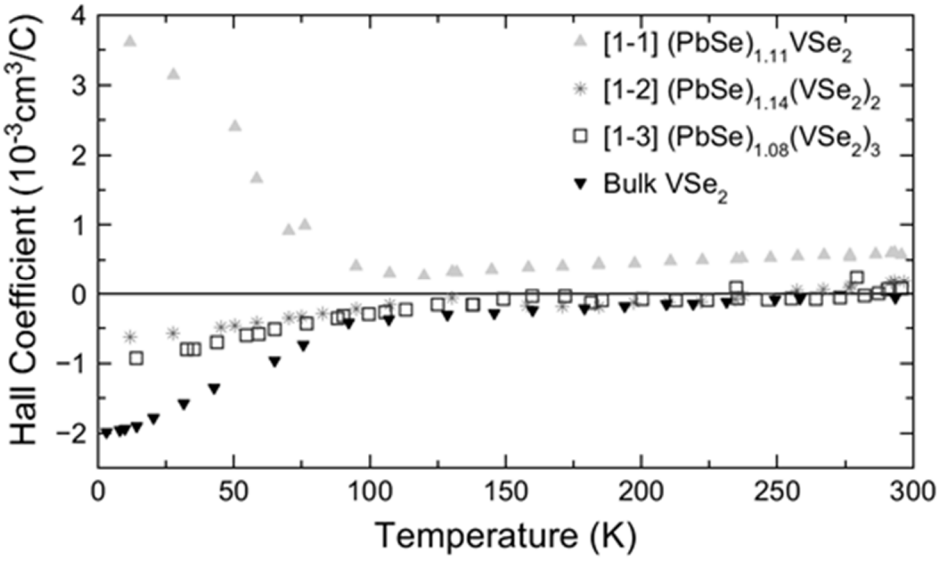


**Figure 8.6.** Temperature dependence of the Hall coefficient for $(PbSe)_{1+\delta}(VSe_2)_n$ $n = 1 – 3$ and bulk single crystal $VSe_2$.[21]

that the PbSe layer contributes to the conduction. And a similar result was found by Falmbigl *et. al.* investigating $([Sn_{1-x}Bi_xSe]_{1.15})_1(VSe_2)_1$ alloys.[76] The temperature dependence of the resistivity and Hall coefficient suggest that the $n = 2$ and 3 compounds are very similar to the bulk, in contrast to the properties measured on liquid and mechanically exfoliated $VSe_2$ thin layers.[22,23] $(PbSe)_{1.11}VSe_2$, however, has a positive Hall coefficient over the entire temperature range and, like $(SnSe)_{1.15}VSe_2$[25] has an abrupt increase in the Hall coefficient at 110 K, the same temperature where the resistivity begins to increase. The Hall coefficient increases by about a factor of 8 as temperature is decreased to 20 K, and using the single conducting band approximation the change in carrier concentration shows that 1.06 holes per vanadium atom are localized over the CDW. This value is almost twice as large as of the analogous $(SnSe)_{1.15}VSe_2$, which was reported at 0.54 holes per vanadium atom.[72] This calculated change in carrier concentration accounts for most of the change in resistivity. The changes in the Hall coefficient and resistivity of the $n = 1$ sample as a function of temperature are consistent with a CDW transition.

Figure 8.7 contains the temperature-dependent single conducting band carrier mobility calculated using $\mu = R_H/\rho$ for $(PbSe)_{1.11}VSe_2$ prepared in this study as well as those of bulk $VSe_2$, $(SnSe)_{1.15}VSe_2$ and $(BiSe)_{1+\delta}VSe_2$.[77] The single band mobility values for the $n = 2$ and 3 compounds were not calculated due to the change in sign of the Hall coefficient in the $n = 2$ compound, which indicates that more than a single band is involved in conduction. The room temperature mobility of the $n = 1$ compounds is very similar, suggesting that the $VSe_2$ layers are the primary conductor in the compounds. While the changes in mobility of the holes in $n = 1$ compounds as temperature is lowered

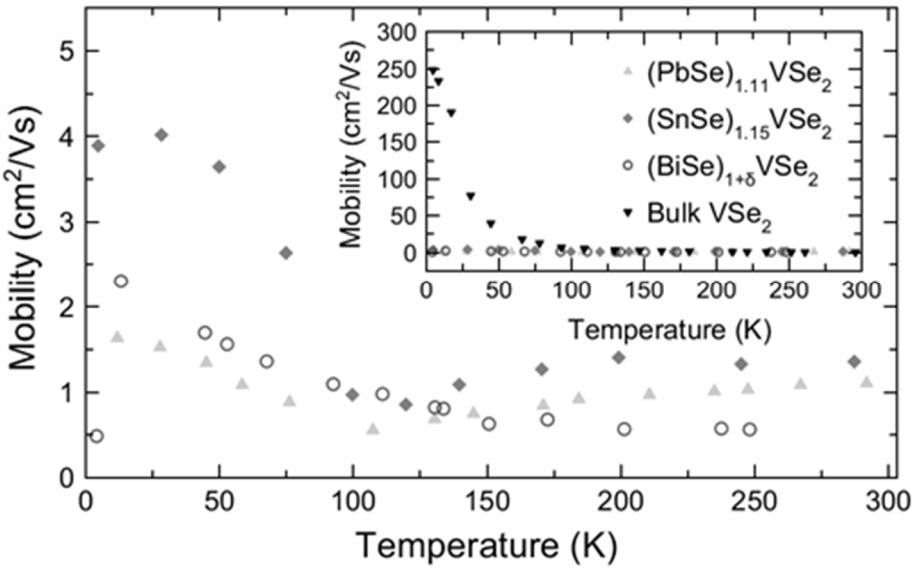


**Figure 8.7.** Temperature-dependent single conducting band carrier mobility of $(PbSe)_{1.11}VSe_2$, $(SnSe)_{1.15}VSe_2$,[24] and $(BiSe)_{1+\delta}VSe_2$.[77] The inset compares the mobility of the three compounds to bulk $VSe_2$.[21]

are all much smaller than observed for the electrons in bulk $VSe_2$, there is a larger increase in mobility as the temperature is lowered in $(SnSe)_{1.15}(VSe_2)$ (a factor of 3) than in either $(PbSe)_{1.11}VSe_2$ or $(BiSe)_{1+\delta}VSe_2$ (a factor of 1.2). There is a small decrease in mobility at the onset of the CDW in both $(PbSe)_{1.11}(VSe_2)$ and $(SnSe)_{1.15}(VSe_2)$, which may be an indicator of CDW formation in these compounds as this feature is not seen in $(BiSe)_{1+\delta}VSe_2$. The differences in the changes in carrier concentration and mobility of carriers in $(PbSe)_{1.11}VSe_2$ compared to $(SnSe)_{1.15}VSe_2$ indicates that CDW formation is a complex process and is sensitive to the degree of charge transfer in these systems.

The change in electrical resistivity and the sign of the Hall coefficient as the number of $VSe_2$ layers in the repeat unit is increased prompted us to perform DFT calculations on both a single layer and a double layer of $VSe_2$. The calculations were done using the bulk 1T crystal structure of $VSe_2$, separating either the single layer or the double layers from one another by vacuum, and allowing the system to relax. The in-

plane lattice parameters are 0.337 nm for the monolayer and 0.338 nm for the bilayer, which is slightly smaller than in the ferecrystals, but consistent with prior theoretical results.[78,79] The distance between the V and Se layers in the monolayer is 0.158 nm, which is consistent with experimental results. For the bilayer, the distances between the V and Se layers are slightly asymmetric: 0.158 nm for the Se layers adjacent to the vacuum, and 0.157 nm for the remaining layers. The distance between the two $VSe_2$ trilayers is 0.316 nm. Both the monolayer and the bilayer are ferromagnetic with a magnetization of 0.64 and 0.66 $\mu_B$/f.u., respectively.

The band structures of a pristine $VSe_2$ monolayer and bilayer (shown in Figure 8.8) are similar to those reported previously.[78,79] The majority spin bands for the monolayer are metallic with a hole-like Fermi surface near the K point, whereas the minority spin bands are semimetallic with a valence band maximum at the Γ point and a conduction band minimum at the M point. The bilayer shows additional bands because of the additional $VSe_2$ trilayer that are mostly degenerate with the bands of the other $VSe_2$ trilayer. However, near the Γ point the additional band is raised in energy for the band right below (majority spin) and above (minority spin) the Fermi level. Just like the

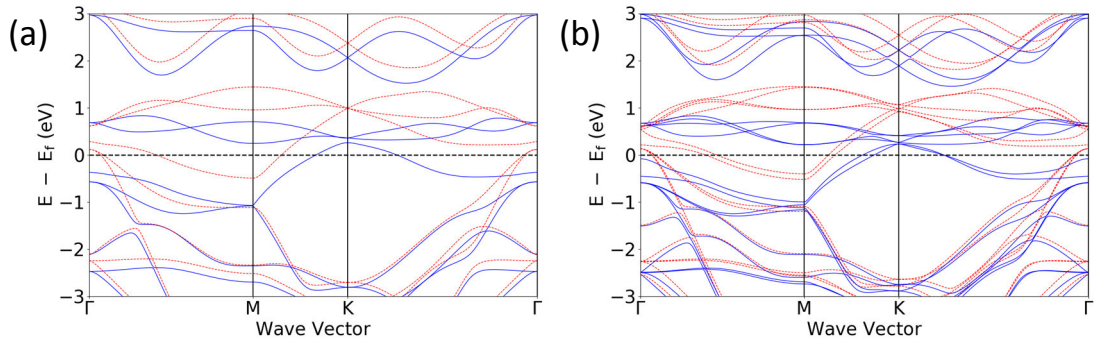


**Figure 8.8.** Band structures of monolayer (a) and bilayer (b) $VSe_2$. Solid blue lines denote majority spin and dashed red lines minority spin bands.

monolayer, the majority spin bands are metallic with a hole-like Fermi surface near the K point, and the minority spin bands are semimetallic with a valence band maximum at the Γ point and a conduction band minimum at the M point. The results suggest that $VSe_2$ monolayers and bilayers should have similar electrical properties with isovalent charge donors such as SnSe and PbSe. The temperature dependence of the electrical resistivity and the Hall coefficient show similar behavior in $[(PbSe)_{1.12}]_1[VSe_2]_1$ and $[(SnSe)_{1.15}]_1[VSe_2]_1$, but the sign of the Hall coefficient is positive for $[(SnSe)_{1.15}]_1[VSe_2]_n$ and negative for $[(PbSe)_{1.12}]_1[VSe_2]_n$ ($n > 1$), indicating significant interactions with the $VSe_2$ layer beyond simple charge transfer. Further research must be conducted to investigate the nature of these interactions.

Unlike what was reported for $MoS_2$ where the Mo has trigonal prismatic coordination,[80] there are only very small differences in the band structure calculated for the single and double layer of $VSe_2$ due to the octahedral local coordination of vanadium atoms and the 1T stacking. Changing the position of the Fermi level in either the single or double layer of $VSe_2$ results in changes in the density of states, but the calculations do not indicate that one or the other have a distinct feature in the band structure that makes them more likely to have a charge density wave transition. Figure 8.9 contains a plot of the temperature dependence of the Hall coefficients of $(PbSe)_{1.11}VSe_2$, $(SnSe)_{1.15}VSe_2$,[25] and $(BiSe)_{1+\delta}VSe_2$,[77] all of which contain single $VSe_2$ trilayers separated by a monochalcogenide bilayer, and the temperature dependence of the Hall coefficients of bulk $VSe_2$.[21] The compounds containing SnSe and PbSe are distinctly different from bulk $VSe_2$ and the compound containing BiSe. However, resistivity and Hall data reported by Alemayehu *et. al.* for a series of $(GeSe_2)_m(VSe_2)_n$ heterostructures[71] indicates that CDW's

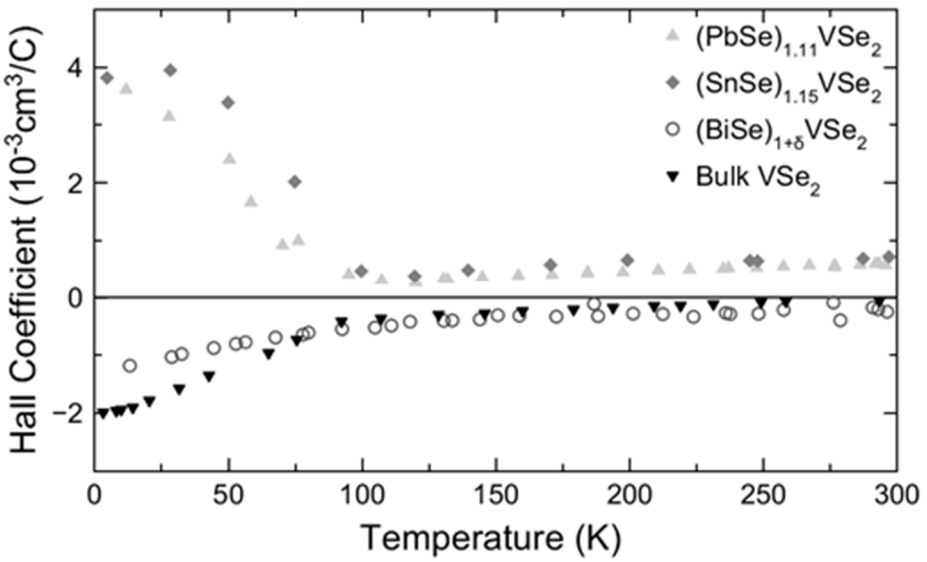


**Figure 8.9.** Hall coefficients for different $(MSe)_{1+\delta}(VSe_2)$ (M = Sn, Pb, Bi) ferecrystals and bulk $VSe_2$.[21]

occur for a number of different *n* values, suggesting that a monolayer of $VSe_2$ is not a necessary condition for the formation of a CDW. The observed differences in transport properties cannot be explained as only being due to a structurally isolated $VSe_2$ monolayer, as all of the ferecrystalline compounds contain isolated monolayers of $VSe_2$ and $(GeSe_2)_m(VSe_2)_n$ contains isolated blocks of *n* $VSe_2$ layers. The electronic structure is heavily influenced by the position of the Fermi level, which can be altered in ferecrystals without purposefully introducing local impurities in the $VSe_2$ layers via charge transfer from the adjacent constituent, a phenomenon referred to as modulation doping. The observed differences in transport properties, however, cannot be explained solely by significant charge transfer between constituents, but that other factors like electron localization need to be taken into consideration.

## VIII.4. Conclusions and Bridge

The compounds $(PbSe)_{1+\delta}(VSe_2)_n$ with $n = 1 – 3$ were prepared from designed precursors. Diffraction and electron microscopy data indicate that the compounds consist of bilayers of PbSe separated from one another by *n* Se-V-Se trilayers. All the compounds are metallic, with discontinuities in the temperature dependence of their resistivity and Hall coefficients, suggestive of charge density waves. Both the carrier type and the charge density wave transition of the compound with $n = 1$ (holes, abrupt change in resistivity) were distinctly different than found for the $n = 2$ and 3 compounds (electrons, change in slope of resistivity). The increased change of the resistivity and Hall coefficient through the charge density wave transition for $(PbSe)_{1.11}VSe_2$ relative to $(BiSe)_{1+\delta}VSe_2$ and bulk $VSe_2$ demonstrates the importance of the companion layer in controlling properties. The extent of charge transfer between constituent layers, the magnitude of the structural misfit at the interface between constituents, the magnitude of electron-electron correlation, and the degree of isolation of the single $VSe_2$ layers from one another may all contribute to the magnitude and the transition temperature of the charge density wave.

To understand the complex properties of $VSe_2$ better, Chapter IX will present a more thorough computational investigation of $VSe_2$ monolayers and bilayers. Especially the effect of electron correlation on their structures and properties will be studied intensely.

# CHAPTER IX

# DYNAMIC INSTABILITIES IN STRONGLY CORRELATED $VSe_2$ MONOLAYERS AND BILAYERS

Portions of this chapters has been co-authored and submitted as Esters, M.; Hennig, R. G.; Johnson, D. C. "Dynamic Instabilities in Strongly Correlated $VSe_2$ Monolayers and Bilayers" and submitted to *Physical Review B*.

## IX.1. Introduction

The discovery of graphene has sparked heightened interest in studying and finding new two-dimensional (2D) materials.[1-3] Apart from graphene, transition metal dichalcogenides (TMDs) have been intensely researched as potential candidates as 2D materials due to their layered structures. TMDs exhibit diverse physical and chemical properties, and reducing dimensionality may yield additional properties due to quantum confinement.[4] Additionally, TMDs are chemically diverse, unlike graphene, which is chemically inert. Thus, while functionalization of graphene leads to the loss of some of its properties, functionalizing TMDs can enhance their properties or create new ones. All these factors make 2D TMDs particularly interesting for applications in electronic and sensing devices, and in catalysis and energy storage. As a result, a large amount of research has been done on 2D TMDs using theoretical and experimental methods such as the transition of $MoS_2$ from an indirect to a direct semiconductor when reducing the dimensions from bulk and multilayers to a monolayer.[4-16] Magnetic 2D materials are especially interesting due to their potential use in spintronic devices.[17-23] The prediction

of magnetic TMD materials has been subject to extensive theoretical investigation, such as the systematic change in magnetic properties through strain,[18,22,24-27] hydrogenation,[27,28] and chemical substitution.[29] Moreover, pristine dichalcogenide monolayers of some first row transition metals (V, Cr, Mn, Fe) are predicted to have magnetic order.[19,20,22,24,30-34]

Bulk $VSe_2$ has been subject to extensive experimental studies due to its ability to intercalate ions[35-39] and its charge density wave (CDW).[40-46] Few-layer $VSe_2$ nanosheets were successfully synthesized using liquid exfoliation. These nanosheets retain the CDW and the metallic properties of its bulk analog, but their magnetic properties were reported to be different: the sheets are ferromagnetic at room temperature, whereas bulk $VSe_2$ exhibits temperature independent paramagnetism.[48-50] Isolated monolayers of $VSe_2$ have not been synthesized yet. However, monolayers of $VSe_2$ can be found in misfit layer compounds and ferecrystals, where they are sandwiched between monochalcogenides that crystallize in a rock-salt type structure.[51-56] While the existence of CDWs is well documented in ferecrystals and absent in misfit layer compounds, presumably due to structural distortions, the magnetic properties have not been reported for any of these compounds.

In recent years, density functional theory (DFT) calculations were performed on single layer and few layer $VSe_2$ where the V atoms were coordinated in a distorted octahedral ($D_{3d}$, 1T-polytype, Figure 9.1a) and a trigonal prismatic geometry ($D_{3h}$, 2H-polytype, Figure 9.1b).[24,30,34,57] These calculations predict the ground state of undistorted $VSe_2$ layers to be the ferromagnetic 2H-polytype with a metal to semimetal/semiconductor transition when going from the bilayer to the monolayer.[30,31,34]

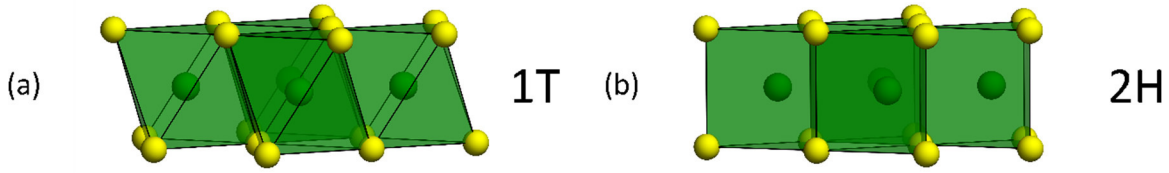


**Figure 9.1.** Structures of monolayer $VSe_2$ with (a) octahedrally coordinated V as in 1T-$VSe_2$ and (b) trigonal-prismatically coordinated V as in the 2H-$VSe_2$ polymorph. Vanadium atoms are shown in dark green and selenium atoms are shown in light yellow.

The dynamic stability, an important predictor of a charge density wave, was not reported. Strong electron correlation may play an important role in monolayer $VSe_2$. Zhuang and Hennig have shown that the strength of electron correlation affects a variety of properties in $VS_2$, such as the electronic structure and the stability of the 1T and 2H-polytype.[32] DFT+U calculations by Huang *et al.* on 2H-$VSe_2$ monolayers have shown that electron correlation in 2H-$VSe_2$ greatly influences the electronic structure.[57]

This work presents DFT calculations to explore correlation effects in monolayer and bilayer $VSe_2$. It will be shown that electron correlation has profound effects on the magnetic properties and electronic structure of the 1T-polytype. First, the van der Waals functionals and the Hubbard-*U* parameter will be benchmarked against the experimental structure. These parameters will be used to determine the magnetic ground state(s) of $VSe_2$ monolayers and bilayers, and to examine the effect of the Hubbard parameter on the electronic structure. At last, it will be shown that the Hubbard parameter changes the dynamic stability and the presence of imaginary modes of ferromagnetic 1T-$VSe_2$ while affecting only the amplitudes in the non-magnetic phase. The non-magnetic phase is able to reproduce the experimentally observed CDW supercell. Fermi surface nesting is likely the cause for the instabilities in non-magnetic 1T-$VSe_2$ but plays no role in ferromagnetic 1T-$VSe_2$.

## IX.2. Computational Methods

All DFT calculations were performed using the Vienna ab initio simulation package (VASP).[58-60] The interactions between the ionic core and the valence electrons were described using the projector-augmented wave (PAW) method using a cutoff energy of 500 eV.[61,62] The $3p^6 3d^4 s^1$ and the $4s^2 4p^4$ states were used as valence electrons for V and Se, respectively. For the exchange-correlation functional, we compare results for the local-density approximation (LDA),[63] the Perdew-Burke-Ernzerhof (PBE)[64] generalized-gradient approximation (GGA), and the Heyd-Scuseria-Ernzerhof (HSE06) hybrid method with the standard exact-exchange mixing parameter of $\alpha = 0.25$.[65] For the Hubbard-$U$ term, Dudarev's approach was used to treat localized $d$-orbitals in V, using the effective $U$ parameter, $U_{\text{eff}} = U - J$, with $U$ and $J$ being the on-site Coulomb and exchange parameters, respectively.[66] Since the interactions between individual $VSe_2$ layers is of van der Waals type, dispersion corrections were included for the GGA functionals using the method of Tkatchenko and Scheffler (TS), Grimme's DFT-D2 method, and Dion's method in the vdW-DF corrected optPBE, optB86b and optB88 functionals.[67-74] Brillouin zone integration was carried out using a Γ-centered k-point grid with a high k-point density of approximately 60 k-points per $Å^{-1}$.[75] Atomic positions and lattice parameters were fully optimized until the forces were smaller than 0.01 eV/Å and the stresses smaller than 0.05 GPa. A vacuum of 30 Å was included for the monolayer and bilayer calculations to minimize interactions between periodic images. For total energy calculations, self-consistency was achieved with an energy convergence of $10^{-6}$ eV. The magnetic anisotropies were obtained by including spin-orbit interactions in a non-selfconsistent calculation using charge and spin densities from calculations

without spin-orbit interactions. Since magnetic anisotropies can be in the sub-meV regime, an energy convergence of $10^{-8}$ eV was used for these calculations. Band structures were visualized and $VSe_2$ slabs were generated using the open source PYTHON packages PYMATGEN in conjunction with MPINTERFACES.[76,77] Spin densities were visualized with the program VESTA.[78] Fermi surfaces were calculated using the Wannier interpolation as implemented in the WANNIER90 code and visualized using XCRYSDEN.[79,80]

## IX.3. Results and Discussion

*Stability of undistorted $VSe_2$ layers with different coordination geometries*

Figure 9.2a shows the differences in formation energy, $\Delta E$, between $VSe_2$ monolayers in the octahedral (1T) and trigonal prismatic (2H) structure as a function of the Hubbard-$U$. $\Delta E$ depends strongly on the exchange correlation functional, $U_{eff}$, and the van der Waals functional, similar to the findings for $VS_2$.[32] For all functionals, $\Delta E$ exhibits a maximum value at intermediate values of $U_{eff}$. For the GGA functional, PBE and the van der Waals corrected GGA functionals vdW-optPBE, vdW-optB88, vdW-optB86b, TS-GGA, and GGA-D2, the maximum occurs at a lower $U_{eff}$ of 0.5 to 1.0 eV compared to a $U_{eff}$ of 2.5 eV for the LDA functional. This is similar to the behavior and values observed for $VS_2$. For most functionals, the maximum value for $\Delta E$ agrees well with the value for HSE06 of 41 meV per formula unit (f.u.), except for the DFT-D2 and the Tkatchenko-Scheffler van der Waals functionals. For the GGA+U methods, the 2H-structure is stable for $U_{eff}$ below about 2 eV. For the LDA+U method, 1T is stable for $U_{eff}$ below 0.5 eV and above 3.5 eV. These trends are similar for the bilayer and the bulk (see Figures B.2 and B.3 in Appendix B). Isaacs and Marianetti atrributed these changes in

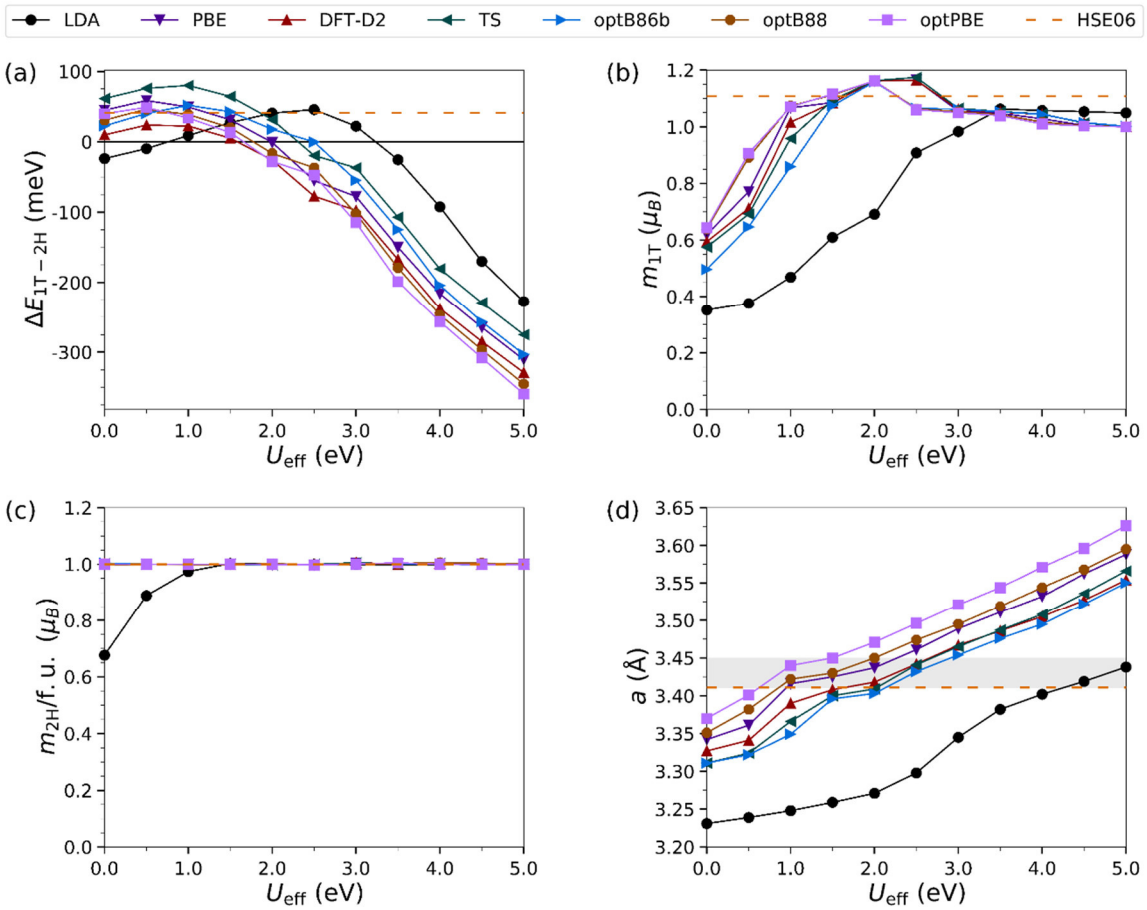


**Figure 9.2.** (a) Energy difference ΔE between 1T and 2H-$VSe_2$ monolayers as a function of $U_{eff}$, exchange-correlation and van der Waals functional. Positive $\Delta E$ indicates that 2H is more stable. (b) Magnetization $m$ of monolayer 1T-$VSe_2$ and (c) 2H-$VSe_2$ as a function of $U_{eff}$, exchange-correlation and van der Waals functional. (d) In-plane lattice parameters $a$ of monolayer 1T-$VSe_2$. The gray shades represent the range of experimental values found for ferecrystals.

energy for $VS_2$ to an increased filling and ordering of the V *d*-orbitals in 1T-$VS_2$, and we observe the same trends in the density matrix elements for $VSe_2$.[81]

The magnetization $m$ of the 1T monolayer as a function of $U_{eff}$ is pictured in Figure 9.2b. The magnetization of the 1T-polytype is very sensitive to $U_{eff}$, and for low $U_{eff}$, also to the choice of van der Waals correction. Using LDA, the magnetization gradually increases until it plateaus at 1.05 $\mu_B$ at $U_{eff}$ = 3.5 eV. For PBE, the magnetization reaches a maximum of 1.15 $\mu_B$ at $U_{eff}$ = 2.5 eV and then decreases to

unity. While LDA+U shows lower magnetization compared to the HSE06 functional, the magnetization of the GGA+U calculations coincide with HSE06 at $U_{eff}$ = 1.5 eV, regardless of the van der Waals functional. PBE without dispersion correction, and the optPBE and optB88 functionals already coincide with HSE06 at $U_{eff}$ = 1.0 eV. For 2H (Figure 9.2c), the magnetization is at unity using HSE06 and PBE, regardless of $U_{eff}$ and van der Waals functional, whereas LDA reaches the same value at $U_{eff}$ = 1.5 eV.

Since isolated monolayers of $VSe_2$ have not been synthesized yet, finding a good benchmark to decide on an exchange-correlaction functional and a value for $U_{eff}$ is challenging. However, ferecrystals contain monolayers of transition metal dichalcogenides and can be used as an approximation. The compounds $[(MSe)_{1+\delta}]_m[VSe_2]_1$ (M = Pb, Sn) have a relatively constant $a$-axis lattice parameter of $a$ = 3.42 Å, regardless of $m$, the thickness of the MSe layer.[52-56,83] The in-plane lattice parameter $a$ of the isolated $VSe_2$ monolayers calculated with different functionals are shown in Figure 9.2d. For all functionals, the $a$-axis lattice parameter increases with increasing $U_{eff}$. As the figure shows, adding a Hubbard-$U$ is necessary to reach the experimental in-plane lattice parameter. LDA agrees with experiments only at $U_{eff}$ = 4.5 eV. optB86b, DFT-D2, and the Tkatchenko-Scheffler functionals need a moderately high $U_{eff}$ of 2.5 eV whereas PBE, optPBE and optB88 only need 1 eV to agree with the experimental lattice parameters. HSE06 underestimates the $a$-axis lattice parameters only slightly. It is clear to see that any functional can reproduce these lattice parameters with a high enough value of $U_{eff}$.

For monolayers, one would expect van-der-Waals forces to be negligible, and the results should coincide well with the PBE functional without dispersion corrections,

which is only true for optPBE and optB88. Since optPBE showed much more stable convergence behavior and also gave a more accurate $c/a$ ratio for the bulk (see Table 9.1), we decided that optPBE with $U_{eff}$ = 1.0 eV is the most suitable functional. We will cross-check select results with calculations using the optB86b functional and $U_{eff}$ = 2.5 eV, which also reproduces the experimental in-plane geometry well.

It is important to note that PBE predicts bulk 1T-$VSe_2$ to be ferromagnetic even though it exhibits temperature-independent paramagnetism in experiments, and should thus converge to a non-magnetic state. Using mean field theory, we estimated the Curie temperature of the bulk structure to be approximately 39 K and 17 K without a Hubbard-$U$ and with $U_{eff}$ = 1.0 eV, respectively, which is significantly below the charge density transition temperature of 100 – 110 K (see Table B.1 and the corresponding text in Appendix B).[40-46] A ferromagnetic ground state is thus not inconsistent with experimental evidence since undistorted 1T-$VSe_2$ is not stable in the temperature regime in which it would be ferromagnetic.

**Table 9.1.** Lattice parameters of the relaxed bulk structure of 1T-$VSe_2$ with $U_{eff}$ = 1.0 eV using standard PBE, vdW-DF-optPBE, and vdW-DF-optB88 functionals.

| | Experiment[48-50] | PBE | optPBE | optB88 |
|---|---|---|---|---|
| $a$ (Å) | 3.35 | 3.42 | 3.46 | 3.44 |
| $c$ (Å) | 6.10 | 6.84 | 6.30 | 6.13 |
| $c/a$ | 1.82 | 2.00 | 1.82 | 1.78 |

*Magnetic structure of 1T-$VSe_2$ and 2H-$VSe_2$*

There are various configurations of magnetic order possible for the single and bilayer 1T and 2H-polytypes of $VSe_2$. Figure 9.3 shows the spin densities for the ferromagnetic (FM) and different antiferromagnetic (AFM) configurations of $VSe_2$

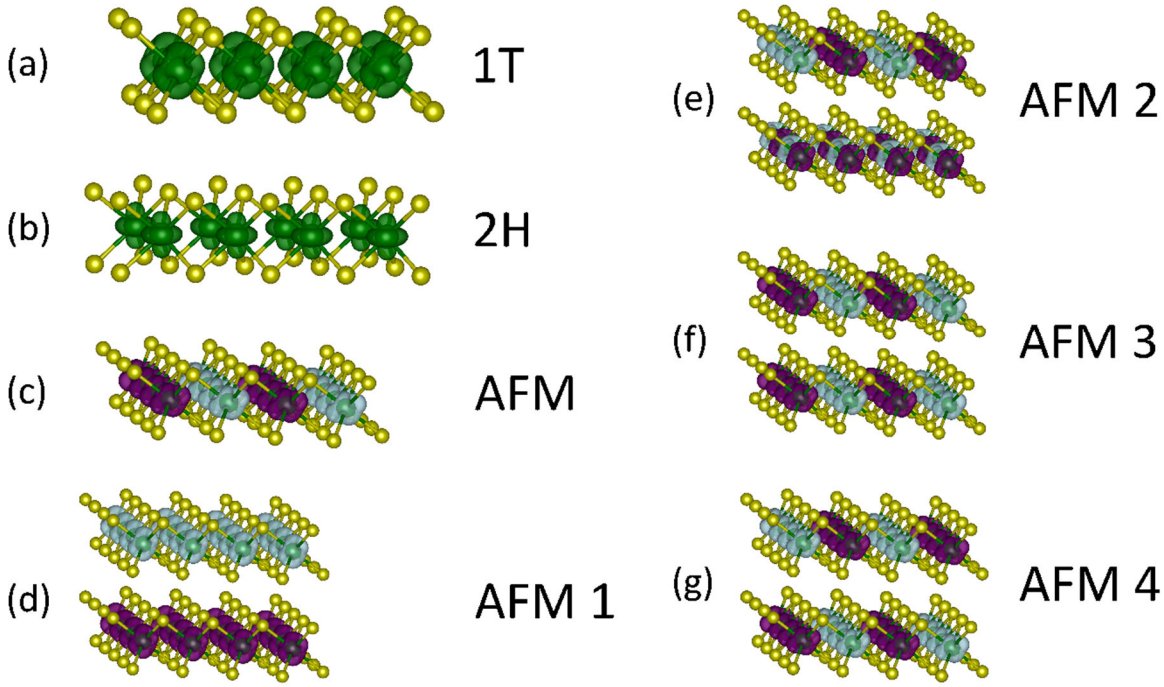


**Figure 9.3.** Spin densities for $VSe_2$ layers. (a) 1T-$VSe_2$ monolayer with ferromagnetic (FM) spin structure. (b) 2H-$VSe_2$ monolayer with FM spin structure. (c) 1T–$VSe_2$ monolayer with antiferromagnetic (AFM) spin orientation. (d – g) 1T-$VSe_2$ bilayer with AFM ordering (AFM 1 – AFM 4). For 2H-$VSe_2$, AFM 3 and AFM 4 are identical. For AFM structures, light red and dark blue spin densities denote opposite spin orientations. The isosurface values are set to 0.01 $e/a_0^3$ where $a_0$ is the Bohr radius.

monolayers and bilayers. For the single layer polytypes, the striped AFM order in Figure 9.3c is considered. Four different AFM configurations are considered for the bilayer polytypes and illustrated in Figure 9.3d – g for the bilayer 1T-structure. They include configurations of parallel spins in each layer in Figure 9.3d, striped configurations where the stripes are oriented perpendicular in Figure 9.3e, oriented parallel in a staggered pattern in Figure 9.3f, and in an eclipsing pattern in Figure 9.3g. Equivalent patterns are considered for the bilayer 2H-structure. Due to the different stacking in the 2H-polytype, the AFM 3 and AFM 4 configurations are identical in 2H-$VSe_2$ bilayers.

Table 9.2 shows the energies of the various possible types of magnetic order in the single and bilayer 1T and 2H-polytypes ($U_{eff}$ = 1.0 eV). Overall, the magnetic configurations are strongly favored, indicating the tendency of $VSe_2$ layers to exhibit some form of magnetic order. Similar to the results of Wasey *et al.* using PBE-D2 without a Hubbard-*U*,[31] monolayer $VSe_2$ is ferromagnetic for both polytypes. As illustrated in Figure 9.3, the spin densities around the V atom show $a_{1g}$ symmetry for the 1T-polytype and $a_1'$ symmetry for the 2H-polytype (the $d_{z^2}$ orbital). For bilayers, the energy of the anti-ferromagnetic order with ferromagnetic intra-layer (AFM 1) coupling is nearly identical to the ferromagnetic order whereas the structures with anti-ferromagnetic intra-layer coupling (AFM 2 – AFM 4) have substantially higher energies. This suggests that there is a strong intra-layer exchange coupling and virtually no inter-layer exchange coupling. The magnetic order of $VSe_2$ multilayers could thus be ferromagnetic or antiferromagnetic, or could show various disordered spin structures along the *c*-axis with ferromagnetic $VSe_2$ sheets. The AFM energies for 1T-$VSe2_2$ are substantially lower than for 2H-$VSe_2$, suggesting much weaker intra-layer exchange coupling in the 1T-structure.

**Table 9.2.** Energy differences $\Delta E_{mag}$ in meV per formula unit with reference to the ferromagnetic order for the non-magnetic (NM) and anti-ferromagnetic (AFM) configurations using $U_{eff}$ = 1.0 eV. For the bilayer, four and three different anti ferromagnetic cells can be created for the 1T and 2H-polytype, respectively.

| | Monolayer | | Bilayer | | | | |
|---|---|---|---|---|---|---|---|
| Polytype | NM | AFM | NM | AFM 1 | AFM 2 | AFM 3 | AFM 4 |
| 1T | 97 | 25 | 94 | 2 | 25 | 24 | 25 |
| 2H | 157 | 106 | 148 | -1 | 102 | 102 | – |

*Effect of the Electron Correlation Strength on the Electronic Structure of $VSe_2$ Layers*

Introducing the Hubbard-*U* parameter has profound effects on the structure of 1T-$VSe_2$ whereas the 2H-polytype remains virtually unaffected. Table 9.3 shows the structural and magnetic parameters of the relaxed monolayers and bilayers in their ground states. For 2H-$VSe_2$, the lattice parameters increase only slightly by 0.1 Å when $U_{eff}$ is increased to 1.0 eV and there is no change in lattice parameters when going from the monolayer to the bilayer. The distance between the Se and V planes also remain unchanged, and the magnetization is approximately unity regardless of Hubbard parameter, number of layers and magnetic structure. For V and Se, the magnitude of the magnetization increases only slightly as well. For 1T-$VSe_2$, increasing $U_{eff}$ to 1.0 eV leads to a "flattening" of the monolayer by increasing the in-plane lattice parameter and decreasing the distance between the Se and V planes. For the bilayer, the same trend can be seen, but there is also a small increase in the distance between $VSe_2$ layers.

The in-plane lattice parameters are in good agreement with the experimental values for ferecrystals, and are larger than in the bulk.[48-56,82] The magnetization increases significantly from 0.6 – 0.7 $\mu_B$ to slightly above unity. This is mostly due to the strong increase of the magnetic moment of the V atom, which almost doubles. Although the magnetic moments of the Se atoms, which are oriented antiparallel to the moments the V atoms, increase as well, they are much smaller in magnitude. The energy of the 1T-polytype decreases with respect to the 2H-polytype, but 2H is still the ground state.
The band structures with $U_{eff}$ = 1.0 eV of the ferromagnetic monolayers and bilayers and the AFM 1 bilayer structures are shown in Figure 9.4. Ferromagnetic 1T-$VSe_2$ is a metal where the Fermi level consists of a minority-spin hole-like part centered around the

**Table 9.3.** Comparison of the structural parameters, and magnetic moments for isolated $VSe_2$ monolayers and bilayers with and without the Hubbard parameter $U_{eff}$ = 1.0 eV. The structural parameters include the in-plane lattice parameter, $a$, the distance between the V and Se planes, $d$(V-Se), and the distance between the two $VSe_2$ layers in the bilayer, $d$($VSe_2$-$VSe_2$). The magnetic moments are given for the unit cell, $m$, and the contribution from the V and Se atoms, $m$(V) and $m$(Se), respectively. $\Delta E$ denotes the energy difference between the 1T and 2H polytype (positive when 2H is more stable).

| Monolayer | | | | |
|---|---|---|---|---|
| | $U_{eff}$ = 0 eV | | $U_{eff}$ = 1.0 eV | |
| Polytype | 1T | 2H | 1T | 2H |
| $a$ (Å) | 3.370 | 3.363 | 3.441 | 3.375 |
| $d_{V\text{-}Se}$ (Å) | 1.581 | 1.606 | 1.559 | 1.608 |
| $m$ ($\mu_B$) | 0.64 | 1.00 | 1.07 | 1.00 |
| $m$(V) ($\mu_B$) | 0.69 | 1.00 | 1.27 | 1.10 |
| $m$(Se) ($\mu_B$) | -0.05 | -0.07 | -0.13 | -0.10 |
| $\Delta E_{1T\text{-}2H}$ (meV) | 39 | | 33 | |

| Bilayer | | | | | | | | |
|---|---|---|---|---|---|---|---|---|
| | $U_{eff}$ = 0 eV | | | | $U_{eff}$ = 1.0 eV | | | |
| Magnetic order | FM | | AFM 1 | | FM | | AFM 1 | |
| Polytype | 1T | 2H | 1T | 2H | 1T | 2H | 1T | 2H |
| $a$ (Å) | 3.379 | 3.367 | 3.376 | 3.367 | 3.447 | 3.378 | 3.446 | 3.379 |
| $d$(V-Se) (Å) | 1.582 | 1.608 | 1.584 | 1.609 | 1.559 | 1.611 | 1.560 | 1.610 |
| | 1.574 | 1.601 | 1.574 | 1.601 | 1.553 | 1.607 | 1.554 | 1.605 |
| $d$($VSe_2$-$VSe_2$) (Å) | 3.252 | 3.337 | 3.245 | 3.307 | 3.230 | 3.393 | 3.261 | 3.334 |
| $m$/f.u. ($\mu_B$) | 0.66 | 0.98 | 0.00 | 0.00 | 1.07 | 1.00 | 0.00 | 0.00 |
| $m$(V) ($\mu_B$) | 0.71 | 0.99 | ±0.68 | ±1.01 | 1.27 | 1.10 | ±1.27 | ±1.01 |
| $m$(Se) ($\mu_B$) | -0.05 | -0.07 | ±0.05 | 0.07 | -0.13 | -0.10 | ±0.13 | ±0.10 |
| $\Delta E_{1T\text{-}2H}$/f.u. (meV) | 32 | | 32 | | 22 | | 25 | |

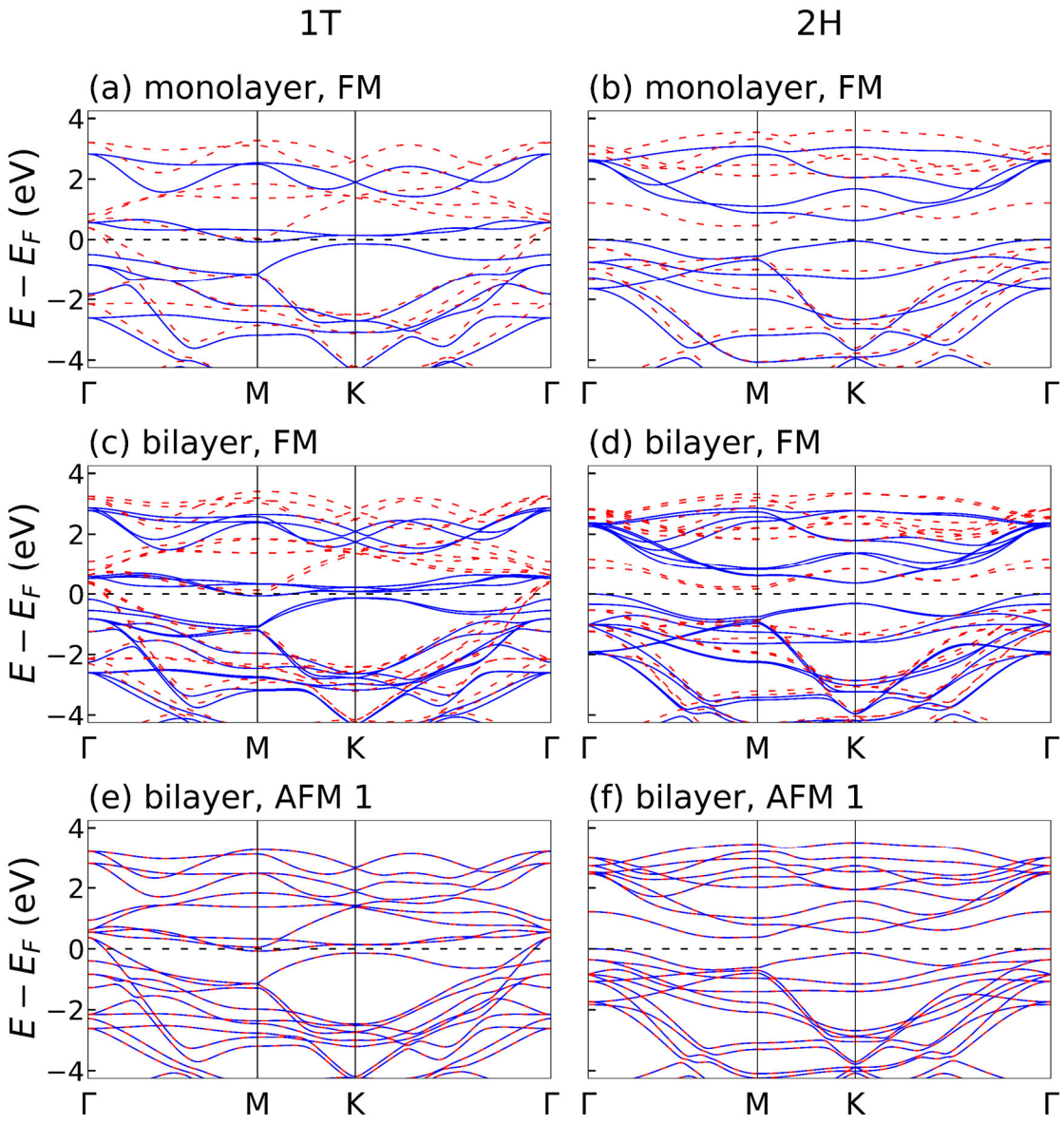


**Figure 9.4.** Spin-polarized band structures for 1T-$VSe_2$ (left) and 2H-$VSe_2$ (right) layers with $U_{eff}$ = 1.0 eV. (a, b) Ferromagnetic monolayer; (c, d) ferromagnetic bilayer; (e, f) bilayer with AFM 1 structure. Solid blue lines correspond to majority and red dashed lines to minority spin bands.

Γ point and a majority-spin electron-like part centered around the M point. Going from the monolayer to the bilayer doubles the number of bands, and the additional bands are degenerate with the bands of the monolayer, except for the highest occupied band near the Γ point where splitting can be observed. This splitting brings the highest occupied

band near the Γ point closer to the Fermi level compared to the monolayer, almost to the same energy as the bands at the K point. This has been observed in other TMDs when transitioning from monolayers to bilayers and is due to the introduction of anti-bonding intra-layer interactions.[4,8,31,83-85] Whereas for example in $MoS_2$, this phenomenon leads to a transition from a direct to an indirect semiconductor, the increase in energy is not sufficient to change the electrical properties in 1T-$VSe_2$. The band structure of the antiferromagnetic 1T-$VSe_2$ bilayer is essentially identical to the sum of two ferromagnetic band structures with opposite spins, providing further evidence that the electronic coupling between individual $VSe_2$ layers is very small. Similar behavior is observed for the band structures of the 2H-$VSe_2$ monolayers and bilayers. The FM 2H-$VSe_2$ monolayer is a semiconductor with an indirect gap between Γ and M and a slightly larger direct band gap at the K point. 2H-$VSe_2$ remains an indirect semiconductor in the FM bilayer. The transition from semiconductor to metal reported in the literature[31] does not occur when the Hubbard-*U* is included in the description. Similar to bilayer 1T-$VSe_2$, the electronic coupling between the layers in 2H-$VSe_2$ layers is very small.

Crystal field theory predicts that the $d$-orbitals in the 2H-polytype with $D_{3h}$ symmetry around the V atom split into $e'$ and $e''$ orbitals, each doubly degenerate, and one $a_1'$ orbital. For the 1T-polytype, the V atom is coordinated in a $D_{3d}$ symmetry and should split into two sets of doubly degenerate $e_g$ orbitals, and one $a_{1g}$ orbital. The orbital-projected band structures of the monolayers in Figure 9.5 show this splitting at the Γ point for both polytypes with the energies increasing from $e'$ ($d_{xy} + d_{x^2-y^2}$) to $e''$ ($d_{xz} + d_{yz}$) and $a_1'$ ($d_{z^2}$), and from both $e_g$ orbitals ($d_{xy} + d_{x^2-y^2}$) and ($d_{xz} + d_{yz}$) to $a_{1g}$ ($d_{z^2}$) for 2H-$VSe_2$ and 1T-$VSe_2$, respectively. Just as in $VS_2$,[32] the $e'$ and $e''$ orbitals

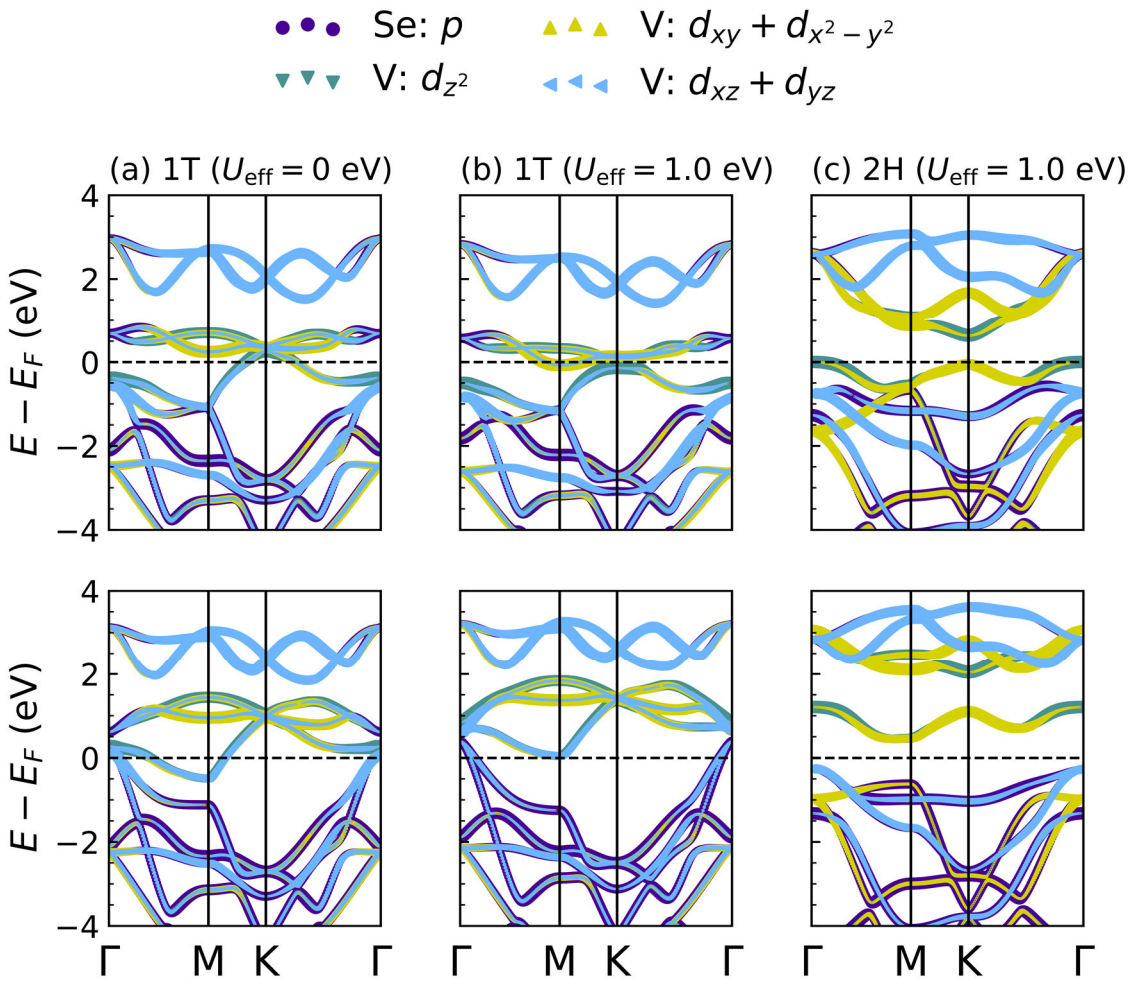


**Figure 9.5.** Orbital resolved majority spin (top) and minority spin (bottom) band structures of monolayer $VSe_2$. (a) 2H-$VSe_2$ with $U_{\mathrm{eff}} = 1.0$ eV; (b) 1T-$VSe_2$ with $U_{\mathrm{eff}} = 0$ eV; (c) 1T-$VSe_2$ with $U_{\mathrm{eff}} = 1.0$ eV.

strongly hybridize with the Se orbitals whereas the $a_1'$ orbital only hybridizes to a small degree. At the Fermi level, the bands are predominantly of $a_1'$ (Γ point) and $e'$ (K point) character, which is consistent with the shape of the spin density shown in Figure 9.3b (the $e'$ orbitals are masked by the “ring" of the $d_{z^2}$ orbital). While changes in $U_{\mathrm{eff}}$ have only negligible effects on the band structure on the 2H polytype, they have strong effects on the band structure of 1T-$VSe_2$. Figures 9.5a and b show that these effects are mostly found at the M and the K point for the majority spin bands, and at the M point for the

minority spin bands. At the M point, the majority spin $e_g$ band that consists of the $d_{xy}$ and $d_{x^2-y^2}$ orbitals is lowered in energy and crosses the Fermi level. Near the K point, a majority spin band with $d_{z^2}$ and partial $e_g$ character crosses the Fermi level for $U_{\text{eff}}$ = 0 eV, whereas for $U_{\text{eff}}$ = 1.0 eV, the band maximum is shifted below the Fermi level at the K point. This changes the character of the Fermi surface from hole-like at K for $U_{\text{eff}}$ = 0 eV to electron-like at M for $U_{\text{eff}}$ = 1.0 eV. The minority spin band structures show that at the M point, the $e_g$ band, which is comprised of the V $d_{xz}$ and $d_{yz}$ orbitals, is raised above the Fermi energy. The same band is also raised in energy at the Γ point. Another consequence is that the minority spin bands that cross the Fermi level near the Γ point are of significantly less $e_g$ character, and remain predominantly of Se $p$ character. At the Γ point, the Se $p$ orbital is also lowered in energy with respect to the $e_g$ and $a_{1g}$ orbitals. This explains the increased magnetization of 1T-$VSe_2$ with increased $U_{\text{eff}}$.

These changes can also be observed at the Fermi surfaces (Figure 9.6). Without a Hubbard-*U*, there are Fermi surface pockets around all high symmetry points. The majority spin bands form almost triangular shaped hole pockets around the K point. The surfaces at neighboring K points are almost parallel to each other, which may result in Fermi surface nesting. Fermi surface nesting is often cited as a cause for charge density waves, but this may not necessarily be the case, as we will discuss in the following section.[86,87] The minority spin bands form cigar shaped electron pockets around the M point that point towards the Brillouin zone center where two circular hole pockets of the minority spin bands can be found. Increasing $U_{\text{eff}}$ to 1.0 eV changes the Fermi surface dramatically. The hole pockets at the K point completely disappear, and the cigar shaped minority spin electron pockets get replaced by small oval majority spin electron pockets

that point towards the K points. The hole pockets at the Γ point increase in size, but overall, the size of the Fermi surface pockets decreases, reducing the intrinsic carrier concentration of the monolayer. Fermi surface nesting is not possible anymore for $U_{eff}$ = 1.0 eV.

For optB86b and $U_{eff}$ = 2.5 eV (see Figure B.4 in Appendix B), the energy of the highest occupied majority spin band decreases further in energy at the K point due to an increased population of the $d_{z^2}$ orbital. In turn, the minority spin band that is just below the Fermi level at the M point for $U_{eff}$ = 0 eV is now completely above the Fermi energy. This decreases the size of the Fermi surface pockets, showing that the electrical and magnetic properties are sensitive to the value of the Hubbard-*U* and not just to the structure. The sensitivity of the carrier type and carrier concentration of the different spin channels suggest that not only strain engineering, but also charge screening can be used

to tune the electrical and magnetic properties of $VSe_2$ layers. The latter could be achieved by using a suitable substrate or by incorporating $VSe_2$ into heterostructures. For example, in the ferecrystalline alloy $[(Sn_{1-x}Bi_xSe)_{1+\delta}][VSe_2]$, the *a*-axis lattice parameter of the $VSe_2$ monolayer increases systematically with increasing *x*, analogous to the trend observed in Figure 9.2d for increasing $U_{eff}$.[88]

Spin-orbit coupling (SOC) was introduced to determine the magnetocrystalline anisotropy energy (MAE) of the $VSe_2$ monolayers. The out-of-plane MAE is shown in Figure 9.7. Here again, correlation has a strong effect on the 1T-polytype whereas the

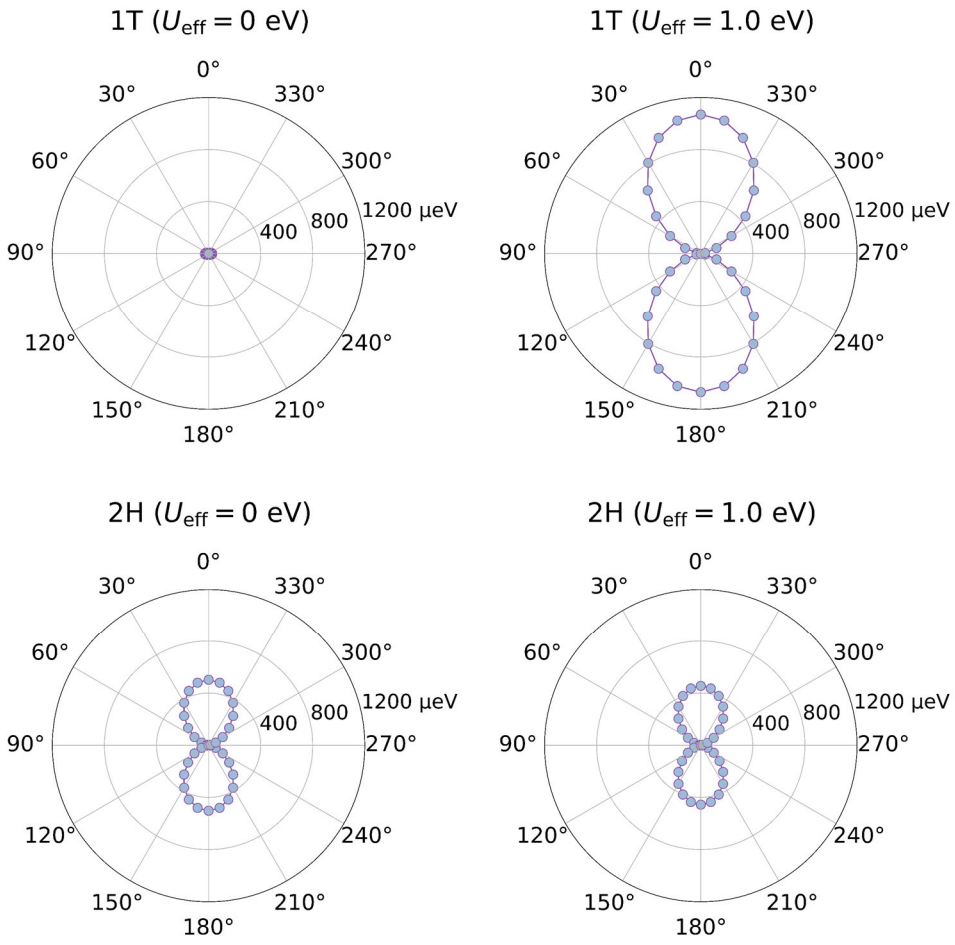


**Figure 9.7.** Angular dependence of the magnetocrystalline anisotropy energy (MAE) with polar angle for monolayer $VSe_2$. 0° points along the positive *z* axis.

2H-polytype is virtually unchanged. Without introducing the Hubbard parameter, 1T-$VSe_2$ is nearly isotropic. For $U_{eff}$ = 1.0 eV, however, 1T-$VSe_2$ monolayers show a large MAE of about 1.1 meV. This is consistent with the MAE obtained with the optB86b functional and $U_{eff}$ = 2.5 eV where the MAE was 1.2 meV. For 2H-$VSe_2$, the MAE only weakly dependents on $U_{eff}$. It is much smaller than the MAE of 1T-$VSe_2$ with 0.46 meV. The 1T and 2H structure both exhibit an easy magnetization plane and belong to the family of *XY* magnets. This means that a Berezinsky-Kosterlitz-Thouless transition could be observed at a critical temperature that can be estimated from a classical *XY* model as $T_c = 0.89Jk_B^{-1}$, where *J* is the exchange integral and $k_B$ the Boltzmann constant. The exchange integral J can be estimated from the energy difference of the FM and AFM configuration, $\Delta E_{mag} = 8J$. $T_c$ computes to 137 K for the 2H-polytype. For the 1T-polytype, $T_c$ is predicted to be 35 K for optPBE and $U_{eff}$ = 1.0 eV, and 14 K for optB86b and $U_{eff}$ = 2.5 eV ($\Delta E_{mag}$ = 11 meV), which is below the experimentally observed charge density wave (CDW) transition temperature of 100 – 110 K (onset).[40-46,52-56] This means that the magnetic transformation in the 1T-structure is unlikely to be observable as the 1T-polytype is unstable at such low temperatures.

*Dynamic Stability of $VSe_2$ Layers*

$VSe_2$ exhibits a charge density wave in bulk, nanosheets and ferecrystals. Density functional perturbation theory (DFPT) as implemented in VASP and the analysis program PHONOPY,[91] was used to calculate phonon dispersion relations for the monolayer and bilayer structures. For these calculations, the structures were relaxed until forces on the ions were below 0.001 Å/s. Phonon dispersion curves were also calculated for the bulk 1T-polytype (Figure B.5 in Appendix B). The soft modes for the bulk agree with the

charge density wave supercell found in experiments, confirming that our functional choice was reasonable.[46,91-94]

The phonon dispersion curves of the ferromagnetic ground states were calculated using a 4 × 4 supercell and displayed in Figure 9.8. For $U_{eff}$ = 0 eV, the monolayers of $VSe_2$ are dynamically stable for both polytypes even though the Fermi surface (Figure 9.6) allows for nesting, showing that Fermi surface nesting does not necessarily lead to dynamic instabilities. Increasing $U_{eff}$ to 1.0 eV, imaginary frequencies appear at the M point for the monolayer of 1T-$VSe_2$ whereas the monolayer of 2H-$VSe_2$ remains dynamically stable. The bilayer shows the same trend with imaginary phonon frequencies at the M point for 1T-$VSe_2$, suggesting that the dyamic instabilities in the bilayer have the same origin as in the monolayer. The soft node is at the **q**-point $\left(\frac{1}{2}, 0\right)$ and its symmetry equivalent points. The Fermi surface for $U_{eff}$ = 1.0 eV shows no parallel surfaces along a vector that corresponds to these points, so Fermi surface nesting cannot be the cause for these imaginary phonon nodes. The soft mode corresponds to either a 2 × 1 or 2 × 2 supercell, which is only half of what was found experimentally for bulk 1T-$VSe_2$.[46,91-94] Using optB86b and $U_{eff}$ = 2.5 eV (Figure B.6a in Appendix B) yields no imaginary phonon modes, which shows that the dynamic stability of spin-polarized 1T-$VSe_2$ is sensitive to the value of $U_{eff}$.

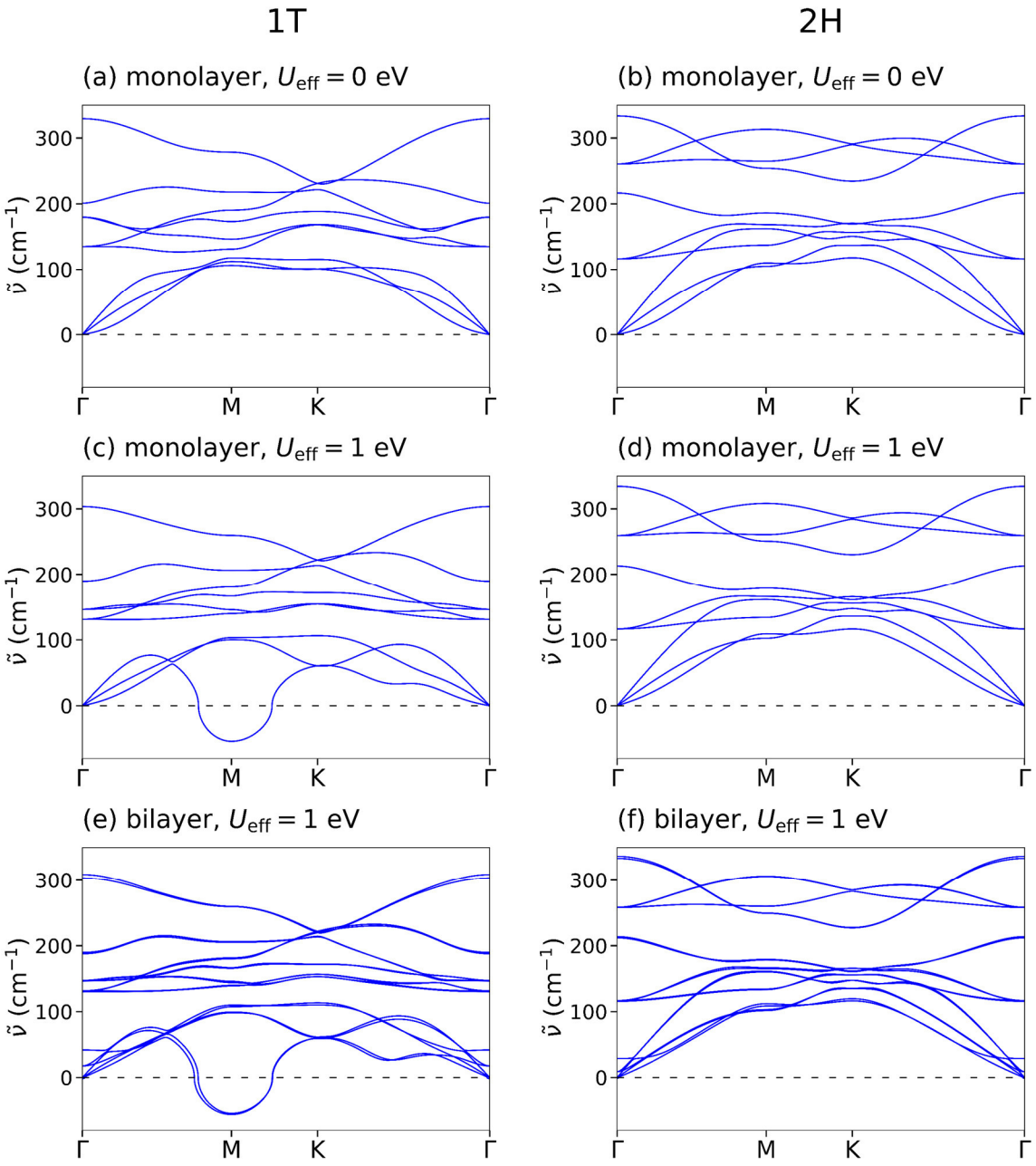


**Figure 9.8.** Phonon dispersion curves for spin-polarized 1T-$VSe_2$ (left) and 2H-$VSe_2$ (right) layers. (a,b) Monolayer with $U_{eff} = 0$ eV; (c,d) monolayer with $U_{eff} = 1.0$ eV; (e,f) bilayer with $U_{eff} = 1.0$ eV; The non-zero acoustical phonons at the Γ point for the bilayer are likely due to numerical inaccuracies.

As elaborated in the previous section, the CDW transition temperature for 1T-$VSe_2$ is above the predicted magnetic transition temperature, so the structural instabilities may be better described using the non-magnetic sturcture. The phonon dispersion curves of the non-spin-polarized $VSe_2$ layers are shown in Figure 9.9. The 1T polytype has a soft mode at $\left(\frac{1}{4}, 0\right)$ $\left(\frac{1}{2}M\right)$, which is consistent with a 4 × 4 supercell as observed for bulk 1T-$VSe_2$. Additional phonon modes with lower imaginary frequency appear at $\left(\frac{1}{6}, \frac{1}{6}\right)$ $\left(\frac{1}{2}K\right)$ and $\left(\frac{1}{8}, \frac{1}{8}\right)$ $\left(\frac{3}{8}K\right)$. The frequencies increase with increasing $U_{\text{eff}}$, indicating that stronger electron localization destabilizes the lattice more. Comparison with optB86b at $U_{\text{eff}}$ = 2.5 eV confirms this trend (Figure B.6b). The node at $\frac{1}{2}K$ increases stronger in frequency with $U$ than then node at $\frac{3}{8}K$, but the node at $\frac{1}{2}M$ remains the strongest. The positions of the soft mode minima are not significantly affected by $U_{\text{eff}}$. The 2H-polytype is not dynamically stable either with a minimum at $\left(\frac{1}{3}, 0\right)$ $\left(\frac{2}{3}M\right)$, suggesting that it distorts into a 3 × 3 or 3 × 1 supercell. Adding a Hubbard-$U$ introduces additional instabilities at the M point, resulting in complex phonon spectra. However, since 2H-$VSe_2$ has not been synthesized yet and since it is predicted to have a fairly high magnetic transition temperature, it is unknown whether it would undergo this CDW transition from the non-magnetic state or if it would become ferromagnetic first, in which case would remain undistorted.

**Figure 9.9.** Phonon dispersion curves for non-magnetic 1T-$VSe_2$ (left) and 2H-$VSe_2$ (right) layers. (a,b) Monolayer with $U_{eff}$ = 0 eV; (c,d) monolayer with $U_{eff}$ = 1.0 eV; (e,f) bilayer with $U_{eff}$ = 1.0 eV

Angle-resolved photoelectron spectroscopy revealed that bulk 1T-$VSe_2$ shows partial Fermi surfaces nesting with a nesting vector of $\left(\frac{1}{4},\frac{1}{4}\right)$.[93,94] The Fermi surface of non-magnetic 1T-$VSe_2$ monolayers (shown in Figure 9.10) is of similar shape as the in-plane Fermi surface determined experimentally. Partial nesting can be observed inside the cigar-like electron Fermi surface pockets. The nesting vectors (gray arrows in Figure 9.10) have the coordinates $\left(\frac{1}{4},\frac{1}{4}\right)$, which is consistent with a Fermi surface nesting mechanism. It can be concluded that the dimensionality does not affect the CDW vector in 1T-$VSe_2$.

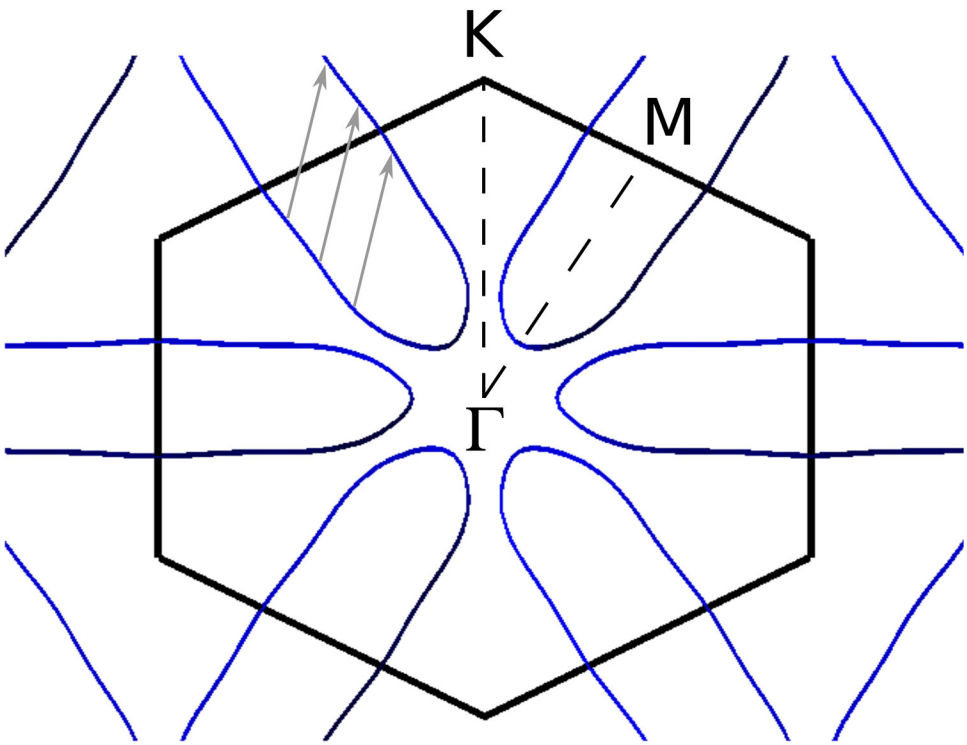


**Figure 9.10** Fermi surface of a non-spin-polarized 1T-$VSe_2$ monolayer. The edges of the Brillouin zone are shown in black solid lines, and the edges of the irreducible Brillouin zone are shown in black dashed lines. Nesting vectors are shown in gray.

## IX.4. Conclusions and Bridge

It was shown using density functional theory including the Hubbard-*U* parameter that the ground state of two-dimensional $VSe_2$ is ferromagnetic for monolayers and that for bilayers, the ferromagnetic and an antiferromagnetic configuration are energetically nearly degenerate due to weak magnetic interactions between the layers. The $VSe_2$ monolayers exhibit an easy magnetization plane and belong to the family of *XY* magnets, but the transition temperature for 1T-$VSe_2$ is below the experimentally observed charge density wave (CDW) transition temperature. 1T-$VSe_2$ displays a charge density wave in bulk, in few layer nanosheets and in ferecrystals. The ferromagnetic monolayers are dynamically stable with the exception of 1T-$VSe_2$ for some *U* values. The non-magnetic layers are unstable with a $4 \times 4$ supercell and a $3 \times 3$ supercell for the 1T and 2H-polytype, respectively. Within the *ab*-plane, non-magnetic 1T-$VSe_2$ monolayers show partial Fermi surface nesting similar to the bulk compound, but Fermi surface nesting does not contribute to the instability of the ferromagnetic layers.

The last two chapters investigated a transition metal dichalcogenide component of ferecrystals. The remaining chapters will move on to the rock salt component of the ferecrystal, which show interesting structural distortions. Chapter X will introduce SnSe and its thickness dependent structure. DFT is used to explain stabilities, and reveals that interactions with the transition metal dichalogenide and nucleation and growth kinetics are driving the stability of the individual polytypes.

# CHAPTER X

# STRUCTURAL CHANGES AS A FUNCTION OF THICKNESS IN $[(SnSe)_{1+\delta}]_mTiSe_2$ HETEROSTRUCTURES

Portions of this chapter are prepared to be submitted as Hamann, D. M.; Lygo, A. C.; Esters, M.; Merrill, D. R.; Ditto, J.; Sutherland, D. R.; Bauers, S. R.; Johnson, D. C. "Structural Changes as a Function of Thickness in $[(SnSe)_{1+\delta}]_mTiSe_2$ Heterostructures" in *ACS Nano*. D.M.H. and A.C.L performed the structural analysis and wrote the paper. M.E. performed the density functional theory calculations and assisted with writing and figure preparation. D.R.M. and D.R.S. synthesized the compounds and collected the structural and electrical data. J.D. performed collected the scanning tunneling electron microscopy images. S.R.B. contributed to data analysis. D.C.J. was the principal investigator. D.C.J. and S.R.B. also provided editorial assistance.

## X.1. Introduction

Two-dimensional (2D) materials continue to attract increasing attention as researchers discover emergent electronic properties in monolayers and heterostructures.[1–5] For example, transitions from an indirect to a direct band gap have been discovered in semiconducting $TX_2$ (T = Mo, W; X = S, Se) compounds in going from a bilayer to a monolayer as interactions with the neighboring $TX_2$ layer are eliminated.[6–8] The properties of single layers are impacted by interactions with the substrate and/or adjacent layers, with the overlap of states and the band offsets suggested as being important factors.[9–12] This has led to the concept of 2D layers acting as building blocks that can be

stacked in specific sequences, yielding heterostructures with desired properties.[13] Understanding how 2D layers interact with one another to yield emergent properties is critical to enable materials design for specific applications and is a current focus of the materials community.

Less well investigated are structural modifications associated with changes in electronic structure as heterostructures are created. There are several reasons for this, including challenges obtaining structural information on small flakes, lack of structural information from common analytical techniques used to confirm layering, and the initial systems investigated being rigid layers with van der Waals gaps on both sides in the bulk (graphene, HBN, transition metal dichalcogenides, etc.) where only small distortions might be expected. Since there are a limited number of rigid structures with a limited subset of properties, researchers have begun to explore 2D layers of compounds with 3D structures. Structural changes are more pronounced in 2D layers of materials with bulk 3D structures as the layers distort to stabilize dangling bonds at the interfaces. For example, bilayers of bulk rock salt structured constituents between dichalcogenide layers distort significantly, with the cations moving as much as 0.2 Å towards the anion layers in the dichalcogenide.[14,15] As the thickness of rock salt layers is increased, the distortions evolve towards a bulk structure with a surface distortion.[14,16] These structural distortions reflect changes in the free energy landscape as the ratio of atoms at the interface relative to the interior decreases. The properties of these heterostructures have been observed to systematically change as layer thicknesses are varied, reflecting the interactions between the layers.[17–19] Understanding how structural distortions in 3D materials change as their

thickness approaches the 2D limit, and how these distortions impact their properties, is important to allow their use in design of heterostructures.

This chapter investigates the structural changes in SnSe as a function of layer thickness in heterostructures with $TiSe_2$ layers. The naming convention for these structures is $[(SnSe)_{1+\delta}]_m[TiSe_2]_1$ where $m$ is the number of SnSe bilayers between the single layers of $TiSe_2$. SnSe was chosen because bulk SnSe undergoes a structural change from the room temperature phase, α-SnSe (GeS structure, *Pcmn*), to the high temperature β-SnSe (TlI structure, *Cmcm*) structure.[20] Von Schnering and coworkers investigated this phase transition in detail as a model system to test Landau theory predictions about symmetry-breaking changes in solids.[21–23] They found that the distortion is second order, with the Sn and Se $x$-coordinates changing continuously between the distorted α-SnSe structure and the undistorted β-SnSe structure. We probe how the SnSe structure is impacted by layer thickness. SnSe has been incorporated into similar heterostructures with several $TSe_2$ layers (T: transition metal). $TiSe_2$ was chosen as a second constituent because $(SnSe)_{1.21}TiSe_2$ prepared from modulated reactants exhibits a SnSe structural distortion due to its surface interaction with $TiSe_2$, which also results regions of long range order.[24] Since increasing the thickness of the SnSe constituent creates an interesting competition between the surface and bulk free energies of SnSe, how is this long range order affected?

In-plane x-ray diffraction revealed that as the thickness of the SnSe layer is increased, the structure changes significantly from a rectangular in-plane unit cell when $m = 1$, to a nearly-square in-plane unit cell for $m = 2$ and 3, to a different rectangular unit cell that is related to the bulk α-SnSe orthorhombic structure for $m = 4$. Scanning

transmission electron microscopy (STEM) images reveal a variety of stacking sequences in the SnSe layers as its thickness increases. Density functional theory calculations suggest that the structural changes cannot be explained by isolated SnSe layers, but are impacted by interactions between the constituent layers. Electrical transport measurements reveal independent changes in the signs of the Hall coefficient and Seebeck coefficient with increasing *m* and changes in temperature, reflecting the complex interactions between the layers. This suggests the interplay between constituent layers provides an opportunity to customize desired properties by adjusting the thickness and/or sequence of 2D layers.

## X.2. Experimental and Computational Methods

Precursors were synthesized in a high-vacuum physical vapor deposition system, with depositions occurring at pressures below $5 \times 10^{-7}$ Torr. Tin (Alfa Aesar, 99.98%) and titanium (Alfa Aesar, 99.99%) metals were deposited using electron beam guns, and selenium was deposited using an effusion cell. A computer controlled pneumatic shutter system was used to control the sequence and thickness of the elemental layers.[25] The rate of deposition and the thickness of the elemental layers were measured using quartz crystal microbalances, with rates maintained at 0.1 - 0.3 Å/s at the substrate. The elemental layers were deposited in a {Ti-Se-(Sn-Se)$_m$} sequence, with the number of sequential Sn|Se repeats, *m*, equal to the number of Sn-Se bilayers desired in the targeted compounds. The {Ti-Se-(Sn-Se)$_m$} sequence was repeated to get a total film thickness of approximately 500 Å, a thickness convenient for thin film diffraction and electrical property measurements. Composition measurements used for the calibration of deposition parameters was performed using electron probe microanalysis (EPMA) using a method

described by Donovan *et al*.[26] The precursors were annealed in an inert nitrogen environment ($p[O_2] \leq 0.8$ ppm) at 350 °C for 30 minutes to let the mostly amorphous precursors self-assemble into the desired products.

The structure of the precursors and products were determined using x-ray diffraction (XRD) and electron microscopy studies. Specular XRD and x-ray reflectivity (XRR) were used to determine the compound's superstructure and the total film thickness, respectively, using a Bruker D8 Discover. Constituent in-plane structures were characterized using an in-plane diffraction geometry on a Rigaku SmartLab diffractometer. All diffraction experiments were conducted using a Cu $K_\alpha$ radiation source. In-plane lattice parameters were refined with the Le Bail Method[27] using the FullProf suite.[28,29] High angle annular dark field scanning transmission electron microscopy (HAADF-STEM) data was collected at Pacific Northwest National Laboratory using a probe aberration-corrected FEI Titan 80-300 STEM.

Electrical resistivity and Hall effect measurements were conducted using the van der Pauw geometry on a home-made closed-cycle helium low temperature system using samples deposited on fused silica. Seebeck measurements were made on bar shaped samples with copper-constantan thermocouples. In this experiment, one end of the sample was cooled and the voltage between the same material thermocouple leads was measured.

Density functional theory (DFT) calculations were performed using the Vienna *ab initio* simulation (VASP) package.[30–32] The projector augmented wave (PAW)[33,34] method was used to describe the interactions between the core and the valence electrons. Exchange and correlation were described using Perdew-Burke-Ernzerhof (PBE)

functionals in the generalized-gradient approximation (GGA).[35] A cut-off energy of 500 eV was used for all calculations. Calculations were carried out on isolated multilayers using a 15 × 15 × 1 Monkhorst-Pack[36] grid for GeS- and TlI-structured layers, and a 11 × 11 × 1 Monkhorst-Pack grid for the other layers. To minimize interactions between periodic images, vacuum spacing of at least 20 Å was included between each multilayer. For bulk calculations, Monkhorst-Pack grids of 15 × 15 × 5, 15 × 5 × 15, and 11 × 11 × 11 were used for the GeS structure, the TlI structure, and the NaCl structure, respectively. Self-consistency was achieved with an energy convergence of $10^{-6}$ eV. Atomic positions and in-plane lattice parameters were allowed to relax until the forces were smaller than 0.005 Å/eV and the stresses were smaller than 0.01 GPa. For α-SnSe, rock salt (NaCl structure, $Fm\bar{3}m$), and a staggered rock salt-related structure, (001) slabs of the bulk structures were used, and a (010) slab for β-SnSe. The calculations were carried out on two, three, and four bilayers of each polytype, and additionally on a single bilayer for the GeS and NaCl structures.

## X.3. Results and Discussion

*X-ray Diffraction Analysis*

The modulated elemental reactants (MER) approach was used to prepare the targeted $[(SnSe)_{1+\delta}]_mTiSe_2$ compounds.[37,38] The deposition parameters required to prepare layered amorphous precursors that closely resemble the targeted structure in both local composition and layer thickness were determined using an iterative approach. This approach involves preparing a series of precursors of the sequence {$n$ × [Ti|Se] + $m$ × [Sn|Se]} with varying $m$ and $n$ values, measuring their compositions via EPMA, measuring the thickness of the repeating amorphous sequence via XRR, and interpolating

to obtain desired compositions and thicknesses as described previously.[39] Once the deposition was calibrated, precursors for each of the targeted $[(SnSe)_{1+\delta}]_mTiSe_2$ compounds were prepared by depositing the $\{[Ti|Se] + m \times [Sn|Se]\}$ sequence the required number of times to obtain the desired total thickness. An annealing study was conducted to determine optimum annealing temperatures and times to transform the designed precursors into the targeted compounds. The line widths and intensities of the reflections in specular XRD were used to assess the quality of the samples. A temperature of 350 °C for 30 minutes was selected as the optimum annealing conditions to crystallize the desired products. These conditions were the same as those used previously for $(SnSe)_{1.2}TiSe_2$.[40]

The specular XRD patterns of the annealed precursors are shown in Figure 10.1. Only (00*l*) reflections are observed in the patterns, indicating that the *c*-axis of the targeted compounds is perpendicular to the Si substrate. All reflections are narrow, sharp,

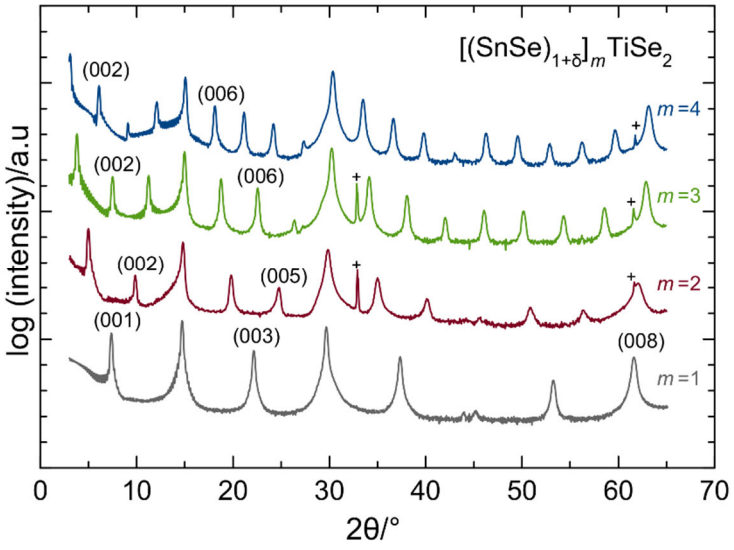


**Figure 10.1.** Specular x-ray diffraction scans of $[(SnSe)_{1+\delta}]_mTiSe_2$ compounds ($m$ = 1-4). The intensity is plotted on a log scale to enhance weak reflections. Miller indices are provided for select reflections and asterisks indicate reflections from the Si substrate.

and can be indexed to a single family of planes suggesting that a single repeating structure is formed. The calculated *c*-axis lattice parameters for the products are summarized in Table 10.1. As the number of SnSe bilayers deposited in the precursor increases, there is a systematic increase in the *c*-axis lattice parameter of 5.79(1) Å per bilayer of SnSe in $[(SnSe)_{1+\delta}]_mTiSe_2$. This result is consistent with the 5.77(5) Å and 5.806(2) Å increase in the *c*-axis lattice parameter per SnSe bilayer reported for $[(SnSe)_{1+\delta}]_m[NbSe_2]_n$ and $[(SnSe)_{1+\delta}]_m[MoSe_2]_n$ based compounds, respectively.[17,41] Extrapolating this relationship to $m = 0$, the thickness of the single $TiSe_2$ layer is 6.25(3) Å in each compound, which is thicker than the *c*-axis lattice parameter of bulk $TiSe_2$ (6.008 Å)[42] and the thickness per $TiSe_2$ layer in $(PbSe)_{1+\delta}[TiSe_2]_n$ (6.03 – 6.04 Å) obtained from the change in *c*-axis lattice parameter as *n* is varried.[18,43,44] The larger value reflects the different species interacting across the van der Waals interface. A single $TiSe_2$ layer has two $TiSe_2$-SnSe interfaces that are mismatched and hence cannot nest together. The increased $TiSe_2$ thickness in the $[(SnSe)_{1+\delta}]_mTiSe_2$ compounds reflects the influence that interactions of different constituent layers have on each other.

In-plane diffraction patterns were collected to characterize the basal plane structures of the constituent layers and are shown in Figure 10.2a. All observed

**Table 10.1.** Lattice parameters, and misfit parameters for $[(SnSe)_{1+\delta}]_mTiSe_2$ compounds.

| *m* | SnSe *a* (Å) | SnSe *b* (Å) | $TiSe_2$ *a* (Å) | 1 + δ | *c* (Å) |
|---|---|---|---|---|---|
| 1 | 6.1036(6) | 5.9787(4) | 3.56(1) | 1.203(9) | 12.04(1) |
| 2 | 4.2320(7) | 4.2887(7) | 3.60(5) | 1.24(7) | 17.84(1) |
| 3 | 4.2487(4) | 4.3126(4) | 3.56(1) | 1.198(7) | 23.64(1) |
| 4 | 4.2401(4) | 4.3196(5) | 3.56(1) | 1.196(8) | 29.42(2) |

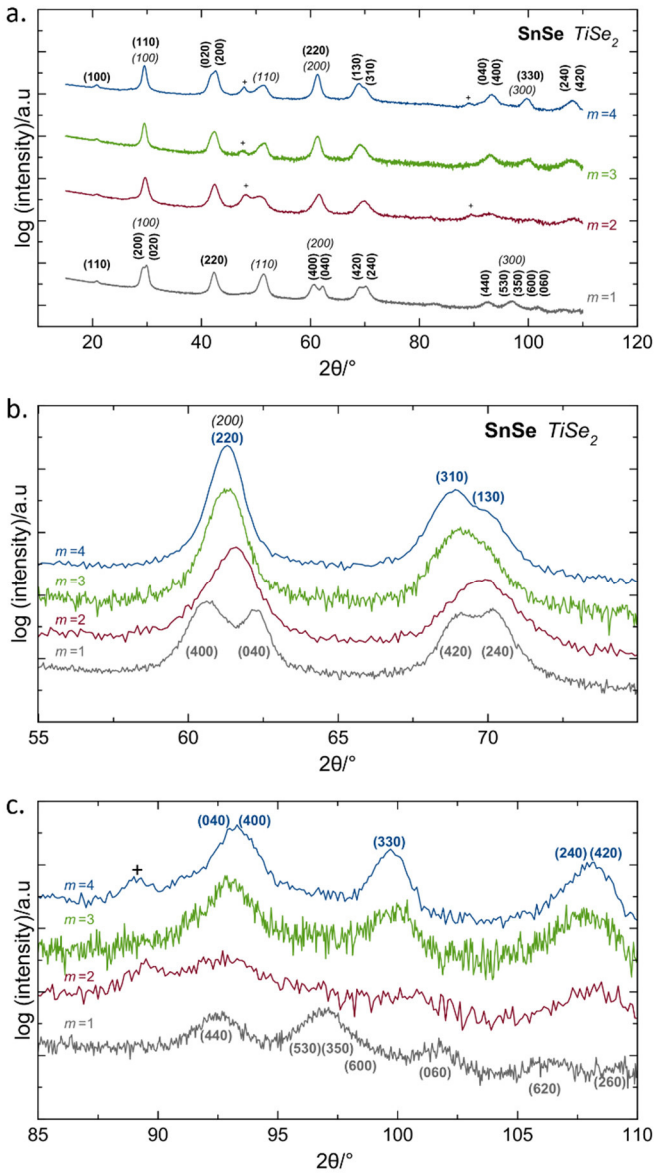


**Figure 10.2.** (a) In-plane diffraction pattern of the $[(SnSe)_{1+\delta}]_mTiSe_2$ compounds where $1 \leq m \leq 4$. The reflections are indexed to either SnSe or $TiSe_2$, with a single impurity peak being indexed to $SnSe_2$ (denoted with a + symbol). (b) Expansion of the high-angle region emphasizing the change in the SnSe reflections at approximately 61° and 69° that occurs as $m$ is increased from 1 to 4. (c) Expansion of a higher angle region that highlights the reflection differences between the $m = 1$ and $m \geq 2$ in-plane diffraction patterns.

reflections can be indexed to either a hexagonal unit cell for $TiSe_2$ or a rectangular unit cell for SnSe, except for reflections marked with a cross. The extra reflections at 48° in the $m = 2$-4 patterns and at 90° for $m = 2$, 4 patterns are consistent with (110) and (300)

$SnSe_2$ reflections and are likely the result of a slight excess of Sn and Se in the precursor. The in-plane lattice parameters for each constituent were refined using a full pattern Le Bail[27] fit and are summarized in Table 10.1. The results of the fits can be found in Figures C.1 – C.4 in Appendix C. The larger errors in the $TiSe_2$ lattice parameters relative to the SnSe lattice parameters result from overlapping reflections, with only the (110) reflection of $TiSe_2$ being distinct from reflections of SnSe. The hexagonal $TiSe_2$ reflections yield *a*-axis lattice parameters of 3.56(1) Å, except for the $m = 2$ compound which has an *a*-axis lattice parameter of 3.60(5) Å. The larger error for the $m = 2$ compound is a consequence of the overlap of the $TiSe_2$ (110) reflection with the (110) $SnSe_2$ reflection (Figure 10.2a). These *a*-axis lattice parameters are within error of each other and are consistent with those previously reported for other ferecrystals containing $TiSe_2$ layers and for the binary $TiSe_2$ compound.[18,43–47] The in-plane structure of $TiSe_2$ is thus independent of the thickness of the SnSe layers.

Surprisingly, the in-plane diffraction patterns for SnSe change considerably as *m* increases. Splitting, merging, and shifting of reflections indicate that the symmetry and lattice parameters change dramatically as *m* is varied. Figure 10.2b contains an expanded view of a high angle region containing several reflections to highlight the changes in the in-plane unit cell of SnSe as *m* is increased. The $m = 1$ compound has two reflections occurring at 60.6º and 62.2° that can be indexed as the (400) and (040) reflections in a distorted rock salt structure. In contrast, the $m = 4$ compound has a single reflection at 61.3° that can be indexed as the (220) consistent with a distorted α-SnSe or β-SnSe structure. The shifts in reflection positions for the $m = 1$ and $m = 4$ patterns require different unit cells and indexing. This is most visible at higher angles (Figure 10.2c). At

higher angles between 85° and 110°, the patterns for the $m = 2$ and $m = 3$ compounds have reflections at the same angles as for $m = 4$. Because of the similarity in the diffraction patterns, the $m = 2$ and 3 compounds can be indexed in the same manner as the $m = 4$ compounds. When looking at the reflection around 69°, the $m = 1$ and 4 compounds are clearly rectangular as indicated by the splitting of the peak. Although no splitting is observed for the $m = 2$ and 3 compounds, a line width broadening of the $h \neq k$ reflections compared to the $h = k$ reflections is present suggesting the basal plane is rectangular for these compounds as well.

Changes in the structure of SnSe layers with thickness have previously been reported for both misfit layer compounds and ferecrystals. In misfit layer compounds, bilayers of SnSe adopt a distorted NaCl structure, where the Sn atoms move towards the dichalcogenide and the Se atoms are displaced away from it.[44] There are additional distortions due to the structures adopting a common in-plane lattice parameter in one direction. In turbostratically disordered polymorphs of misfit layer compounds (ferecrystals), the structure of the SnSe layer changes with thickness. SnSe layers have a square or are approaching a square in-plane unit cell as one approaches $m = 1$ while thicker SnSe layers trend towards the bulk low temperature structure ($\alpha$-SnSe). This trend is observed for the $m \geq 2$ compounds reported herein, with $m = 1$ deviating significantly. As reported previously, however, $(SnSe)_{1.21}TiSe_2$ prepared via the low temperature self-assembly of a layered precursor is the only example of a compound that forms large domains with ordering between the constituent layers prompted by a lattice match between SnSe and $TiSe_2$.[24] The $m = n = 1$ compound is best described as a misfit layer compound with a large number of rotational defects present, likely at the grain interfaces

formed from several distinct nucleation events. The changes in structure as $m$ is increased reflect the increased importance of surface free energy in thinner layers.

In contrast to the $m = 1$ compound, the SnSe layer in the $m = 4$ compound has an in-plane structure that is closest to the bulk, reflecting a decrease in the surface to volume ratio of the SnSe layer. The structure is indexed to a rectangular in-plane unit cell and the $a$ and $b$ lattice parameters are similar to those measured for the bulk as a function of temperature, as previously observed in the $[(SnSe)_{1+\delta}]_m[TaSe_2]_n$ and $[(SnSe)_{1+\delta}]_m[MoSe_2]_n$ systems.[39,48] The lattice parameters for the compounds with $m = 2$ and 3 are smaller than those reported for the bulk. If the $m \geq 2$ compounds possessed the GeS or a different SnSe bulk structure, the (100) reflection would be extinct. Its presence indicates the existence of small distortions that change the atomic positions within the $ab$-plane. The large difference between the lattice parameters for $m = 1$ and $m \geq 2$ results from redefining the unit cell from a face centered unit cell to a primitive unit cell which is caused by a shift in atomic positions, as shown in Figure 10.3. The redefinition of the unit cell results in a change in the formula units per cell from 4 to 2 which, despite the change in lattice parameters, results in misfit parameters $1+\delta$ (the ratio of the in-plane packing density between the two constituents) ranging from 1.20 to 1.24 that are within error of each other. There is no evidence that long range order occurs in the $m \geq 2$ compounds. This suggests that the energetic cost of distorting the interior of the SnSe layer to achieve a lattice match is higher than the energy gain resulting from a more coherent interface with $TiSe_2$. In the $m = 1$ case, however, there are no interior atoms to compete with the surface stabilization gained by the tetragonal distortion.

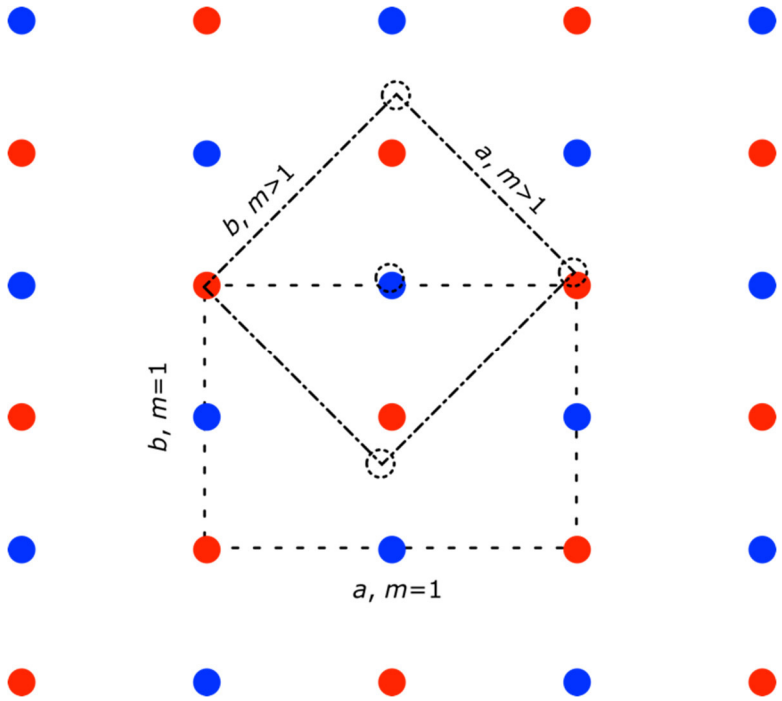


**Figure 10.3.** Schematic of shifting atomic positions of the SnSe constituent of $[(SnSe)_{1+\delta}]_mTiSe_2$ causing a redefinition of the in-plane unit cell from the $m = 1$ compound to the $m \geq 2$ compounds.

*Electron Microscopy Images*

HAADF-STEM was collected to further probe the layering, in-plane structure, and connectivity between the layers of the compounds. Representative images are shown in Figure 10.4. The two constituents are distinguished by the different contrasts in the image, with the SnSe layers appearing brighter and the $TiSe_2$ appearing darker. The interfaces between the different constituents are atomically abrupt and smooth, reflecting the extent of local diffusion during the self-assembly process, which corrects for local variations in either thickness or composition. Where zone axes are observed for the darker $TiSe_2$ layers, they are those expected for a $CdI_2$-structured $TiSe_2$ with octahedrally coordinated Ti. The SnSe layers are consistent with a distorted rock salt structure in agreement with in-plane diffraction data. Figure 10.4a shows that the sequence of layers is consistently repeated throughout the entire film in agreement with the diffraction data.

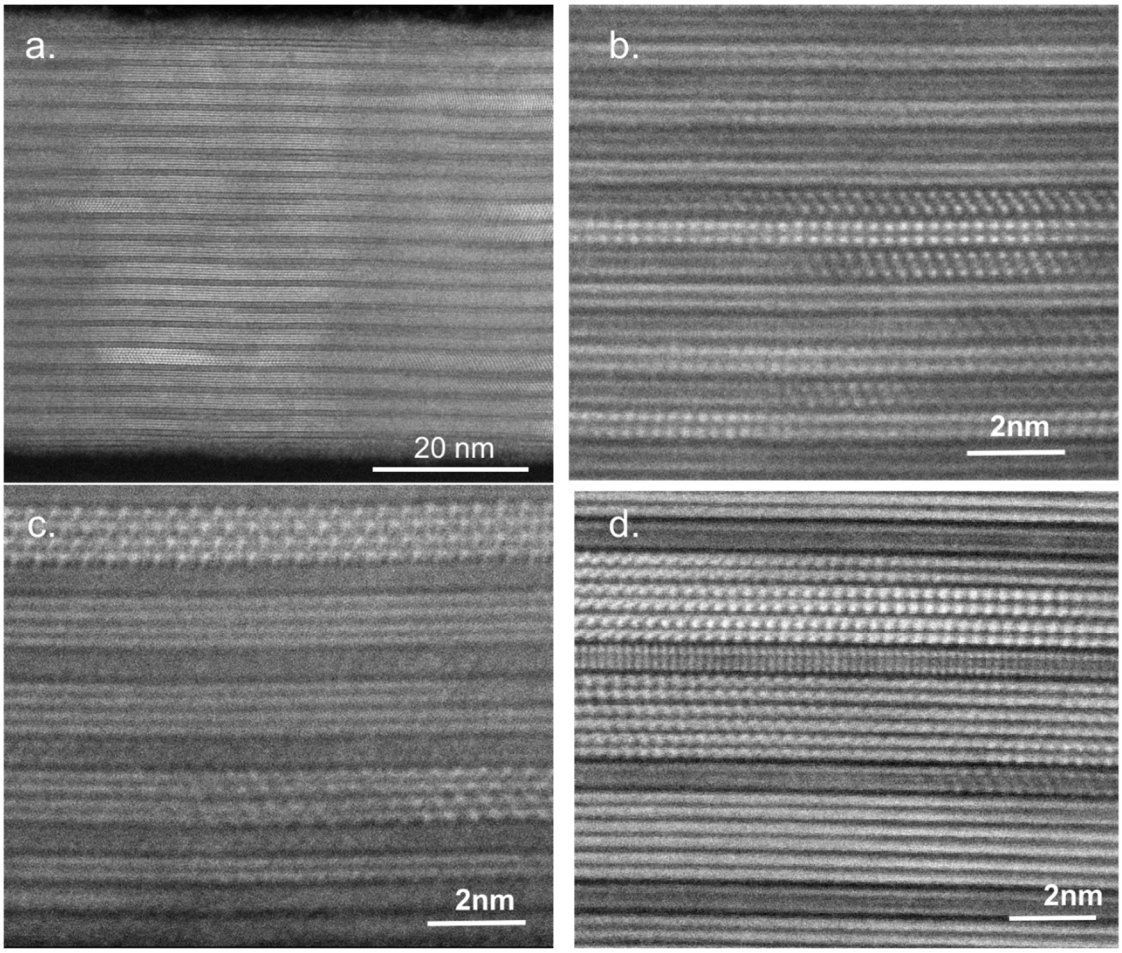


**Figure 10.4.** HAADF-STEM images of $[(SnSe)_{1+\delta}]_mTiSe_2$ compounds ($m \leq 3$). (a) An image of $(SnSe)_{1.20}TiSe_2$ showing the consistent alternation of the two constituent structures throughout the entire film. The bright layers correspond to SnSe while the darker layers correspond to $TiSe_2$. (b) Enlarged image of $[(SnSe)_{1.20}]_1TiSe_2$ showing the local atomic structure. Repeating orientations in some areas of the film support previous reports of regions of long range coherence. (c) A magnified image of $[(SnSe)_{1.24}]_2TiSe_2$ showing the pairing of the SnSe layers. Multiple orientations for the same constituent are observed throughout the film demonstrating the turbostratic disorder present in all compounds. (d) An expanded image of $[(SnSe)_{1.20}]_3TiSe_2$ showing the disorder between the different bilayers of SnSe.

The images of the $m = 1$, $m = 2$, and $m = 3$ compounds, Figures 4b, 4c, and 4d, respectively, show that the targeted structures were prepared. Small regions with substitutional defects, where $TiSe_2$ replaces a portion of an SnSe bilayer, can be found.[49] These types of substitutional defects have been observed previously in ferecrystalline

compounds and are an artifact of the self-assembly and correlated with small deviations in precursor composition from that of the targeted compound.[50,51] Small regions of $SnSe_2$ are observed at the surface and the film/substrate interface in some films (Figure C.5 in Appendix C), explaining the low intensity $SnSe_2$ reflection observed in the in-plane diffraction. This surface $SnSe_2$ is thought to form as excess Sn and Se migrate out of the sample as the superstructure self-assembles.

The HAADF-STEM images provide the information about the alignment between constituent layers at the atomic level that is lacking in the diffraction data due to the turbostratic disorder. Consistent with prior observations and the previously discussed in-plane diffraction, regions with long range order and regions of rotational disorder are observed in the $m = 1$ compound (Figure 10.4b).[24] In the $m \geq 2$ images no long-range order between constituent layers is observed. Extensive rotational disorder between SnSe and $TiSe_2$ layers supports the structural non-alignment of the constituents suggested by the independent in-plane lattice parameters. The rotational disorder in the $m \geq 2$ compounds is consistent with previous reports of analogous SnSe containing compounds synthesized from the modulated elemental reactants approach.[39,48]

The STEM images reveal several structural changes and stacking sequences in SnSe layers that are not expected from the bulk structure. The SnSe layers in compounds with $m \geq 2$ distort, forming pairs of atomic planes referred to in the following as bilayers. A similar distortion into pairs of layers was observed for thin PbSe layers and rationalized as an interplay between volume and surface free energy.[14] The spacing between bilayers is larger than the spacing within them, consistent with distorted α-SnSe (GeS structure) or β-SnSe (TlI structure) and in contrast to the equally spaced atomic

planes in a rock salt structure (Figures 4c and 4d). Where zone axes are observed for the SnSe layers, most of the layers stack on top of one another with the cations alternating with the anions in a face centered arrangement, which is consistent with a distorted rock salt structure but also with the (100) zone axis of α-SnSe and β-SnSe. Occasionally, the bilayers stack with the cations aligned above each other as found along the (010) axis of the bulk α-SnSe structure and the (001) axis of the bulk β-SnSe structure, evident in areas highlighted in Figure 10.5. This unexpected stacking arrangement may reflect the mechanism of formation, as the crystallographic alignment of the two constituent

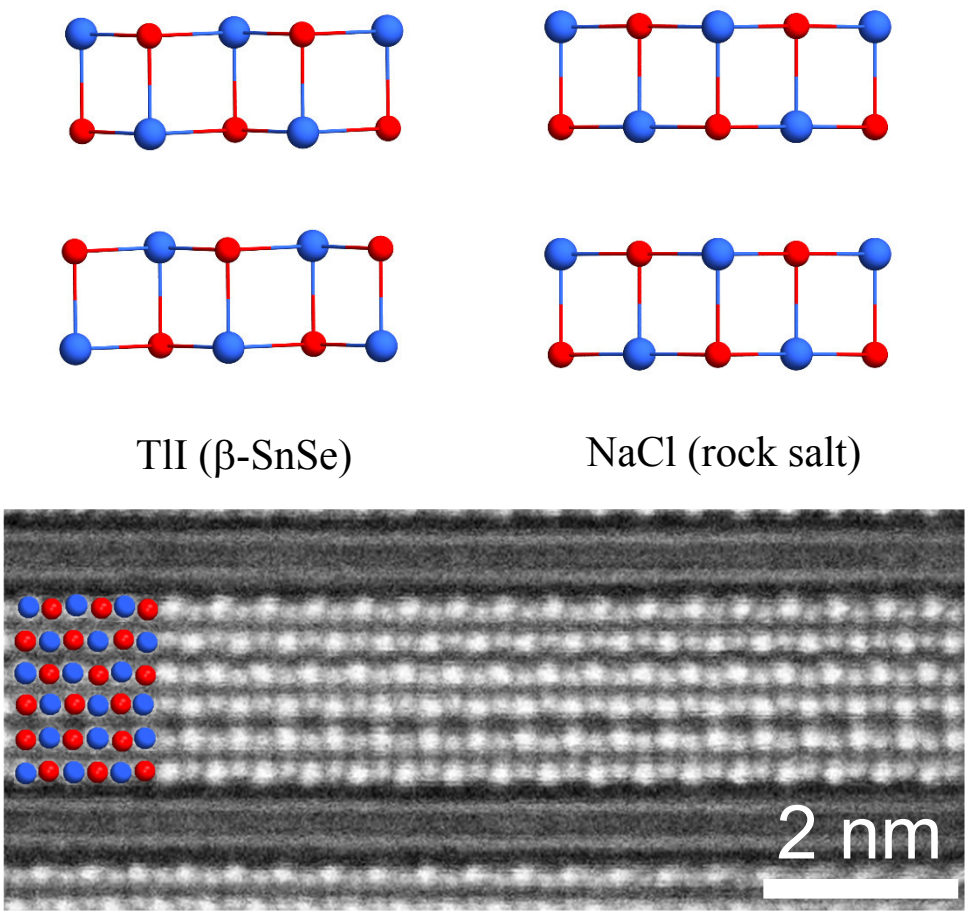


**Figure 10.5.** An expanded HAADF-STEM image showing two different SnSe orientations within the same layer of $[(SnSe)_{1+\delta}]_3TiSe_2$.

structures suggests that the layers template off of each other,[52] or it may reflect the competition between the bulk SnSe structure and a NaCl structured SnSe.

*Density Functional Theory Calculations on Isolated SnSe Layers*

Density functional theory (DFT) calculations were carried out on isolated multi-layers ($1 \leq m \leq 4$) using four different SnSe structures, as shown in Figure 10.6, to probe the observed structure changes as $m$ is increased. Figure 10.7a shows the evolution of the lattice parameters as a function of the number of bilayers. The GeS structure is the only

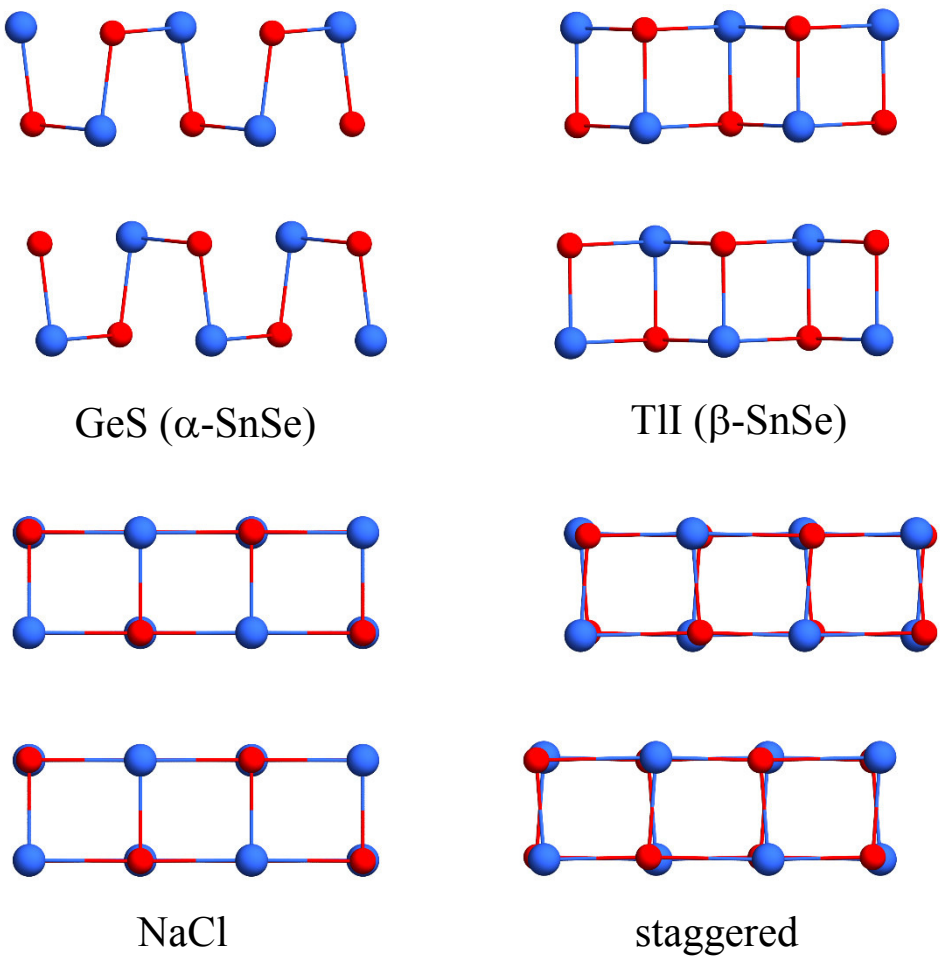


**Figure 10.6.** Relaxed structures of two SnSe bilayers for the different polytypes used in the DFT calculations viewed along the [010] axis. Sn atoms are blue and Se atoms are red.

structure type where the lattice parameters change significantly with thickness. The lattice parameters trend towards the calculated lattice parameters of the bulk structure ($a$ = 4.56 Å, $b$ = 4.21 Å) as thickness is increased. This is consistent with DFT calculations published elsewhere,[53] and with the experimental data for SnSe layers as a function of thickness in ferecrystals with a variety of dichalcogenide layers.[54] The lattice parameters for the GeS and NaCl-structured bulk structures are larger than the experimental bulk and thin film lattice parameters (GeS: $a$ = 4.450 Å, $b$ = 4.153 Å[21]; NaCl: $a$ = 5.99 Å[55]) as expected from GGA. The calculated bulk TlI structure on the other hand has smaller lattice parameters ($a$ = 4.301 Å, $b$ = 11.808 Å, $c$ = 4.293 Å) than experimentally determined in bulk β-SnSe ($a$ = 4.310 Å, $b$ = 11.705 Å, $c$ = 4.318 Å, 825 K).[21] The staggered variety converges to a rectangular basal plane, even when started as a square lattice. The structure distorts along the $c$-axis where the Se atoms are distorted into the vacuum region with respect to the Sn atoms, except for the single bilayer where

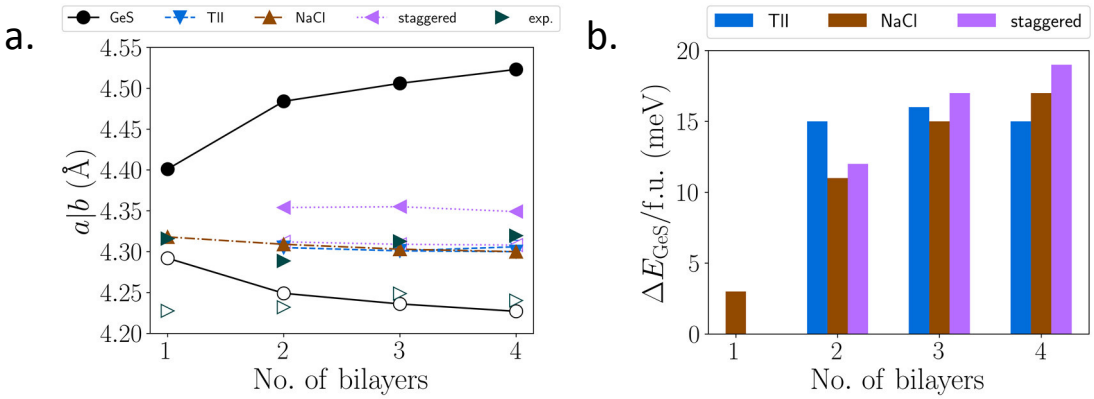


**Figure 10.7.** (a) In-plane lattice parameters of the different SnSe polymorphs as a function of the number of bilayers. Closed markers and open markers denote $a$-axis and $b$-axis lattice parameters, respectively. The lattice parameters for the NaCl and staggered structures are given in their primitive lattices. The experimental lattice parameters for $m$ = 1 were normalized to give a better comparison to the lattice parameters for $m$ > 1. (b) Total energy differences per formula unit $\Delta E_{GeS}$ of the polymorphs with respect to the GeS (α-SnSe) structure as a function of the number of bilayers.

the Sn atoms are distorted into the vacuum region. The degree of distortion increases with increasing number of bilayers from 0.01 Å to 0.04 Å. Layers adjacent to the vacuum region show larger distortions than layers adjacent to other SnSe layers. The trends of the distortion with *m* are consistent with structural refinements of SnSe layers observed in $[(SnSe)_{1+\square}]_m[(NbSe_2)]_n$ and $[(SnSe_{1+\delta})]_m[(MoSe_2)]_n$,[48,56] although the magnitude is smaller than observed experimentally.

Total energies were also calculated for each of the structures for different thicknesses as shown in Figure 10.7b. The GeS structure has the lowest total energy per formula unit (f.u.) for all investigated numbers of bilayers. The TlI structure is 15 – 17 meV/f.u. higher in energy than GeS, and this energy difference is nearly independent of the number of bilayers. The energy differences to the NaCl structure and its staggered derivative systematically increase relative to the GeS structure as the SnSe thickness is increased. However, for one bilayer the energy difference between the GeS and the NaCl structure is only 3 meV/f.u., indicating that both structures are almost equally stable. It is known that in ferecrystals, compounds with SnSe monolayers can, depending on the adjacent transition metal dichalcogenide, adopt square (V, Mo, Ta) or rectangular (Ti, Nb) basal planes.[54] $[(SnSe)_{1+\delta}]_1TiSe_2$ is the lone example of samples grown with the modulated elemental reactants technique where epitaxy occurs, and this is a result of an accidental epitaxial relationship between SnSe and $TiSe_2$. To probe the energy penalty for creating the rectangularly distorted NaCl lattice, additional calculations were performed. Calculations with a rectangular NaCl starting structure lattice converged to a square structure. However, relaxing only the atomic positions and the in-plane lattice parameters while keeping the *a*/*b* ratio fixed at the experimentally

determined ratio yields a rectangular structure with a total energy that is only 3 meV/f.u. larger than the undistorted NaCl structure. The relaxed lattice parameters, 6.169 Å and 6.047 Å for the *a*-axis and the *b*-axis, respectively, are in good agreement with the experimental lattice parameters for $(SnSe)_{1.20}TiSe_2$. Any surface stabilization by forming a commensurate interface with the $TiSe_2$ layers is not included in these calculations, so the small energy difference in our calculations suggest that a single SnSe bilayer can easily distort to form a commensurate lattice with $TiSe_2$. However, additional interactions must be present that raise the energy of the GeS structure above the energy of the NaCl structure.

For $m > 1$, the energy of the NaCl structure per formula unit increases significantly, so it is not energetically favorable to achieve a lattice match with the $TiSe_2$ layers. Instead, the symmetry of the in-plane lattice is consistent with the GeS or TlI structure with a steadily increasing *a*-axis lattice parameter and a nearly constant *b*-axis lattice parameter. This behavior is consistent with the DFT results of GeS-structured SnSe layers, albeit with a much smaller slope. The values of the experimental lattice parameters on the other hand are more consistent with the TlI structure. The transition from the GeS to the TlI structure is second order, and the observed (100) reflection in the inplane diffraction pattern should be extinct in either structure, suggesting that neither structure describes the in-plane symmetry completely. The interactions with the $TiSe_2$ layers that raise the energy of the GeS structure above the energy of the NaCl structure for $m = 1$ could also raise the energy of the GeS structure to a value similar to the energy of the TlI structure for $m > 1$, resulting in a competition between these two structure types. It is thus plausible that the actual structure is an interpolation between the GeS and

the TlI structure, which cannot be determined conclusively without including the interactions between the $TiSe_2$ and SnSe layers. More experimental evidence is needed to determine the exact structure the SnSe layers adopt for $m = 2$ and 3. These results in combination with experimental data suggest that the interactions between the $TiSe_2$ and SnSe layers destabilize the GeS structure in a way to allow competition between the GeS and TlI structure.

The HAADF-STEM image of $[(SnSe)_{1.20}]_3TiSe_2$ (Figure 10.4d) shows SnSe layers that are inconsistent with any zone axis of a single SnSe structure, but instead appear to show a single β-SnSe unit cell with half of another β-SnSe unit cell shifted by half a lattice constant. DFT calculations on these shifted unit cells show only a small energy difference between them and undistorted β-SnSe with three bilayers (see Appendix C Figure C.6 and Table C.1). This suggests that there is little penalty to grow these layers with or without this defect, so the structure of SnSe with three bilayers may depend entirely on nucleation and growth kinetics

*Electrical Transport Properties*

The structural changes with thickness produce changes in the electronic structure, which will impact the trends in transport properties of these compounds. Temperature dependent resistivity data collected on the title compounds are shown in Figure 10.8. The resistivity of the $m = 2$, 3 and 4 compounds are all larger than the previously reported $m = 1$ compound.[40] The highest resistivity measured is for the $m = 2$ compound, with subsequent increases in $m$ resulting in lower resistivity. This behavior is opposite to that observed previously for $[(SnSe)_{1+\delta}]_mNbSe_2$, where an increase in the thickness of SnSe resulted in a systematic increase in resistivity.[44] This difference reflects the impact of

structural changes with thickness of the SnSe layer on the electronic properties of these materials. At low temperatures, the resistivity increases as temperature is decreased for all compounds, where the overall magnitude of this upturn decreases with increasing *m*. The increase in resistivity is not exponential as expected for a traditional semiconductor and is not pronounced enough to suggest a metal-insulator transition.[57] The much weaker temperature dependence is consistent with a metal or heavily doped semiconductor where carrier localization is occurring at low temperatures, but the possibility of the upturn being the result of a charge density wave in the $TiSe_2$ layer cannot be ruled out.[58,59]

Hall effect measurements (Figure 10.9) were collected to provide additional information about the electronic properties. For all compounds, the Hall coefficient changes only slightly with temperature in an approximately linear fashion, which is inconsistent with semiconducting behavior. This suggests the low temperature upturns in resistivity are caused by a change in mobility with temperature or a more complex two-

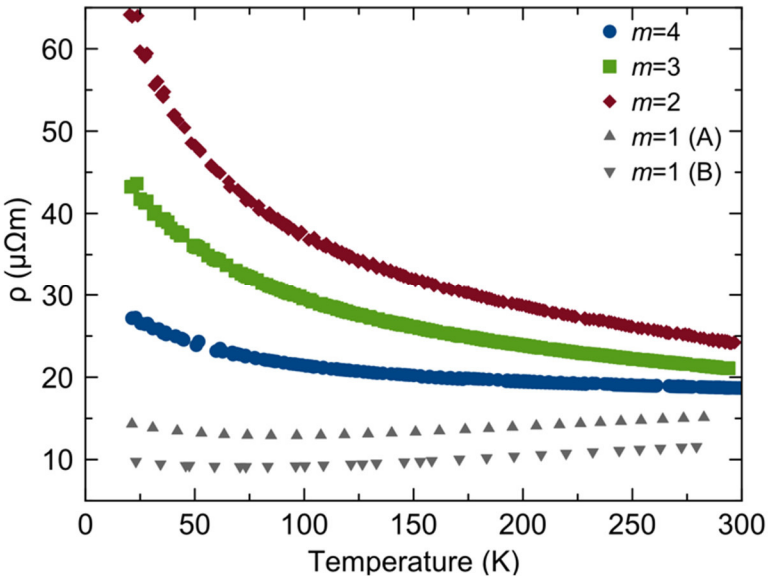


**Figure 10.8.** Temperature dependent resistivity measurements of the $[(SnSe)_{1+\delta}]_mTiSe_2$ compounds with $m = 1 – 4$. Measurements of two different $m = 1$ samples are plotted to show reproducibility of their behavior.

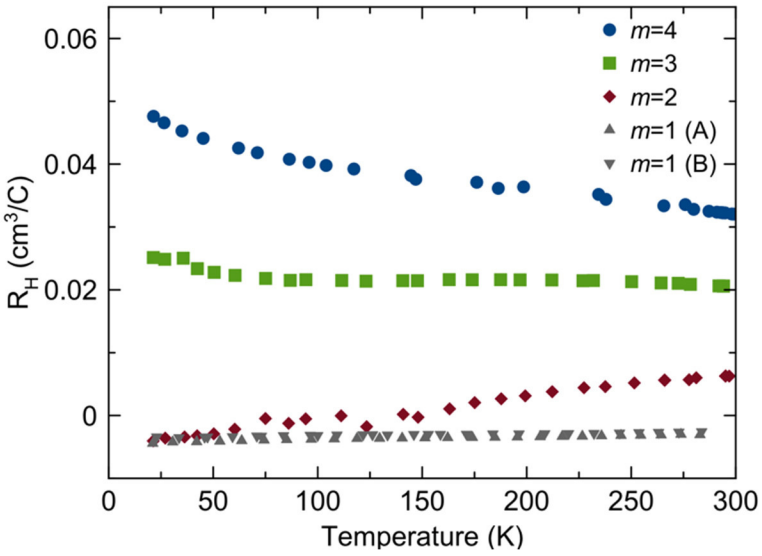


**Figure 10.9.** Temperature dependent Hall coefficients for $[(SnSe)_{1+\delta}]_mTiSe_2$ compounds.

carrier behavior. Surprisingly, the Hall coefficient varies systematically with *m* and changes sign as *m* is increased. The Hall coefficient for the *m* = 1 compound is negative and stays constant with temperature, as expected for a simple metal, indicating electrons are the majority carrier. The Hall coefficient for the *m* = 2 compound decreases as the temperature is lowered, switching sign at approximately 160 K, indicating a change in the majority carrier type from holes to electrons. The *m* = 3 compound has a positive Hall coefficient at all temperatures and the *m* = 4 compound has a larger positive Hall coefficient at all temperatures. The positive room temperature Hall coefficients suggest holes are the majority carriers. The changes in the magnitude of the Hall coefficient as *m* increases and as temperature is decreased, combined with the resistivity data discussed previously, suggests that the average carrier mobility significantly increases as *m* is increased and varies with temperature.

Room temperature Seebeck coefficients (α) were measured for all the compounds to gain more information about the change of carrier type as *m* and temperature are

varied. The results are summarized in Table 10.2. Like the Hall coefficient, the Seebeck coefficient also changes sign as *m* is increased. The sign of the Seebeck coefficient agrees with the sign of the Hall coefficient for *m* = 1, 3, 4, indicating agreement in majority carrier type. The *m* = 2 compound, however, displays a positive Hall coefficient and a negative Seebeck coefficient, which indicates that both carrier types contribute to the observed conductivity. This is consistent with the change in the Hall coefficient as a function of temperature. It is useful to compare this data to the analogous $[(PbSe)_{1+\delta}]_m[TiSe_2]_n$ compounds where *m* = *n*.[60] For all PbSe thicknesses, upturns in resistivity are observed at low temperatures, similar to those seen for the $[(SnSe)_{1+\delta}]_mTiSe_2$ (*m* = 2-4) compounds. Unlike the $[(SnSe)_{1+\delta}]_mTiSe_2$ compounds, the $[(PbSe)_{1+\delta}]_m[TiSe_2]_n$ compounds decrease in resistivity prior to the upturn. However, the $[(PbSe)_{1+\delta}]_m[TiSe_2]_n$ compounds do not display a change in the sign of the Hall coefficient or Seebeck coefficient with PbSe thickness as is seen with increasing SnSe thickness. A donor-acceptor behavior between the PbSe and $TiSe_2$ layers and subsequent establishment of a space-charge region near the interface was used to describe the transport in the the $[(PbSe)_{1+\delta}]_m[TiSe_2]_n$ compounds. In that case, the relative position of the Fermi level should remain unchanged as *m* and *n* are simultaneously increased. Here,

**Table 10.2.** Room temperature transport properties for $[(SnSe)_{1+\delta}]_mTiSe_2$ compounds.

| *m* | ρ (T = 295 K) (μΩm) | $R_H$ ($cm^3$/C) | α (μV/K) |
|---|---|---|---|
| 1 (A) | 15 | -0.0044 | -75 |
| 1 (B) | 12 | -0.0034 | -77 |
| 2 | 24 | 0.0064 | -28 |
| 3 | 21 | 0.0206 | 3 |
| 4 | 19 | 0.0322 | 22 |

since the amount of SnSe is increasing relative to $TiSe_2$, the position of the equilibrium Fermi level is changing with *m* along with the SnSe structure and convoluting the cause of the sign change in the Hall and Seebeck coefficients. However, the results within this work suggest the structural changes in SnSe should persist with increasing $TiSe_2$ layer thickness. Thus, an additional series of ferecrystals with simultaneously increasing *m* and *n* might be used to decouple whether the observed behavior is due to moving the Fermi level within a composite compound, or if it is due to a fundamental change in the band structure of the material, likely due to structural distortions within the SnSe or due to differences in surface and bulk states that become less prominent as *m* increases. For a better comparison to the $[(PbSe)_{1+\delta}]_m[TiSe_2]_n$ compounds and to understand the role of nanoarchitecture, studying a series of $[(PbSe)_{1+\delta}]_m[TiSe_2]_n$ where *m* is increased while *n* is held constant at 1 or a series of $[(SnSe)_{1+\delta}]_m[TiSe_2]_n$ where $m = n$ would be required.

Historically, the band structures of these compounds has been discussed under a rigid band approximation, with SnSe bands and $TiSe_2$ bands only slightly perturbed by the interface and the charge transfer between them.[61] However, the complex carrier properties in our compounds are inconsistent with that simple band model.[62–64] Since the DFT, XRD, and STEM data indicate that the structure of the SnSe constituent is changing with thickness, a rigid band model is certainly not appropriate. This complex electronic behavior agrees with the theoretical calculations on the structure of SnSe as a function of thickness. The complex variation of the structure and electrical properties indicate that these compounds cannot be thought of as simple composites where the properties of the individual constituents can be summed to obtain the properties of the intergrowth. Charge transfer is likely a function of structure and as the SnSe structures change with thickness,

there is no surprise that different carrier properties are observed. If this is the case, the unique temperature dependent electrical data could be a result of temperature dependent structural changes. Further studies are needed to correlate the temperature dependent transport properties to structural changes.

## X.4. Conclusions and Bridge

Three new $[(SnSe)_{1+\delta}]_mTiSe_2$ compounds were synthesized from modulated elemental reactants. Control of the nanoarchitecture by systematically increasing the number of SnSe layers in the repeating unit was observed via specular x-ray diffraction. As the SnSe block thickness is increased, the basal plane structure evolves from rectangular ($m$ = 1) to a structure that is related to orthorhombic GeS ($m$ = 4) with the $m$ = 2, 3 compounds having a nearly square variation. This evolution toward the bulk structure reflects that the energetic cost of distorting interior atoms to form an epitaxial interface with $TiSe_2$ increases with decreasing surface to volume ratio, which is consistent with DFT calculations.

For SnSe blocks with $m$ = 3, shear defects are observed within the same repeating unit. DFT calculations showed that the energies of different defect structures and the undistorted structure of β-SnSe are very close in energy, suggesting that the existence of these defects depend on nucleation and growth kinetics.

The compounds also display unexpectedly complex electrical properties, with resistivity decreasing as the thickness of the SnSe layer is increased, and the carrier type changing as $m$ and temperature are varied. The evolving structure and electrical properties suggest the interactions between constituents are complicated and the previously used models based on rigid bands and charge transfer between the constituents

is not appropriate for these compounds. Further investigations into this behavior are necessary to fully understand the cause of the upturn at low temperatures in the resistivity and the change in carrier type with increasing number of SnSe layers.

This chapter used DFT to explain the stabilities of different polytypes, but also revealed that ferecrystals do not behave as simple composites and that an isolated layer model has limitations in what it can describe. In Chapter XI, DFT is used to corroborate experimental evidence in BiSe-containing ferecrystals. Specifically the flexibility of its in-plane lattice will be discussed.

# CHAPTER XI

# STRUCTURAL CHANGES IN 2-D BISE BILAYERS AS *n* INCREASES IN $(BiSe)_{1+\delta}(NbSe_2)_n$ ($n$ = 1 – 4) HETEROSTRUCTURES

This chapter was previously published as Mitchson, G.; Hadland, E.; Göhler, F.; Wanke, M.; Esters, M.; Ditto, J.; Bigwood, E.; Ta, K.; Hennig, R. G.; Seyller, T.; Johnson, D. C. "Structural Changes in 2D BiSe Bilayers as *n* Increases in $(BiSe)_{1+\delta}(NbSe_2)_n$ ($n$ = 1−4) Heterostructures" *ACS Nano*, **2016**, *10*, 9489 – 9499. G.M. is the primary author of this publication. Co-author E.H. assisted with sample synthesis, characterization, and provided advice during writing of the manuscript. F.G., M.W., and T.S. contributed to the XPS data collection, analysis, and discussion. M.E. and R.G.H. performed the DFT calculations and provided general feedback of the manuscript. J.D. assisted with collection and analysis of the HAADF STEM images. E.B. and K.T. assisted with general data collection and analysis

## XI.1. Introduction

Heterostructures of mono- and few-layer films have recently captured significant scientific attention.[1,2] While most of the attention has been paid to heterostructures incorporating graphene,[3] other materials, such as boron nitride[4,5] and transition metal dichalcogenides,[6–8] are seeing increasing interest. Despite the increased interest, many challenges remain in overcoming synthetic hurdles and in understanding the structure and properties of low-dimensional materials.[9] Complicating this territory, simulations and experiments indicate that the structure and properties of low-dimensional materials can

be strongly affected by their local environment.[10–12] Understanding how and why low-dimensional materials respond to changes in their local environment will be critical to advance this field. The modulated elemental reactants (MER) technique is a means of making kinetically stable, turbostratically-disordered heterostructures.[13] The MER method does not require lattice matching or epitaxy between constituents, allowing the synthesis of designed heterostructures of varied composition and nanoarchitecture.[14–16] This synthetic flexibility readily permits investigations of how a constituent structure depends on layer thickness, the ratio of constituents, and the identity of adjacent layers.

Recently, we used the MER method to prepare a $(BiSe)_{1+\delta}NbSe_2$ heterostructure, which can also be called a turbostratically-disordered misfit compound.[17] The analogous Bi-containing fully-ordered crystalline misfit layer compounds have structures in which the two constituents are either fully commensurate, such as for $(BiS)_{1.07}TaS_2$ and $(BiSe)_{1.09}TaSe_2$,[18,19] or much closer to fully commensurate than what is usual for misfit layer compounds,[20] such as for $(BiS)_{1.11}NbS_2$.[21] This phenomenon was attributed to a structural modulation occurring in the BiX (X = S or Se) bilayers, first called by Wulff *et al.* an "antiphase boundary",[22] which is characterized by periodic Bi-Bi bonds and X-X non-bonds along one in-plane axis. The Bi-Bi bonds are about the same length as observed in Bi metal, 0.31 nm, while the X-X non-bonds are significantly longer than is typically observed in X-X bonding interactions. These compounds also exhibit minimal or no charge transfer between constituents, which was initially unexpected because trivalent rare earth cations do show significant charge transfer.[23] The lack of charge transfer resulted in speculation that electrons are localized in Bi-Bi bonds at the antiphase boundaries.[20] The correlation of the BiX structural modulation with commensurate

superlattices and the lack of charge transfer led Pervov and Makhonina to speculate that interlayer coherency strain may drive the formation of the structural modulation.[24] However, we still observed the characteristic structural modulation in the BiSe bilayers of the turbostratically-disordered $(BiSe)_{1+\delta}NbSe_2$ misfit layer compound, even though the turbostratic disorder results in minimal interlayer strain.[17] This suggests that the structural modulation may depend more on the local electronic environment of the BiSe bilayers than on a specific structural relationship between the constituent layers.

In this chapter, we test this idea by exploring whether changing the BiSe bilayer electronic environment through increased number of $NbSe_2$ layers in $(BiSe)_{1+\delta}(NbSe_2)_n$ heterostructures affects the structure of the BiSe bilayers and the resulting electrical transport properties. For consistency with prior misfit compound literature, we refer to the BiSe layers as "bilayers" because they are a two-atom thick double layer of atoms.[20] Although the $NbSe_2$ layers are three-atom thick sandwiches, we refer to them as "monolayers" as is currently done in the literature. Our specular and grazing incidence in-plane X-ray diffraction (XRD) measurements of the MER-prepared samples indicate that the BiSe bilayer basal plane structure converts from rectangular for $n = 1$ to square for $n = 2 – 4$, and the magnitude of puckering distortion in the (001) planes doubles. The structure of the BiSe bilayer is also influenced by the structure of the precursors (composition or layer thickness) for constant $n$, although the $c$-axis lattice parameter and value of $\delta$ are not significantly affected. Density-functional theory (DFT) calculations indicate there is only a small energy difference between the basal planes of BiSe being either square or rectangular. Small perturbations to the BiSe environment may then influence which structure is adopted in the kinetically trapped compound, providing a

rationale for the rectangular basal planes observed in the $n = 2 – 4$ compounds with different stoichiometry or layer thickness.

High-angle annular dark field scanning transmission electron microscopy (HAADF STEM) confirms that these compounds have the targeted layering schemes and are turbostratically disordered. The HAADF-STEM images also indicate that the frequency of the BiSe antiphase boundaries are significantly reduced in the $n = 2 – 4$ samples relative to the $n = 1$ sample. X-ray photoelectron spectra (XPS) show that the Bi peaks are broadened towards lower binding energies for the $n = 1$ compound relative to the $n = 2$ compound, suggesting a change in the Bi coordination environment for $n = 1$ relative to $n = 2$.

Electrical resistivity and Hall coefficients measured from 20 to 295 K indicate that the compounds exhibit p-type electrical conduction with minimal temperature dependence. Assuming a single rigid band model, the measured carrier concentrations at 50 K for the $n > 1$ compounds are greater than would be expected based on the measured carrier concentration for the $n = 1$ compound. Assuming the amount of doping is the same value and constant for the BiSe layer in the $n = 2 – 4$ compounds, the higher measured carrier concentrations suggest a reduction in the amount of charge transfer between constituents for the $n = 2 – 4$ compounds relative to the $n = 1$ compound, which correlates with the reduction in antiphase boundaries for $n > 1$. However, the structural refinements and XPS data indicate there is no significant change in interlayer charge transfer with $n$, suggesting the kinetic synthesis method employed may account for the variation in carrier concentration. Assuming no change in interlayer charge transfer then

implies that factors other than the presence of antiphase boundaries may play a role in determining interlayer interactions in BiSe-containing misfit compounds.

## XI.2. Methods

Precursors targeting $(BiSe)_{1+\delta}(NbSe_2)_n$ with $n = 1 – 4$ were prepared using the Modulated Elemental Reactants (MER) technique.[14,25] Similar deposition parameters to those previously reported[17] were used and total film thicknesses of 35-40 nm were obtained by varying the number of repeating layers deposited in the precursors. The precursors for each sample were deposited simultaneously onto cleaved Si pieces for diffraction experiments and quartz slides for electrical measurements. The precursors were annealed at 350 °C for 30 minutes in $N_2$ (< 1 ppm $O_2$).

The superlattice structure of each compound was assessed through specular X-ray reflectivity (XRR) and X-ray diffraction (XRD) scans acquired on a Bruker D8 Discover diffractometer with Cu $K_\alpha$ radiation. The compounds on both the quartz and silicon substrates were confirmed to be the same using XRR and XRD. Rietveld refinements of the *c*-axis XRD scans on silicon substrates were performed using the Fullprof software package.[26] The in-plane structure of each sample was determined from grazing incidence XRD scans acquired using a Rigaku Smartlab diffractometer with Cu Kα radiation. The in-plane lattice parameters were determined from the reflection positions using least-squares regression in the WinCSD program.[27] The sample compositions were measured using a Rigaku ZSX-II X-ray fluorescence (XRF) instrument, which was calibrated for similar-thickness films containing a range of Bi, Nb, and Se contents by using standard thin film samples whose compositions were determined using electron probe microanalysis.[28]

Selected samples were also characterized via high angle annular dark field scanning transmission electron microscopy (HAADF STEM) using an aberration-corrected FEI Titan S/TEM operating at 300 keV at Pacific Northwest National Laboratory. Specimens for HAADF STEM imaging were prepared using an FEI Helios 600 DualBeam FIB/SEM instrument. A procedure was followed similar to the wedge-prep method described by Schaffer *et al.*,[29] with final thinning performed using 2 keV $Ga^+$ ions. Interplanar spacings were determined from HAADF images by Gaussian peak fitting intensity profiles from several off-zone axis repeat units and averaging the results.

X-ray photelectron spectroscopy (XPS) measurements were carried out in a UHV chamber at a pressure of $3 \times 10^{-9}$ mbar. Monochromated Al-$K_\alpha$ radiation (photon energy $h\nu = 1486.6$ eV) was provided by a SPECS XR 50 M X-ray source equipped with a SPECS FOCUS 500 crystal monochromator. For analysis and detection of the photoelectrons a SPECS Phoibos 150 MCD-9 hemispherical analyzer (HSA) with nine channeltrons was used. The binding energy was referenced to the Au 4f core level at 84.00 eV. Samples were cleaved under flow of nitrogen inside the loadlock of the XPS system and immediately transferred into the UHV analysis chamber. The temperature-dependent film resistivities and Hall coefficients were measured using the van der Pauw method.[30] The measurements were conducted using a custom-built, LabVIEW-controlled system with a He closed cycle cryostat capable of reaching 10 K.

Density functional theory (DFT) calculations on isolated BiSe slabs were performed using the Vienna ab initio simulation package (VASP).[31-34] Electron-ion interactions were described using the projector augmented wave (PAW) method.[35,36] A cutoff energy of 500 eV was used for the plane wave basis set. For the exchange and

correlation, the local density approximation (LDA)[37] and the generalized gradient approximation (GGA) of Perdew-Burke-Ernzerhof (PBE)[38] were employed. In order to minimize interactions between periodic images, a vacuum spacing of 30 Å was included between single BiSe-bilayers. Brillouin zone integration was carried out with the Monkhorst-Pack method,[39] using a 15 × 15 × 1 k-point mesh, which was sufficient to converge total energies within less than 1 meV/atom. Spin orbit coupling (SOC) was included in all calculations. The $5d^{10}6s^26p^3$ states of Bi and the $3s^24p^4$ states of Se were treated as valence states.

## XI.3. Results and Discussion

*Structure of the $(BiSe)_{1+\delta}(NbSe_2)_n$ Compounds*

We made numerous precursors targeting the $n = 1 – 4$ compounds in the $(BiSe)_{1+\delta}(NbSe_2)_n$ series and annealed them using the same conditions that were determined to be optimal for the $n = 1$ compound.[17] After annealing the samples, their out-of-plane and in-plane structures were characterized using XRD and their compositions measured using XRF. Table 11.1 provides a summary of the structural and composition data obtained from selected samples. All reflections observed in the specular XRD patterns for all samples (11.1a) can be indexed as 00*l* reflections, indicating strong crystallographic alignment of the layers. The *c*-axis lattice parameter of the compounds increases by 0.640(1) nm with n, consistent with the expected repeat unit thickness increase by the addition of monolayers of $NbSe_2$.[40,41]

The strong crystallographic alignment of the compounds with the substrate is also supported by the grazing incidence in-plane XRD scans of the same samples (Table 11.1b), in which only (*hk*0) reflections from each constituent species are observed. The

**Table 11.1.** Summary table of X-ray diffraction and composition measurements from samples with $n = 1 - 4$, including the off-stoichiometry compounds.

| Sample | *n* | BiSe basal plane | BiSe *a* (Å) | BiSe *b* (Å) | $NbSe_2$ *a* (Å) | *c* (Å) | XRD $1 + \delta$ | XRF $n\times$Bi/Nb |
|---|---|---|---|---|---|---|---|---|
| 1a | 1 | Rect. | 4.45(2) | 4.23(2) | 3.47(1) | 12.081(1) | 1.11(2) | 1.12 |
| 2a | 2 | Square | 4.24(2) | | 3.47(1) | 18.447(1) | 1.16(2) | 1.14 |
| 2b | 2 | Rect. | 4.40(3) | 4.19(3) | 3.367(3) | 18.6(3) | 1.13(2) | 1.11 |
| 2c | 2 | Rect. | 4.47(2) | 4.22(2) | 3.47(3) | 18.58(2) | 1.11(3) | 0.95 |
| 3a | 3 | Square | 4.24(1) | | 3.47(1) | 24.682(2) | 1.16(1) | 1.13 |
| 3b | 3 | Rect. | 4.46(3) | 4.21(3) | 3.46(2) | 25.14(5) | 1.10(3) | 0.91 |
| 4a | 4 | Square | 4.24(1) | | 3.47(1) | 31.230(2) | 1.16(1) | 1.12 |

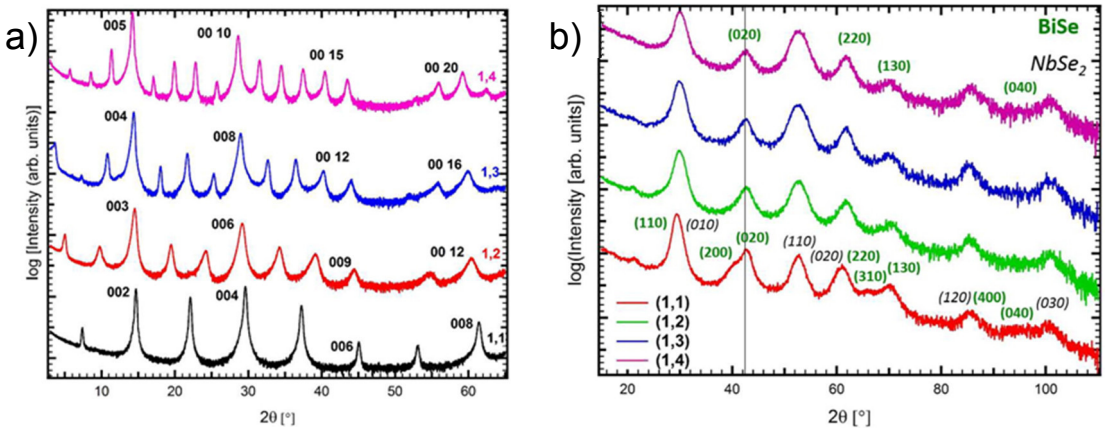


**Figure 11.1.** (a) Specular XRD patterns obtained for the samples in Table 11.1, labeled as "1, *n*". Select 00l reflections are labeled in the figure. (b) In-plane XRD scans of the samples in Table 11.1. The legend notation is (1, *n*), where n in the number of $NbSe_2$ monolayers in the c-axis of the unit cell. Reflections arising from planes in the BiSe bilayers are marked in bold green font, and those from planes in the $NbSe_2$ monolayers in italicized black font. The vertical black line at ~41° $2\theta$ highlights the disappearance of the (200) shoulder from the (020) reflection for samples with $n > 1$.

in-plane unit cell dimensions determined from the indexed in-plane data indicate the lattices of the components are entirely incommensurate, which is consistent with other compounds prepared using the modulated elemental reactants technique.[42] Surprisingly, the BiSe basal plane changes symmetry as $n$ is increased from 1 to 2, as is most easily seen in the loss of the (200) shoulder on the (020) BiSe reflection at approximately 42° 2$\theta$ (marked in Figure 11.1b by the vertical black line) and the loss of distinguishable (310) and (130) BiSe reflections at 66 and 70° 2$\theta$, respectively. Using the primitive setting described by Falmbigl *et al.*,[42] the BiSe $a$-axis lattice parameter for samples with $n > 1$ is approximately 0.424(1) nm. This is slightly greater than the 0.421 nm reported for bulk BiSe, but is within the range of $a$-axis lattice parameters reported for $Bi_xSe_y$ compounds for which $x \approx y$ (0.416 – 0.427 nm).[43] In BiSe-containing misfit layer compounds, the lattice parameters are typically reported in a face-centered setting. Converting literature values from a face centered setting to the primitive setting yields $a$-axis parameters ranging from 0.436(2) – 0.4464(4) nm and $b$-axis parameters ranging from 0.4220(1) to 0.441(3) for compounds with Ti, Nb, and Ta as the transition metal.[44-46] The change in symmetry with increasing thickness of $NbSe_2$ reported here is similar to what was observed by Otero-Diaz and coworkers,[47] who made $(BiS)_{1+\delta}(NbS_2)_n$ misfit compounds with $n$ = 1, 2, or 3. They observed a change in the in-plane structure in the BiS bilayers from orthorhombic for $n$ = 1 to monoclinic for $n$ = 2, but did not further refine the structure of their compounds. In the only other set of BiSe-containing turbostratically disordered misfit compounds reported, the $(BiSe)_{1+\delta}(TiSe_2)_n$ series, the basal plane was rectangular for all compounds with $a$ = 0.456 nm and $b$ = 0.424 nm.[48,49]

The $NbSe_2$ in-plane structure does not significantly change as the value of *n* is increased, even though the BiSe symmetry changes. The $NbSe_2$ *a*-axis lattice parameter for all of the samples was around 0.347(1) nm, consistent with the 0.346(1) nm reported by Alemayehu *et al.* for the $(SnSe)_{1.16}(NbSe_2)_n$ series of turbostratically disordered misfit compounds.[41] We observe a broadening of the $NbSe_2$ (110) reflections as n increases, which may be due to a reduction in $NbSe_2$ crystallite size with increasing n, also observed by Alemayehu and coworkers.[41] The reduction in BiSe basal plane area from $n = 1$ to $n = 2$, 3, and 4 leads to a larger misfit ratio, 1.16(1), than was reported for the $n = 1$ misfit compound.[17,45]

During synthesis of the compounds reported here, we also observed experimental evidence that the BiSe bilayer structure depends on the compound stoichiometry. Compounds with $n \times$ Bi/Nb atomic ratios less than the desired 1.10 maintained rectangular basal planes as *n* was increased beyond 1 (see Figure D.1 in Appendix D and Table 11.1). Despite being significantly off-stoichiometry in some cases, these compounds formed with structural misfit ratios close to 1.10, indicating that there must be either inclusions or extra layers distributed throughout the samples.[50,51] An $n = 2$ compound with the right stoichiometric ratio of Bi to Nb, but too thick of precursor layers, also formed with a rectangular BiSe basal plane with a misfit ratio of 1.13(2), intermediate between the on- and off-stoichiometry compounds. These results suggest that the BiSe bilayers may be able to accommodate an excess or deficiency of material by forming a rectangular structure

To gain structural information about the position of atomic planes along the *c*-axis of the on-stoichiometry compounds as *n* increased across the rectangular to square

transition, we conducted Rietveld refinements of the specular diffraction scans. Figure D.2 and Tables D.1 and D.2 in Appendix D contain the refinement plots and summary tables of the refinement statistics. The refinement results are illustrated schematically in Figure 11.2 and are consistent with the layered structures installed in the precursors. As is typical for misfit layered compounds, the BiSe bilayers are distorted from an ideal rock salt structure such that the Bi and Se planes are no longer coincident with one another on the (001) faces of the bilayer. This distortion is commonly referred to as a "puckering" effect and is typically on the order of 20 - 60 pm.[52] In the $n = 1$ heterostructure, the puckering distortion is 27(2) pm, consistent with the 29 nm reported by Petříček *et al.*[19] and Zhou *et al.*[45] for the crystalline $(BiSe)_{1.09}NbSe_2$ misfit layer compound. Just as the in-plane structures change when n increases from 1 to 2, the puckering distortion is also different for the $n = 2 – 4$ heterostructures, doubling in magnitude to approximately 52 pm. The spacing between planes of Bi atoms in the BiSe bilayer is the same in all 4 compounds, approximately 0.3 nm, so the increase in puckering effectively pushes the inner planes of Se atoms closer together. This also decreases the intra layer Bi-Se distance along the *c*-axis by 23 pm, suggesting a stronger

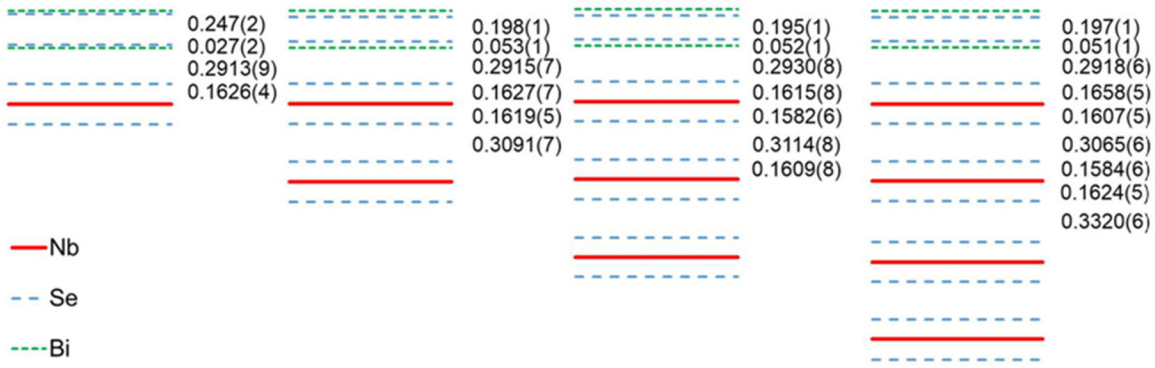


**Figure 11.2.** Schematic illustration of Rietveld refinement results showing *c*-axis atomic plane spacings (drawn to scale). The dashed blue lines represent planes of Se atoms; the solid red lines are planes of Nb atoms, and the dashed green lines are planes of Bi atoms. The dimensions to the right of each schematic are given in nanometers.

bonding interaction between these atoms. The interlayer gap distance between the BiSe and $NbSe_2$ layers is maintained at approximately 0.292(1) nm for all of the compounds. The constant interlayer gap distance suggests a consistent magnitude of interaction between the two constituents despite the structural changes.[23]

Structural changes also occur within the blocks of $NbSe_2$ layers as $n$ is increased due to the asymmetric environment along the the $c$-axis. In bulk 2H-$NbSe_2$, the layer environment is symmetric and the Se – Nb interplanar spacing within a monolayer is 0.1666 nm.[53] In the $(BiSe)_{1+\delta}(NbSe_2)_n$ compounds, the interplanar Se-Nb distance ranges between 0.158-0.166 nm, and for the $n$ = 3 and 4 compounds the Se – Nb interplanar spacing is asymmetric about the Nb planes. For the $n$ = 3 compound, the Se – Nb plane spacing adjacent to the BiSe constituent, is 0.161(1) nm while the distance to the Se plane on the other side of the Nb plane is 0.158(1) nm. For the $n$ = 4 compound, the Se – Nb plane spacing adjacent to the BiSe constituent is 0.166(1) nm while the the inner Se – Nb plane spacing is 0.161(1) nm. The asymmetry reverses for the inner pair of $NbSe_2$ layers in the $n$ = 4 compound, with the outer plane spacing 0.158(1) nm vs 0.162(1) nm for the inner plane spacing. Asymmetries have been reported previously, with Auriel and co-workers[54] reporting significantly larger asymmetries in the Se – Nb spacings in the $(PbSe)_{1.12}(NbSe_2)_2$ misfit layer compound. The van der Waals gap between $NbSe_2$ layers increases with increased distance from the BiSe layers, reaching a maximum of 0.332 nm between the middle two $NbSe_2$ layers in the $n$ = 4 compound. This is significantly larger than the interlayer gap distance, 0.2939 nm, between $NbSe_2$ layers in the bulk 2H polytype.[53] The increased interlayer gap distance between adjacent $NbSe_2$ layers suggests

that the presence of BiSe perturbs the adjacent $NbSe_2$ monolayer, influencing its structure and relationship with the other $NbSe_2$ layers.

To further probe the structure of the title compounds, HAADF STEM images of the samples with $n$ = 2, 3, and 4, and are shown in Figure 11.3. The images provide confirmation of the layering schemes for each sample determined from the XRD data: single BiSe bilayers interleaved with n $NbSe_2$ layers. The images also indicate the presence of turbostratic disordering of the layers, with different layers having different crystallographic orientations, characteristic of compounds prepared using the MER technique.[15] In addition to the turbostratic disorder occurring from layers of one

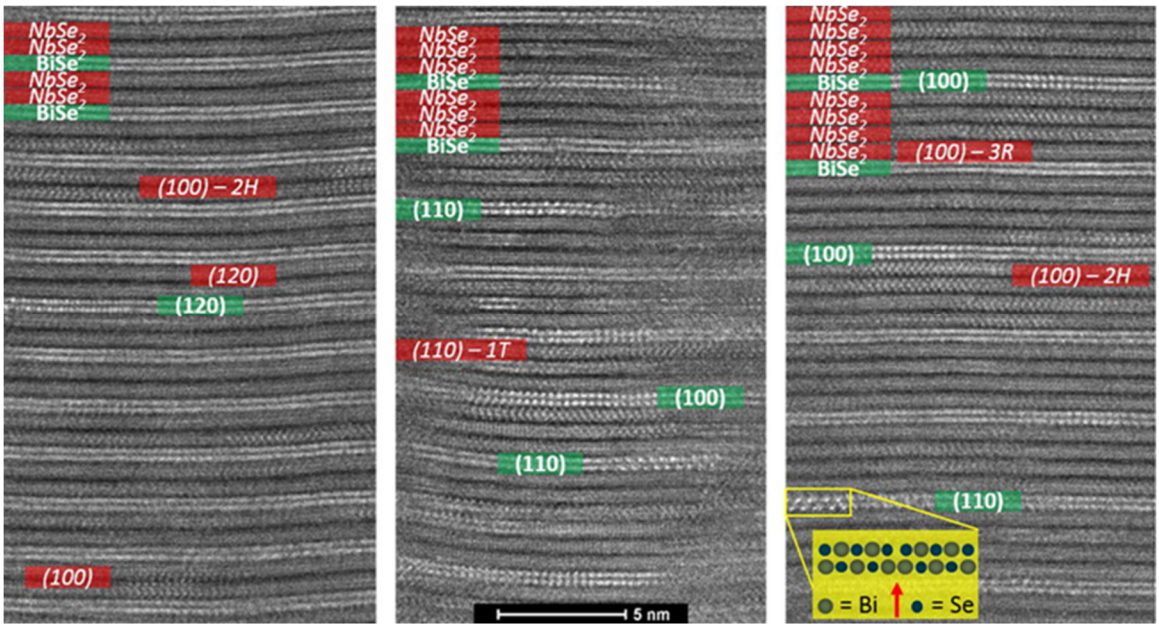


**Figure 11.3.** Representative HAADF-STEM images from $(BiSe)_{1+\delta}(NbSe_2)_n$ samples with $n$ = 2, 3, and 4 from left to right. All images have the same magnification represented by the scale bar in the center panel. Brighter regions correspond to increased scattering of the primary beam, primarily due to greater effective atomic mass in that area. Thus, the Bi-containing layers (labeled with bold text in green boxes) appear brighter than the Nb-containing layers (labeled with italic text in red boxes). Selected zone axes (relative to a face-centered setting) are labeled for several of the layers. The small inset in the right panel shows a schematic depiction of an antiphase boundary (indicated by the red arrow) observed in a BiSe bilayer oriented along the [110] zone axis for the $n$ = 4 sample.

constituent to layers of the other, disorder is also present from monolayer to monolayer within the $NbSe_2$ layer blocks of the $n$ = 3 and 4 samples. $NbSe_2$ is known to form multiple polytypes,[40] and this stacking disorder is consistent with reports of other MER-prepared films containing compounds with trigonal prismatically coordinated transition metals that form 2H polytypes.[41,55] Consistent with the global structure of the compounds determined from the Rietveld refinements discussed earlier, the HAADF-STEM determined spacing between Nb planes (0.64(2) nm in the $n$ = 3 compound) is greater than the spacing between the Nb and Bi planes (0.44(1) nm in the $n$ = 3 compound). Within error, this difference is the same as the 0.176 nm difference determined from the Rietveld refinement of the same sample and supports the hypothesis that the BiSe layer's interaction with the adjacent $NbSe_2$ monolayer influences its structure and its relationship with the other $NbSe_2$ layers.

The HAADF STEM images provide insight into the frequency of the antiphase boundaries in the BiSe bilayer, which cannot be determined from *hk*0 in-plane XRD scans. The antiphase boundaries are visible in [110] zone axis-oriented grains (relative to a face-centered lattice for consistency with prior literature reports), shown schematically in the rightmost panel of Figure 11.3.[54] In the $n$ = 1 samples, approximately 75% of the resolved [110]-oriented BiSe grains contained antiphase boundaries. In the n = 2, 3, and 4 samples, the rate of antiphase boundary occurrence dropped to roughly 5-15%. This decrease in the occurrence of antiphase boundaries correlates with the structural changes observed using XRD techniques.

*X-ray Photoelectron Spectroscopy Analysis*

The drastic reduction in antiphase boundaries observed in the HAADF STEM images and the structural changes determined from XRD suggest that the Bi bonding environment is different in samples with $n = 1$ relative to those with $n = 2$ or larger. To probe the electronic states directly, XPS measurements were made. The small changes in the peak shape of the Se and Nb spectra (see Figure D.3 in Appendix D) can be attributed to a change in the ratio of Se bound in $NbSe_2$ relative to Se bound in BiSe and a change of the environment of the $NbSe_2$-layers (no longer symmetrical) on increasing $n$ from 1 to 2. There are more significant changes in the Bi spectra. Since the Bi 4f doublet overlaps with the Se 3p doublet, we focused our analysis on the Bi 5d doublet (Figure 11.4). Both peaks show a broadening towards lower binding energies for $n = 1$ relative to $n = 2$, consistent with an increase in the number of Bi atoms having Bi-Bi bonds relative to Bi-

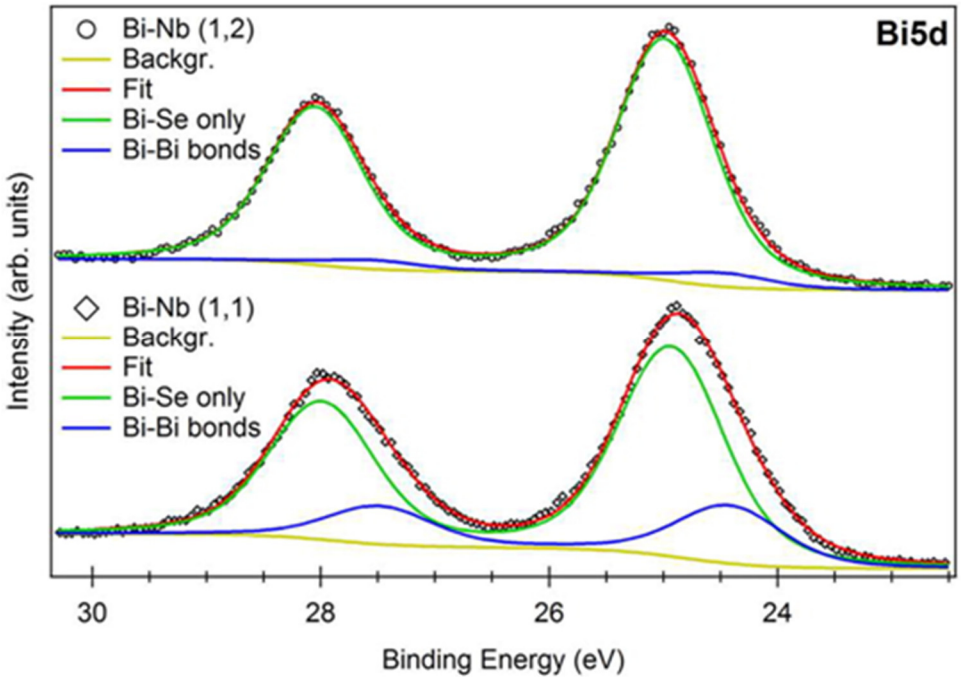


**Figure 11.4.** Bi 5d core level spectra of the $n = 1$ (bottom) and $n = 2$ (top) compounds. The spectra were fitted using two Voigt doublets.

Se bonds in the $n = 1$ compound (see Figure D.4 in Appendix D). In order to analyze the spectra in more detail, they were both fitted with two doublets consisting of two Voigt lines separated by the spin-orbit coupling, which amounts to 3.06 eV, and a branching ratio of 0.65. The Lorentzian broadening was 0.44 eV for all components. The fitted Gaussian widths were around 0.86 ± 0.10 eV. As a boundary condition, the Gaussian width of the peaks was kept roughly the same for both spectra. A Shirley background was used. Two components of identical peak shape were used for fitting each doublet. The binding energy of the Bi $5d_{3/2}$ component representing Bi atoms in Bi-Se bonds (green) is the same within error for both compounds, 24.93 eV in the $n = 1$ compound and 24.99 eV for $n = 2$. These values are greater than our binding energy measurement of elemental bismuth (23.88 eV, which is within the 23.4-24.3 eV range of literature values).[56] The component assigned to the atoms at the antiphase boundary (with Bi-Bi bonds, blue) is also the same within error for both the $n = 1$ and $n = 2$ compounds, shifted by 0.51 eV towards lower binding energies.

In a very simplified approximation, assuming only simple initial state effects, we can estimate the expected chemical shift to be 1/5 of the energy difference between elemental bismuth and BiSe, as one of the 5 Bi-Se bonds is substituted by a Bi-Bi bond. This yields an estimated expected shift of 0.22 eV (= (24.99-23.88)/5), which is less than what we experimentally observe. Although this seems to indicate that the observed shift of 0.51 eV is not only caused by simple initial state effects, it goes in the correct direction. Moreover, the ratio of the area of each doublet used to fit the spectra divided by the total area provides an estimate of the percentage of atoms with Bi-Bi bonds ($A_{Bi\text{-}Bi}$ / $A_{total}$). We estimate 22% Bi atoms are involved in Bi-Bi bonds in the $n = 1$ compound and

**Table 11.2.** Summary statistics for the HAADF STEM image analysis of $n > 1$ compounds. "ABs" stands for antiphase boundaries. The [110] zone axis orientation is relative to an fcc lattice.

| *n* | no. of [110] grains with ABs | no. of [110] grains without ABs | % of [110] grains with ABs |
|---|---|---|---|
| 2 | 6 | 21 | 22 |
| 3 | 6 | 33 | 15 |
| 4 | 2 | 41 | 5 |

5% in the $n = 2$ compound. This agrees with the analysis of the HAADF-STEM images (see Table 11.2), which also indicated a drastically reduced number of grains containing antiphase boundaries (and thus number of Bi atoms involved in Bi–Bi bonds) upon increasing *n* from 1 to 2.

*Electrical Transport Properties*

The structural changes caused by increasing n influence the electrical transport properties of the compounds as well. The measured temperature-dependent in-plane electrical resistivity of samples 1a, 2a, 3a, and 4a are plotted in Figure 11.5. The resistivity of all of the samples are a factor of 2-3 higher than for previously measured $[(SnSe)_{1+\delta}]_1(NbSe_2)_n$ compounds and similarly have only a weak temperature dependence.[41] For the $n = 1$ compound, the resistivity increases slightly with decreasing temperature. For the $n > 1$ compounds, the resistivity initially decreases slightly with decreasing temperature, then increases as the temperature is decreased below about 150 K. The increase in resistivity at low temperatures is typical for turbostratically-disordered misfit compounds and has been attributed to carrier localization.[47,48] The magnitude of the resistivity does not vary systematically as *n* is changed, but drops

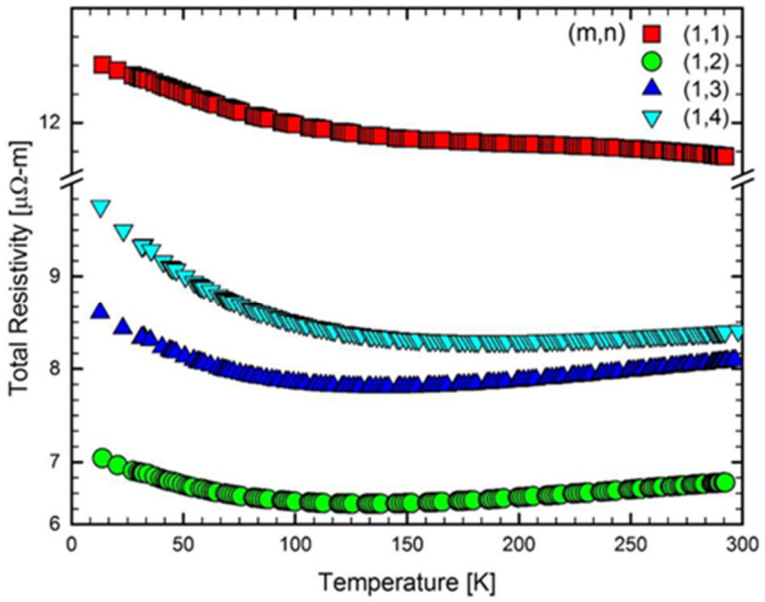


**Figure 11.5.** Temperature-dependent electrical resistivity measurements for the $n = 1 - 4$ samples.

approximately in half as $n$ is increased from 1 to 2 and then increases slightly as $n$ is increased to 3 and then again to 4. Assuming the $NbSe_2$ layers are responsible for the majority of charge carrier conduction, as found for $[(SnSe)_{1+\delta}]_m(NbSe_2)_n$ and $[(PbSe)_{1+\delta}]_m(NbSe_2)_n$ compounds, this result is counterintuitive. Conductivity suppression due to charge density wave formation is predicted to occur for monolayer $NbSe_2$ relative to the bulk.[59] This effect could explain the decreased resistivity in the $n = 2$ compound relative to $n = 1$, but the magnitude of suppression here is much smaller than would be expected were that the case. Petříček and co-workers[19] suggested that the antiphase boundaries in Bi-containing misfit compounds stabilized the Bi in the BiSe bilayers as a mixture of $Bi^0$ and $Bi^{3+}$, leading to less charge transfer than expected if all the Bi atoms were trivalent. For the compounds with $n > 1$, for which far fewer antiphase boundaries are present, we might then expect to see more charge transfer leading to p-type carrier depletion and increased resistivity of the $NbSe_2$ layers. However, resistivity also depends

on the carrier mobility. Alemayehu *et al.*[41] found that increasing $n$ in $(SnSe)_{1.16}(NbSe_2)_n$ misfit compounds decreased the carrier mobility and suggested this was caused by both decreased grain sizes and disruption of polytypic order in the $NbSe_2$ layers. The HAADF STEM images for the samples with $n = 3$ and 4 (Figure 11.2) indicate the presence of multiple $NbSe_2$ layer stacking arrangements within each $NbSe_2$ block, suggesting that the increased resistivity for the $n = 3$ and 4 compounds might also result from a mix of polytypes and small grain sizes decreasing mobility. We also note that both the *c*-axis structural refinements and the HAADF STEM images revealed increased gap distances between adjacent $NbSe_2$ layers relative to bulk $NbSe_2$, suggesting less interaction between layers than would be expected. However, increased charge transfer from BiSe due to fewer antiphase boundaries could also explain the resistivity data.

In order to determine whether changes in the carrier concentration or in the carrier mobility are the cause of the resistivity changes, we measured the temperature-dependent Hall coefficients (Figure 11.6). The Hall coefficients for all samples are positive, suggesting p-type majority charge carriers consistent with conduction through the $NbSe_2$ layers, as was previously observed in other $NbSe_2$-containing misfit compounds.[41,52,60] The Hall coefficients decrease systematically as n increases. For the compounds with $n = 2 – 4$, the room temperature Hall coefficients are similar to bulk $NbSe_2$, $4 – 5 \times 10^{-4}$ $cm^3/C$),[61] but the $n = 1$ compound's Hall coefficient is a factor of 2 larger. The Hall coefficients also increase slightly with decreasing temperature, suggesting that the carrier concentration decreases as the temperature decreases.

The systematic change in Hall coefficient with m and n has been reported previously in $[(SnSe)_{1+\delta}]_m(NbSe_2)_n$ and $[(PbSe)_{1+\delta}]_m(NbSe_2)_n$ ferecrystals[41,52,60] and has

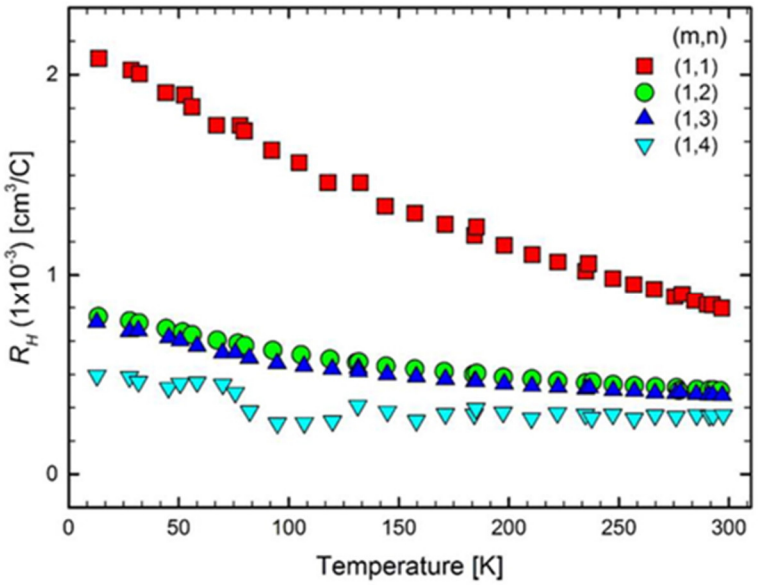


**Figure 11.6.** Hall coefficients measured as a function of temperature for samples with $n = 1 - 4$. The scatter in the $n = 4$ sample measurements may have been due to thermal fluctuations during the measurement.

been explained via charge donation from the monochalcogenide bilayers to the $NbSe_2$ layers. In bulk $NbSe_2$, the Nb $d_{z^2}$ conduction band is half-filled, leading to approximately one hole per Nb atom.[61] If the monochalcogenide donates electrons to $NbSe_2$, then the number of holes should decrease as the thickness of the monochalcogenide ($m$) increases holding $n$ constant and increase as the thickness of the dichalcogenide ($n$) increases holding $m$ constant. Assuming a single rigid parabolic band model is valid at 50 K where thermally activated defects may provide less contribution to the measured Hall coefficient, the Hall coefficient and structural data can be used to calculate that there are 0.41, 0.85, 0.81, and 1.14 $h^+$/Nb atom as n increases from 1 to 4. For the $n = 1$ sample, the carrier concentration is about 0.5 holes/Nb, which in this model suggests that the BiSe bilayer donates about 0.5 electrons per Nb atom. If the amount of charge donated by BiSe remains constant, the $n = 2$ compound is predicted to have 0.75 holes per Nb, as there are twice the number of $NbSe_2$ layers to divide the electrons from BiSe. Experimentally, the

calculated carrier concentration for the $n = 2$ compound, 0.85 per Nb, is larger than that of the $n = 1$ compound and is close to the predicted value. Based on the $n = 1$ compound, a carrier concentration of about 0.83 holes per Nb is predicted for the $n = 3$ compound, which is again close to the experimental value of 0.81. The predicted value for the carrier concentration of the $n = 4$ compound is 0.88 holes per Nb, while the experimental value, assuming a single band, is 1.14. Interlayer charge transfer from the BiSe constituent qualitatively explains the reduction in the $NbSe_2$ charge carrier concentration as holes are filled in by donated electrons. However, this is obviously a simplified picture as the charge donation would create holes in the BiSe layer that could also contribute to the conductivity and the rigid band interpretation ignores changes in the BiSe band structure as its structure changes.

Samples 1a - 4a were prepared from precursors with compositions and initial layer thicknesses close to that of the targeted heterostructure compounds, but these compounds form over a relatively wide range of composition ratios and thicknesses, and the electrical properties vary depending on the composition and structure of the initial precursor. An investigation of the electrical properties of multiple $n = 1$ compounds indicated that varying defect concentrations resulting from the kinetic synthesis of the compounds also causes variation in the absolute magnitude of the temperature dependent electrical transport measurements.[17] Other $n = 1$ samples with similar resistivity values showed variation in their Hall coefficients, indicating that mobility varies with carrier concentration. Some of the $n = 1$ compounds in the previous study have lower resistivity and Hall coefficient values than the $n = 1$ compound measured in this study, similar in magnitude to the $n = 3$ sample discussed above. This suggests that the changes in carrier

concentration we observe here as a function of varying the thickness of the $NbSe_2$ layer may be due in part to differences in defect concentrations between samples. Taken in conjunction with the refined c-axis structures of the compounds, which indicated a constant BiSe – $NbSe_2$ gap distance as n increased, and the lack of a significant shift between the Bi core levels for the $n = 1$ and $n = 2$ compounds, this suggests that there is no significant change in charge transfer with $n$. This is surprising given the large change in antiphase boundary frequency and the subsequently anticipated effect on interlayer charge transfer in these compounds.

*Flexibility of the BiSe Lattice*

Given the large variation in the structure of the BiSe layer observed experimentally, we carried out density-functional theory calculations using the local-density approximation (LDA) and the Perdew-Burke-Ernzerhof (PBE) generalized-gradient approximation for the exchange-correlation functional to determine the ground state of isolated BiSe bilayers. The results of calculations testing starting geometries with square and rectangular basal planes, excluding both puckering and antiphase boundaries, and allowing the atomic positions and in-plane lattice parameters to relax to find the most stable structure, are presented in Table 11.3. As the antiphase boundary crystal structure is not yet understood for these compounds, we seek only to understand the apparent structural flexibility of these layers through the calculations. The experimental in-plane lattice parameters are reproduced well by the LDA functional when a square starting geometry is used, whereas using the PBE functional leads to overestimated lattice parameters, as is common for generalized-gradient approximations. A striking difference is obvious when comparing the results with a rectangular starting geometry: LDA

**Table 11.3.** Results of structural relaxation calculations of the BiSe bilayer as a function of exchange-correlation (XC) functional and starting geometry. *d*(Bi-Bi) represent the *c*-axis distance distances between the Bi planes and *d*(Bi-Se) is the puckering distance. $E_{total}$ is the total energy after relaxation.

| XC functional | starting geometry | *a* (nm) | *b* (nm) | *d*(Bi-Bi) (nm) | *d*(Bi-Se) (pm) | $E_{total}$/f.u. (eV) |
|---|---|---|---|---|---|---|
| LDA | square | 0.422 | --- | 0.306 | 21 | -9.742 |
| | rectangular | 0.438 | 0.406 | 0.306 | 21 | -9.746 |
| PBE | square | 0.436 | --- | 0.303 | 16 | -8.540 |
| | rectangular | 0.439 | 0.433 | 0.303 | 16 | -8.539 |

converges to a rectangular basal plane in which the in-plane lattice parameters are underestimated, which is expected from LDA due to overbinding, while the PBE functional converges to an almost square basal plane geometry, for which the differences in *a* and *b* are likely within error. Even though puckering was not included in the starting geometries, the relaxed structures show out-of-plane distortions with Se puckering to the inside of the bilayer, as was observed experimentally. The puckering, given in Table 11.3 as *d*(Bi-Se), is virtually unaffected by the starting geometry and the choice of exchange-correlation functional, but differs from experimental results. While the theoretical distances between Bi and Se layers are close to the experimentally-determined 27(2) pm for n = 1, they are significantly smaller than the 52(2) pm observed experimentally for the $n = 2 – 4$ compounds. The large deviation suggests that interactions with the $NbSe_2$ layers contribute to the enhanced puckering within the BiSe bilayers.

Surprisingly, the calculated total energies, and thus the formation energies of the BiSe bilayers with either square or rectangular in plane structures are nearly degenerate and lie within only a few meV/formula unit, which may explain the ability of BiSe to form different lattice geometries. In order to investigate the flexibility of the BiSe lattice, calculations were performed over a range of starting in-plane lattice parameters. At each starting position, the lattice parameters were held fixed and only the ionic positions were allowed to relax. As discussed above, antiphase boundaries were not incorporated into the BiSe layer structure for these calculations. The total energy per formula unit relative to the minimum total energy is displayed in Figure 11.7 for calculations using (a) LDA and (b) PBE. The contour plots show that there is a wide range of lattice parameters where the difference in total energy is less than 5 meV/formula unit. Especially using PBE, there is a significant variation in the in-plane lattice parameters that are separated in energy by less than 2 meV/formula unit, which results from the fact that PBE functionals are much less localized than in LDA. These results suggest that a BiSe bilayer is quite flexible and can easily adopt many different lattice geometries such that even small

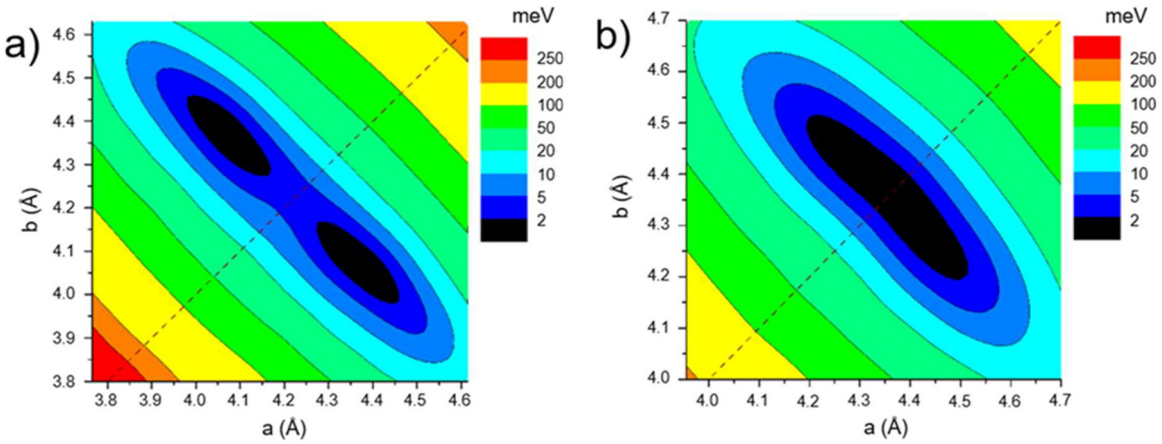


**Figure 11.7.** Total energies per formula unit relative to the minimum total energy for the (a) LDA and (b) PBE functional. The dashed lines represent square basal plane geometries and were added as a guide for the eye

changes in the local environment can affect the lattice geometry. These calculations, however, do not explain the experimental lattice parameters of the BiSe bilayers or why the experimental structures contain varying densities of antiphase boundaries when the fraction of $NbSe_2$ trilayers present in the repeat unit is changed. Clearly, more experiments and theoretical work are needed to better understand the effects of local environment on these kinds of 2D material structures.

The structural flexibility of the BiSe bilayers has interesting implications for the field of multiple-constituent heterostructure design. Although significant research effort has been devoted to understanding the properties of thin $Bi_2Se_3$ films (a promising topological insulator and thermoelectric material),[62-64] little is known about BiSe. As material properties are strongly dependent on structure, selection of an appropriate local environment could enable tuning of the BiSe bilayer properties. Furthermore, a 2D bridging layer could prove useful when trying to form epitaxial heterostructures out of structurally dissimilar materials. For example, a recent attempt to make an epitaxial heterostructure out of topologically insulating $Bi_2Se_3$ with superconducting $NbSe_2$ led to the unexpected formation of a BiSe interfacial layer.[65] We hypothesize that the structural flexibility of BiSe bilayers and their intentional incorporation during heterostructure design and synthesis may provide an important avenue to creating new 2D heterostructures out of lattice-mismatched materials.

## XI.4. Conclusions and Bridge

We prepared a series of turbostratically-disordered $(BiSe)_{1+\delta}(NbSe_2)_n$ heterostructures with $n$ = 1 - 4 using modulated elemental reactants and found that the structure of the BiSe bilayers changes from a rectangular basal plane when $n$ = 1 to a square basal plane when $n$ is greater than 1. The heterostructures formed over a significant range of compositions and thicknesses of the layers in of the precursors, with little variation in the diffraction patterns of the crystallographically aligned products or in the values of $\delta$, suggesting the variations in local composition were accommodated via inclusions. Neither constituent appears to have distorted its structure in order form an epitaxial relationship with the other. Surprisingly, the in-plane structure of the BiSe bilayer can change from square to rectangular as a result of variation in the precursor. Refinements of the *c*-axis structure of the same samples show a doubling in the degree of puckering in the BiSe bilayers when n is increased from 1 to 2, although the BiSe – $NbSe_2$ gap distance maintains a constant value. From HAADF STEM images, compounds with $n$ = 1 compound have significantly more antiphase boundaries in the BiSe bilayers than do the compounds with $n$ > 1. This is consistent with information from XPS measurements, which also indicate that there are more antiphase boundaries in the $n$ = 1 sample than there are in the $n$ = 2 sample. The temperature-dependent electrical resistivity of the samples decreases when increasing $n$ from 1 to 2, as expected, but then the resistivity increased for the $n$ = 3 and 4 samples. The magnitude of the resistivity change is also influenced by carrier mobility, which is decreased by disorder in the stacking arrangement of the conducting NbSe2 layers. The temperature-dependent Hall coefficients decreased significantly relative to $n$ = 1 for the $n$ > 1 samples, suggesting that

the number of holes increased significantly upon increasing *n* beyond 1. The increase is slightly greater than would be expected from assuming a constant amount of interlayer charge transfer and could be correlated with the reduction in antiphase boundary frequency. However, variability due to the kinetic synthesis method may also account for the variation in Hall coefficients, as the *c*-axis structure refinements and XPS data both suggest no significant changes in interlayer charge transfer occur. The results clearly demonstrate that modifying the local electronic environment of the BiSe bilayers by varying nanoarchitecture, composition, and layer thickness of the precursor result in substantial changes in the bilayer structure. DFT calculations suggest that the energy of the BiSe bilayer lattice is relatively insensitive to structural variations, so small changes in the local environment could easily change the ground state structure of the BiSe bilayers. However, more work is needed to understand how the structural changes impact layer interactions and material properties. The structural flexibility of the BiSe layer may be useful in designing multiple constituent heterostructures as an interlayer between structurally dissimilar constituents and is a new and unexpected emergent property of a 2D layer.

Chapter XII will expand the computational investigation of BiSe layers to multilayers and antiphase boundaries. It will be shown that Bi-Bi bonds are bonding, that BiSe layers become less stable with increasing thickness, and that charge is localized in antiphase boundaries.

# CHAPTER XII

# STABILITY OF BiSe LAYERS IN FERECRYSTALLINE COMPOUNDS

## XII.1. Introduction

Since the discovery of the three-dimensional (3D) topological insulator (TI) $Bi_xSb_{1-x}$,[1,2] compounds containing bismuth have received considerable scientific attention. 3D TIs have a bulk band gap, but also exhibit Dirac-like states near the surface and are predicted to exhibit quantum Hall (QH) and quantum spin Hall (QSH) effects, making them promising candidates for spintronic applications and as materials for quantum computations.[3–5] The bismuth chalcogenides $Bi_2X_3$ (X = Se, Te), were soon afterwards predicted and discovered to show Dirac surface states.[6,7]

The Bi-Se system is a phase-rich binary system where about a dozen stable binary phases have been characterized.[8] These phases can be described as an infinitely adaptive superlattice phase between elemental Bi and $Bi_2Se_3$ where Bi bilayers are stacked between $Bi_2Se_3$ quintuple layers as shown in Figure 12.1a for BiSe.[9,10] The stability of this structure type was attributed to bonding Bi-Bi bonds from the Bi bilayers.[11] The bismuth bilayers themselves are predicted to have QSH states,[12–17] which sparked experimental and theoretical investigations into the properties of $Bi_xSe_y$ compounds, predicting the monoselenide BiSe to be semimetallic or a weak topological insulator, depending on the spin-orbit coupling strength.[18,19]

When the dimensionality is reduced, however, BiSe adopts a very different structure. The misfit layer compounds $(BiX)_{1+\delta}[TX_2]_n$ (T = Ti, V, Cr, Nb, Ta; X = S, Se; $0.08 \leq \delta \leq 0.23$) contain single BiX bilayers that crystallize in a NaCl-like structure with

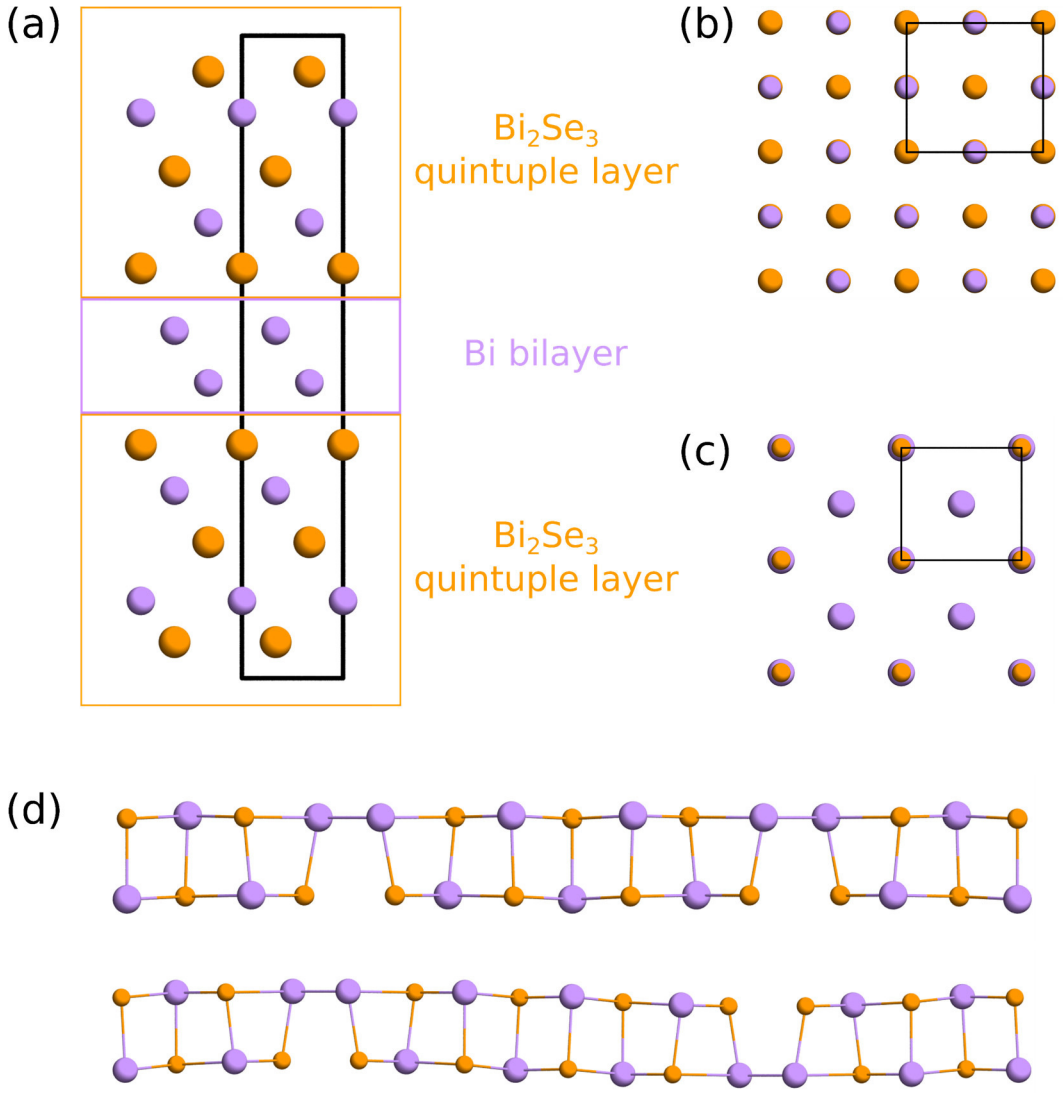


**Figure 12.1.** (a) Crystal structure of bulk BiSe as viewed along the *b*-axis. (b, c) Structure of the BiSe layer in (b) misfit layer compounds and (c) ferecrystals as viewed along the *c*-axis. (d) Two examples for an antiphase boundary (APB) as viewed along the *b*-axis. Bi atoms are purple, Se atoms are orange. The unit cell edges are shown in black.

a rectangular basal plane (Figure 12.1b).[20–31] For T = Cr, even a monoclinic distortion has been observed.[24] In ferecrystals (turbostratically disordered members of the misfit layer compound family), the axes of the transition metal dichalcogenide (TMD) and the BiSe layer are incommensurate. It was found that the symmetry of the basal plane is reduced compared to a NaCl-like lattice as shown in Figure 12.1c.[32–37] The lattice in ferecrystals

shows a large tolerance to distortions, and square and rectangular basal planes were found for the same family of compounds.[37] The synthesis of MLCs with thicker BiSe layers has been challenging. Heideman *et al.* noted that precursors deposited to form $[(BiSe)_{1+\delta}]_m[NbSe_2]_n$ ferecrystals did not form as a single phase film for $m = 2$ and 3.[38] For $4 \leq m \leq 15$, single phase superlattices were found, but no in-plane structures or compositions of the final compounds were reported. Lygo *et al.* (manuscript in preparation) found that attempting to synthesize $[(BiSe)_{1+\delta}]_2[TiSe_2]_2$ results in disproportionation into $[(BiSe)_{1+\delta}]_1[TiSe_2]_1$ and that a precursor designed to form $[(BiSe)_{1+\delta}]_3[TiSe_2]_3$ forms mixed phases containing $[(BiSe)_{1+\delta}]_1[TiSe_2]_1$ and $Bi_2Se_3$. A precursor designed to form $[(BiSe)_{1+\delta}]_3[TiSe_2]_1$ forms a single phase $[(BiSe)_{1+\delta}(Bi_2Se_3)_\gamma(BiSe)_{1+\delta}]_1[TiSe_2]_1$ superlattice.

Compared to SnX and PbX, BiX has an additional valence electron that it could donate to the TMD layer, and transport properties of MLCs containing $TiX_2$ point to the donation of one electron from the BiX to the $TiX_2$ layer.[23,31,33] However, MLCs containing $TaX_2$ and $NbX_2$ show the same electrical transport behavior as the SnX and PbX analogs, indicating that little or no charge transfer occurs.[22,39] It was found that for $TaX_2$ and $NbX_2$, the NaCl structure rearranges to periodic Bi-Bi pairings called antiphase boundaries (APBs) with modulation wavelengths of 34 – 38 Å. Examples of such APBs are shown in Figure 12.1d. It was hypothesized that they localize charge inside the BiX layer.[20,21,25,27]

For ferecrystals, APBs were found with all transition metals and even in alloyed BiSe layers such as in $[(Sn_{1-x}Bi_xSe)_{1+\delta}]_1[TSe_2]_1$ (T = Ti, Nb; $x \geq 0.5$).[34–37,40,41] The modulation wavelength varies considerably with different TMDs inside the ferecrystal

between 15 Å and 35 Å. Another difference between ferecrystals and MLCs is that APBs are not found in every BiSe layer. The abundance of APBs depends on the transition metal in the TMD but also on the TMD thickness where thicker TMD layers decrease the abundance of observed APBs.[37] Hadland *et al.* (manuscript in preparation) synthesized ferecrystals containing $MoSe_2$ where BiSe does not show APBs. Instead, $MoSe_2$ crystallizes in its octahedrally coordinated (1T) polytype alongside its trigonal prismatically coordinated (2H) polytype, whereas in other ferecrystals, the 2H polytype forms exclusively.

The diverse behavior of BiSe layers raises a host of questions about the stability of BiSe layers in ferecrystalline compounds, such as why ferecrystals with two BiSe bilayers are only metastable and why ferecrystals with three BiSe layers do not form at all. Moreover, the role and the properties of APBs needs to be explored, especially why different TMDs cause the formation of APBs with different periods and abundances.

This chapter will use density functional theory (DFT) to investigate some of these questions. First, it will be shown that Bi-Bi bonds stabilize the bulk BiSe compound whereas the NaCl structure has antibonding interactions at the Fermi level. Crystal orbital Hamilton population (COHP) analysis will then be used to show that BiSe layers in the structure found in ferecrystals will become more antibonding with increasing number of layers. It will also be shown that APBs stabilize the BiSe structure and localize charge with exactly one electron per Bi-Bi bond. This charge localization leads to a lower binding energy in XPS spectra. Electronic structure calculations on transition metal dichalcogenide (TMD) layers reveal different capabilities for accepting charge, which explains the different abundances of APBs in different ferecrystals.

## XII.2. Computational Methods

Density functional theory calculations were performed using the Vienna *ab initio* simulation package (VASP).[42–44] Within the generalized gradient approximation (GGA), functionals by Perdew, Burke, and Ernzerhof (PBE) were employed to describe exchange and correlation.[45] A cutoff energy of 500 eV and Γ-centered k-point grids with a density of at least 50 k-points per $Å^{-1}$ were used for all calculations.[46] Projector augmented wave (PAW) pseudopotentials were employed, considering the $5d^{10}6s^26p^3$ and $3s^23p^4$ electrons valence electrons for Bi and Se, respectively.[47,48] Spin-orbit coupling was introduced in all calculations. Self-consistency was achieved with an energy convergence of $10^{-6}$ eV. Atomic positions and lattice parameters were allowed to relax until the forces on the ions were below 0.0025 eV $Å^{-1}$.

For isolated layers, a vacuum spacing of at least 20 Å was used to minimize interactions between periodic images. Transition metal dichalcogenide monolayers were calculated using the HSE06 hybrid method of Heyd, Scuseria, and Ernzerhof with the standard exchange-mixing parameter $\alpha = 0.25$.[49]

Crystal Orbital Hamilton Populations (COHPs)[50] were calculated using the linear muffin-tin orbital atomic sphere approximation (LMTO-ASA) as implemented in the Stuttgart LMTO-ASA code.[51,52] Only bonds shorter than 4 Å were considered. For bulk structures, the results were cross-checked with projected COHPs (pCOHPs) as implemented in the Local-Orbital Basis Suite Towards Electronic-Structure Reconstruction (LOBSTER) code.[53–56] COHPs and band structures were plotted using a modified version of PYMATGEN.[57]

## XII.3. Results and Discussion

*Bulk BiSe*

Since the interactions between layers are of van-der-Waals type, PBE overestimates the *c*-axis lattice parameter in BiSe.[10] To account for these dispersion forces, the structure of BiSe (space group $P\bar{3}m1$, no. 164) was calculated using the van-der-Waals methods DFT-D2,[58] zero damping DFT-D3,[59] and DFT-D3 with Becke-Johnson (BJ) damping[60] by Grimme *et al.*, the van-der-Waals method by Tkatchenko and Scheffler (TS),[61,62] the PBE functional revised for solids (PBEsol),[63] and the local density approximation (LDA).[64] The results are summarized in Table 12.1 along with experimental values.[9–11] The value calculated for PBE without corrections has a larger *a*-axis lattice parameter and a smaller *c*-axis lattice parameter calculated by Lind *et al.* who did not include spin-orbit interactions, which is the reason for the deviations.[10] There is a

**Table 12.1.** Structural Parameters for bulk BiSe using different functionals. *a* and *c* are the *a*-axis and *c*-axis lattice parameters, respectively, and *V* is the volume of the unit cell.

| Functional | *a* (Å) | *c* (Å) | *c*/*a* | *V* (Å$^3$) |
|---|---|---|---|---|
| PBE | 4.281 | 23.673 | 5.530 | 376 |
| DFT-D2 | 4.284 | 22.614 | 5.279 | 359 |
| DFT-D3 | 4.267 | 22.760 | 5.334 | 359 |
| DFT-D3 BJ | 4.228 | 22.585 | 5.342 | 350 |
| TS | 4.284 | 22.606 | 5.277 | 359 |
| PBEsol | 4.218 | 22.551 | 5.347 | 347 |
| LDA | 4.191 | 22.214 | 5.300 | 338 |
| Experiments | 4.238(8) | 22.52(1) | 5.314 | 346.8(5) |
| | 4.2320(7) | 22.715(6) | 5.367 | 352.33(3) |
| | 4.212(1) | 22.942(8) | 5.447 | 352.5(2) |

wide range of experimental lattice parameters, especially with respect to the *c*-axis lattice parameter, which makes a comparison with DFT results challenging. PBEsol and the DFT-D3 method with zero or BJ damping reproduce the experimental values well. Of these functionals, DFT-D3 with BJ damping agrees best with the experimental unit cell volume and will thus be used for the remainder of this section.

Since ferecrystals and MLCs crystallize in a NaCl-like structure, bulk BiSe was also calculated in the NaCl (space group $Fm\bar{3}m$, no. 225) structure using standard PBE functionals. The calculated lattice parameter is 6.21 Å, which is larger than what was reported for thin films (5.99 Å).[65]

The band structures of BiSe in both structure types are shown in Figure 12.2a. In the NaCl ($Fm\bar{3}m$) structure type, BiSe is metallic with multiple Fermi level crossings along the high symmetry paths in the irreducible Brillouin zone. In the experimental structure, spin-orbit coupling opens small band gaps.[10,19] With 52 meV, the smallest band gap is 10 meV larger than reported by Majhi *et al.* who used uncorrected PBE and fixed the *c*-axis lattice parameter to an experimental value.[19] This difference is well within the error of the PBE functional.

To investigate the stability of each phase, crystal orbital Hamilton populations (COHPs) were calculated using the Stuttgart LMTO-ASA code,[51,52] which uses linear muffin-tin orbitals (LMTOs), and LOBSTER, which projects PAW wavefunctions onto localized orbitals,[53–56] and are shown in Figures 12.2b and c, respectively. Positive COHP values correspond to antibonding states (left hand side of the plot), negative values to bonding states (right hand side of the plot).

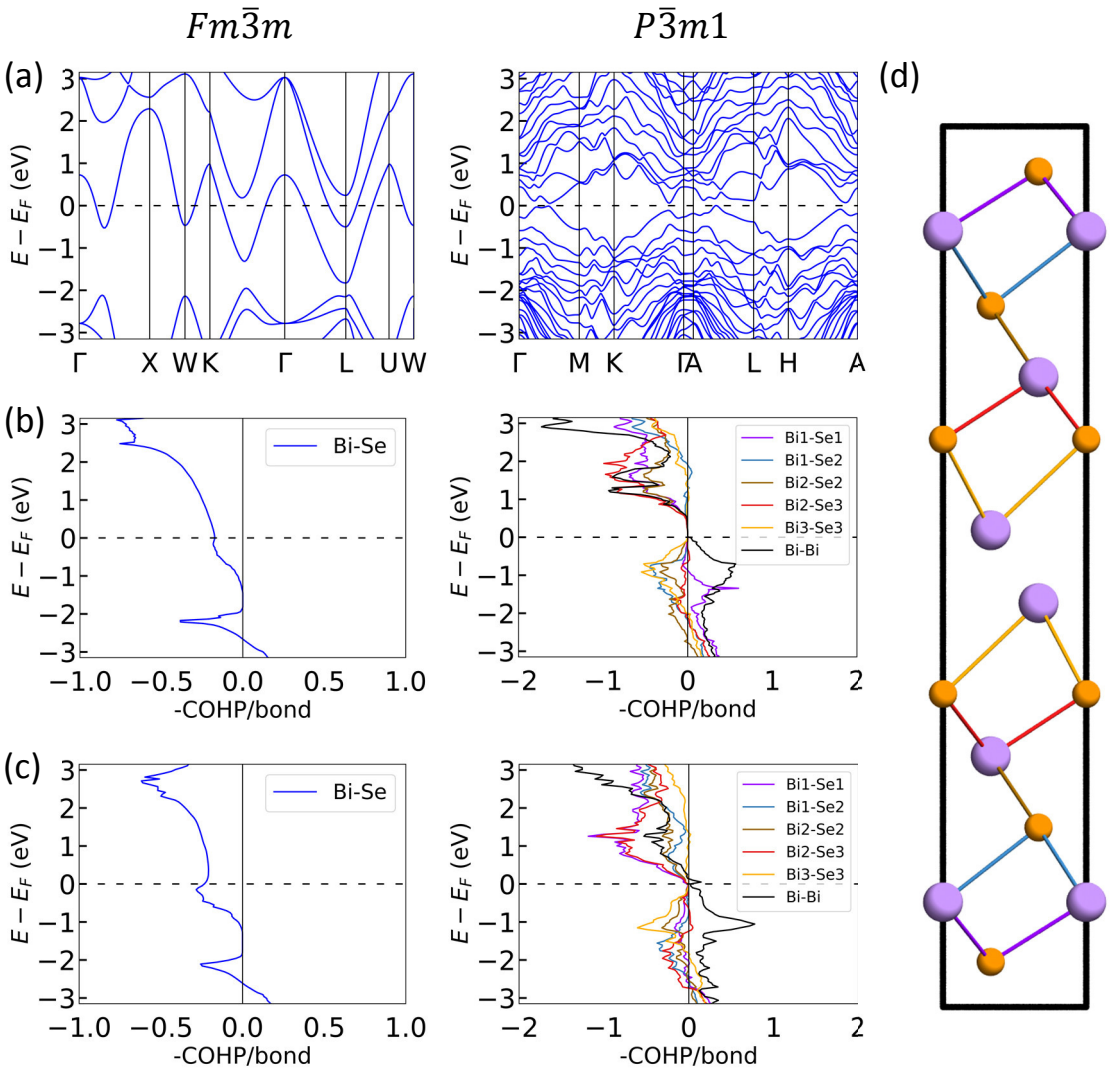


**Figure 12.2.** (a) Band structure of bulk BiSe in the $P\bar{3}m1$ and $Fm\bar{3}m$ structure. (b, c) COHP curves calculated with (b) LMTO and (c) LOBSTER. Negative values in the plot correspond to antibonding states, positive values bonding states. (d) BiSe structure with color coded Bi-Se bonds.

In the NaCl structure, the Bi-Se bonds have occupied antibonding states near the Fermi level $E_F$, making this structure type inherently unstable for Bi-Se. In the $P\bar{3}m1$ structure, there are no occupied states at the Fermi level (see Figures 12.2b and c on the right, and Figure 12.2d for a key of the different Bi–Se bonds). Below the Fermi level are mainly antibonding Bi–Se states, but also bonding Bi–Bi states stemming from the Bi bilayer. Table 12.2 shows the Bi–Se and Bi–Bi bonds and their integrated COHP values

**Table 12.2.** Bond length *d* and ICOHP values at the Fermi level $E_F$ calculated using the LMTO and the LOBSTER code.

| Bond | *d* (Å) | ICOHP($E_F$) LMTO (eV) | ICOHP($E_F$) LOBSTER (eV) |
|---|---|---|---|
| Bi1–Se1 | 2.88 | -1.28 | -2.18 |
| Bi1–Se2 | 3.10 | -0.48 | -1.14 |
| Bi2–Se2 | 3.05 | -0.74 | -1.30 |
| Bi2–Se3 | 2.92 | -1.19 | -1.97 |
| Bi3–Se3 | 3.38 | -0.05 | -0.48 |
| Bi–Bi | 3.07 | -1.72 | -2.24 |

at the Fermi level (ICOHP($E_F$)). More negative ICOHP($E_F$) values point to stronger bonds. The Bi–Se bond strength correlates with the length of the bond where the bond strength decreases with increasing bond length. The Bi–Bi bond is the strongest bond in the bulk phase. Crystal orbital overlap population analysis using extended Hückel methods by Gaudin *et al.* have identified the Bi–Bi bond as the stabilizing factor in the bulk structure.[11] This is corroborated by the COHP calculations presented here. On the other hand, these strong Bi–Bi bonds are missing in the NaCl structure, which explains why BiSe does not crystallize in this structure type, but adopts are more complex structure instead.

Both the LMTO and the LOBSTER code produce the same qualitative results. The shapes of the curves are similar, and the bonds have same order with respect to their ICOHP($E_F$) values. The different absolute values are due to the different basis sets that are used in each implementation, and do not change the qualitative interpretation of the COHP curves.

*Stability of BiSe Multilayers*

Structural relaxation calculations on two (1L), four (2L), six (3L), and eight (4L) BiSe bilayers were performed using the unit cell shown in Figure 12.1c.[32] The basal planes converged into a square lattice with a lattice parameter of 4.36 Å for all layer thicknesses. In ferecrystals, BiSe can adopt both square and rectangular basal planes, and it was shown that the total energy of the lattice is not very sensitive to distortions.[37]

Figure 12.3 shows the interplanar distances in the relaxed structures. In all layers, puckering can be observed where the Bi atoms are distorted to the outside of each bilayer. The puckering distance for the 1L structure, 0.14 Å, is smaller than the puckering found

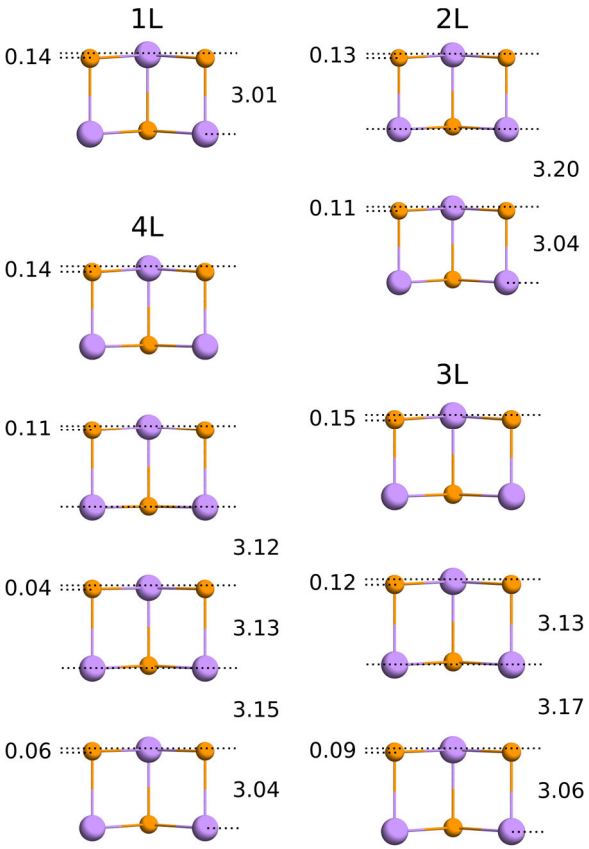


**Figure 12.3.** Relaxed structures of BiSe with two (1L), four (2L), six (3L), and eight (4L) bilayers as viewed along the *b*-axis. The inter-planar distances are given in Ångström. Bi atoms are purple, and Se atoms are orange.

in ferecrystals (0.19 – 0.51 Å).[34–37] One the other hand, the distance between two Bi planes (3.01 Å), agrees well with values found in ferecrystals (~ 3.0 Å). For the 2L structure, the distance between Bi planes inside a bilayer is much smaller than between bilayers with 3.04 Å and 3.20 Å, respectively. This difference decreases with increasing amount of bilayers, which was observed experimentally for PbSe in the ferecrystals $[(PbSe)_{1+\delta}]_m[MoSe_2]_n$.[66] If 2L, 3L, 4L structures of BiSe could be synthesized, the same trend would be expected. However, these structural trends provide no explanation for the different stabilities of the BiSe layers.

To gain further insight into the electronic structure of BiSe layers, orbital projected band structures were calculated and are shown in Figure 12.4. Like the NaCl bulk structure, BiSe layers are metallic with Fermi level crossings between all high

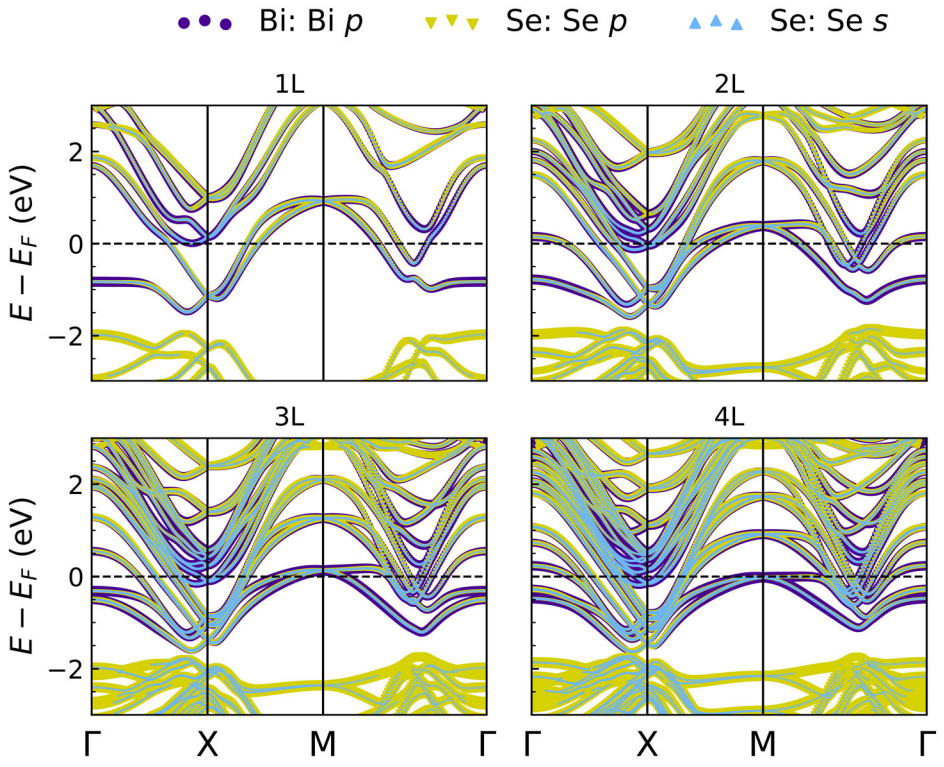


**Figure 12.4.** Orbital projected band structures of BiSe in the 1L, 2L, 3L, and 4L structures. The dot size is scaled by the contributions of each orbital.

symmetry points in the irreducible Brillouin zone. Between the Γ and the X point, the Bi *p* bands hybridize with both the Se *s* and *p* bands near the Fermi level. Near the M point, the Bi *p* bands hybridize with both Se bands for the 1L and 2L structures, whereas for the 3L and 4L structures, the bands Bi *p* bands near the Fermi level only hybridize with the Se *s* bands.

The changes in the band structure from adding additional bilayers are most pronounced near the Γ and the M point. At the Γ point, additional bands appear right above the Fermi level for the 2L and 4L structure, creating small Fermi surface hole pockets around the Γ point. At the M point, two bands become degenerate above the Fermi level. As the number of bilayers increases, these degenerate bands decrease in energy and in Se *p* character. For the 2L and 3L structures, Fermi surface pockets at the M point are created, which disappear again for the 4L structure as this band is just below the Fermi level. These degenerate bands may be responsible for dynamic instabilities through Fermi surface nesting, and future research needs to investigate the Fermi surface and phonon spectra of these layers. However, while these dynamic instabilities may predict stable distorted 2L and 3L structures, they would not explain why the 2L structure decomposes at low temperatures into 1L structures or why 3L structures do not form at all in ferecrystals and MLCs.

BiSe crystallizes in a NaCl-type structure in ferecrystals, and COHP calculations for bulk BiSe in the NaCl structure showed that there are occupied antibonding states near the Fermi level, which is why BiSe crystallizes in a trigonal structure instead. To investigate whether a similar rationale can be applied to the BiSe layers, COHPs were

calculated for each structure (see Figure 12.5). For 1L BiSe, there are occupied antibonding states at the Fermi level, similar to what was found for the NaCl-structured bulk. The out-of-plane Bi–Se bond is considerably weaker with ICOHP($E_F$) = -0.61 eV compared to the in-plane bond with ICOHP ($E_F$) = -2.05 eV. This means that isolated 1L BiSe is not stable. In order to form in ferecrystals and MLCs, it can donate charge to the transition metal dichalcogenide (TMD) layer until the Fermi level is outside the

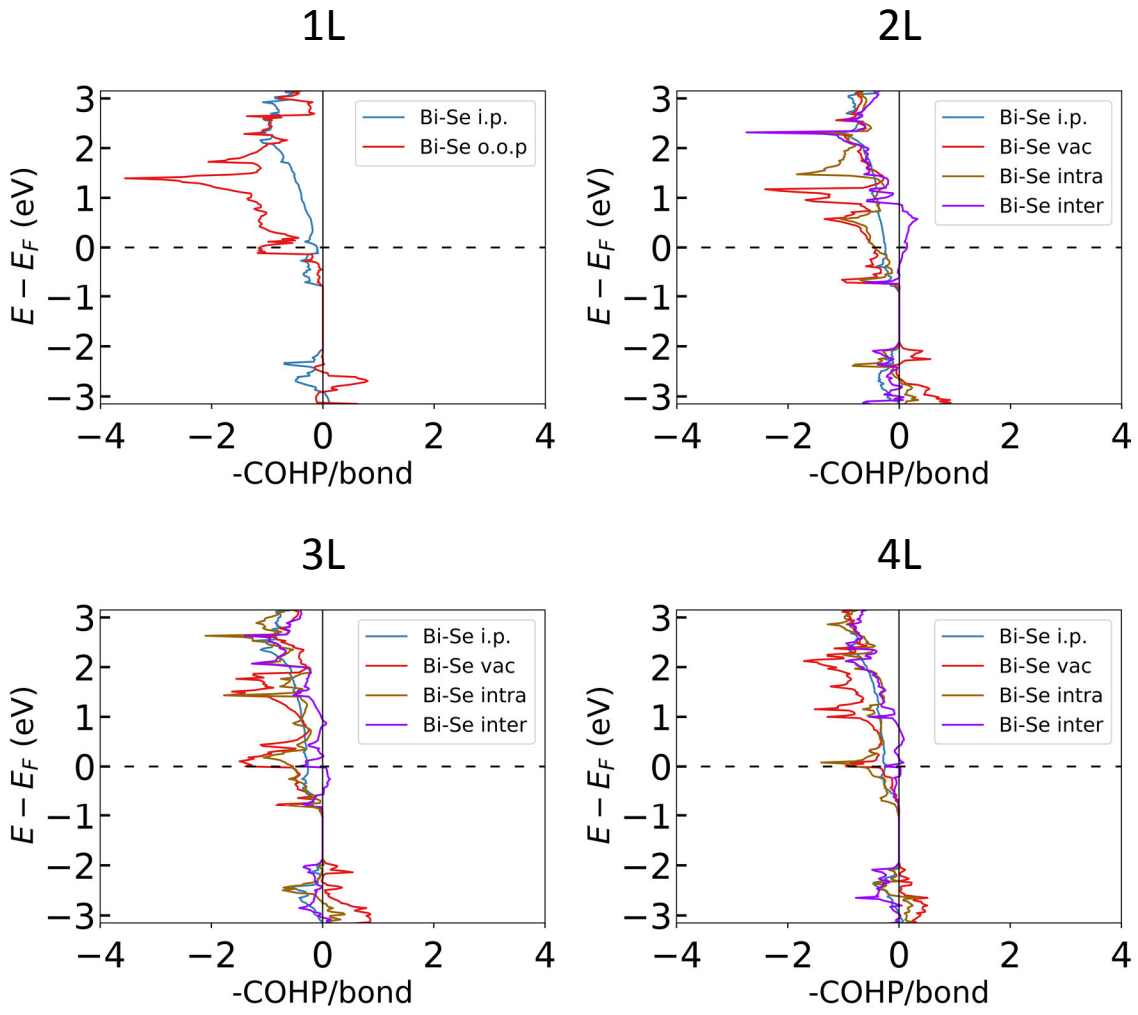


**Figure 12.5.** COHP curves for 1L, 2L, 3L, and 4L BiSe. "Bi-Se i.p." represents the in-plane Bi–Se bonds, "Bi-Se o.o.p." (1L) the out-of-plane Bi–Se bonds, and "Bi-Se vac" means the Bi–Se bond adjacent to the vacuum (2L – 4L). "Bi–Se intra" and "Bi–Se inter" are Bi–Se out-of-plane bonds inside and between BiSe bilayers, respectively. Only one representative COHP curve for each type of bond is shown.

antibonding regime (approximately 1 eV lower). The integrated density of states (DOS) calculated at $E_F$ and $E_F$ – 1 eV are 21 and 20 electrons per formula unit (f.u.), i.e. to depopulate the antibonding states at the Fermi level, BiSe would have to donate one electron to the TMD layer, which is what is found for MLCs containing $TiX_2$ layers.[23,31,33] Another possibility is to introduce Bi–Bi bonds, which are bonding in bulk BiSe, via antiphase boundaries.

2L, 3L, and 4L BiSe show four types of bonds with distinct COHPs: the in-plane Bi–Se bonds ("Bi-Se i.p."), the out-of-plane Bi–Se adjacent to the vacuum region ("Bi-Se vac"), out-of-plane Bi–Se bonds within a BiSe bilayer ("Bi-Se intra"), and out-of-plane Bi–Se bonds between BiSe bilayers ("Bi-Se inter"). Of these bonds, only the bonds between bilayers are not antibonding near $E_F$. The bond between bilayers is bonding for 2L BiSe, but it is also the bond with the lowest ICOHP($E_F$) value of -0.32 eV. With increasing number of bilayers, the distance between the bilayers decreases and the bonds between bilayers become increasingly less bonding at the Fermi level. This trend could point to why 2L BiSe forms at low temperature, but not 3L and 4L BiSe. However, since the bonding between the bilayers is so weak, 2L BiSe eventually disproportionates into two 1L BiSe layers.

In order to leave the antibonding regime, integrated DOS at $E_F$ and $E_F$ – 1eV show that each structure has to donate one electron per f.u. to leave the antibonding regime just like for 1L BiSe. There are two possible reasons for why this does not happen in ferecrystals and MLCs: first, the number of antibonding interactions is larger inside, say, 3L BiSe than inside 1L BiSe; second, and more likely, 3L BiSe would have to donate three electrons per $[(BiSe)_{1+\delta}]_3[TSe_2]_3$ unit, which would lead to highly charged

layers. Decomposing into $[(BiSe)_{1+\delta}]_1[TSe_2]_1$ on the other hand has a more even charge distribution and thus exerts less stress onto the crystal. $[(BiSe)_{1+\delta}]_2[TSe_2]_2$ would then present a middle ground where the electrostatic and thermal stress through annealing would lead to disproportionation into $[(BiSe)_{1+\delta}]_1[TSe_2]_1$. For $[(BiSe)_{1+\delta}]_3[TSe_2]_1$, there may not be enough acceptor states available to donate charge into, so the complex superlattice $[(BiSe)_{1+\delta}(Bi_2Se_3)_\gamma(BiSe)_{1+\delta}]_1[TSe_2]_1$ with APBs forms instead.

*Charge Localization in Antiphase Boundaries*

BiSe is known to form antiphase boundaries (APBs) in ferecrystals and misfit layer compounds (MLCs). Two examples of such APBs are shown in Figure 12.6. DFT calculations were performed on BiSe layers containing APBs with varied periodicity. In this chapter, the different APB structures will be distinguished using the number of Bi-Se pairings $\nu$ before each APB. Figure 12.6a shows an APB structure with five Bi-Se pairings ($\nu = 5$) and Figure 12.6b shows an APB structure with six Bi-Se pairings ($\nu = 6$)

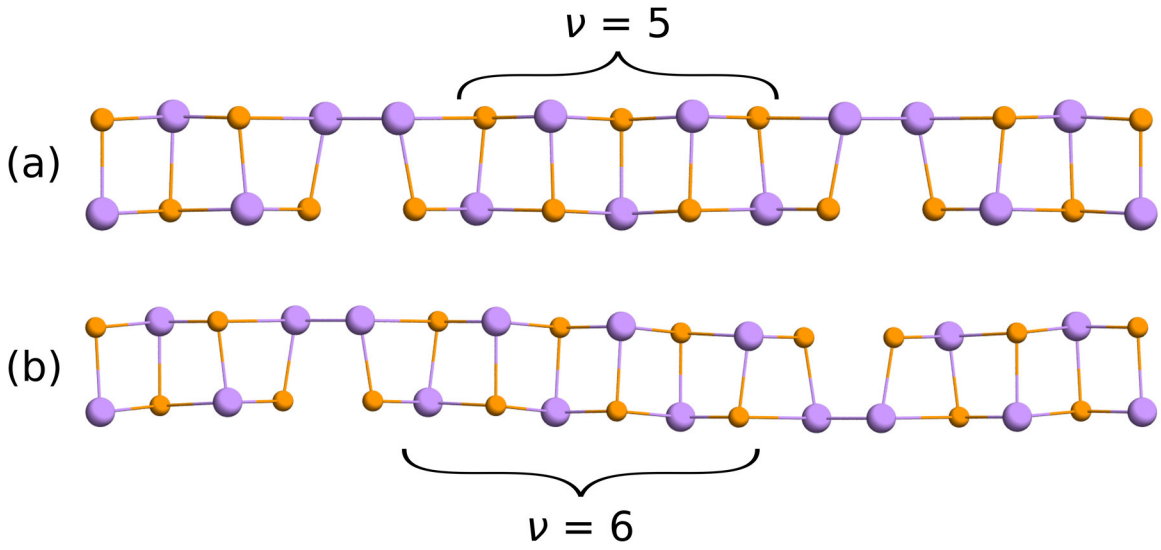


**Figure 12.6.** Two examples for an antiphase boundary (APB) as viewed along the *b*-axis with (a) 5 and (b) 6 Bi-Se pairings before each APB. Bi atoms are purple, Se atoms are orange.

before each APB. Figure 12.7a shows the energy difference $\Delta E_{1L}$ per formula unit between the APB structures and 1L BiSe as a function of $\nu$. The APB structure becomes more stable than a BiSe layer without APBs with $\nu = 2$. Maximum stabilization is

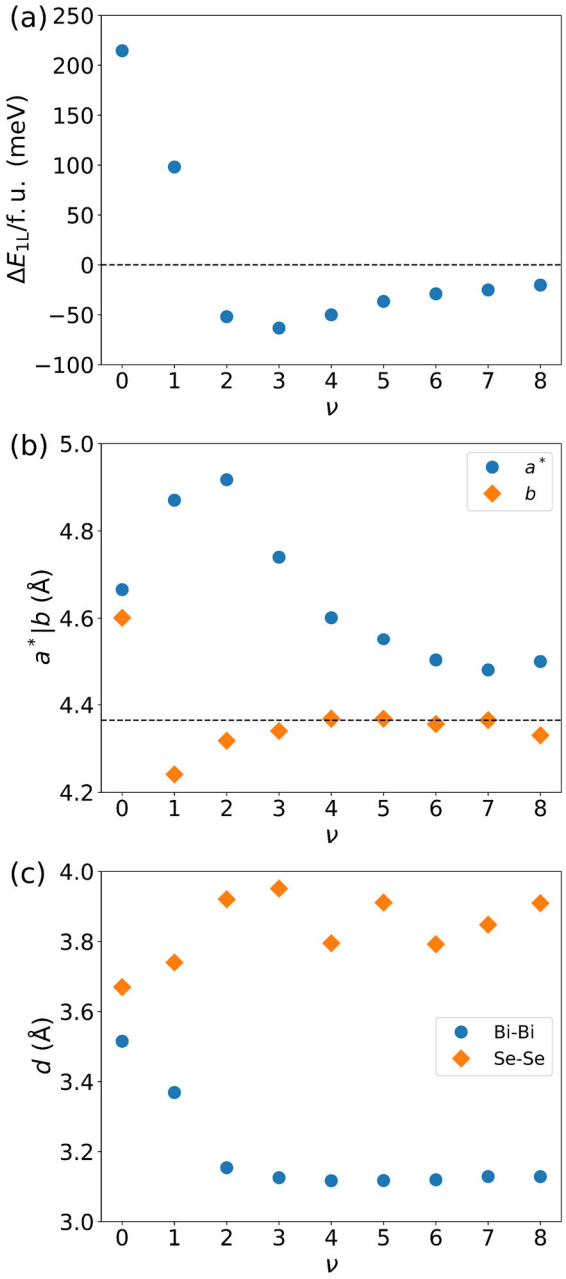


**Figure 12.7.** (a) Energy per formula unit relative to 1L BiSe without APBs. Points below the dashed line indicate that the APB structure is more stable. (b) Normalized *a*-axis parameter $a^*$ and *b*-axis parameter of the APB structures. The dashed line corresponds to the in-plane lattice parameter of 1L BiSe. (c) Bi-Bi and Se-Se distances *d* in the APB.

achieved at $\nu = 3$ with 63 meV/f.u. Afterwards, $\Delta E_{1L}$ increases and converges towards the energy of the structure without APBs as the APB density decreases. At $\nu = 8$, the energy difference is still 20 meV/f.u., which shows how important APBs are for the stability of the BiSe layers. Figure 12.7b shows the in-plane lattice parameters of the APB structures. The *a*-axis lattice parameters are normalized to one BiSe unit cell. For $\nu = 0$, the basal plane is nearly square with large lattice parameters of 9.33 Å ($a^* = 4.67$ Å) and 4.60 Å, respectively. $a^*$ increases until $\nu = 2$ and then asymptotically decreases to the lattice parameter of the structure without APBs. The *b*-axis lattice parameter drops to 4.24 Å at $\nu = 1$ and then asymptotically increases to the lattice parameter of 1L BiSe. The maximum for $a^*$ does not coincide with the minimum of $\Delta E_{1L}$, so the area of the basal plane is not strongly correlated to stability. Good correlation can be found with the Bi-Bi distances inside the APB (Figure 12.7c). For $\nu = 2$, $\Delta E_{1L}$ is below zero where the Bi-Bi distance is 3.13 Å and stays relatively constant afterwards. This distance is close to the distance found in Bi metal, which was also found in APBs in MLCs.[25] The Se-Se distances show some variation and do not seem to affect the stability of the structure.

A closer look at the APB structures reveals several in-plane distortions. The interatomic distances for the $\nu = 5$ APB structure are shown in Figure 12.8a. The Bi-Bi distance is 3.12 Å, and the Bi-Se distances adjacent to these Bi atoms is fairly large with 3.44 Å. The other Bi-Se distances in this layer are of average length with 2.97Å and 3.09 Å. The Se-Se distance in the layer below is very large with 3.91 Å. The adjacent Bi-Se distance is shorter than average with 2.89 Å, which is followed by a larger Bi-Se distance of 3.21 Å. The remaining distances are of average length with 3.02 Å. A bird's

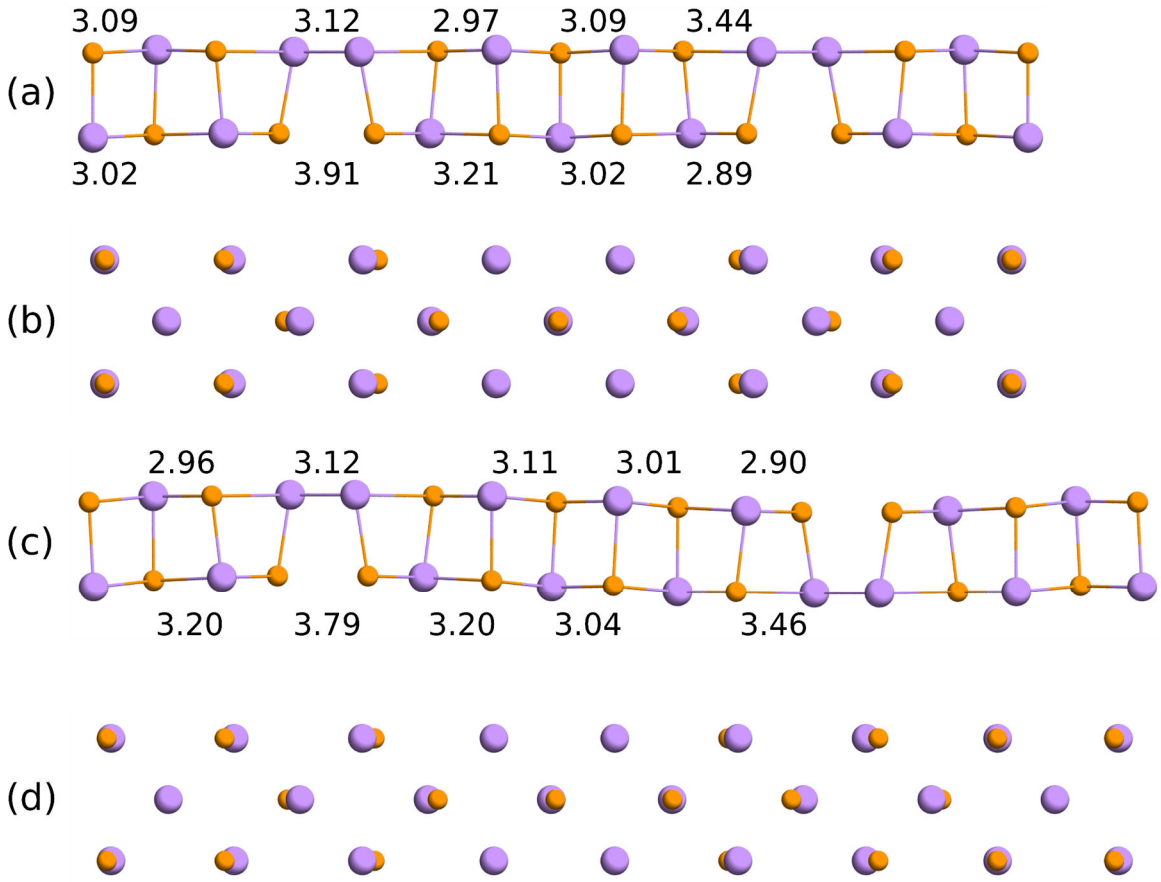


**Figure 12.8.** (a) $\nu = 5$ APB structure as viewed along the *b*-axis with interatomic distances given in Ångström. (b) The $\nu = 5$ structure as viewed along the *c*-axis. (c) $\nu = 6$ APB structure as viewed along the *b*-axis with interatomic distances given in Ångström. (d) The $\nu = 6$ structure as viewed along the *c*-axis.

eye view of the structure (Figure 12.8b) reveals the in-plane distortions in the APB structures, which are similar to the distortions observed in MLCs.[21,25,27,29] Despite these distortions, the APB structures exhibit symmetry with mirror planes along the *a*- and *b*-axes. The same structural trends can be observed for all APB structures. Another example is shown in Figures 12.8c and d for $\nu = 6$. APB structures with even $\nu$ also have a mirror plane along the *a*-axis and a $\bar{2}$ axis along the *b*-axis.

It was hypothesized that APBs localize charges that would otherwise be donated to the TMD layers in the ferecrystal and MLC.[20,21,25,27] Mitchson *et al.* conducted x-ray

photoelectron spectroscopy measurements on $[(BiSe)_{1+\delta}][NbSe_2]_n$ to investigate this hypothesis. It was found that for $n = 1$, the Bi 5d doublet attributed to Bi in the Bi-Se bonds broadened, and added an additional peak 0.51 eV lower in binding energy to the peak fit. This peak was assigned to the Bi atoms at the Bi-Bi atoms, but the observed shift in binding energy was larger than expected and it was concluded that initial state effects were not exclusively responsible for the shift. Using the initial state approximation as implemented in VASP,[67] DFT was used to determine the energy levels of the 5d electrons. The results are shown in Table 12.3. For most APBs, the binding energy shift agrees remarkably well with the experimentally determined shift of 0.51 eV. Transmission electron microscopy images on $[(BiSe)_{1+\delta}][NbSe_2]_n$ ferecrystals showed APBs with $\nu = 5$, for which the DFT calculations predict a binding energy shift of 0.54(4) eV towards lower binding energies, which is within the error of the experimental value. The shift can thus be traced back to initial state effects.

The shift to lower binding energies indicates an increased oxidation state of the Bi atoms. To analyze the charge distribution in APB structures, a Bader charge analysis was conducted on each structure.[68–70] As Table 12.3 shows, the Bi atoms inside the APBs contain more electrons than the Bi atoms outside the APBs. For $\nu \geq 2$, the number of electrons at the Bi atoms inside the APBs is 0.5 electrons higher than the at the Bi atoms outside the APBs, i.e. one electron is localized in each Bi–Bi bond. The number of electrons in these Bi atoms is close to 15, indicating nearly neutral Bi atoms, which is consistent with the Bi-Bi distances in the APBs being close to metallic bismuth. The Bader charges of the remaining Bi atoms and the Se atoms are close to the charges found for the BiSe layer without APBs (14.31 and 6.68, respectively), and indicate that Bi and

**Table 12.3.** Bi 5d core energy levels $E_{5d}^{Bi}$ of Bi atoms outside and inside an APB, binding energy shift $\Delta E_{Bi,5d}^{bind}$, and Bader charges of Bi atoms outside and inside the APB and of the Se atoms. Standard deviations are given where available. Neutral Bi atoms have 15 and neutral Se atoms 6 electrons with the employed pseudopotentials.

| ν | $E_{5d}^{Bi}$ (eV) no APB | $E_{5d}^{Bi}$ (eV) in APB | $\Delta E_{Bi,5d}^{bind}$ (eV) | Charge Bi no APB | Charge Bi APB | Charge Se |
|---|---|---|---|---|---|---|
| 1 | -25.51 | -25.20 | -0.31 | 14.15 | 14.56 | 6.57(2) |
| 2 | -25.61 | -24.99 | -0.61 | 14.09 | 14.65 | 6.62(6) |
| 3 | -25.59(4) | -24.98 | -0.61(4) | 14.15(1) | 14.67(1) | 6.64(6) |
| 4 | -25.53(4) | -24.97 | -0.57(4) | 14.19(3) | 14.69 | 6.64(6) |
| 5 | -25.52(4) | -24.99 | -0.54(4) | 14.22(4) | 14.69(1) | 6.64(5) |
| 6 | -25.48(7) | -24.97 | -0.51(7) | 14.23(3) | 14.69(2) | 6.65(6) |
| 7 | -25.44(7) | -24.94 | -0.50(7) | 14.25(5) | 14.68(1) | 6.65(5) |
| 8 | -25.42(8) | -24.96 | -0.46(8) | 14.24(4) | 14.68(1) | 6.66(6) |

Se only exchange at most one electron, contrary to prior estimations which estimated Bi to be trivalent.[11] The Bader charges indicate that the bonds between Bi and Se are partially ionic and partially covalent, which is consistent with the hybridization between Bi *p* and Se *s* and *p* orbitals found in the band structure of 1L BiSe (Figure 12.4). These findings are not surprising since the electronegativities of Bi and Se are close to each other (2.55 and 2.02, respectively, on the Pauling scale).[71]

*Electronic Structure of Transition Metal Dichalcogenide Monolayers*

While the findings in the prior sections can explain the necessity to donate charge and the charge localization of APBs, they cannot explain the differences in APB formation for different TMDs. In order for BiSe to donate charge, the TMD must have empty states that can accept these electrons. Density of states (DOS) were calculated for

monolayers of $TiSe_2$, $NbSe_2$, and $MoSe_2$ for the 1T and 2H polytypes using the HSE06 hybrid functional. The DOS diagrams are shown in Figure 12.9. Monolayer 1T-$TiSe_2$ is a small band gap semiconductor with a band gap of 0.09 eV. 2H-$TiSe_2$ is a semiconductor with a band gap of 1.41 eV. 1T- and 2H-$NbSe_2$ are both metallic as is 1T-$MoSe_2$. Monolayer 2H-$MoSe_2$ is a semiconductor with a band gap of 1.94 eV.

Table 12.4 shows these band gaps and the Fermi levels of the monolayers alongside 1L BiSe. $TiSe_2$ crystallizes in the 1T structure in bulk, ferecrystals, and MLCs.

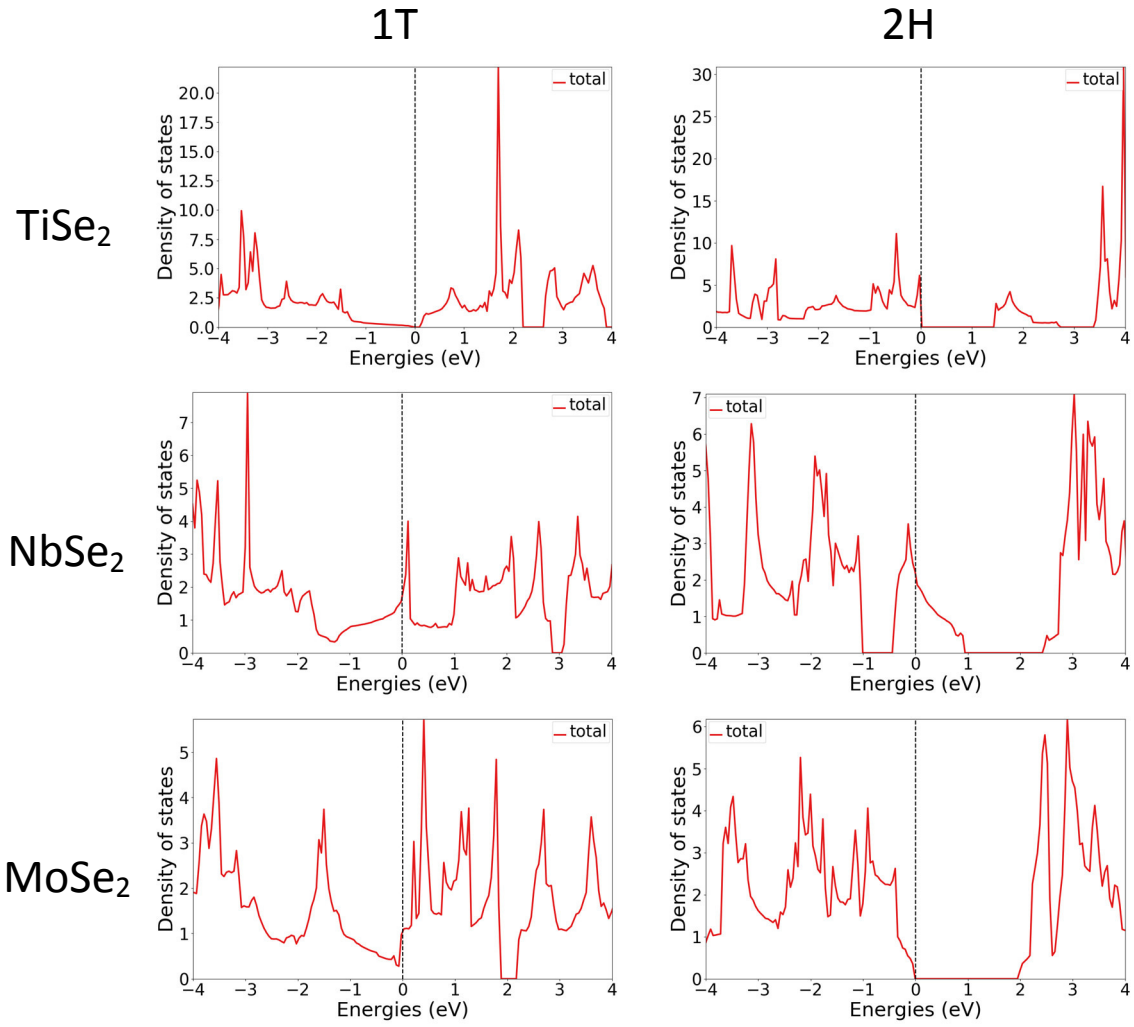


**Figure 12.9.** Density of States (DOS) of monolayer $TiSe_2$, $NbSe_2$, and $MoSe_2$ in the 1T and 2H structure.

**Table 12.4.** Band gaps $E_g$ and Fermi energies $E_F$ for monolayer $TiSe_2$, $NbSe_2$, and $MoSe_2$ in the 1T and 2H structures. The results for 1L BiSe are added for comparison.

| | $TiSe_2$ | | $NbSe_2$ | | $MoSe_2$ | | BiSe |
|---|---|---|---|---|---|---|---|
| | 1T | 2H | 1T | 2H | 1T | 2H | 1L |
| $E_g$ (eV) | 0.09 | 1.41 | 0.0 | 0.0 | 0.0 | 1.94 | 0.0 |
| $E_F$ (eV) | -3.43 | -4.81 | -3.06 | -3.78 | -2.08 | -3.29 | -1.40 |

The Fermi level of monolayer 1T-$TiSe_2$ is approximately 2 eV below 1L BiSe. Assuming a rigid band model, BiSe can donate charge into the $TiSe_2$ layer, which has many states available to accept the electron. The Fermi level of $NbSe_2$, which crystallizes in the 2H structure, is also lower than the Fermi level of BiSe, but does not have as many states available to accept electrons as $TiSe_2$ due to the band gap above the Fermi level. This explains why the abundance of APBs in ferecrystals containing $NbSe_2$ is much higher than for ferecrystals containing $TiSe_2$, as the electrons that cannot be accepted by the $NbSe_2$ layer need to be localized using APBs. With increasing $NbSe_2$ thickness, more empty states become available and the abundance of APBs decreases. $MoSe_2$, which crystallizes in the 2H structure, presents a peculiar case as it also forms 1T-$MoSe_2$ when BiSe is present. For BiSe to donate charge, the large band gap of 2H-$MoSe_2$ needs to be overcome. However, the next available empty state is at $E_F + E_g = -1.35$ eV, which is slightly above the Fermi level of BiSe. However, the 1T polytype has many states available that BiSe can donate charge into. This could be the reason for the 1T phase and the lack of APBs being observed in ferecrystals containing BiSe and $MoSe_2$.

These considerations do not explain the differences between MLCs and ferecrystals. One possibility is that the lattice match in MLCs prevents mixed layers of BiSe with and without APBs. This will be subject to future research.

## XII.4. Conclusions

BiSe exhibits a diverse set of structures and electronic properties in ferecrystals and misfit layer compounds (MLCs). In bulk, it crystallizes in a trigonal structure, whereas it crystallizes in a NaCl-like structure in ferecrystals and MLCs. With some transition metal dichalcogenides (TMDs), antiphase boundaries (APBs) are present in the BiSe layer.

Crystal orbital Hamilton populations (COHPs) show that Bi–Se bonds are antibonding, which destabilizes the bulk NaCl structure. The trigonal bulk structure is stabilized by Bi–Bi bonds. These antibonding properties are also found in isolated BiSe multilayers. To leave the antibonding regime, BiSe layers need to donate one electron per formula unit (f.u.), which experimentally is only observed for 1L BiSe, likely due to the amount of charge thicker layers would have to transfer.

The introduction of antiphase boundaries (APBs) significantly stabilizes the BiSe lattice with up to 63 meV/f.u. The length of the Bi–Bi bonds in the stable APB structures are comparable to the Bi-Bi distances in bismuth metal. The Bi 5d core level shifts in the APB structures calculated using the initial state approximations are in excellent agreement with experimental values. Bader charge analysis revealed that APBs localize charge in the BiSe layer with one electron per APB. The bonds inside BiSe are partially covalent and ionic, which is consistent with the hybridization of Bi *p* and Se *s* and *p* orbitals observed in orbital projected band structures.

Density of states of isolated TMD layers revealed the different capacities of different TMDs to accept charge from BiSe. This could be correlated to the abundance of APBs in ferecrystals. Based on a rigid band model, it was predicated that BiSe cannot

donate charge into a 2H-$MoSe_2$ layer, which is why 1T-$MoSe_2$ with its available empty states to accept charge is observed in ferecrystals containing BiSe and $MoSe_2$.

Future research needs to analyze the bonding in the APB structures to explain the different periods of APBs found in ferecrystals and investigate the differences between ferecrystals and MLCs. COHP calculations of APB structures are currently ongoing to address these questions.

# CHAPTER XIII

# CONCLUSIONS AND OUTLOOK

## XIII.1. Summary and Conclusions

This dissertation provided insight into the structures, formation, and properties of thin films synthesized using the Modulated Elemental Reactants (MER) method, which was introduced extensively in Chapter I, using a variety of experimental and computational methods.

Chapter II described the synthesis of ferromagnetic $CuCr_2Se_4$ thin films. It was shown that these films are strongly textured and aligned along the [111] axis, and that the degree of crystallographic alignment could be controlled kinetically by adjusting the annealing time. The magnetic properties of these thing films are enhanced with stronger magnetic anisotropy compared to bulk $CuCr_2Se_4$. Chapter III performed an in-depth analysis of the magnetization processes and showed that there is a competition of in-plane shape anisotropy and out-of-plane magnetocrystalline anisotropy, with the latter dominating at low temperatures. The films show unusual magnetotransport properties, such as negative magnetoresistivity. This was the first time negative magnetoresistivity was found in $CuCr_2Se_4$.

Chapter IV introduced ferecrystals, rotationally disordered members of the misfit layer compound (MLC) family. Using the MER method, the nanoarchitecture of these compounds can be controlled so that it is possible to synthesize ferecrystals with the same *c*-axis lattice parameter but different stacking sequences. This approach lead to a new type of structural isomerism, and the first synthesis of these isomers was described in Chapter V. It was shown that different isomers have different electrical properties despite

having the same total amount of layers, likely due to different numbers of interfaces and layer thicknesses. The ability to synthesize these isomers makes tens of thousands of compounds available for one combination of rock salt metal selenide and transition metal dichalcogenide. Chapter VI described the formation of the ferecrystal $[(SnSe)_{1+\delta}]_1[VSe_2]_1$ and revealed simultaneous, independent crystallization events. It was observed that $SnSe_2$ forms alongside SnSe at lower temperatures. $SnSe_2$ decomposes at 400 °C to SnSe and the ferecrystal $[(SnSe)_{1+\delta}]_1[VSe_2]_1$ is formed.

The last part of this dissertation used *ab initio* methods to explain properties of ferecrystal constituents. Chapters VIII and IX investigated $VSe_2$ layers, and found that electron correlation has profound effects on the electronic structure and magnetic properties of the 1T-polytype. It was found that $VSe_2$ has a ferromagnetic ground state and belongs to the family of *XY* magnets. However, the transition temperature is below the experimentally observed charge density wave transition. Non-magnetic 1T-$VSe_2$ is not dynamically stable due to Fermi surface nesting. The resulting charge density vector is $\left(\frac{1}{4},\frac{1}{4}\right)$ which is consistent with the bulk form. The charge density wave vector is independent of electron correlation strength and dimensionality. Chapter X used DFT to explain the stabilities of different polytypes in $[(SnSe)_{1+\delta}]_mTiSe_2$ ferecrystals. The different SnSe polytypes are similar in energy and it is plausible that interactions with the $TiSe_2$ layers destabilize the α-SnSe structure. For $m = 3$, shear defects were found which are due to nucleation and growth kinetics and not due to thermodynamic stabilities. DFT revealed that ferecrystals do not behave as simple composites and that an isolated layer model has limitations in what it can describe. Chapter XI presented $[(BiSe)_{1+\delta}][NbSe_2]_n$ ferecrystals containing BiSe. Anti-phase boundaries were present, but the abundances

decreased with increasing *n*. Depending on the precursor composition, the BiSe basal plane may either be square or rectangular. DFT calculations showed that the total energy of a BiSe bilayer is insensitive to small distortions, i.e. BiSe can easily distort to accommodate deviations from the ideal Bi:Nb ratio and still form a ferecrystal.

In Chapter XII, the bonding in BiSe was analyzed. Crystal orbital Hamilton populations (COHPs) showed that Bi–Se bonds are antibonding, which destabilizes the NaCl structure, so that BiSe either needs to donate one electron into the transition metal dichalcogenide layer or form antiphase boundaries. Antiphase boundaries significantly stabilize the BiSe lattice and lead to localization of charge in the Bi–Bi bonds. Using a rigid band model, it could be shown that $TiSe_2$ and $NbSe_2$ have empty states that BiSe can donate electrons into. Since $NbSe_2$ has less available empty states, the abundance of antiphase boundaries is higher in ferecrystals containing $NbSe_2$ than in ferecrystals containing $TiSe_2$. $MoSe_2$ has no empty states available to accept charge so that it transforms into its 1T polytype.

### XIII.2. Outlook

The MER method is a synthesis method that achieves kinetic control in a solid state reaction, which is rare in solid state synthesis methods. The resulting thin film compounds show different properties than the bulk, as was demonstrated for $CuCr_2Se_4$. The crystallographic alignment of this compound makes it a suitable component for ferecrystals, for example, as a substitute for the transition metal dichalcogenide, and may result in interesting magnetic behavior.

Along with its ability to control the nanoarchitecture of its product, the MER method can be used to synthesize a variety of metastable compounds. The existence of

isomers has been shown, which opens up the possibility for a large number of new compounds to be synthesized. Systematically varying the stacking sequences may give profound insights in the interactions inside these compounds, which may be applied to other surface chemistry problems.

Studying the formation of ferecrystals revealed the presence of the unexpected intermediate product $SnSe_2$. It is conceivable that intergrowth compounds using $SnSe_2$ and another transition metal dichalcogenide can be synthesized if the temperature is chosen low enough or if a sufficient excess pressure of Se vapor is added. There are synthesis efforts underway in the Dave Johnson group and the preliminary results are promising. Studying the formation of other ferecrystals, especially when the rock salt structure is not the only stable structure, can reveal other possible intergrowth compounds with interesting physical properties.

Density functional theory has been successfully employed to describe constituents in ferecrystals. Since ferecrystals are rotationally disordered, using lattice-matched layers to form a superlattice is not an appropriate model, making the *ab initio* description of these compounds challenging. An isolated layer model has shown potential to describe certain properties and stabilities of the constituents in ferecrystals. These insights can be used to better target the synthesis of new ferecrystalline compounds, and can also be used for the development of two-dimensional materials.

The isolated layer approach, however, has limits, especially when interactions between layers are not negligible. New theoretical models need to be developed to properly account for these interactions, especially charge transfer and charge screening, beyond using Hubbard-*U* terms.

# APPENDIX A

## PYTHON CODE TO CALCULATE ALL FERECRYSTAL ISOMERS

This appendix contains the source code of a python module to calculate all isomers in a ferecrystal with given composition. It is published online under https://github.com/marcoesters/ferecrystal_isomers. The module to be loaded is ferecrystal_isomers.py, which used module bracelets.py to perform all necklace combinatorics calculations. The code is current as of the date of this dissertation and can be found in Schemes A.1 and A.2.

**Scheme A.1.** Syntax-highlighted code of ferecrystal_isomers.py

```
"""
This module creates all ferecrystal isomers with a given composition.
It also has a method to filter isomers according to thickness or
interface criteria (see function get_isomer subset for details). It
uses the algorithm by Karim et al. to create bracelets with fixed
content to create the isomers (see bracelets module for full citation).
"""

from __future__ import division, unicode_literals, print_function
from bracelets import Bracelets
from string import ascii_uppercase

__author__ = "Marco Esters"
__copyright__ = "Copyright 2017, Marco Esters"
__version__ = "1.0"
__maintainer__ = "Marco Esters"
__email__ = "esters@uoregon.edu"
__date__ = "03/06/2017"


class Isomers(object):
    """
    Isomer class to generate all ferecrystal isomers. Uses the
    algorithm Karim et al. (DOI: 10.1016/j.tcs.2012.11.024) to
    generate bracelets with fixed content.
    """
    def __init__(self, composition, elements=None):
        """
        Checks for invalid input and generates all isomers.
        Args:
            composition (list or tuple): A list or tuple representation
                of the formula of the ferecrystal repeating unit.
                List items must be integers.
            elements (list or tuple): A list or a touple of the
                constituents in the ferecrystal for the output of the
                isomers. The list must have the same length as the
```

```
                composition, and the list items must be string.
                Defaults to None. If it is None, uppercase letters are
                used for the output instead.
        """
        if not (isinstance(composition, list)
                or isinstance(composition, tuple)):
            raise TypeError('Composition must be list or tuple')
        if len(composition) < 2:
            raise ValueError('Composition must have at least 2 items.')
        if len(composition) > 26:
            raise ValueError('Composition cannot have more than 26 items.')
        for i in composition:
            if not isinstance(i, int):
                raise TypeError('Values must be a integers.')
        self._composition = composition
        if elements:
            if not (isinstance(elements, list)
                    or isinstance(elements, tuple)):
                raise TypeError('Elements must be None, list, or tuple.')
            if len(self._composition) != len(elements):
                raise ValueError('Elements must be of the '
                                 'same size as composition.')
            for element in elements[:-1]:
                if elements.count(element) > 1:
                    raise ValueError('Element list contains duplicates.')

        self._elements = elements
        self._bracelets = Bracelets(composition)
        self._all_isomers = self._isomers_from_bracelets()

    def _as_tuples(self):
        """
        Converts the bracelets into isomer tuples, i.e. the numbers
        be replaced with the element strings.
        """
        isomer_tuples = []
        for brac in self._bracelets.as_tuple():
            isomer = [(self._elements[t[0]], t[1]) for t in brac]
            isomer_tuples.append(isomer)
        return isomer_tuples

    def _isomers_from_bracelets(self):
        """
        Formats the tuples returned from the bracelet algorithm and
        outputs a list of formatted strings
        """
        isomers = []
        for brace in self._bracelets.as_tuple():
            istring = ''
            for b, brc in enumerate(brace):
                if self._elements is None:
                    letter = ascii_uppercase[brc[0]]
                else:
                    letter = self._elements[brc[0]]
                istring = '%s(%s)%d' % (istring, letter, brc[1])
                if b != len(brace) - 1:
                    istring = '%s-' % istring
            isomers.append(istring)
        return isomers

    def _isomers_from_tuples(self, isomers):
```

```
        """
        Converts the isomer tuples into string. This function converts
               the output of 'get_isomer_subset' into a list of strings.
               Args:
                   isomers (list): A list of isomers as tuples.
               """
               isomer_tuples = []
               for isomer in isomers:
                   istring = ''
                   for i, iso in enumerate(isomer):
                       istring += '(%s)%d' % (iso[0], iso[1])
                       if i != len(isomer) - 1:
                           istring += '-'
                   isomer_tuples.append(istring)

               return isomer_tuples

           def _transform_to_letter(self, element_string):
               """
               Transforms the isomers strings that use elements instead of
               uppercase letters into a string of uppercase letters to
               simplify the interface filter. The function sorts the elements
               by length in reverse order so that e.g. 'SnSe2' is not seen as
               'SnSe' by the algorithm.
               Args:
                   element_string (string): An isomer as a concatenated string
                       of its constituents.
               """
               element_indices = {element: e
                                  for e, element in enumerate(self._elements)}

               for element in sorted(self._elements[:])[::-1]:
                   letter = ascii_uppercase[element_indices[element]]
                   element_string = element_string.replace(element, letter)
               return element_string

           def _filter_interface(self, isomers, interface_conditions):
               """
               A function to return only the isomers that satisfy the
               thickness conditions.
               Args:
                   isomers (list): A list of tuples with either all isomers or
                                   the isomers that remain after going through
                                   the thickness filter.
                   interface_conditions (dict): The interface conditions as
                       described in the function 'get_isomer_subset'.
               """
               filtered_isomers = []
               inter_cond = interface_conditions.copy()
               if self._elements:
                   for key in inter_cond:
                       newkey = self._transform_to_letter(key)
                       inter_cond[newkey] = inter_cond.pop(key)
               for isomer in isomers:
                   append_isomer = True
                   istring = ''.join([i[0]*i[1] for i in isomer])
                   if self._elements:
                       istring = self._transform_to_letter(istring)
                   for key in inter_cond:
                       val = inter_cond[key]
                       if type(val) is bool:
```

```
                            interface = key in istring or key[::-1] in istring
                            if interface != inter_cond[key]:
                                append_isomer = False
                                break
                        else:
                            istring_extd = istring + istring[0:len(key)-1]
                            occ = istring.count(key)
                            if key != key[::-1]:
                                occ += istring.count(key[::-1])

                            if occ < val[0] or (val[1] > 0 and occ > val[1]):
                                append_isomer = False
                                break
                    if append_isomer:
                        filtered_isomers.append(isomer)
                return filtered_isomers

            def _filter_thickness(self, isomers, thickness_conditions):
                """
                A function to return only the isomers that satisfy the
                thickness conditions.
                Args:
                    isomers (list): All isomers as a list of tuples.
                    thickness_conditions (dict): The thickness conditions as
                        described in the function 'get_isomer_subset'.
                """
                filtered_isomers = []
                intvals = {key: False for key in thickness_conditions
                           if type(thickness_conditions[key]) is int}
                for isomer in isomers:
                    append_isomer = True
                    intvals = {key: False for key in intvals}
                    for i in isomer:
                        if i[0] in thickness_conditions:
                            val = thickness_conditions[i[0]]
                            if type(val) is int:
                                if i[1] == val:
                                    intvals[i[0]] = True
                            elif i[1] < val[0] or (val[1] > 0 and i[1] > val[1])
    :
                                append_isomer = False
                                break
                    if append_isomer and False not in intvals.values():
                        filtered_isomers.append(isomer)
                return filtered_isomers

            def get_formula(self):
                """
                Returns the chemical formula of the ferecrystal as a string.
                """
                formula_string = ''
                if self._elements:
                    for c, comp in enumerate(self._composition):
                        formula_string += '(%s)%d' % (self._elements[c], comp)
                else:
                    for c, comp in enumerate(self._composition):
                        formula_string += '(%s)%d' % (ascii_uppercase[c], comp)

                return formula_string

            def get_isomer_subset(self,
```

```
                                  thickness_conditions=None,
                                  interface_conditions=None):
                """
                Overhead function to filter isomers based on the input
                thickness and interface conditions.
                Args:
                    interface_donditions (dict):
                        A dictionary describing interface conditions. Defaults
                        to None. Dictionary keys are entered as they would
                        appear in the isomer. Examples:
                            * 'PbSeSnSe' checks for interfaces between one PbSe
                              and one SnSe layer. Note that the occurrence of
                              PbSe-SnSe-PbSe constitutes two interfaces.
                            * To check for occurrences of '(PbSe)2(SnSe)2', the
                              key 'PbSePbSeSnSeSnSe' needs to be used.
                        Acceptable value formats:
                            False: Returns only isomers where the interface(s)
                                   described in the key do(es) not exist. For
                                   example {'PbSeSnSe': False} omits all
                                   isomers with a PbSe-SnSe interface.
                            True: Returns any isomers that have the interface(s)

                                  described in the key. Equivalent to (1, 0).
                            int: Returns isomers that have exactly 'int' number
                                 of interface(s) described in the key.
                            (int1, int2): Returns isomers with at least 'int1'
                                          and at most 'int2' number of
                                          occurrences of the interface(s)
                                          described in the key.
                            (0, int2): Returns isomers with at most 'int2'
                                       number of occurences of the interface(s)
                                       described in the key.
                        (int1, 0): Returns isomers with at least 'int1' number
                                   of occurences of the interface(s) described
                                   in the key. (1, 0) is equivalend to True.
                thickness_conditions (dict):
                    A dictionary describing thickness conditions for each
                    element. Defaults to None. Acceptable value formats:
                        int: Returns isomers with at least one instance of the
                             element with thickness 'int' (integer). To return
                             isomers where the element exclusively has the
                             thickness 'int', use (int, int).
                        (int1, int2): Returns isomers with a thickness of the
                                      element of at least 'int1' and at most
                                      'int2'. Can also be of format list.
                        (0, int2): Returns isomers with a maximum thickness of
                                   the element of 'int2'. Can also be a list.
                        (int1, 0): Returns isomers with a minimum thickness of
                                   the element of 'int1'. Can also be a list.
                """
                isomer_subset = self._as_tuples()
                if thickness_conditions:
                    if not isinstance(thickness_conditions, dict):
                        raise ValueError('Thickness conditions must be a diction
    ary.')
                    else:
                        for key in thickness_conditions:
                            val = thickness_conditions[key]
        #                    if type(val) is int:
        #                        thickness_conditions[key] = [val, val]
                        isomer_subset = self._filter_thickness(isomer_subset,
```

```
                                                                thickness_conditi
    ons)
                if interface_conditions:
                    if not isinstance(interface_conditions, dict):
                        raise ValueError('Interface conditions must be a diction
    ary.')
                    for key in interface_conditions:
                        val = interface_conditions[key]
                        if type(val) is int:
                            interface_conditions[key] = [val, val]
                    isomer_subset = self._filter_interface(isomer_subset,
                                                           interface_conditions)

                return self._isomers_from_tuples(isomer_subset)

            @property
            def isomers(self):
                """
                Returns all isomers as a list of formatted strings.
                """
                return self._all_isomers
```

**Scheme A.2.** Syntax-highlighted code of bracelets.py. This module is imported by ferecrystal_isomers.py (see line 10 in Scheme A.2).

```
1.  """
2.  This module creates bracelets with fixed content according to
3.  Karim, S.; Sawada, J.; Alambir; Z.; and Husnine, S. M. "Generating
4.  bracelets with fixed content", Theor. Comput. Sci., 2013, 475,
5.  103 - 112, DOI: 10.1016/j.tcs.2012.11.024
6.  """
7.
8.  from __future__ import division, unicode_literals, print_function
9.  from string import ascii_uppercase
10.
11. __author__ = "Marco Esters"
12. __copyright__ = "Copyright 2017, Marco Esters"
13. __version__ = "1.0"
14. __maintainer__ = "Marco Esters"
15. __email__ = "esters@uoregon.edu"
16. __date__ = "03/06/2017"
17.
18.
19. class Bracelets(object):
20.
21.     """
22.     Object for the bracelets to be instantiated by the
23.     ferecrystal_isomer module.
24.     """
25.
26.     def __init__(self, components):
27.         """
28.         Args:
29.            components (list or tuple): A list of integers representing
30.                the fixed content.
31.         """
32.         if not isinstance(components, list):
33.             raise TypeError("Components must be list.")
34.         if len(components) < 2:
35.             raise ValueError("Components must have at least 2 items.")
36.
37.         self._components = components
38.         dll = DoubleLinkedList(self._components)
39.         self._bracelets = sorted(list(self.get_bracelets(dll)))
40.
41.     def as_string(self):
42.         string_list = [''] * len(self.bracelets)
43.         for b, brace in enumerate(self.bracelets):
44.             for s in brace:
45.                 string_list[b] += ascii_uppercase[s]
46.         return string_list
47.
48.     def as_tuple(self):
49.         bracelet_tuple = []
50.         for brac in self.bracelets:
51.             tuple_list = []
52.             curr = 0
53.             n = 1
54.             for b in brac[1:]:
55.                 if b == curr:
56.                     n += 1
57.                 else:
```

```
                    tuple_list.append((curr, n))
                    curr = b
                    n = 1
            tuple_list.append((curr, n))
            bracelet_tuple.append(tuple_list)
        return bracelet_tuple

    @property
    def bracelets(self):
        return self._bracelets

    def build_bracelets(self, a, dll, lenenc, run, t, p, r, z, b, RS):
        if t - 1 > r + (dll.n_tot-r)/2:
            if a[t-2] > a[dll.n_tot-t+r+1]:
                RS = False
            elif a[t-2] < a[dll.n_tot-t+r+1]:
                RS = True

        if dll.n[-1] == dll.n_tot - t + 1:
            if dll.n[-1] > run[t-p-1]:
                p = dll.n_tot

            if dll.n[-1] > 0 and r + 1 != t:
                if lenenc[b+1][0] == dll.n_items - 1\
                      and lenenc[b+1][1] > dll.n[-1]:
                    RS = True

                elif (lenenc[b+1][0] != dll.n_items - 1
                      or lenenc[b+1][1] < dll.n[-1]):
                    RS = False

            if not RS and dll.n_tot == p:
                yield a

        elif dll.n[0] != dll.n_tot - t + 1:
            j = dll.head
            while j >= a[t-p-1]:
                run[z-1] = t - z
                lenenc = self.update_run_length(j, lenenc)
                dll.n[j] -= 1
                if dll.n[j] == 0:
                    dll.remove(j)

                    a[t-1] = j
                    z2 = z
                    if j != dll.n_items - 1:
                        z2 = t + 1
                    if j != a[t-p-1]:
                        p2 = t
                    else:
                        p2 = p

                    c = self.check_rev(lenenc)
                    if c == 0:
                        for brac in self.build_bracelets(a[:], dll, lenenc,
                                                         run, t + 1, p2, t,
                                                         z2, lenenc[0], Fals
e):
                            yield brac
```

```
116.
117.                     elif c == 1:
118.                         for brac in self.build_bracelets(a[:], dll, lenenc,
119.                                                          run, t + 1, p2, r,
120.                                                          z2, b, RS):
121.                             yield brac
122.
123.                     if dll.n[j] == 0:
124.                         dll.add(j)
125.                     dll.n[j] += 1
126.                     lenenc = self.restore_run_length(lenenc)
127.                     j = dll.next[j]
128.
129.                 a[t-1] = dll.n_tot - 1
130.
131.         def check_rev(self, lenenc):
132.             i = 1
133.             m = lenenc[0]
134.             while lenenc[i] == lenenc[m-i+1] and i <= m/2:
135.                 i += 1
136.             if i > m/2:
137.                 return 0
138.             if lenenc[i][0] < lenenc[m-i+1][0]:
139.                 return 1
140.             if lenenc[i][0] > lenenc[m-i+1][0]:
141.                 return -1
142.             if ((lenenc[i][1] < lenenc[m-i+1][1]
143.                  and lenenc[i+1][0] < lenenc[m-i+1])
144.                 or (lenenc[i][1] > lenenc[m-i+1][1]
145.                     and lenenc[i][0] < lenenc[m-i][0])):
146.                 return 1
147.             return -1
148.
149.         def get_bracelets(self, dll):
150.             run = [0] * dll.n_tot
151.
152.             a = [dll.n_items - 1] * dll.n_tot
153.             a[0] = 0
154.             dll.n[0] -= 1
155.             lenenc = [1, [0, 1]]
156.             if dll.n[0] == 0:
157.                 dll.remove(0)
158.
159.             for brac in self.build_bracelets(a, dll, lenenc, run,
160.                                              2, 1, 1, 2, 1, False):
161.                 yield brac
162.
163.         def restore_run_length(self, lenenc):
164.             if lenenc[-1][1] == 1:
165.                 lenenc[0] -= 1
166.                 del lenenc[-1]
167.             else:
168.                 lenenc[-1][1] -= 1
169.
170.             return lenenc
171.
172.         def update_run_length(self, j, lenenc):
173.             if lenenc[-1][0] == j:
174.                 lenenc[-1][1] += 1
```

```
            else:
                lenenc[0] += 1
                lenenc.append([j, 1])

            return lenenc


    class DoubleLinkedList(object):
        """
        Object for the double linked list to efficiently implement add
        and remove operations. See Karim's paper for details.
        """
        def __init__(self, component_list):
            """
            Generates the double linked list.
            Args:
                component_list (list or tuple): integer list representing
                    the fixed content.
            """
            self.n = component_list[:]
            self.n_items = len(component_list)
            self.n_tot = sum(component_list)
            self.next = []
            self.prev = []
            for i in range(self.n_items+1):
                self.next.append(i-1)
                self.prev.append(i+1)
            self._head = self.n_items - 1

        def add(self, j):
            """
            The 'add(j)' operation as outlined in Karim's publication.
            """
            n = self.next[j]
            p = self.prev[j]
            self.prev[n] = j
            self.next[p] = j
            if self.prev[j] == self.n_items:
                self._head = j

        @property
        def head(self):
            """
            The 'head' operation as outlined in Karim's publication.
            """
            return self._head

        def remove(self, j):
            """
            The 'remove(j)' operation as outlined in Karim's publication.
            """
            if j == self._head:
                self._head = self.next[j]
            n = self.next[j]
            p = self.prev[j]
            self.next[p] = n
            self.prev[n] = p
```

APPENDIX B

SUPPLEMENTAL MATERIAL TO CHAPTER IX

## B.1. Computational Methods

All DFT calculations were performed using the Vienna ab initio simulation package (VASP).[1-3] The interactions between the ionic core and the valence electrons were described using the projector-augmented wave (PAW) method using a cutoff energy of 500 eV.[4,5] The $3p^6 3d^4 s^1$ and the $4s^2 4p^4$ states were used as valence electrons for V and Se, respectively. For the exchange-correlation functional, we compare results for the local-density approximation (LDA), the Perdew-Burke-Ernzerhof (PBE)[7] generalized-gradient approximation (GGA), and the Heyd-Scuseria-Ernzerhof (HSE06) hybrid method with the standard exact-exchange mixing parameter of $\alpha = 0.25$.[8] For the Hubbard-*U* term, Dudarev's approach was used to treat localized d-orbitals in V, using the effective *U* parameter, $U_{eff} = U - J$, with *U* and *J* being the on-site Coulomb and exchange parameters, respectively.[9] Since the interactions between individual $VSe_2$ layers is of van der Waals type, dispersion corrections were included for the GGA functionals using the method of Tkatchenko and Scheffler (TS), Grimme's DFT-D2 method, and Dion's method in the vdW-DF corrected optPBE, optB86b and optB88 functionals.[10-17] Brillouin zone integration was carried out using a Γ-centered k-point grid with a high k-point density of approximately 60 k-points per $Å^{-1}$.[18] Atomic positions and lattice parameters were fully optimized until the forces were smaller than 0.01 eV/Å and the stresses smaller than 0.05 GPa. A vacuum of 30 Å was included for the monolayer and bilayer calculations to minimize interactions between periodic images. For total energy calculations, self-consistency was achieved with an energy convergence

of $10^{-6}$ eV. Band structures were visualized and $VSe_2$ slabs were generated using the open source PYTHON packages PYMATGEN in conjunction with MPINTERFACES.[19,20] Spin densities were visualized with the program VESTA.[21] Fermi surfaces were calculated using the Wannier interpolation as implemented in the WANNIER90 code and visualized using XCRYSDEN.[22,23]

## B.2. Energy and Magnetization of Undistorted 1T- and 2H-$VSe_2$

Figures B.1a, B.2a, and B.3a show the difference in total energy, $\Delta E$, between $VSe_2$ in the octahedral (1T) and trigonal prismatic (2H) structure as a function of $U_{\text{eff}}$ for monolayers, bilayers, and bulk, respectively. $\Delta E$ depends strongly on the exchange-correlation functional, $U_{\text{eff}}$, and the van der Waals functional. For all functionals, $\Delta E$ exhibits a maximum value at intermediate values for $U$. For the GGA functional PBE and the van der Waals corrected GGA functionals vdW-optPBE, vdW-optB88, vdW-optB86b, TS-GGA, and GGA-D2, the maximum occurs at a lower $U_{\text{eff}}$ of 0.5 eV – 1.0 eV compared to a $U_{\text{eff}}$ of 2.5 eV for the LDA functional. For the GGA+U methods, the 2H structure is stable for $U_{\text{eff}}$ below about 2 eV. For the LDA+U method, 1T is stable for $U_{\text{eff}}$ below 0.5 eV and above 3.5 eV. For the LDA functional, going from monolayer to bilayer to bulk shifts the transition from 2H being more stable to 1T being more stable to lower $U_{\text{eff}}$ from approximately 3.25 eV for monolayers to 3.0 eV for bilayers and 2.75 eV for bulk. The same trend can be observed for the GGA functionals.

The magnetization of the monolayer (Figure B.1b) as a function of $U_{\text{eff}}$ is described in the main publication in detail. The magnetization of the 2H polytype is approximately unity for all PBE functionals and all $U_{\text{eff}}$ values (Figure B.1c). For LDA, it is around 0.7 $\mu_B$ without a Hubbard-$U$ and reaches unity for $U_{\text{eff}}$ = 1 eV. The bilayer of

the 1T-polytype behaves like the monolayer, except for the LDA functional, which predicts an unmagnetized bilayer for $U_{\text{eff}} \leq 1$ eV before it reaches unity per formula unit (f.u.) at $U_{\text{eff}} = 3.5$ eV (Figure B.2b). Additionally, all PBE functionals show a maximum at 2.5 eV. The 2H-polytype (Figure B.2c) shows the same trend as the monolayer with a few deviations: except for PBE and optPBE, the PBE functionals exhibit a magnetization slightly below unity per formula unit without a Hubbard-$U$. All PBE functionals reach a magnetization of 1 $\mu_{\text{B}}$/f.u. at $U_{\text{eff}} = 1.5$ eV. LDA has a lower magnetization per formula unit without a Hubbard-$U$ compared to the monolayer and only reaches unity at $U_{\text{eff}} = 3.5$ eV, which is 2.5 eV higher than for the monolayer. The bulk magnetization of the 1T-polytype (Figure B.3b) follows the same trend as the monolayer and the bilayer. The major difference is that the PBE functionals that show a maximum at 2.5 eV for the monolayer do not have this maximum in the bulk and vice versa. Using the LDA functional, the magnetization stays at zero until $U_{\text{eff}} = 0.5$ eV and increases to reach unity at $U_{\text{eff}} = 4.0$ eV. The 2H-polytype (Figure B.3c) shows the same behavior as for the bilayer until $U_{\text{eff}}$ reaches 3.0 eV (TS and optB88), 3.5 eV (other PBE functionals), and 4.0 eV (LDA) where the magnetization per formula unit increases beyond unity, likely due to a semiconductor-metal transition.

The $a$-axis lattice parameters of 1T-$VSe_2$ are shown in Figures B.1d, B.2d, B.3d for monolayers, bilayers, and bulk, respectively. The lattice parameters increase with increasing $U_{\text{eff}}$ and increase in a similar manner regardless of dimensionality. The $c$-axis lattice parameters of bulk 1T-$VSe_2$ are shown in Figure B.3e and are independent of $U_{\text{eff}}$ and only depend on the van der Waals functional. The $c/a$-ratio consequently decreases with increasing $U_{\text{eff}}$ as shown in Figure B.3f.

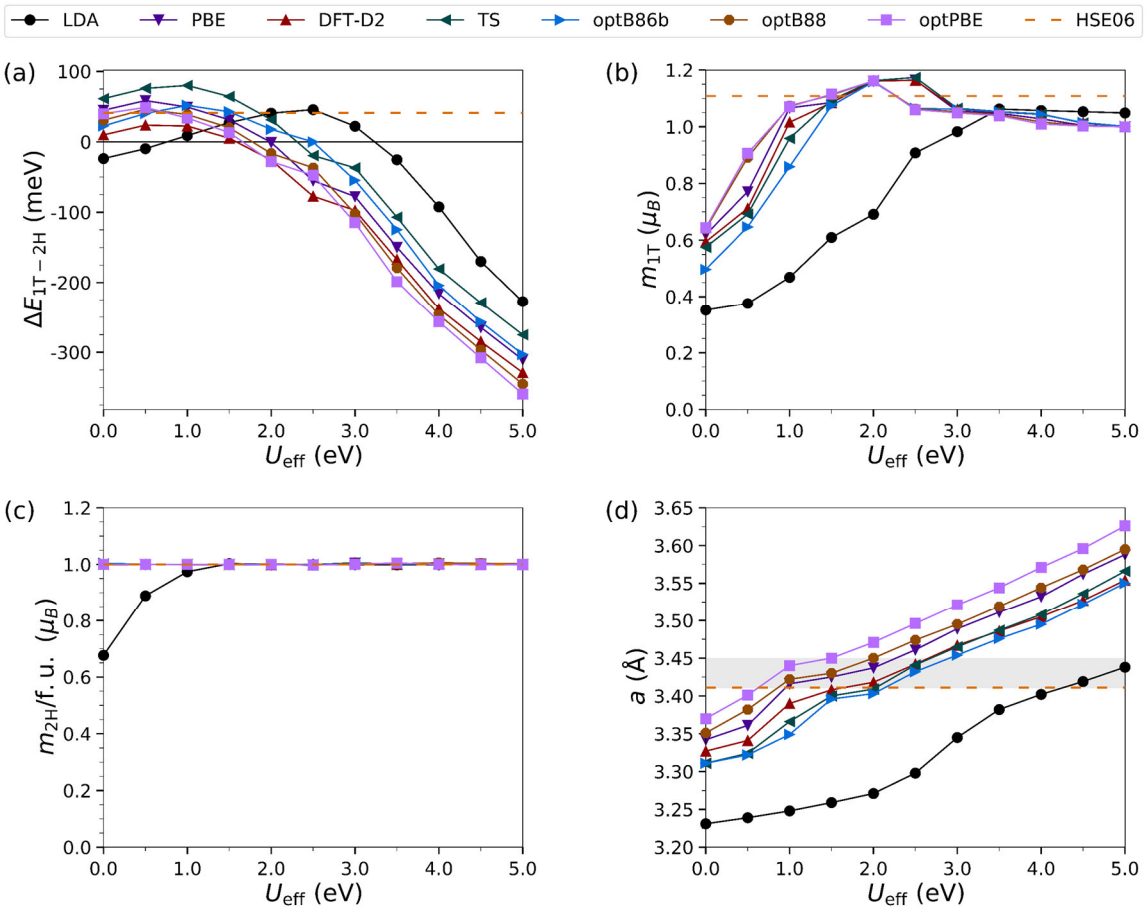


**Figure B.1.** (a) Energy difference $\Delta E$ between 1T and 2H-$VSe_2$ monolayers as a function of $U_{eff}$, exchange-correlation and van der Waals functional. Positive $\Delta E$ indicates that 2H is more stable. (b) Magnetization $m$ of monolayer 1T-$VSe_2$ and (c) 2H-$VSe_2$ as a function of $U_{eff}$, exchange-correlation and van der Waals functional. (d) In-plane lattice parameters $a$ of monolayer 1T-$VSe_2$. The gray shades represent the range of experimental values found for ferecrystals.[24-29]

**Figure B.2.** (a) Energy difference $\Delta E$ per formula unit (f.u.) between 1T and 2H-$VSe_2$ bilayers as a function of $U_{eff}$, exchange-correlation and van der Waals functional. Positive $\Delta E$ indicates that 2H is more stable. (b) Magnetization $m$ per f.u. of bilayer 1T-$VSe_2$ and (c) 2H-$VSe_2$ as a function of $U_{eff}$, exchange-correlation and van der Waals functional. (d) In-plane lattice parameters $a$ of bilayer 1T-$VSe_2$. The gray shades represent the range of experimental values found for ferecrystals.[24-29]

**Figure B.3.** (a) Energy difference $\Delta E$ per formula unit (f.u.) between bulk 1T and 2H-$VSe_2$ as a function of $U_{eff}$, exchange-correlation and van der Waals functional. Positive $\Delta E$ indicates that 2H is more stable. (b) Magnetization $m$ per f.u. of bulk 1T-$VSe_2$ and (c) 2H-$VSe_2$ as a function of $U_{eff}$, exchange-correlation and van der Waals functional. (d) $a$-axis lattice parameters $a$, (e) $c$-axis lattice parameters $c$, and (f) $c/a$ ratios of bulk 1T-$VSe_2$. The gray shades represent the range of experimental values found for the bulk.[30-32]

PBE predicts that $VSe_2$ is ferromagnetic, but it exhibits temperature-independent paramagnetism.[33-39] To reconcile these differences, the Curie temperature $T_c$ was estimated using the mean field approximation as $T_c = \frac{3}{2} J k_B^{-1}$, where $J$ is the exchange integral and $k_B$ the Boltzmann constant. Using the Heisenberg model, the exchange integral $J$ can be estimated from the magnetization $m$ and the energy difference between the ferromagnetic and antiferromagnetic configuration $\Delta E_{\mathrm{mag}}$ as $J = (1/12)\Delta E_{\mathrm{mag}}/2m^2$. The results are shown in Table B.1. The estimated Curie temperatures are significantly below the experimentally observed charge density wave transition temperature of 100 – 110 K (onset), so the ferromagnetic phase resists in a temperature regime in which undistorted 1T-$VSe_2$ not stable and can thus not be experimentally observed.

**Table B.1.** Magnetization $m$ of bulk 1T-$VSe_2$, energy difference between ferromagnetic and antiferromagnetic order $\Delta E$mag, and the resulting estimate for the Curie temperature $T_c$ for $U_{\mathrm{eff}}$ = 0 eV and 1.0 eV using the optPBE functional.

| $U_{\mathrm{eff}}$ (eV) | $m$ ($\mu_B$) | $\Delta E_{\mathrm{mag}}$/f.u. (meV) | $T_c$ (K) |
|---|---|---|---|
| 0 | 4.301 | 0 | 15 |
| 1.0 | 4.304 | 0.2 | 15 |

## B.3. Band Structure of 1T-$VSe_2$ Monolayers Using optB86b

Figure B.4a shows the orbital-projected band structure of monolayer 1T-$VSe_2$ using the optB86b functional and $U_{eff}$ = 2.5 eV. It is similar to the band structure found for optPBE and $U_{eff}$ = 1.0 eV, but there are some major differences at the K point for the majority spin bands, where the $d_{z^2}$ band is shifted far below the Fermi level because of increasing occupation of the $d_{z^2}$ orbtal, and the M point for the minority spin bands where the $d_{xz} + d_{yz}$ band is shifted further above the Fermi level. The Fermi surface (Figure B.4b) reveals that the majority spin electron pockets around the M point maintain their shape but decrease in size. The minority spin hole pockets do not change significantly.

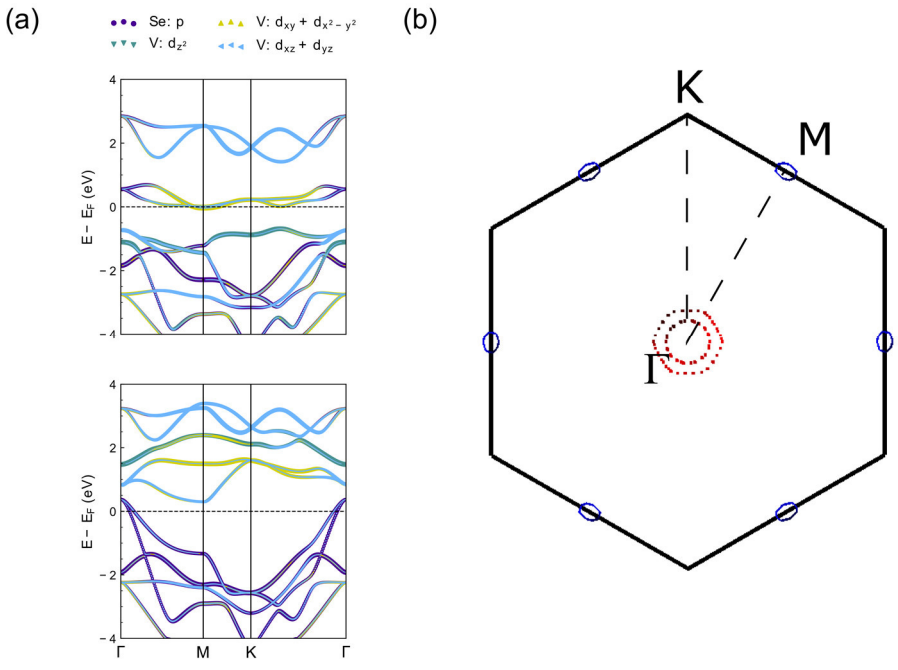


**Figure B.4.** (a) Orbital-resolved band structure of monolayer 1T-$VSe_2$ using the optB86b functional and $U_{eff}$ = 2.5 eV. (b) The Fermi surface using the same parameters. Solid blue surfaces are from the majority spin and dashed red surfaces are from the minority spin.

## B.4. Phonon Dispersion Curves of 1T-$VSe_2$

Phonon dispersion curves were calculated using density functional perturbation theory (DFPT) as implemented in VASP and the analysis program PHONOPY,[40] and are shown in Figure B.5 for $U_{eff}$ = 0 and 1.0 eV. Therere are imaginary phonon modes at several places in the Brillouin zone that increase in frequency with increasing $U_{eff}$, suggesting that the lattice destabilizes with increasing value of $U_{eff}$. The mode with the lowest frequency is at $\left(\frac{1}{4}, 0, \frac{1}{2}\right)$, which corresponds to a $4 \times 1 \times 2$ or a $4 \times 4 \times 2$ supercell. Varying the wave vector along the out-of-plane direction shows that the actual minimum is at $\approx 0.6c^*$. There is inconsistency in the literature about the exact value and commensurability of the $z$ component of the charge density wave (CDW) vector, and even a transition from a $4 \times 4 \times 3$ to a $4 \times 4 \times 2$ supercell has been reported.[39,41-44] The in-plane component of the CDW vector agrees with the CDW vector found in the literature, and the range of the out-of-plane component agrees with the range of values found in experiments. The results are consistent with the results obtained by Zhang *et al.* who used the LDA functional and norm-conserving pseudopotentials.[45]

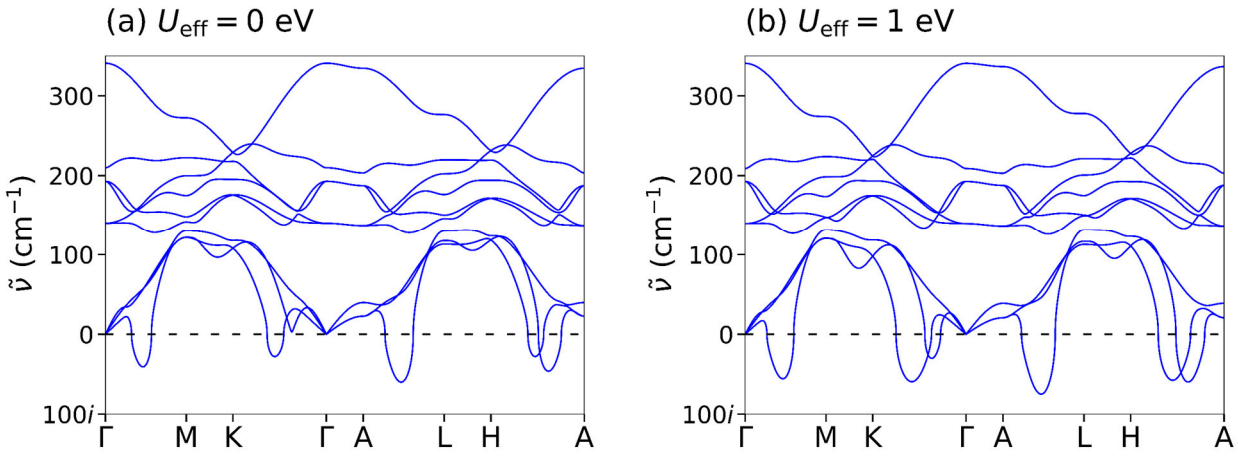


**Figure B.5.** Phonon dispersion curves for bulk 1T-$VSe_2$ using optPBE and (a) no Hubbard-$U$, (b) $U_{eff}$ = 1.0 eV.

The phonon dispersion curves for monolayer 1T-$VSe_2$ using the optB86b functional and $U_{eff}$ = 2.5 eV are shown in Figure B.6 for ferromagnetic (a) and non-magnetic (b) structures. Unlike for the ferromagnetic monolayer using optPBE and $U_{eff}$ = 1.0 eV, there are no imaginary phonons present for the ferromagnetic monolayer using optB86b and $U_{eff}$ = 2.5 eV, showing that the dynamic stability of ferromagnetic 1T-$VSe_2$ monolayers is sensitive to the Hubbard-U. The nonmagnetic monolayer is less sensitive to $U_{eff}$. The positions of the imaginary phonon modes are independent of the Hubbard-$U$, but the frequencies of the imaginary modes increase, suggesting that electron correlation destabilizes the lattice. For optB86b and $U_{eff}$ = 2.5 eV, an additional acoustic phonon becomes imaginary at $\frac{1}{2}M$.

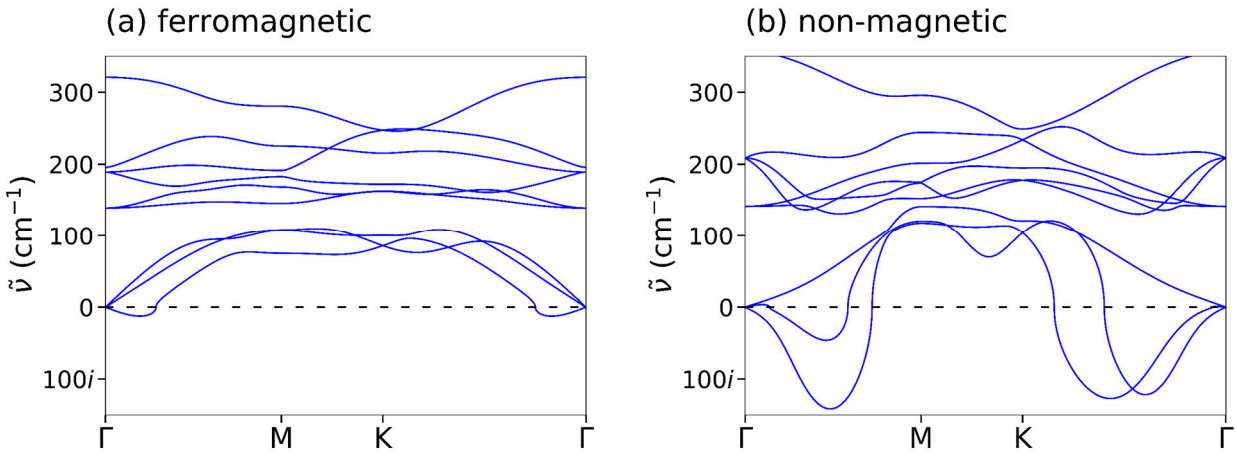


**Figure B.6.** Phonon dispersion curves for (a) ferromagnetic and (b) non-magnetic monolayers of 1T-$VSe_2$ using the optB86b functional and $U_{eff}$ = 2.5 eV.

# APPENDIX C

# SUPPLEMENTAL INFORMATION TO CHAPTER X

## C.1. Le Bail Fits on In-plane Diffraction Patterns

Le Bail fits on in-plane x-ray diffraction patterns of $[(SnSe)_{1+\delta}]_mTiSe_2$ were performed using the FullProf suite. The background was fit using a linear interpolation between points. The SnSe phase was modeled using an orthorhombic crystal system and the $TiSe_2$ phase was modeled using a hexagonal crystal system. The peak shapes were fitted using pseudo-Voigt functions. The lattice parameters, line width parameters, and pseudo-Voigt weighting term were refined until convergence was reached. The (110) reflection of $SnSe_2$ in the $m \geq 2$ compounds were included in the background.

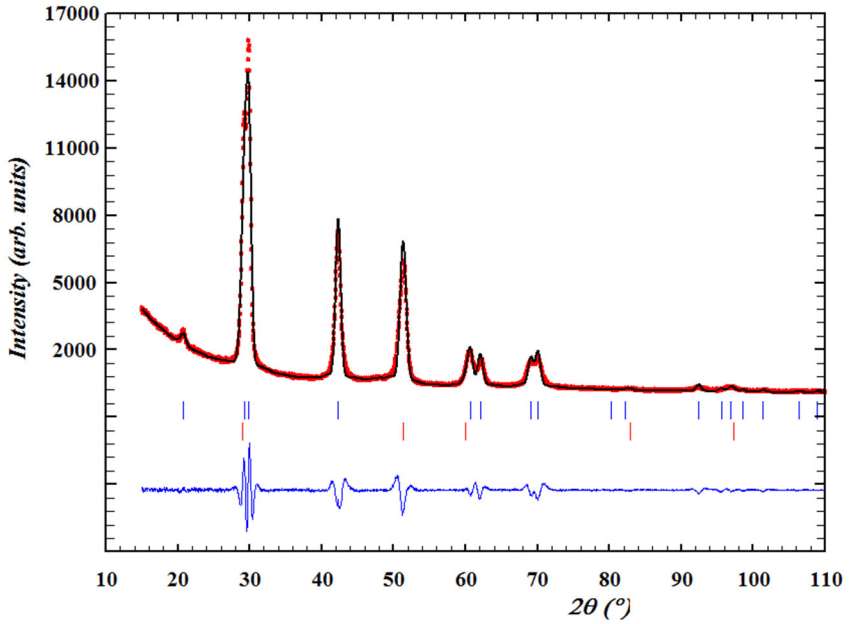


**Figure C.1.** Le Bail fit of the in-plane diffraction pattern for $m = 1$. Blue tick marks indicate the position of SnSe reflections and red tick marks indicate the position of $TiSe_2$ reflections.

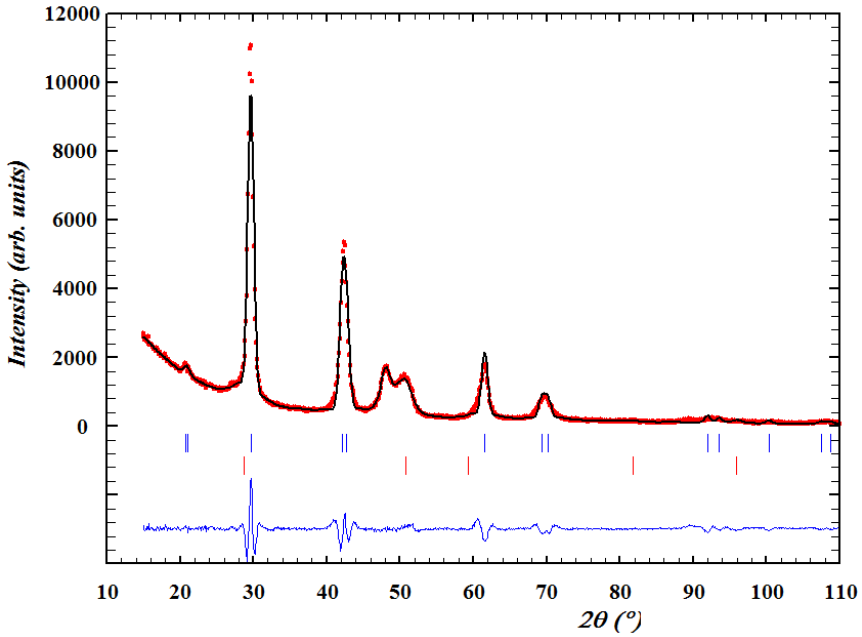


**Figure C.2.** Le Bail fit of the in-plane diffraction pattern for $m = 2$. Blue tick marks indicate the position of SnSe reflections and red tick marks indicate the position of $TiSe_2$ reflections. The reflection at approximately 47° is the (110) reflection of $SnSe_2$.

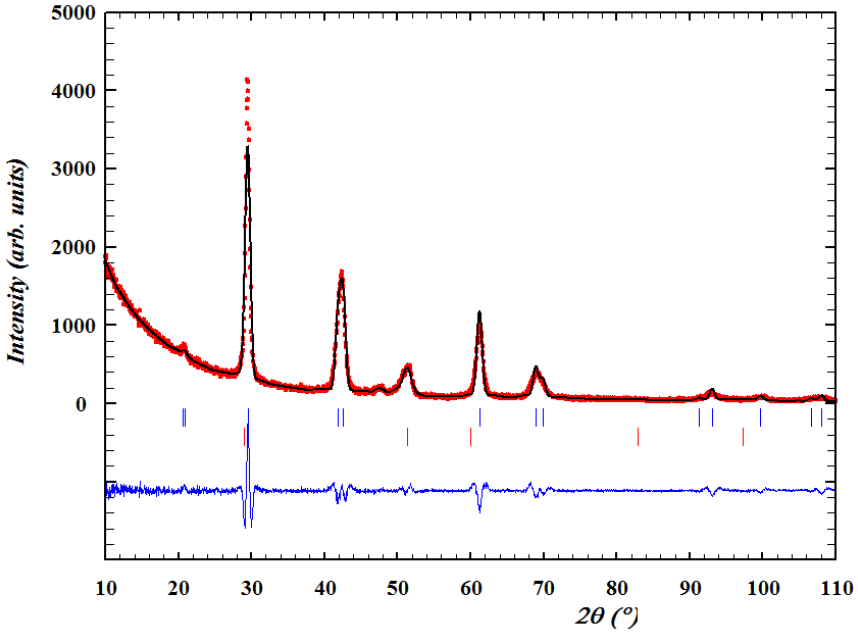


**Figure C.3.** Le Bail fit of the in-plane diffraction pattern for $m = 3$. Blue tick marks indicate the position of SnSe reflections and red tick marks indicate the position of $TiSe_2$ reflections. The reflection at approximately 47° is the (110) reflection of $SnSe_2$.

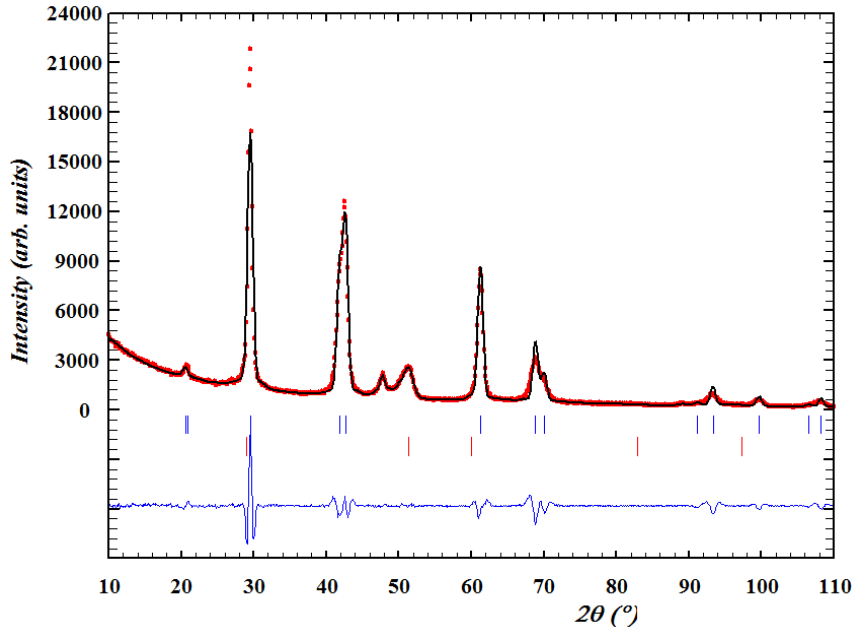


**Figure C.4.** Le Bail fit of the in-plane diffraction pattern for $m = 4$. Blue tick marks indicate the position of SnSe reflections and red tick marks indicate the position of $TiSe_2$ reflections. The reflection at approximately 47° is the (110) reflection of $SnSe_2$.

## C.2. Surface $SnSe_2$ in $[(SnSe)_{1+\delta}]_mTSe_2$

Cross sectional HAADF-STEM image of $(SnSe)_{1.2}TiSe_2$ displaying both the top and bottom interface of the film. $SnSe_2$ is visible on the top of the film as a result of excess Sn and Se migrating to the surface.

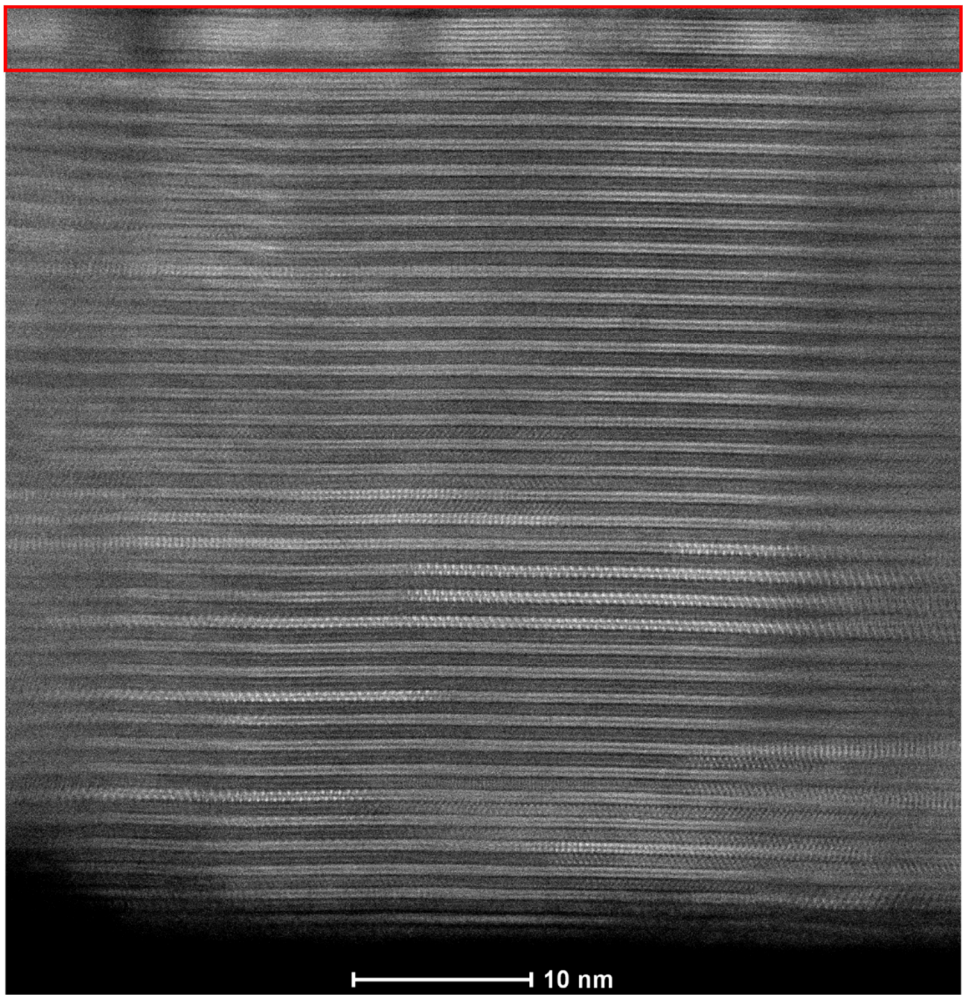


**Figure C.5.** HAADF-STEM of $(SnSe)_{1.2}TiSe_2$ showing $SnSe_2$ on the surface, outlined in red.

## C.3. Density Functional Theory on Defects in SnSe

To explain the different structural distortions that are seen in the HAADF-STEM images (Figure 10.5 in Chapter X), structural relaxation calculations were performed on distorted TlI structure shown in Figure C.6. The type I distortion is a shift of the top bilayer by the vector $\left(\frac{a}{2}, 0, 0\right)$, and type II describes a shift of the top bilayer along $\left(\frac{a}{2}, \frac{b}{2}, 0\right)$. As Table C.1 shows, the in-plane lattice parameters of the distorted types deviate by less than 0.005 Å from the undistorted type, so it would be impossible to resolve these differences using the x-ray diffraction we employed.

The energy differences between the distorted and undistorted TlI structures are very small with less than 4 meV per formula unit, so there is little energy loss from adopting the distorted structure instead of the undistorted structure. The energy of type II is practically the same as the energy of the undistorted TlI structure. Comparing those two structures, one can see that along each axis, one unit cell of the undistorted TlI structure (top two bilayers along *a* and bottom two bilayers along *b*) is visible along with an extra layer that is shifted by half a unit cell. This results in an equal number of Sn-Sn, Sn-Se, and Se-Se stackings in each structure, which explains why the energies are equal. The overall similar energies indicate that the structure observed in the HAADF-STEM images is a result of nucleation and growth kinetics rather than thermodynamic stability.

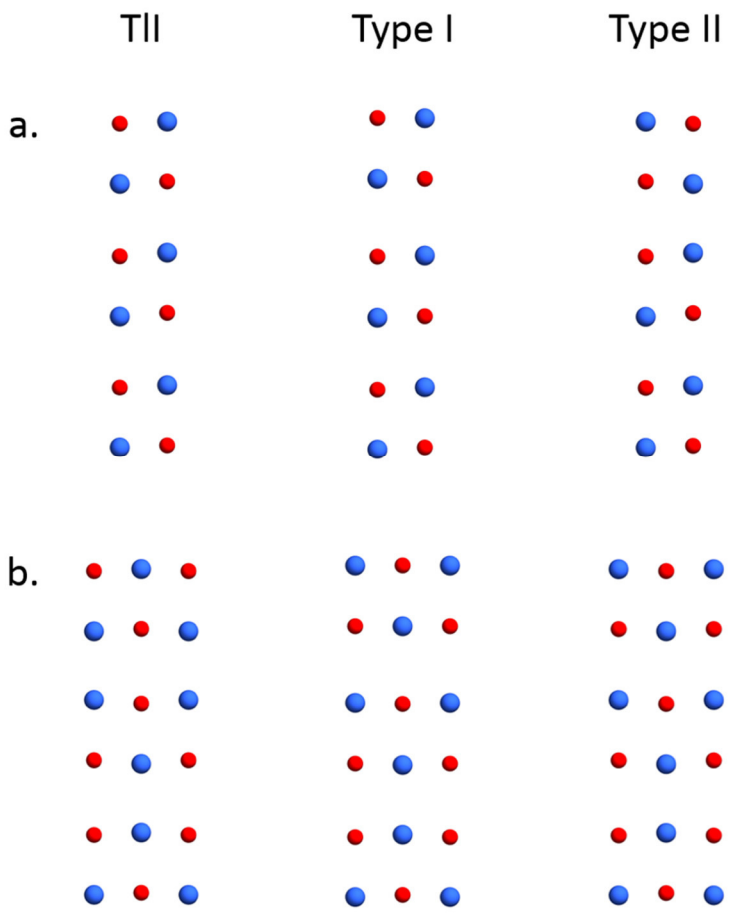


**Figure C.6.** Relaxed structures of an (010) slab of SnSe with three bilayers in the TlI structure and its distorted relatives (see text) as viewed along (a) the [100] axis and (b) the [010] axis. Sn atoms are blue and Se atoms are red.

**Table C.1.** In-plane lattice parameters *a* and *b* of the structures shown in Figure S6, and the energy differences per formula unit between these structures and the undistorted slab in the TlI structure $\Delta E_{\mathrm{TlI}}$. The energy difference per formula unit to a (001) slab of three bilayers in the GeS structure $\Delta E_{\mathrm{GeS}}$ is added for comparison.

| Structure | *a* (Å) | *b* (Å) | $\Delta E_{\mathrm{TlI}}$/f.u. (meV) | $\Delta E_{\mathrm{GeS}}$/f.u. (meV) |
|---|---|---|---|---|
| TlI | 4.301 | 4.309 | 0 | 15 |
| Type I | 4.301 | 4.313 | 3.7 | 19 |
| Type II | 4.304 | 4.305 | 0.2 | 15 |

APPENDIX D

SUPPLEMENTAL MATERIAL TO CHAPTER XI

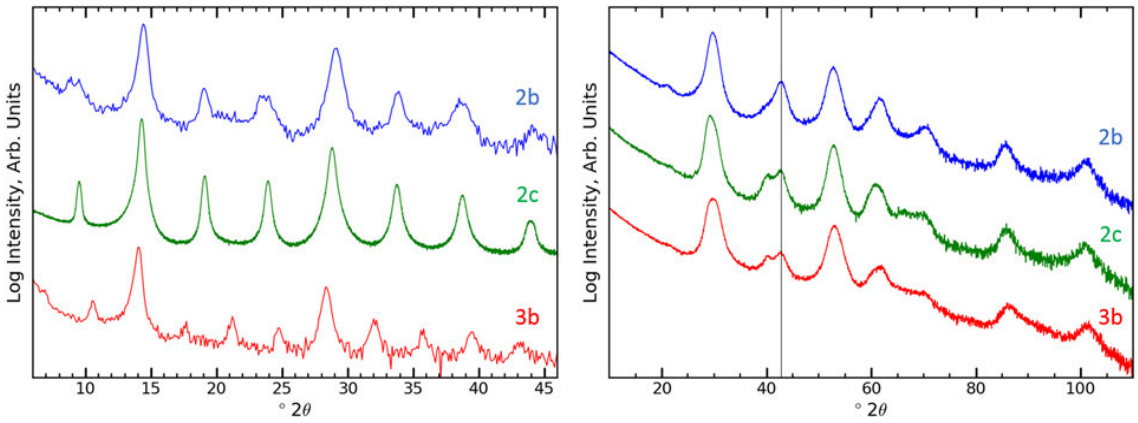


**Figure D.1.** (left) 00*l* XRD scans for samples 2b and 2c ($n$ = 2) and 3b ($n$ = 3). (right) *hk*0 XRD scans for the same samples. The black line at ~42° 2$\theta$ serves to highlight the shoulder present on left side of the BiSe (020) reflections for all three samples. Although all expected 00*l* reflections are present in these samples, some have weak intensities (2b and 3b) or misshapen peaks (2b). Hence although sample 2b has a measured Bi/Nb ratio similar to that of 2a, the weaker and somewhat misshaped XRD intensities suggest that the sample is not as well-formed. This could be due to the right ratio of Bi and Nb in the precursor, but too much absolute material in each layer of the precursor to form the targeted compound (the overall film thickness of the sample measured using XRR was greater than that predicted based on the number of repeat units deposited in the precursor times the repeat unit thickness in the annealed sample). Interestingly, the 00*l* scan for sample 2c suggests that despite a measured Bi/Nb ratio of only 0.95, this sample formed with a high degree of crystallographic alignment to the substrate. A similar observation is made for sample 3b, with a measured Bi/Nb ratio of only 0.91. All of these samples show a rectangular basal plane, instead of the square basal plane found in the higher quality or on-stoichiometry compounds. These observations suggest that the ratio of Bi/Nb in the film or the absolute amount of material within the precursor layers also influences the BiSe bilayer structure.

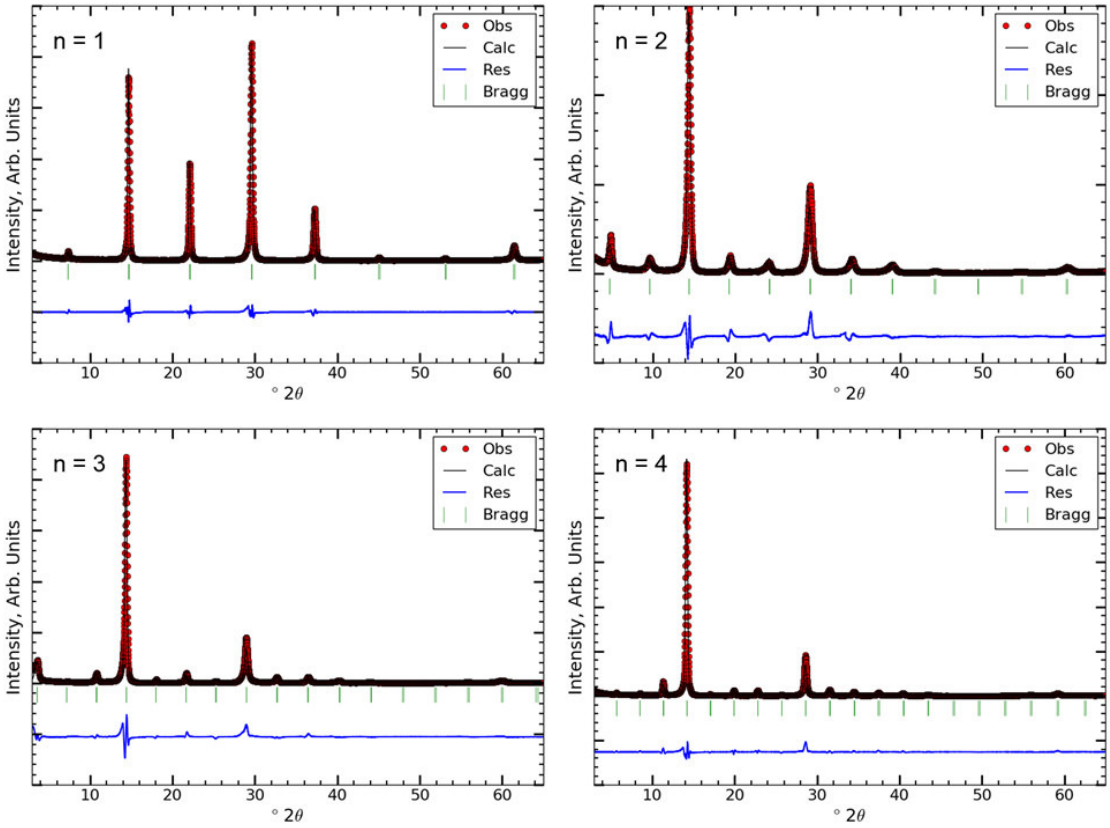


**Figure D.2.** Comparison of observed XRD data (red circles) with refined model fit (black line) for the $n = 1 – 4$ samples. The blue trace plots the residuals of the model fit and the green vertical lines mark the locations of Bragg reflections.

**Table D.1.** Rietveld refinement results from specular X-ray diffraction data for samples of $[(BiSe)_{1+\delta}]_1(NbSe_2)_n$ with $n = 1$ and 3. The refinements were carried out using the space group $P\bar{3}m1$.

| | $n = 1$ | $n = 3$ |
|---|---|---|
| Composition from refinement | $[BiSe_{1.01}]_1(NbSe_2)_1$ | $[BiSe_{0.99}]_1(NbSe_2)_3$ |
| Composition from XRF | $[BiSe_{1.12}]_1(NbSe_2)_1$ | $[BiSe_{1.13}]_1(NbSe_2)_3$ |
| Radiation | Bruker D8, Cu $K_\alpha$ | Bruker D8, Cu $K_\alpha$ |
| 2θ range (degrees) | $3 \leq 2\theta \leq 65$ | $3 \leq 2\theta \leq 65$ |
| $c$ (Å) | 12.08(1) | 24.683(4) |
| Reflections in refinement | 8 | 17 |
| Number of variables | 12 | 16 |
| $R_F = \Sigma \lvert F_o - F_c \rvert / \Sigma F_o$ | 0.0103 | 0.0108 |
| $R_I = \Sigma \lvert I_o - I_c \rvert / \Sigma I_o$ | 0.0130 | 0.0114 |
| $R_{wP} = [\Sigma w_i \lvert y_{oi} - y_{ci} \rvert^2 / \Sigma w_i \lvert y_{oi} \rvert^2]^{1/2}$ | 0.129 | 0.297 |
| $R_P = \Sigma \lvert y_{oi} - y_{ci} \rvert / \Sigma \lvert y_{oi} \rvert$ | 0.0844 | 0.237 |
| $R_e = [(N-P+C)/(\Sigma w_i y^2_{oi})]^{1/2}$ | 0.0452 | 0.0468 |
| $\chi^2 = (R_{wP}/R_e)^2$ | 8.10 | 40.2 |
| **Atom Parameters** | | |
| Nb1 in 1$a$ (0) | | |
| Occ. | 1.0 | 1.0 |
| Se1 in 2$c$ ($z$), $z$ | 0.1346(1) | 0.0652(1) |
| Occ. | 2.0 | 2.0 |
| Se2 in 2$c$ ($z$), $z$ | | 0.1914(1) |
| Occ. | | 1.0 |
| Nb2 in 2$c$ (0), $z$ | | 0.2555(1) |
| Occ. | | 2.0 |
| Se3 in 2$c$ ($z$) | | 0.3209(1) |
| Occ. | | 2.0 |
| Bi in 2$c$ ($z$), $z$ | 0.3757(3) | 0.4396(1) |
| Occ. | 1.01(1) | 0.99(1) |
| Se4 in 2$c$ ($z$), $z$ | 0.3977(6) | 0.4606 |
| Occ. | 1.01(1) | 0.99(1) |

**Table D.2.** Rietveld refinement results from specular X-ray diffraction data for samples of $[(BiSe)_{1+\delta}]_1(NbSe_2)_n$ with $n = 2$ and 4. The refinements were carried out using the space group $P\bar{3}m1$.

| | $n = 2$ | $n = 4$ |
|---|---|---|
| Composition from refinement | $[BiSe_{0.99}]_1(NbSe_2)_2$ | $[BiSe_{1.03}]_1(NbSe_2)_4$ |
| Composition from XRF | $[BiSe_{1.14}]_1(NbSe_2)2$ | $[BiSe_{1.12}]_1(NbSe_2)_4$ |
| Radiation | Bruker D8, Cu $K_\alpha$ | Bruker D8, Cu $K_\alpha$ |
| 2θ range (degrees) | $3 \leq 2\theta \leq 65$ | $3 \leq 2\theta \leq 65$ |
| $c$ (Å) | 18.447(8) | 31.231(6) |
| Reflections in refinement | 12 | 21 |
| Number of variables | 15 | 17 |
| $R_F = \Sigma \lvert F_o - F_c \rvert / \Sigma F_o$ | 0.0325 | 0.0778 |
| $R_I = \Sigma \lvert I_o - I_c \rvert / \Sigma I_o$ | 0.0598 | 0.0581 |
| $R_{wP} = [\Sigma w_i \lvert y_{oi} - y_{ci} \rvert^2 / \Sigma w_i \lvert y_{oi} \rvert^2]^{1/2}$ | 0.235 | 0.208 |
| $R_P = \Sigma \lvert y_{oi} - y_{ci} \rvert / \Sigma \lvert y_{oi} \rvert$ | 0.201 | 0.148 |
| $R_e = [(N-P+C)/(\Sigma w_i y^2_{oi})]^{1/2}$ | 0.0637 | 0.0487 |
| $\chi^2 = (R_{wP}/R_e)^2$ | 13.6 | 18.2 |
| **Atom Parameters** | | |
| Se1 in 2$c$ ($z$), $z$ | 0.0838(1) | 0.0531(1) |
| Occ. | 2.0 | 2.0 |
| Nb1 in 2$c$ ($z$), $z$ | 0.1715(1) | 0.1051(1) |
| Occ. | 2.0 | 2.0 |
| Se2 in 2$c$ ($z$) | 0.2597(1) | 0.1559(1) |
| Occ. | 2.0 | 2.0 |
| Se3 in 2$c$ ($z$) | | 0.2540(1) |
| Occ. | | 2.0 |
| Nb2 in 2$c$ ($z$) | | 0.3055(1) |
| Occ. | | 2.0 |
| Se4 in 2$c$ ($z$) | | 0.3586(1) |
| Occ. | | 2.0 |
| Bi in 2$c$ ($z$), $z$ | 0.4178(1) | 0.4520(1) |
| Occ. | 0.99(1) | 1.03(1) |
| Se5 in 2$c$ ($z$), $z$ | 0.4464(1) | 0.4684(1) |
| Occ. | 0.99(1) | 1.03(1) |

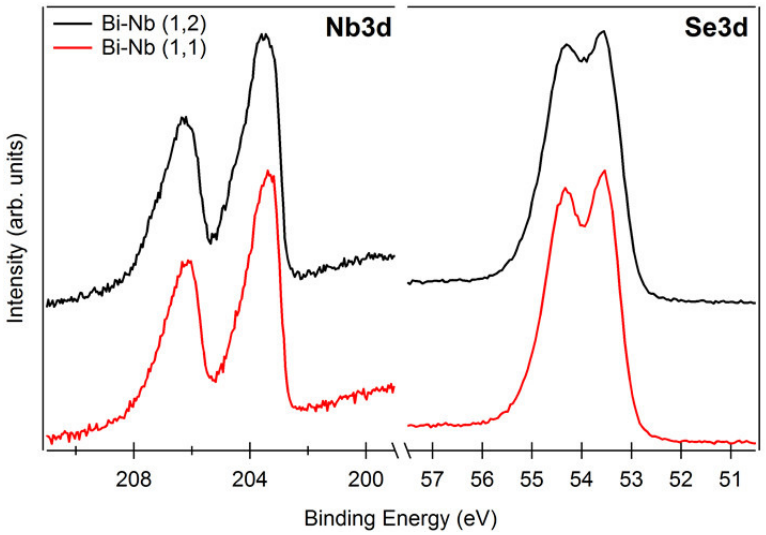


**Figure D.3.** Core level XPS spectra for Nb 3d and Se 3d from the $n = 1$ (red) and $n = 2$ (black) compounds. The small changes in the peak shapes of the Se and Nb spectra be attributed to a change in the ratio of Se bound in $NbSe_2$ relative to Se bound in BiSe and a change of the environment of the $NbSe_2$ layers (no longer symmetrical).

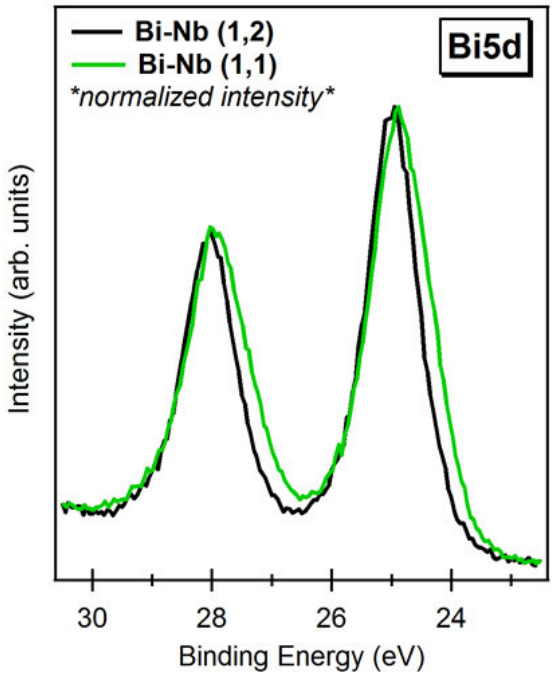


**Figure D.4.** Overlaid Bi5d core level spectra of the $n = 1$ (green) and n = 2 (black) compounds. The high binding energy side of the peaks is the same, while the low binding energy side is broadened for the $n = 1$ compound relative to $n = 2$, indicating there is an additional component.

REFERENCES CITED

## CHAPTER I


(1) Jansen, M. *Angew. Chemie Int. Ed.* 2002, *41*, 3746.

(2) Tipton, W. W.; Hennig, R. G. *J. Phys. Condens. Matter*. **2013**, *25*, 495401.

(3) Schön, J. C. *Process. Appl. Ceram.* **2015**, *9*, 157.

(4) Corey, E. J. *Angew. Chemie Int. Ed.* **1991**, *30*, 455.

(5) Law, J.; Zsoldos, Z.; Simon, A.; Reid, D.; Liu, Y.;Knew, S. Y.; Johnson, A. P.; Major, S.; Wade, R. A.; Ando, H. Y. *J. Chem. Inf. Model*. **2009**, *49*, 593.

(6) Davis, M. E.; Lobo, R. F. *Chem. Mater.* **1992**, *4*, 756.

(7) Goebel, T.; Prots, Y.; Ormeci, A.; Pecher, O.; Haarmann, F. *Z. Anorg. Allg. Chem.* **2011**, *637*, 1982.

(8) Pecher, O.; Esters, M.; Görne, A.; Mausolf, B.; Ormeci, A.; Haarmann, F. *Z. Anorg. Allg. Chem.* **2014**, *640*, 2169.

(9) Gopalakrishnan, J. *Chem. Mater.* **1995**, *7*, 1265.

(10) Gopalakrishnan, J.; Bhuvanesh, N. S. P.; Rangan, K. K. *Curr. Opin. Solid State Mater. Sci.* **1996**, *1*, 285.

(11) Johnson, D. C. *Curr. Opin. Solid State Mater. Sci*. **1998**, *3*, 159.

(12) Fister, L.; Li, X.-M.; McConnell, J.; Novet, T.; Johnson, D. C. *J. Vac. Sci. Technol. A* **1993**, *11*, 3014.

(13) Phung, T. M.; Jensen, J. M.; Johnson, D. C.; Donovan, J. J.; McBurnett, B. G. *X-Ray Spectrom*. **2008**, *37*, 608.

(14) Sitko, R.; Zawisza, B. "Quantification in X-Ray Fluorescence Spectrometry". In: *X-Ray Spectrosc.*; Sharma, S. K., Ed.; InTech, 2012; p. 137–162.

(15) Fukuto, M.; Hornbostel, M. D.; Johnson, D.C. *J. Am. Chem. Soc.* **1994**, *116*, 9136.

(16) Fister, L.; Johnson, D. C. *J. Am. Chem. Soc.* **1992**, *114*, 4639.

(17) Walser, R. M.; Bené, R. W. *Appl. Phys. Lett.* **1976**, *28*, 624.

(18) Köster, W.; Gödecke, T. "Fe-Si Phase Diagram". In: *ASM Alloy Phase Diagrams Database*; P. Villars, H. Okamoto, K. Cenzual, Eds.; ASM International, Materials Park, OH, 2016; http://www.asminternational.org.

(19) Novet, T.; Johnson, D. C. *J. Am. Chem. Soc*. **1991**, *113*, 3398.

(20) Novet, T.; McConnell, J. M.; Johnson, D. C. *Chem. Mater.* **1992**, *4*, 473.

(21) Gorelkin, O. S.; Mikhailov, V. S. *Russ. J. Phys. Chem*. *(English Transl.)* **1971**, *45*, 1523.

(22) Jounel, B.; Mathieu, J.-C.; Desré, P. *Comptes Rendus Hebd. Des Séances l'Académie Des Sci. Série C, Sci. Chim.* **1968**, *266*, 773.

(23) Sommer, F. *J. Therm. Anal.* **1988**, *33*, 15.

(24) Oyelaran, O.; Novet, T.; Johnson, C. D.; Johnson, D. C. *J. Am. Chem. Soc.* **1996**, *118*, 2422.

(25) Sergent, M.; Chevrel, R. *Comptes Rendus Hebd. Des Séances l'Académie Des Sci. Sér*ie C, *Sci. Chim.* **1972**, *274*, 1965.

(26) Flükinger, R.; Baillif, R.; Walker, E. *Mater. Res. Bull.* **1978**, *13*, 743.

(27) Fister, L.; Johnson, D. C.; Brown, R. *J. Am. Chem. Soc.* **1994**, *116*, 629.

(28) Schneidmiller, R.; Hornbostel, M. D.; Johnson, D. C. *Inorg. Chem.* **1997**, *36*, 5894.

(29) Schneidmiller, R.; Bentley, A.; Hornbostel, M. D.; Johnson, D. C. *J. Am. Chem. Soc.* **1999**, *121*, 3142.

(30) Hornbostel, M. D.; Hyer, E. J.; Thiel, J.; Johnson, D. C. *J. Am. Chem. Soc.* **1997**, *119*, 2665.

(31) Sellinschegg, H.; Stuckmeyer, S. L.; Hornbostel, M. D.; Johnson, D.C. *Chem. Mater.* **1998**, *10*, 1096.

(32) Nolas, G. S.; Yoon, H.; Sellinschegg, H.; Smalley, A.; Johnson, D.C. *Appl. Phys. Lett.* **2005**, *86*, 42111.

(33) Anderson, M. D.; Thompson, J. O.; Johnson, D. C. *Chem. Mater.* **2013**, *25*, 3996.

## CHAPTER II

(1) Hirohata, A.; Takanashi, K. *J. Phys. D Appl. Phys.* **2014**, *47*, 193001.

(2) Žutić, I.; Fabian, J.; Das Sarma, S. *Rev. Mod. Phys.* **2004**, *76*, 323.

(3) Coey, J. M. D.; Chien, C. L. *MRS Bull.* **2003**, *28*, 720.

(4) Bibes, M.; Barthélémy, A. *IEEE Trans. Electron Devices* **2007**, *54*, 1003.

(5) Lotgering, F. K. *Solid State Commun.* **1964**, *2*, 55.

(6) Bouchard, R. J.; Russo, P. A.; Wold, A. *Inorg. Chem.* **1965**, *4*, 685.

(7) Baltzer, P. K.; Lehmann, H. W.; Robbins, M. *Phys. Rev. Lett.* **1965**, *15*, 493.

(8) Menyuk, N. *J. Appl. Phys.* **1966**, *37*, 1387.

(9) Baltzer, P. K.; Wojtowicz, P. J.; Robbins, M.; Lopatin, E. *Phys. Rev.* **1966**, *151*, 367.

(10) Goodenough, J. B. *Solid State Commun.* **1967**, *5*, 577.

(11) Robbins, M.; Lehmann, H. W.; White, J.G. *J. Phys. Chem. Solids* **1967**, *28*, 897.

(12) Bongers, P. F. *J. Appl. Phys.* **1969**, *40*, 958.

(13) Nakatani, I.; Nosé, H.; Masumoto, K. *J. Phys. Chem. Solids* **1977**, *39*, 743.

(14) Ramirez, A. P.; Cava, R.J.; Krajewski, J. *Nature* **1997**, *386*, 156.

(15) Jendrzejewska, I.; Mydlarz, T.; Okońska-Kozłowska, I.; Heimann, J. *J. Magn. Magn. Mater.* **1998**, *186*, 381.

(16) Groń, T.; Maciążek, E.; Heimann, J.; Kusz, J.; Okońska-Kozłowska, I.; Bärner, K.; Kleeberg, Ch. *Phys. B Condens. Matter.* **1998**, *254*, 84.

(17) Warczewski, J.; Krok-Kowalski, J. *J. Phys. Chem. Solids* **2003**, *64*, 1609.

(18) Krok-Kowalski, J.; Warczewski, J.; Koroleva, L. I.; Krajewski, K.; Gusin, P.; Duda, H.; Zajdel, P.; Pacyna, A.; Mydlarz, T.; Matyjasik, S.; Demin, R. V. *J. Alloys Compd.* **2004**, *377*, 53.

(19) Suzuyama, T.; Awaka, J.; Yamamoto, H.; Ebisu, S.; Ito, M.; Suzuki, T.; Nakama, T.; Yagasaki, K.; Nagata, S. *J. Solid State Chem.* **2006**, *179*, 140.

(20) Berry, F. J.; Dmitrieva, T. V.; Ovanesyan, N. S.; Lyubutin, I. S.; Thomas, M. F.; Sarkisyan, V. A.; Ren, X.; Aminov, T. G.; Shabunina, G. G.; Rudenko, V.; Vorotynov, A.; Dubinskaya, Y. L. *J. Phys. Condens. Matter.* **2007**, *19*, 266204.

(21) Ohgushi, K.; Okimoto, Y.; Ogasawara, T.; Miyasaka, S.; Tokura, Y. *J. Phys. Soc. Japan.* **2008**, *77*, 034713.

(22) Berry, F. J.; Lyubutin, I. S.; Moore, E. A.; Thomas, M. F.; Dmitrieva, T. V. *Mater. Chem. Phys.* **2009**, *113*, 714.

(23) Bordács, S.; Kézsmárki, I.; Ohgushi, K.; Tokura, Y. *New J. Phys.* **2010**, *12*, 053039.

(24) Tsoi, G. M.; Wenger, L. E.; Wang, Y.-H. A.; Gupta, A. *J. Magn. Magn. Mater.* **2010**, *322*, 142.

(25) Ramasamy, K.; Sims, H.; Gupta, R. K.; Kumar, D.; Butler, W. H.; Gupta, A. *Chem. Mater.* **2013**, *25*, 4003.

(26) Pankrats, A. I.; Vorotynov, A. M.; Tugarinov, V. I.; Zharkov, S. M.; Velikanov, D. A.; Abramova, G. M.; Zeer, G. M.; Ramasamy, K.; Gupta, A. *J. Appl. Phys.* **2014**, *116*, 054302.

(27) Szymczak, R.; Szewczyk, A.; Baran, M.; Tsurkan, V. V. *J. Magn. Magn. Mater.* **1990**, *83*, 481.

(28) Wang, Y. H. A.; Bao, N.; Shen, L.; Padhan, P.; Gupta, A. *J. Am. Chem. Soc.* **2007**, *129*, 12408.

(29) Berzhansky, V. N.; Drokin, N. A.; Ivanov, V. I.; Kononov, V. P.; Edelman, I. S.; Havrichkov, S. A.; Chernov, V. K.; Shishkov, A. G.; Pirogova, A. M. *Thin Solid Films* **1990**, *190*, 199.

(30) Bettinger, J. S.; Chopdekar, R. V.; Liberati, M.; Neulinger, J. R.; Chshiev, M.; Takamura, Y.; Alldredge, L. M. B.; Arenholz, E.; Idzerda, Y. U.; Stacy, A. M.; Butler, W. H.; Suzuki, Y. *J. Magn. Magn. Mater.* **2007**, *318*, 65.

(31) Anderson, M. D.; Thompson, J. O.; Johnson, D. C. *Chem. Mater.* **2013**, *25*, 3996.

(32) Fister, L.; Li, X.-M.; McConnell, J.; Novet, T.; Johnson, D. C. *J. Vac. Sci. Technol. A.* **1993**, *11*, 3014.

(33) Akselrud, L.; Y. Grin, Y. *J. Appl. Crystallogr.* **2014**, *47*, 803.

(34) Rietveld, H. M. *J. Appl. Crystallogr.* **1969**, *2*, 65.

(35) Roisnel, T.; Rodríguez-Carvajal, J. *Mater. Sci. Forum* **2001**, *378-381*, 118.

(36) Okońska-Kozlowska, I.; Kopyczok, J.; Lutz, H. D.; Stingl, T. *Acta Crystallogr. Sect. C Cryst. Struct. Commun.* **1993**, *49*, 1448.

(37) Zhang, L.; Fan, J.; Zhu, X.; Ning, W.; Qu, Z.; Ge, M.; Pi, L.; Zhang, Y. *Appl. Phys. A.* **2013**, *113*, 201.

(38) Colominas, C. *Phys. Rev.* **1967**, *153*, 558.

## CHAPTER III


(1) Hirohata, A.; Sukegawa, H.; Yanagihara, H.; Zutic, I.; Seki, T.; Mizukami, S.; Swaminathan, R. *IEEE Trans. Magn.* **2015**, *51*, 1.

(2) Borisov, P.; Hochstrat, A.; Shvartsman, V. V.; Kleemann, W.; Hauck, P. M. *Integrated Ferroelectrics* **2008**, *99*, 69.

(3) Lu, Y. X.; Claydon, J. S.; Ahmad, E.; Xua, Y. B. *J. Appl. Phys.* **2005**, *97*, 10C313.

(4) Majumdar, S.; van Dijken, S. *J. Phys. D: Appl. Phys.* **2013**, *47*, 034010.

(5) Brändle, H.; Schoenes, J.; Wachter, P.; Hulliger, F.; Reim, W. *Appl. Phys. Lett.* **1990**, *56*, 602.

(6) Kim, D.; Chung, K. C.; Choi, C. J. *J. Korean Phys. Soc.* **2013**, *62(12)*, 2210.

(7) Antonov, V. N.; Antropov, V. P.; Harmon, B. N.; Yaresko, A. N.; Perlov, A. Ya. *Phys. Rev. B* **1999**, *59*, 14552.

(8) Bordacs, S.; Kezsmarki, I.; Ohgushi, K.; Tokura, Y. *New J. Phys.* **2010**, *12*, 053039.

(9) Ogata, F.; Hamajima, T.; Kambara, T.; Gondaira, K.I. *J. Phys. C: Sol. St. Phys.* **1982**, *15*, 3483.

(10) Hahn, H.; de Lorent, C.; Harder, B. *Z. Anorg. Chem.* **1956**, *283*, 138.

(11) Lotgering, F. K.; van Stapele, R. P. *J. Appl. Phys.* **1968**, *39*, 417.

(12) Nakatani, I.; Nose, H.; Masumoto, K. *J. Phys. Chem. Solids* **1978**, *39*, 743.

(13) Zhang, L.; Tong, W.; Fan, J.; Zhang, C.; Li, R.; Zhang, Y. *Eur. Phys. J. B* **2011**, *83*, 325.

(14) Li, R.; Qu, Z.; Zhang, L.; Ling, L.; Tong, W.; Zhang, Y. *Sol. State Commun.* **2010**, *150*, 2289.

(15) Bedanta, S.; Kleemann, W. *Supermagnetism, J. Phys. D: Appl. Phys.* **2009**, *42*, 013001.

(16) Ramesha, K.; Seshadri, R. *Sol. St. Sci.* **2004**, *6*, 841.

(17) Aktas, Y.; Akman, O.; Ozdem, M. *Balkan Phys. Lett.* **2009**, *15*, 151053.

(18) Lin, C.-R.; Yeh, C.-L.; Lu, S.-Z.; Lyubutin, I. S.; Wang, S.-C.; Suzdalev, I. P. *Nanotechnology* **2010**, *21*, 235603.

(19) Kim, D.; Rusnak, A. N.; Parameswaran, S.; Patra, C. R.; Trofimov, V. B.; Harpness, R.; Gedanken, A.; Tver'yanovich, Yu. S. *Glass. Phys. Chem.* **2006**, *32*, 330.

(20) Tsoi, G. M.; Wenger, L. E.; Wang, Y.-H. A.; Gupta, A. *J. Magn. Magn. Mater.* **2010**, *322*, 142.

(21) Rao, M. L.; Shamsuzzoha, M.; Gupta, A. *J. Cryst. Growth* **2007**, *306*, 321.

(22) Ivantsov, R. D.; Edelman, I. S.; Zharkov, S. M.; Velikanov, D. A.; Petrov, D. A.; Ovchinnikov, S. G.; Lin, C.-R.; Li, O.; Tseng, Y.-T. *J. Alloys Comp.* **2015**, *650*, 887.

(23) Berzhansky, V. N.; Drokin, N. A.; Ivanov, V. I.; Kononov, V. P.; Edelman, I. S.; Havrichkov, S. A.; Chernov, V. K.; Shishkov, A. G.; Pirogova, A. M. *Thin Solid Films* **1990**, *190*, 199.

(24) Bettinger, J. S.; Chopdekar, R. V.; Liberati, M.; Neulinger, J. R.; Chshiev, M.; Takamura, Y.; Alldredge, L. M. B.; Arenholz, E.; Idzerda, Y. U.; Stacy, A. M.; Butler, W. H.; Suzuki, Y. *J. Magn. Magn. Mater.* **2007**, *318*, 65.

(25) Anderson, M. D.; Roberts, J.; Kirchgessner, K.; LaRossa, L.; Anderson, I. M.; Johnson, D. C. *Microsc. Microanal.* **2009**, *15(Suppl 2)*, 550.

(26) Anderson, M. D.; Thompson, J. O.; Johnson, D. C. *Chem. Mater.* **2013**, *25*, 3996.

(27) Esters, M.; Liebig, L.; Ditto, J. J.; Falmbigl, M.; Albrecht, M.; Johnson, D. C. *J. Alloys Compd.* **2016**, *671*, 220.

(28) Fister, L.; Li, X.-M.; McConnell, J.; Novet, T.; Johnson, D. C. *J. Vac. Sci. Technol. A* **1993**, *11*, 3014.

(29) Rietveld, H. M. *Z. Kristallogr.* **2010**, *225*, 545.

(30) Volkov, N. V.; Tarasov, A. S.; Eremin, E. V.; Baron, F. A.; Varnakov, S. N.; Ovchinnikov, S. G. *J. Appl. Phys.* **2013**, *114*, 093903.

(31) Lyashchenko, S. A.; Tarasov, I. A.; Varnakov, S. N.; Shevtsov, D. V.; Shvets, V. A.; Zabluda, V. N.; Ovchinnikov, S. G.; Kosyrev, N. N.; Bondarenko, G. V.; Rykhlitskii, S. V. *Tech. Phys.* **2013**, *58*, 1529.

(32) Brandle, H.; Schoenes, J.; Wachter, P.; Hulliger, F.; Reim, W. *J. Magn. Magn. Mater.* **1991**, *93*, 207.

(33) Tarasov, A. S.; Rautskii, M. V.; Lukyanenko, A. V.; Volochaev, M. N.; Eremin, E. V.; Korobtsov, V. V.; Balashev, V. V.; Vikulov, V. A.; Solovyov, L. A.; Volkov, N. V. *J. Alloy Compd.* **2016**, *688*, 1095.

(34) Helman, J. S.; Abeles, B. *Phys. Rev. Lett.* **1976**, *37*, 1429.

(35) Li, P.; Zhang, L. T.; Mi, W. B.; Jiang, E. Y.; Bai, H. L. *J. Appl. Phys.* **2009**, *106*, 033908.

**CHAPTER IV**

(1) Wiegers, G.A. *Prog. Solid State Chem.* **1996**, *24*, 1.

(2) Atkins, R.; Disch, S.; Jones, Z.; Häusler, I.; Grosse, C.; Fischer, S. F.; Neumann, W.; Zschack, P.; Johnson, D. C. *J. Solid State Chem*. **2013**, *202*, 128.

(3) Heideman, C.; Nyugen, N.; Hanni, J.; Lin, Q.; Duncombe, S.; Johnson, D. C.; Zschack, P. *J. Solid State Chem.* **2008**, *181*, 1701.

(4) Lin, Q.; Smeller, M.; Heideman, C. L.; Zschack, P.; Koyano, M.; Anderson, M. D.; Kykyneshi, R.; Keszler, D. A.; Anderson, I. A.; Johnson, D. C. *Chem. Mater.* **2010**, *22*, 1002.

(5) Atkins, R.; Wilson, J.; Zschack, P.; Grosse, C.; Neumann, W.; Johnson, D. C. *Chem. Mater.* **2012**, *24*, 4594.

(6) Moore, D. B.; Stolt, M. J.; Atkins, R.; Sitts, L.; Jones, Z.; Disch, S.; Beekman, M.; Johnson, D. C. *Emerg. Mater. Res.* **2012**, *1*, 292.

(7) Anderson, M. D.; Heideman, C. L.; Lin, Q.; Smeller, M.; Kokenyesi, R.; Herzing, A. A.; Anderson, I. M.; Keszler, D. A.; Zschack, P.; Johnson, D. C. *Angew. Chemie Int. Ed.* **2013**, *52*, 1982.

(8) Moore, D. B.; Beekman, M.; Disch, S.; Zschack, P.; Häusler, I.; Neumann, W.; Johnson, D. C. *Chem. Mater.* **2013**, *25*, 2404.

(9) Heideman, C. L.; Johnson, D. C. *Semicond. Sci. Technol.* **2014**, *29*, 64007.

(10) Alemayehu, M. B.; Mitchson, G.; Hanken, B. E.; Asta, M.; Johnson, D. C. *Chem. Mater.* **2014**, *26*, 1859.

(11) Merrill, D. R.; Moore, D. B.; Coffey, M. N.; Jansons, A. W.; Falmbigl, M.; Johnson, D. C. *Semicond. Sci. Technol.* **2014**, *29*, 64004.

(12) Merrill, D. R.; Moore, D. B.; Ditto, J.; Sutherland, D. R.; Falmbigl, M.; Winkler, M.; Pernau, H.-F.; Johnson, D. C. *Eur. J. Inorg. Chem*. **2015**, *2015* (1), 83.

(13) Hite, O. K.; Nellist, M.; Ditto, J.; Falmbigl, M.; Johnson, D. C. *J. Mater. Res.* **2015**, *8*, 886.

(14) Mitchson, G.; Falmbigl, M.; Ditto, J.; Johnson, D. C. *Inorg. Chem*. **2015**, *54*, 10309.

(15) Wood, S. R.; Merrill, D. R.; Falmbigl, M.; Moore, D. B.; Ditto, J.; Esters, M.; Johnson, D. C. *Chem. Mater.* **2015**, *27*, 6067.

(16) Moore, D. B.; Beekman, M.; Disch, S.; Johnson, D. C. *Angew. Chemie Int. Ed.* **2014**, *53*, 5672.

(17) Falmbigl, M.; Fiedler, A.; Atkins, R. E.; Fischer, S. F.; Johnson, D. C. *Nano Lett.* **2015**, *15*, 943.

(18) Atkins, R.; Dolgos, M.; Fiedler, A.; Grosse, C.; Fischer, S. F.; Rudin, S. P.; Johnson, D. C. *Chem. Mater.* **2014**, *26*, 2862.

(19) Beekman, M.; Disch, S.; Gunning, N.; Johnson, D.C. *Inorg. Chem.* **2015**, *54*, 1091.

(20) Giang, N.; Xu, Q.; Hor, Y.; Williams, A.; Dutton, S.; Zandbergen, H.; Cava, R. J. *Phys. Rev. B.* **2010**, *82*, 24503.

(21) Trump, B. A.; Livi, K. J. T.; McQueen, T. M. *J. Solid State Chem*. **2014**, *209*, (2014) 6.

**CHAPTER V**

(1) Corey, E. J. *Angew. Chem. Int. Ed.* **1991**, *30*, 455.

(2) Hollingsworth, M. *Science* **2002**, *295*, 2410.

(3) DiSalvo, F. J. *Science* **1990**, *247*, 649.

(4) Wiegers, G. A. *Prog. Solid St. Chem.* **1996**, *24*, 1.

(5) Noh, M.; Theil, J.; Johnson, D. C. *Science* **1995**, *270*, 1181.

(6) Hornbostel, M. D.; Hyer, E. J. Thiel, J. P. Johnson, D. C. *J. Amer. Chem. Soc.* **1997**, *119*, 2665.

(7) Oosawa, Y.; Gotoh, Y.; Akimoto, J.; Tsunoda, T.; Sohma, M.; Onoda, M. *Jpn. J. Appl. Phys.* **1992**, *31*, 1096.

(8) Nader, A.; Recherches, C. D.; Fourier, U. J.; Earth, R. *Solid State Commun.* **1992**, *102*, 401.

(9) Auriel, C.; Roesky, R.; Meerschaut, A.; Rouxel, J. *Mat. Res. Bull*. **1993**, *28*, 247.

(10) Heideman, C.; Nyugen, N.; Hanni, J.; Lin, Q.; Duncombe, S.; Johnson, D. C.; Zschack, P. *J. Solid State Chem.* **2008**, *181*, 1701.

(11) Alemayehu, M. B.; Mitchson, G.; Ditto, J.; Hanken, B.E.; Asta, M.; Johnson, D. C. *Chem. Mater.* **2014**, *26*, 1859.

(12) Atkins, R.; Wilson, J.; Zschack, P.; Grosse, C.; Neumann, W.; Johnson, D. C. *Chem. Mater.* **2012**, *24*, 4594.

(13) Anderson, M. D.; Heideman, C. L.; Smeller, M.; Kykyneshi, R.; Herzing, A. A.; Anderson, I. M.; Keszler, D.A.; Zschack, P.; Johnson, D. C. *Angew. Chem. Int. Ed.* **2013**, *52*, 1.

(14) Beekman, M.; Disch, S.; Rouvimov, S.; Kasinathan, D.; Koepernik, K.; Rosner, H.; Zschack, P.; Neumann, W. S.; Johnson, D. C. *Angew. Chem. Int. Ed.* **2013**, *52*, 13211.

(15) van der Pauw, L. J. *Philips Tech. Rev.* **1958**, *20*, 220.

(16) Moore, D. B.; Beekman, M.; Disch, S.; Johnson, D. C. *Angew. Chem. Int. Ed.* **2014**, *53*, 5672.

(17) Karim, S.; Sawada, J.; Alamgir, Z.; Husnine, S. M. *Theor. Comput. Sci.* **2013**, *475*, 103.

**CHAPTER VI**

(1) Wiegers, G. A. *Prog. Solid State Chem.* **1996**, *24*, 1.

(2) Alemayehu, M. B.; Ta, K.; Falmbigl, M.; Johnson, D. C. *J. Am. Chem. Soc.* **2015**, *137*, 4831.

(3) Falmbigl, M.; Fiedler, A.; Atkins, R. E.; Fischer, S. F.; Johnson, D. C. *Nano Lett.* **2015**, 15, 943.

(4) Beekman, M.; Heideman, C. L.; Johnson, D. C. *Semicond. Sci. Technol.* **2014**, *29*, 64012.

(5) Alemayehu, M. B.; Falmbigl, M.; Ta, K.; Johnson, D. C.; *ACS Nano* **2015**, *9*, 4427.

(6) Esters, M.; Alemayehu, M. B.; Jones, Z.; Nguyen, N.T.; Anderson, M. D.; Grosse, C.; Fischer, S. F.; Johnson, D. C. *Angew. Chemie - Int. Ed.* **2015**, *54*, 1130.

(7) Gunning, N. S.; Feser, J.; Beekman, M.; Cahill, D. G.; Johnson, D. C. *J. Am. Chem. Soc.* **2015**, *137*, 8803.

(8) Noh, M.; Thiel, J.; Johnson, D. C. *Adv. Sci.* **1995**, *270*, 1181.

(9) Noh, M.; Johnson, C. D.; Hornbostel, M. D.; Thiel, J.; Johnson, D. C. *Chem. Mater.* **1996**, *8*, 1625.

(10) Atkins, R.; Disch, S.; Jones, Z.; Haeusler, I.; Grosse, C.; Fischer, S. F.; Neumann, W.; Zschack, P.; Johnson, D. C. *J. Solid State Chem.* **2013**, *202*, 128.

(11) Falmbigl, M.; Putzky, D.; Ditto, J.; Esters, M.; Bauers, S. R.; Ronning, F.; Johnson, D. C. *ACS Nano* **2015**, *9*, 8440.

(12) Fister, L.; Li, X.-M.; McConnell, J.; Novet, T.; Johnson, D. C. *J. Vac. Sci. Technol. A Vacuum, Surfaces, Film* **1993**, *11*, 3014.

(13) Phung, T. M.; Jensen, J. M.; Johnson, D. C.; Donovan, J. J.; McBurnett, B. G. *X-Ray Spectrom.* **2008**, *37*, 608.

(14) Falmbigl, M.; Alemayehu, M. B.; Merrill, D. R.; Beekman, M.; Johnson, D. C. *Cryst. Res. Technol.* **2015**, 50, 464.

(15) Rigoult, J.; Guidi-Morosini, C.; Tomas, A.; Molinie, P. *Acta Crystallogr.* **1982**, *B38*, 1557.

(16) Harbec, J. Y.; Paquet, Y.; Jandl, S. *Can. J. Phys.* **1978**, *56*, 1136.

(17) Wiedemeier, H.; Schnering, H. G. *Z. Kristallogr.* **1978**, *148*, 295.

(18) Chattopadhyay, T.; Pannetier, J.; Schnering, H. G. *J. Phys. Chem. Solids* **1986**, *47*, 879.

(19) Beekman, M.; Disch, S.; Rouvimov, S.; Kasinathan, D.; Koepernik, K.; Rosner, H.; Zschack, P.; Neumann, W. S.; Johnson, D. C. *Angew. Chemie - Int. Ed.* **2013**, *52*, 13211.

(20) Shimada, T.; Ohuchi, F.; Parkinson, B. *J. Vac. Sci. Technol. A Vacuum, Surfaces, Film* **1992**, *10*, 539.

(21) Fernandes, P. A.; Sousa, M. G.; Salomé, P. M. P.; Leitão, J. P.; da Cunha, A. F. *Cryst. Eng. Comm.* **2013**, *15*, 10278.

(22) Novet, T.; Johnson, D. C. *J. Am. Chem. Soc.* **1991**, *113*, 3398.

(23) Blitz, W.; Mecklenburg, W. *Z. Anorg. Allg. Chemie.* **1909**, *64*, 226.

(24) Rost, E.; Gjertsen, L. *Z. Anorg. Allg. Chemie.* **1964**, *328*, 299.

(25) Salem, S. I.; Chang, C.N.; Nash, T. J. *Phys. Rev. B.* **1978**, *18*, 5168.

(26) Agarwal, B. K.; Verma, L. P.; *J. Phys. C Solid St. Phys.* **1970**, *3*, 535.

## CHAPTER VII


(1) Schrödinger, E. *Ann. Phys.* **1926**, *384* (4), 361.

(2) Schrödinger, E. *Ann. Phys.* **1926**, *384* (6), 489.

(3) Levine, I. N. *Quantum Chemistry*, 5th ed.; Prentice Hall: Upper Saddle River, NJ, 1999.

(4) Born, M.; Oppenheimer, R. *Ann. Phys.* **1927**, *84* (20), 457.

(5) Slater, J. C. *Phys. Rev.* **1929**, *34* (10), 1293.

(6) Hohenberg, P.; Kohn, W. *Phys. Rev. B* **1964**, *136* (3), 864.

(7) Kohn, W.; Sham, L. J. *Phys. Rev.* **1965**, *140* (4), A1133.

(8) Perdew, J. P.; Zunger, A. *Phys. Rev. B* **1981**, *23* (10), 5048.

(9) Perdew, J. P.; Burke, K.; Ernzerhof, M. *Phys. Rev. Lett.* **1996**, *77* (18), 3865.

(10) Leung, T. C.; Chan, C. T.; Harmon, B. N. *Phys. Rev. B* **1991**, *44* (7), 2923.

(11) Shen, Z.-X.; List, R. S.; Dessau, D. S.; Wells, B. O.; Jepsen, O.; Arko, A. J.; Barttlet, R.; Shih, C. K.; Parmigiani, F.; Huang, J. C.; Lindberg, P. A. P. *Phys. Rev. B* **1991**, *44* (8), 3604.

(12) Towler, M. D.; Allan, N. L.; Harrison, N. M.; Saunders, V. R.; Mackrodt, W. C.; Aprà, E. *Phys. Rev. B* **1994**, *50* (8), 5041.

(13) Dufek, P.; Blaha, P.; Sliwko, V.; Schwarz, K. *Phys. Rev. B* **1994**, *49* (15), 10170.

(14) Powell, R. J.; Spicer, W. E. *Phys. Rev. B* **1970**, *2* (6), 2182.

(15) Kuiper, P.; Kruizinga, G.; Ghijsen, J.; Sawatzky, G. A.; Verweij, H. *Phys. Rev. B* **1989**, *62* (2), 221.

(16) Hüfner, S.; Steiner, P.; Reinert, F.; Schmitt, H.; Sandl, P. *Zeitschrift für Phys. B Condens. Matter* **1992**, *88* (2), 247.

(17) Hubbard, J. *Proc. R. Soc. London Ser. A - Mathet. Phys. Sci.* **1963**, *276* (1365), 238.

(18) Dudarev, S. L.; Botton, G. A.; Savrasov, S. Y.; Humphreys, C. J.; Sutton, A. P. *Phys. Rev. B* **1998**, *57* (3), 1505.

(19) Heyd, J.; Scuseria, G. E.; Ernzerhof, M. *J. Chem. Phys.* **2003**, *118* (18), 8207.

(20) Bloch, F. *Zeitschrift für Phys.* **1929**, *52* (7), 555.

(21) Blöchl, P. E. *Phys. Rev. B* **1994**, *50* (24), 17953.

(22) Grimme, S. *J. Comput. Chem.* **2006**, *27* (15), 1787.

(23) Grimme, S.; Antony, J.; Ehrlich, S.; Krieg, H. *J. Chem. Phys.* **2010**, *132* (15).

(24) Tkatchenko, A.; Scheffler, M. *Phys. Rev. Lett.* **2009**, *102* (7), 73005.

(25) Tkatchenko, A.; DiStasio, R. A.; Car, R.; Scheffler, M. *Phys. Rev. Lett.* **2012**, *108* (23), 236402.

(26) Dion, M.; Rydberg, H.; Schröder, E.; Langreth, D. C.; Lundqvist, B. I. *Phys. Rev. Lett.* **2004**, *92* (24), 246401.

(27) Klimeš, J.; Bowler, D. R.; Michaelides, A. *J. Phys. Condens. Matter* **2010**, *22* (2), 22201.

(28) Klimeš, J.; Bowler, D. R.; Michaelides, A. *Phys. Rev. B* **2011**, *83* (19), 195131.

(29) Zhang, Y.; Yang, W. *Phys. Rev. Lett.* **1998**, *80* (4), 890.

(30) Becke, A. D. *J. Chem. Phys.* **1986**, *84* (8), 4524.

(31) Becke, A. D. *Phys. Rev. A* **1988**, *38* (6), 3098.

(32) Reich, S.; Maultzsch, J.; Thomsen, C.; Ordejo, P. *Phys. Rev. B* **2002**, *66* (3), 35412.

(33) Bostwick, A.; Ohta, T.; Seyller, T.; Horn, K.; Rotenberg, E. *Nat. Phys.* **2007**, *3* (1), 36.

(34) Wigner, E.; Seitz, F. *Phys. Rev.* **1933**, *43*, 804.

(35) Wigner, E.; Seitz, F. *Phys. Rev.* **1934**, *46*, 509.

(36) Dronskowski, R. *Computational Chemistry of Solid State Materials*; WILEY-VCH Verlag: Weinheim, 2005.

(37) Wills, J. M.; Alouani, M.; Andersson, P.; Delin, A.; Eriksson, O.; Grechnyev, O. In *Full-Potential Electronic Structure Method: Energy and Force Calculations with Density Functional and Dynamical Mean Field Theory*; Springer Berlin Heidelberg: Berlin, Heidelberg, 2010; pp 35–46.

(38) Andersen, O. K. *Phys. Rev. B* **1975**, *12* (8), 3060.

(39) Andersen, O. K.; Jepsen, O. *Phys. Rev. Lett.* **1984**, *53* (27), 2571.

(40) Hughbanks, T.; Hoffmann, R. *J. Am. Chem. Soc.* **1983**, *105* (20), 3528.

(41) Dronskowski, R.; Blöchl, P. E. *J. Phys. Chem.* **1993**, *97* (33), 8617.

(42) Deringer, V. L.; Tchougréeff, A. L.; Dronskowski, R. *J. Phys. Chem. A* **2011**, *115* (21), 5461.

(43) Maintz, S.; Deringer, V. L.; Tchougréeff, A. L.; Dronskowski, R. **2013**, 2557.

## CHAPTER VIII

(1) Novoselov, K. S.; Geim, A. K.; Morozov, S. V.; Jiang, D.; Zhang, Y.; Dubonos, S. V.; Grigorieva, I. V; Firsov, A. A. *Science* **2004**, *306*, 666.

(2) Kim, K. K.; Hsu, A.; Jia, X.; Kim, S.M.; Shi, Y.; Hofmann, M.; Nezich, D.; Rodriguez-Nieva, J. F.; Dresselhaus, M.; Palacios, T.; Kong, J. *Nano Lett.* **2011**, *12*, 161.

(3) Peng, Q.; Ji, W.; De, S. *Comput. Mater. Sci.* **2012**, *56*, 11.

(4) Duan, X.; Wang, C.; Pan, A.; Yu, R.; Duan, X. *Chem. Soc. Rev.* **2015**, *44*, 8859.

(5) Tan, C.; Zhang, H. *Chem. Soc. Rev.* **2015**, *44*, 2713.

(6) Wang, H.; Yuan, H.; Sae Hong, S.; Li, Y.; Cui, Y. *Chem. Soc. Rev.* **2015**, *44* (9), 2664.

(7) Gomes, L. C.; Carvalho, A. *Phys. Rev. B* **2015**, *92* (8), 085406.

(8) Fujimoto, Y.; Koretsune, T.; Saito, S. *J. Ceram. Soc. Japan* **2014**, *122* (5), 346.

(9) Wang, M.-X.; Li, P.; Xu, J.-P.; Liu, Z.-L.; Ge, J.-F.; Wang, G.-Y.; Yang, X.; Xu, Z.-A.; Ji, S.-H.; Gao, C. L.; Qian, D.; Luo, W.; Liu, C.; Jia, J.-F. *New J. Phys.* **2014**, *16* (12), 123043.

(10) Xu, J.-P.; Wang, M.-X.; Liu, Z. L.; Ge, J.-F.; Yang, X.; Liu, C.; Xu, Z.A.; Guan, D.; Gao, C.L.; Qian, D.; Liu, Y.; Wang, Q.-H.; Zhang, F.-C.; Xue, Q.-K.; Jia, J.-F. *Phys. Rev. Lett.* **2015**, *114* (1), 017001.

(11) Geim, A. K.; Grigorieva, I. V. *Nature* **2013**, *499*, 419–425.

(12) Furchi, M. M.; Pospischil, A.; Libisch, F.; Burgdörfer, J.; Mueller, T. *Nano Lett.* **2014**, *14* (8), 4785.

(13) Hong, X.; Kim, J.; Shi, S.-F.; Zhang, Y.; Jin, C.; Sun, Y.; Tongay, S.; Wu, J.; Zhang, Y.; Wang, F. *Nat. Nanotechnol.* **2014**, *9*, 682.

(14) Rivera, P.; Schaibley, J. R.; Jones, A. M.; Ross, J. S.; Wu, S.; Aivazian, G.; Klement, P.; Seyler, K.; Clark, G.; Ghimire, N. J.; Yan, J.; Mandrus, D. G.; Yao, W.; Xu, X. *Nat. Commun.* **2015**, *6*, 6242.

(15) Grønborg, S. S.; Ulstrup, S.; Bianchi, M.; Dendzik, M.; Sanders, C. E.; Lauritsen, J. V.; Hofmann, P.; Miwa, J. A. *Langmuir* **2015**, *31*, 9700.

(16) El-Bana, M. S.; Wolverson, D.; Russo, S.; Balakrishnan, G.; Paul, D. M.; Bending, S. J. *Supercond. Sci. Technol.* **2013**, *26* (12), 125020.

(17) Frindt, R. F. *Phys. Rev. Lett.* **1972**, *28* (5), 299.

(18) Grosse, C.; Alemayehu, M. B.; Falmbigl, M.; Mogilatenko, A.; Chiatti, O.; Johnson, D. C.; Fischer, S. F. *Sci. Rep.* **2016**, *6*, 33457.

(19) Gao, D.; Xue, Q.; Mao, X.; Wang, W.; Xu, Q.; Xue, D. *J. Mater. Chem. C* **2013**, *1* (37), 5909.

(20) Zhang, H.; Liu, L.-M.; Lau, W.-M. *J. Mater. Chem. A* **2013**, *1*, 10821.

(21) Bayard, M.; Sienko, M. J. *J. Solid State Chem.* **1976**, *19* (4), 325.

(22) Xu, K.; Chen, P.; Li, X.; Wu, C.; Guo, Y.; Zhao, J.; Wu, X.; Xie, Y. *Angew. Chemie Int. Ed.* **2013**, *52*, 10477.

(23) Yang, J.; Wang, W.; Liu, Y.; Du, H.; Ning, W.; Zheng, G.; Jin, C.; Han, Y.; Wang, N.; Yang, Z.; Tian, M.; Zhang, Y. *Appl. Phys. Lett.* **2014**, *105* (6), 063109.

(24) Atkins, R.; Disch, S.; Jones, Z.; Häusler, I.; Grosse, C.; Fischer, S. F.; Neumann, W.; Zschack, P.; Johnson, D. C. *J. Solid State Chem.* **2013**, *202*, 128.

(25) Falmbigl, M.; Fiedler, A.; Atkins, R. E.; Fischer, S. F.; Johnson, D. C. *Nano Lett.* **2015**, *15* (2), 943.

*(26)* Goli, P.; Khan, J.; Wickramaratne, D.; Lake, R. K.; Balandin, A. A. *Nano Lett.* - **2012**, 12, 5941.

(27) Samnakay, R.; Wickramaratne, D.; Pope, T. R.; Lake, R. R.; Salguero, T. T.; Balandin, A. A. *Nano Lett.* **2015**, 15, 2965.

(28) Atkins, R.; Dolgos, M.; Fiedler, A.; Grosse, C.; Fischer, S. F.; Rudin, S. P.; Johnson, D. C. *Chem. Mater.* **2014**, *26* (9), 2862.

(29) Fister, L.; Li, X.-M.; McConnell, J.; Novet, T.; Johnson, D. C. *J. Vac. Sci. Technol. A* **1993**, *11* (6), 3014.

(30) Phung, T. M.; Jensen, J. M.; Johnson, D. C.; Donovan, J. J.; McBurnett, B. G. *X-Ray Spectrom.* **2008**, *37*, 608.

(31) Schaffer, M.; Schaffer, B.; Ramasse, Q. *Ultramicroscopy* **2012**, *114*, 62.

(32) van der Pauw, L. J. *Philips Tech. Rev.* **1958**, *26*, 220.

(33) Alemayehu, M. B.; Mitchson, G.; Hanken, B. E.; Asta, M.; Johnson, D. C. *Chem. Mater.* **2014**, *26* (5), 1859.

(34) Kresse, G.; Hafner, J. *Phys. Rev. B* **1993**, *47* (1), 558.

(35) Kresse, G.; Hafner, J. *Phys. Rev. B* **1994**, *49* (20), 14251.

(36) Kresse, G.; Furthmüller, J. *Comput. Mat. Sci.* **1996**, *6* (1), 15.

(37) Kresse, G.; Furthmüller, J. *Phys. Rev. B* **1996**, *54* (16), 11169.

(38) Blöchl, P. E. *Phys. Rev. B* **1994**, *50* (24), 17953.

(39) Kresse, G.; Joubert, D. *Phys. Rev. B* **1999**, *59* (3), 1758.

(40) Perdew, J. P.; Burke, K.; Ernzerhof, M. *Phys. Rev. Lett.* **1996**, *77* (18), 3865.

(41) Dion, M.; Rydberg, H.; Schröder, E.; Langreth, D. C.; Lundqvist, B. I. *Phys. Rev. Lett.* **2004**, *92* (24), 246401.

(42) Román-Pérez, G.; Soler, J. M. *Phys. Rev. Lett.* **2009**, *103* (9), 96102.

(43) Klimeš, J.; Bowler, D. R.; Michaelides, A. *J. Phys. Condens. Matter* **2010**, *22* (2), 22201.

(44) Klimeš, J.; Bowler, D. R.; Michaelides, A. *Phys. Rev. B* **2011**, *83* (19), 195131.

(45) Atkins, R.; Wilson, J.; Zschack, P.; Grosse, C.; Neumann, W.; Johnson, D. C. *Chem. Mater.* **2012**, *24* (23), 4594.

(46) Bauers, S. R.; Merrill, D. R.; Moore, D. B.; Johnson, D. C. *J. Mater. Chem. C* **2015**, *3* (40), 10451.

(47) Merrill, D. R.; Moore, D. B.; Ditto, J.; Sutherland, D. R.; Falmbigl, M.; Winkler, M.; Pernau, H.-F.; Johnson, D. C. *Eur. J. Inorg. Chem.* **2015**, *2015* (1), 83.

(48) de Boer, J. L.; Meetsma, A.; Zeinstra, T. J.; Haange, R. J.; Wiegers, G. A. *Acta Crystallogr. C* **1991**, *47* (5), 924.

(49) van Smaalen, S.; Meetsma, A.; Wiegers, G. A.; de Boer, J. L. *Acta Crystallogr. B* **1991**, *47* (3), 314.

(50) Wiegers, G. A. *Prog. Solid State Chem.* **1996**, *24* (1), 1.

(51) Wiegers, G. A.; Meetsma, A.; de Boer, J. L.; van Smaalen, S.; Haange, R. J. *J. Phys. Condens. Matter* **1991**, *3*, 2603.

(52) Wiegers, G. A.; Meetsma, A.; Haange, R. J.; van Smaalen, S.; de Boer, J. L.; Meerschaut, A.; Rabu, P.; Rouxel, J. *Acta Crystallogr. B* **1990**, *46* (3), 324.

(53) Wiegers, G. A.; Meetsma, A.; van Smaalen, S.; Haange, R. J.; de Boer, J. L. *Solid State Commun.* **1990**, *75* (9), 689.

(54) Meerschaut, A.; Guemas, L.; Auriel, C.; Rouxel, J. *Eur. J. Solid State Inorg. Chem.* **1990**, *27* (4), 557.

(55) Smeller, M. M.; Heideman, C. L.; Lin, Q.; Beekman, M.; Anderson, M. D.; Zschack, P.; Anderson, I. M.; Johnson, D. C. *Z. Anorg. Allg. Chem.* **2012**, *638* (15), 2632.

(56) Moore, D. B.; Beekman, M.; Disch, S.; Zschack, P.; Häusler, I.; Neumann, W.; Johnson, D. C. *Chem. Mater.* **2013**, *25* (12), 2404.

(57) Ren, Y.; Baas, J.; Meetsma, A.; de Boer, J. L.; Wiegers, G. A. *Acta Crystallogr. B* **1996**, *52* (3), 398.

(58) Gotoh, Y.; Onoda, M.; Akimoto, J.; Oosawa, Y. *Jpn. J. Appl. Phys.* **1992**, *30*, L1039.

(59) Gotoh, Y.; Onoda, M.; Akimoto, J.; Goto, M.; Oosawa, Y. *Jpn. J. Appl. Phys.* **1992**, *31*, 3946.

(60) Gotoh, Y.; Goto, M.; Kawaguchi, Y.; Onoda, M. *Mater. Res. Bull.* **1990**, *25* (3), 307.

(61) Wiegers, G. A.; Haange, R. J. *Eur. J. Solid State Inorg. Chem.* **1991**, *28*, 1071.

(62) Wiegers, G. A.; Meetsma, A.; Haange, R. J.; de Boer, J. L. *Mater. Res. Bull.* **1988**, *23* (11), 1551.

(63) Wulff, J.; Meetsma, A.; Haange, R. J.; de Boer, J. L.; Wiegers, G. A. *Synth. Met.* **1990**, *39* (1), 1.

(64) Yarmoshenko, Y. M.; Trofimova, V. A.; Shamin, S. N.; Solovyev, N. V; Kurmaev, E. Z.; Ettema, A. R. H. F.; Haas, C. *J. Phys. Condens. Matter* **1994**, *6* (21), 3993.

(65) Meerschaut, A. *Curr. Opin. Solid State Mater. Sci.* **1996**, *1* (2), 250.

(66) Meerschaut, A.; Auriel, C.; Rouxel, J. *J. Alloys Compd.* **1983**, *183*, 129.

(67) Meerschaut, A.; Deudon, C. *Mater. Res. Bull.* **2001**, *36* (9), 1721.

(68) Meerschaut, A.; Roesky, R.; Lafond, A.; Deudon, C.; Rouxel, J. *J. Alloys Compd.* **1995**, *219* (1), 157.

(69) Meetsma, A.; Wiegers, G. A.; Haange, R. J.; de Boer, J. L. *Acta Crystallogr. A* **1989**, *45* (4), 285.

(70) Onoda, M.; Kato, K.; Gotoh, Y.; Oosawa, Y. *Acta Crystallogr. B* **1990**, *46* (4), 487.

(71) Beekman, M.; Heideman, C. L.; Johnson, D. C. *Semicond. Sci. Technol.* **2014**, *29* (6), 064012.

(72) Falmbigl, M.; Putzky, D.; Ditto, J.; Esters, M.; Bauers, S. R.; Ronning, F.; Johnson, D. C. *ACS Nano* **2015**, *9* (8), 8440.

(73) Barrios-Salgado, E.; Rodríguez-Guadarrama, L. A.; Garcia-Angelmo, A. R.; Campos Álvarez, J.; Nair, M. T. S.; Nair, P.K. *Thin Solid Films* **2016**, *615*, 415.

(74) Wrasse, E. O.; Schmidt, T. M. *Nano Lett.* **2014**, *14*, 5717.

(75) Alemayehu, M. B.; Falmbigl, M.; Ta, K.; Grosse, C.; Westover, R.D.; Bauers, S.R.; Fischer, S.F.; Johnson, D.C. *Chem. Mater.* **2015**, *27* (3), 867.

(76) Falmbigl, M.; Hay, Z.; Ditto, J.; Mitchson, G.; Johnson, D.C. *J. Mater. Chem. C* **2015**, *3* (47), 12308.

(77) Li, F.; Tu, K.; Chen, Z. *J. Phys. Chem.* **2014**, *118*, 21264.

(78) Wasey, A. H. M. A.; Chakrabarty, S.; Das, G.P. *J. Appl. Phys.* **2015**, *117* (6), 064313.

(79) Chhowalla, M.; Shin, H. S.; Eda, G.; Li, L.-J.; Loh, K. P.; Zhang, H. The Chemistry of Two-Dimensional Layered Transition Metal Dichalcogenide Nanosheets. *Nat. Chem.* **2013**, *5* (4), 263.

(80) Hite, O. K.; Nellist, M.; Ditto, J.; Falmbigl, M.; Johnson, D. C. Transport Properties of $VSe_2$ Monolayers Separated by Bilayers of BiSe. *J. Mater. Res.* **2016**, *31* (07), 886.

(81) Alemayehu, M. B.; Falmbigl, M.; Ta, K.; Ditto, J.; Medlin, D. L.; Johnson, D. C. *Angew. Chemie Int. Ed.* **2015**, *54*, 15468.

## CHAPTER IX


(1) Novoselov, K. S.; Geim, A. K.; Morozov, S. V.; Jiang, D.; Zhang, Y.; Dubonos, S. V.; Grigorieva, I. V.; Firsov, A. A. *Science* 2004 *306*, 666.

(2) Novoselov, K. S.; Jiang, D.; Schedin, F.; Booth, T. J.; Khotkevich, V. V.; Morozov, S. V.; Geim, A. K. *Proc. Natl. Acad. Sci.* **2005**, *102*, 10451.

(3) Geim, A.; Novoselov, K. *Nat. Mater.* **2007**, *6*, 183.

(4) Duan, X.; Wang, C.; Pan, A.; Yu, R.; Duan, X. *Chem. Soc. Rev.* **2015**, *44*, 8859.

(5) Chhowalla, M.; Shin, H. S.; Eda, G.; Li, L.-J.; Loh, K. P.; Zhang, H. Nat. Chem. **2013**, *5*, 263.

(6) Lebègue, S.; Eriksson, O. *Phys. Rev. B* **2009**, *79*, 115409.

(7) Kuc, A.; Zibouche, N.; Heine, T. Phys. Rev. B **2011**, *83*, 245213.

(8) Xiao, D.; Liu, G.-B.; Feng, W.; Xu, X.; Yao, W. *Phys. Rev. Lett.* **2012**, *108*, 196802.

(9) Zhuang, H. L.; Hennig, R. G. J. Phys. Chem. C **2013**, *117*, 20440.

(10) Wang, C.-Y.; Guo, G.-Y. *J. Phys. Chem. C* **2015**, *119*, 13268.

(11) Wang, H.; Yuan, H.; Sae Hong, S.; Li, Y.; Cui, Y. Chem. Soc. Rev. **2015**, *44*, 2664.

(12) Pandey, M.; Vojvodic, A.; Thygesen, K. S.; Jacobsen, K. W. J. Phys. Chem. Lett. **2015**, *6*, 1577.

(13) Voiry, D.; Mohite, A.; Chhowalla, M. Chem. Soc. Rev. **2015**, *44*, 2702.

(14) Maniadaki, A. E.; Kopidakis, G.; Remediakis, I. N. Solid State Commun. **2016**, *227*, 33.

(15) Li, W.; Li, J. *Nat. Commun.* **2016**, *7*, 10843.

(16) Tan, T. L.; Ng, M. F.; Eda, G. *J. Phys. Chem. C* **2016**, *120*, 2501.

(17) Zhou, J.; Sun, Q. *J. Am. Chem. Soc.* **2011**, *133*, 15113.

(18) Zhou, Y.; Wang, Z.; Yang, P.; Zu, X.; Yang, L.; Sun, X.; Gao, F. *ACS Nano* **2012**, *6*, 9727.

(19) Zhang, H.; Liu, L.-M.; Lau, W.-M. *J. Mater. Chem. A* **2013**, *1*, 10821.

(20) Kan, M.; Zhou, J.; Sun, Q.; Kawazoe, Y.; Jena, P. *J. Phys. Chem. Lett.* **2013**, *4*, 3382.

(21) Zhang, S.; Li, Y.; Zhao, T.; Wang, Q. Sci. Rep. **2014**, *4*, 5241.

(22) Kan, M.; Adhikari, S.; Sun, Q. *Phys. Chem. Chem. Phys.* **2014**, *16*, 4990.

(23) Li, X.; Yang, J. *J. Mater. Chem. C* **2014**, *2*, 7071.

(24) Ma, Y.; Dai, Y.; Guo, M.; Niu, C.; Zhu, Y.; Huang, B. *ACS Nano* **2012**, *6*, 1695.

(25) Guo, H.; Lu, N.; Wang, L.; Wu, X.; Zeng, X. C. *J. Phys. Chem. C* **2014**, *118*, 7242.

(26) Lv, H. Y.; Lu, W. J.; Shao, D. F.; Liu, Y.; Sun, Y. P. *Phys. Rev. B* **2015**, *92*, 214419.

(27) Manchanda, P.; Sharma, V.; Yu, H.; Sellmyer, D. J.; Skomski, R. *Appl. Phys. Lett.* **2015**, *107*, 032402.

(28) Pan, H. J. Phys. Chem. C **2014**, *118*, 13248.

(29) Zhou, Y.; Yang, C.; Xiang, X.; Zu, X. *Phys. Chem. Chem. Phys.* **2013**, *15*, 14202.

(30) Li, F.; Tu, K.; Chen, Z. *J. Phys. Chem. C* **2014**, *118*, 21264.

(31) Wasey, A. H. M. A.; Chakrabarty, S.; Das, G. P. *J. Appl. Phys.* **2015**, *117*, 064313.

(32) Zhuang, H. L.; Hennig, R. G. *Phys. Rev. B* **2016**, *93*, 054429.

(33) Fex, X. O.; Xiang, G.; Lan, M.; Nie, Y.; Yang, D.; Zhang, X. *RSC Adv.* **2016**, *6*, 31758.

(34) Lebègue, S.; Björkman, T.; Klintenberg, M.; Nieminen, R. M.; Eriksson, O. *Phys. Rev. X* **2013**, *3*, 031002.

(35) Thompson, A. H.; Scanlon, J. C.; Symon, C. R. *Solid State Ionics* **1980**, *1*, 47.

(36) Starnberg, H. I.; Brauer, H. E.; Holleboom, L. J.; Hughes, H. P. Phys. Rev. Lett. **1993**, *70*, 3111.

(37) Brauer, H. E.; Starnberg, H. I.; Holleboom, L. J.; Hughes, H. P. Surf. Sci. **1995**, *331 – 333*, 419.

(38) Brauer, H. E.; Ekvall, I.; Olin, H.; Starnberg, H. I.; Wahlström, E.; Hughes, H. P.; Strocov, V. N. Phys. Rev. B **1997**, *55*, 10022.

(39) Ekvall, I.; Brauer, H. E.; Olin, H.; Starnberg, H. I.; Wahlström, E. *Appl. Phys. A* **1998**, *66*, S197.

(40) Thompson A. H.; Silbernagel, B. G. *Phys. Rev. B* **1979**, *19*, 3420.

(41) Schneemeyer, L. F.; Stacy, A.; Sienko, M. *J. Inorg. Chem.* **1980**, *19*, 2659.

(42) Giambattista, B.; Slough, C. G.; McNairy, W.W.; Coleman, R. V. *Phys. Rev. B* **1990**, 41, 10082.

(43) Kamarchuk, G. V.; Khotkevich, A. V.; Bagatsky, V. M.; Ivanov, V. G.; Molinié, P.; Leblanc, A.; Faulques, E. *Phys. Rev. B* **2011**, *63*, 073107.

(44) Gospodarev, I. A.; Eremenko, A. V.; Ignatova, T. V.; Kamarchuk, G. V.; Kolobov, I. G.; Minaev, P. A.; Syrkin, E. S.; Feodosyev, S. B.; Fil, V. D.; Soreau-Leblanc, A.; Molinie, P.; Faulques, E. C. *Low Temp. Phys.* **2003**, *29*, 151.

(45) Horiba, K.; Ono, K.; Oh, J. H.; Kihara, T.; Nakazono, S.; Oshima, M.; Shiino, O.; Yeom, H. W.; Kakizaki, A.; Y. Aiura, *Phys. Rev. B* **2003**, *68*, 155108.

(46) Eaglesham, D. J.; Withers, R. L.; Bird, D. M. J. Phys. C: Solid State Phys. **1986**, *19*, 359.

(47) Xu, K.; Chen, P.; Li, X.; Wu, C.; Guo, Y.; Zhao, J.; Wu, X.; Xie, Y. *Angew. Chemie Int. Ed.* **2013**, *52*, 10477.

(48) Bayard, M.; Sienko, M. J. *J. Solid State Chem.* **1976**, *19*, 325.

(49) van Bruggen, C. F.; Haas, C. *Solid State Commun.* **1976**, *20*, 251.

(50) Thompson, A. H.; Silbernagel, B. G. *J. Appl. Phys.* **1978**, *49*, 1477.

(51) Wiegers, G. A. *Prog. Solid State Chem.* **1996**, *24*, 1.

(52) Atkins, R.; Disch, S.; Jones, Z.; Häusler, I.; Grosse, C.; Fischer, S. F.; Neumann, W.; Zschack, P.; Johnson, D. C. *J. Solid State Chem.* **2013**, *202*, 128.

(53) Atkins, R.; Dolgos, M.; Fiedler, A.; Grosse, C.; Fischer, S. F.; Rudin, S. P.; Johnson, D. C. *Chem. Mater.* **2014**, *26*, 2862.

(54) Alemayehu, M. B.; Falmbigl, M.; Ta, K.; Ditto, J.; Medlin, D. L.; Johnson, D. C.; *Angew. Chemie Int. Ed.* **2015**, *54*, 15468.

(55) Falmbigl, M.; Putzky, D.; Ditto, J.; Esters, M.; Bauers, S. R.; Ronning, F.; Johnson, D. C. *ACS Nano* **2015**, *9*, 8440.

(56) Falmbigl, M.; Fiedler, A.; Atkins, R. E.; Fischer, S. F.; Johnson, D. C. Nano Lett. **2015**, *15*, 943.

(57) Huang, P.-R.; He, Y.; Pal, H. K.; Kindermann, M. Prediction of switchable half semiconductor in $d^1$ transition metal dichalcogenide monolayers. **2015**, arXiv:1501.00760. arXiv.org e-Print server. http://arxiv.org/abs/1501.0760 (accessed Oct 15 2017).

(58) Kresse, G.; Hafner, J. *Phys. Rev. B* **1994**, *49*, 14251.

(59) Kresse, G.; Furthmüller, J. *Comput. Mat. Sci.* **1996**, *6*, 15.

(60) Kresse, G.; Furthmüller, J. *Phys. Rev. B* **1996**, *54*, 11169.

(61) Blöchl, P. E. *Phys. Rev. B* **1994**, *50*, 17953.

(62) Kresse, G.; Joubert, D. *Phys. Rev. B* **1999**, *59*, 1758.

(63) Perdew, J. P.; Zunger, A. *Phys. Rev. B* **1981**, *23*, 5048.

(64) Perdew, J. P.; Burke, K.; Ernzerhof, M. *Phys. Rev. Lett.* **1996**, *77*, 3865.

(65) Heyd, J.; Scuseria, G. E.; Ernzerhof, M. *J. Chem. Phys.* **2003**, *118*, 8207.

(66) Dudarev, S. L.; Botton, G. A.; Savrasov, S. Y.; Humphreys, C. J.; Sutton, A. P. *Phys. Rev. B* **1998**, *57*, 1505.

(67) Tkatchenko, A.; Scheffler, M. *Phys. Rev. Lett.* **2009**, *102*, 073005.

(68) Tkatchenko, A.; DiStasio, R. A.; Car, R.; Scheffler, M. *Phys. Rev. Lett.* **2012**, *108*, 236402.

(69) Grimme, S. *J. Comput. Chem.* **2006**, *27*, 1787.

(70) Bučko, T.; Hafner, J.; Lebègue, S.; Ángyán, J. G. *J. Phys. Chem. A* **2010**, *114*, 11814.

(71) Dion, M.; Rydberg, H.; Schröder, E.; Langreth, D. C.; Lundqvist, B. I. *Phys. Rev. Lett.* **2004**, *92*, 246401.

(72) Román-Pérez, G.; Soler, J. M. *Phys. Rev. Lett.* **2009**, *103*, 096102.

(73) Klimeš, J.; Bowler, D. R.; Michaelides, A. *J. Phys. Condens. Matter* **2010**, *22*, 022201.

(74) Klimeš, J.; Bowler, D. R.; Michaelides, A. *Phys. Rev. B* **2011**, *83*, 195131.

(75) Monkhorst, H. J.; Pack, J. D. *Phys. Rev. B* **1976**, *13*, 5188.

(76) Ong, S. P.; Richards, W. D.; Jain, A.; Hautier, G.; Kocher, M.; Cholia, S.; Gunter, D.; Chevrier, V. L.; Persson, K. A.; Ceder, G. *Comput. Mater. Sci.* **2013**, *68*, 314.

(77) Mathew, K.; Singh, A. K.; Gabriel, J. J.; Choudhary, K.; Sinnott, S. B.; Davydov, A. V.; Tavazza, F.; Hennig, R. G. *Comput. Mater. Sci.* **2016**, *122*, 183.

(78) Momma, K.; Izumi, F. *J. Appl. Crystallogr.* **2011**, *44*, 1272.

(79) Mostofi, A. A.; Yates, J. R.; Pizzi, G.; Lee, Y.-S.; Souza, I.; Vanderbilt, D.; Marzari, N. *Comp. Phys. Commun.* **2014**, *185*, 2309.

(80) Kokalj, A. *Comp. Mater. Sci.* **2003**, *28*, 155.

(81) Isaacs, E. B.; Marianetti, C. A. *Phys. Rev. B* **2016**, *94*, 035120.

(82) Hite, O. K.; Falmbigl, M.; Alemayehu, M. B.; Esters, M.; Wood, S. R.; Johnson, D. C. *Chem. Mater.* **2017**, *29*, 5646.

(83) Schmidt, H.; Giustiniano, F.; Eda, G. *Chem. Soc. Rev.* **2015**, *44*, 7715.

(84) Zhang, Y.; Chang, T.-R.; Zhou, B.; Cui, Y.-T.; Yan, H.; Liu, Z.; Schmitt, F.; Lee, J.; Moore, R.; Chen, Y.; Lin, H.; Jeng, H.-T.; Mo, S.-K.; Hussain, Z.; Bansil, A.; Shen, Z.-X. *Nat. Nanotechnol.* **2014**, *9*, 111.

(85) Splendiani, A.; Sun, L.; Zhang, Y.; Li, T.; Kim, J.; Chim, C. Y.; Galli, G.; Wang, F. *Nano Lett.* **2010**, *10*, 1271.

(86) Whangbo, M. H.; Canadell, E. *J. Am. Chem. Soc.* **1992**, *114*, 9587.

(87) Calandra, M.; Mazin, I. I.; Mauri, F. *Phys. Rev. B* **2009**, *80*, 241108(R).

(88) Falmbigl, M.; Hay, Z.; Ditto, J.; Mitchson, G.; Johnson, D. C. *J. Mater. Chem. C* **2015**, *3*, 12308.

(89) Fernández, J. F.; Ferreira, M. F.; Stankiewicz, J. *Phys. Rev. B* **1986**, *34*, 292.

(90) Togo, A.; Tanaka, I. *Scr. Mater.* **2015**, *108*, 1.

(91) Hughes, H. P.; Webb, C.; Williams, P. M. *J. Phys. C: Solid State Phys.* **1980**, *13*, 1125.

(92) Kim, J.-J.; Park, C.; Olin, H. *J. Korean Phys. Soc.* **1997**, *31*, 713.

(93) Terashima, K.; Sato, H.; Komatsu, H.; Takahashi, T.; Maeda, N.; Hayashi, K. *Phys. Rev. B* **2003**, *60*, 155108

(94) Strocov, V. N.; Shi, M.; Kobayashi, M.; Monney, C.; Wang, X.; Krempasky, J.; Schmitt, T.; Patthey, L.; Berger, H.; Blaha, P. *Phys. Rev. Lett.* **2012**, *109*, 086401.

(95) Zhang, D.; Ha, J.; Baek, H.; Chan, Y.-H.; Natterer, F. D.; Myers, A. F.; Schumacher, J. D.; Cullen, W. G.; Davydov, A. V.; Kuk, Y.; Chou, M. Y.; Zhitenev, N. B.; Stroscio, J. A. *Phys. Rev. Materials* **2017**, *1*, 024005.

## CHAPTER X


(1) Novoselov, K. S. *Science (80-. ).* **2004**, *306* (5696).

(2) Novoselov, K. S. *Rev. Mod. Phys.* **2011**, *83* (3), 837.

(3) Geim, A. K. *Rev. Mod. Phys.* **2011**, *83* (3), 851.

(4) Hamann, D. M.; Hadland, E. C.; Johnson, D. C. *Semicond. Sci. Technol.* **2017**, *32* (9), 93004.

(5) Jariwala, D.; Marks, T. J.; Hersam, M. C. *Nat. Mater.* **2016**, *16* (2), 170.

(6) Mak, K. F.; Lee, C.; Hone, J.; Shan, J.; Heinz, T. F. *Phys. Rev. Lett.* **2010**, *105* (13).

(7) Zhao, W.; Ghorannevis, Z.; Chu, L.; Toh, M.; Kloc, C.; Tan, P.-H.; Eda, G. *ACS Nano* **2013**, *7* (1), 791.

(8) Komsa, H.-P.; Krasheninnikov, A. V. *Phys. Rev. B* **2013**, *88*, 85318.

(9) Ulstrup, S.; Čabo, A. G.; Miwa, J. A.; Riley, J. M.; Grønborg, S. S.; Johannsen, J. C.; Cacho, C.; Alexander, O.; Chapman, R. T.; Springate, E.; Bianchi, M.; Dendzik, M.; Lauritsen, J. V.; King, P. D. C.; Hofmann, P. *ACS Nano* **2016**, *10* (6), 6315.

(10) Ugeda, M. M.; Bradley, A. J.; Shi, S.-F.; da Jornada, F. H.; Zhang, Y.; Qiu, D. Y.; Ruan, W.; Mo, S.-K.; Hussain, Z.; Shen, Z.-X.; Wang, F.; Louie, S. G.; Crommie, M. F. *Nat. Mater.* **2014**, *13* (12), 1091.

(11) Grubišić Čabo, A.; Miwa, J. A.; Grønborg, S. S.; Riley, J. M.; Johannsen, J. C.; Cacho, C.; Alexander, O.; Chapman, R. T.; Springate, E.; Grioni, M.; Lauritsen, J. V.; King, P. D. C.; Hofmann, P.; Ulstrup, S. *Nano Lett.* **2015**, *15* (9), 5883.

(12) Bruix, A.; Miwa, J. A.; Hauptmann, N.; Wegner, D.; Ulstrup, S.; Grønborg, S. S.; Sanders, C. E.; Dendzik, M.; Grubišić Čabo, A.; Bianchi, M.; Lauritsen, J. V.; Khajetoorians, A. A.; Hammer, B.; Hofmann, P. *Phys. Rev. B* **2016**, *93* (16), 165422.

(13) Geim, A. K.; Grigorieva, I. V. *Nature* **2013**, *499*, 419.

(14) Anderson, M. D.; Heideman, C. L.; Lin, Q.; Smeller, M.; Kokenyesi, R.; Herzing, A. A.; Anderson, I. M.; Keszler, D. A.; Zschack, P.; Johnson, D. C. *Angew. Chemie Int. Ed.* **2013**, *52* (7), 1982.

(15) Smeller, M. M.; Heideman, C. L.; Lin, Q.; Beekman, M.; Anderson, M. D.; Zschack, P.; Anderson, I. M.; Johnson, D. C. *Z. Anorg. Allg. Chemie* **2012**, *638*, 2632.

(16) Feng, W.; Zhou, H.; Chen, F. *Vacuum* **2015**, *114*, 82.

(17) Alemayehu, M. B.; Falmbigl, M.; Ta, K.; Grosse, C.; Westover, R. D.; Bauers, S. R.; Fischer, S. F.; Johnson, D. C. *Chem. Mater.* **2015**, *27* (3), 867.

(18) Bauers, S. R.; Merrill, D. R.; Moore, D. B.; Johnson, D. C. *J. Mater. Chem. C* **2015**, *3* (40), 10451.

(19) Falmbigl, M.; Fiedler, A.; Atkins, R. E.; Fischer, S. F.; Johnson, D. C. *Nano Lett.* **2015**, *15*, 943.

(20) Helmholz, L. *Z. Kristallogr.* **1936**, *95*, 129–137.

(21) Chattopadhyay, T.; Pannetier, J.; Von Schnering, H. G. *J. Phys. Chem. Solids* **1986**, *47* (9), 879.

(22) Wiedemeier, H.; von Schnering, H. G. *Z. Kristallogr.* **1978**, *148*, 295.

(23) Schnering, H. G. von; Wiedemeier, H. *Z. Krist. - Cryst. Mater.* **1981**, *156* (1–2), 143.

(24) Hamann, D. M.; Merrill, D. R.; Bauers, S. R.; Mitchson, G.; Ditto, J.; Rudin, S. P.; Johnson, D. C. *Inorg. Chem.* **2017**, *56* (6), 3499.

(25) Esters, M. Deposition Software for the Inficon IC6 Deposition Controller, https://github.com/marcoesters/deposition_ic6.

(26) Phung, T.; Jensen, J.; Jonshon, D.; Donovan, J.; McBurnett, B. *X-Ray Spectrom.* **2008**, *37*, 608.

(27) Le Bail, A.; Duroy, H.; Fourquet, J. L. *Mater. Res. Bull.* **1988**, *23*, 447.

(28) Roisnel, T.; Rodríquez-Carvajal, J. *Mater. Sci. Forum* **2001**, *378–381*, 118.

(29) Rodríguez-Carvajal, J. *Phys. B Condens. Matter* **1993**, *192* (1–2), 55.

(30) Kresse, G.; Hafner, J. *Phys. Rev. B* **1994**, *49* (20), 14251.

(31) Kresse, G.; Furthmüller, J. *Phys. Rev. B* **1996**, *54*, 11169.

(32) Kresse, G.; Furthmüller, J. *Comput. Mater. Sci.* **1996**, *6* (1), 15.

(33) Blöchl, P. E. *Phys. Rev. B* **1994**, *50*, 17953.

(34) Kresse, G.; Joubert, D. *Phys. Rev. B* **1999**, *59*, 1758.

(35) Perdew, J. P.; Burke, K.; Ernzerhof, M. *Phys. Rev. Lett.* **1996**, *77* (18), 3865.

(36) Monkhorst, H. J.; Pack, J. D. *Phys. Rev. B* **1976**, *13* (12), 5188.

(37) Johnson, D. C. *Curr. Opin. Solid State Mater. Sci.* **1998**, *3* (2), 159.

(38) Esters, M.; Johnson, D. C. Targeted Synthesis of Metastable Compounds and Intergrowths: The Moduclated Elemental Reactants Method. In *Crystal Growth: Concepts, Mechanisms, and Applications*; Li, J., Li, J., Chi, Y., Eds.; Nova Science Publishers: New York, 2017; pp 35–118.

(39) Atkins, R.; Wilson, J.; Zschack, P.; Grosse, C.; Neumann, W.; Johnson, D. C. *Chem. Mater.* **2012**, *24* (23), 4594.

(40) Merrill, D. R.; Moore, D. B.; Ditto, J.; Sutherland, D. R.; Falmbigl, M.; Winkler, M.; Pernau, H.-F.; Johnson, D. C. *Eur. J. Inorg. Chem.* **2015**, *2015* (1), 83.

(41) Beekman, M.; Cogburn, G.; Heideman, C.; Rouvimov, S.; Zschack, P.; Neumann, W.; Johnson, D. C. *J. Electron. Mater.* **2012**, *41* (6), 1476.

(42) Moore, D. B.; Sitts, L.; Stolt, M. J.; Beekman, M.; Johnson, D. C. *J. Electron. Mater.* **2013**, *42* (7), 1647.

(43) Moore, D. B.; Stolt, M. J.; Atkins, R.; Sitts, L.; Jones, Z.; Disch, S.; Matt, B.; Johnson, D. C. *Emerg. Mater. Res.* **2012**, *1*, 292.

(44) Moore, D. B.; Beekman, M.; Disch, S.; Zschack, P.; Häusler, I.; Neumann, W.; Johnson, D. C. *Chem. Mater.* **2013**, *25*, 2404.

(45) Merrill, D. R.; Moore, D. B.; Coffey, M. N.; Jansons, A. W.; Falmbigl, M.; Johnson, D. C. *Semicond. Sci. Technol.* **2014**, *29*, 64004.

(46) Wood, S. R.; Merrill, D. R.; Falmbigl, M.; Moore, D. B.; Ditto, J.; Esters, M.; Johnson, D. C. *Chem. Mater.* **2015**, *27* (17), 6067.

(47) Merrill, D. R.; Sutherland, D. R.; Ditto, J.; Bauers, S. R.; Falmbigl, M.; Medlin, D. L.; Johnson, D. C. *Chem. Mater.* **2015**, *27*, 4066.

(48) Beekman, M.; Disch, S.; Rouvimov, S.; Kasinathan, D.; Koepernik, K.; Rosner, H.; Zschack, P.; Neumann, W. S.; Johnson, D. C. *Angew. Chemie Int. Ed.* **2013**, *52*, 13211.

(49) Bauers, S. R.; Moore, D. B.; Ditto, J.; Johnson, D. C. *J. Alloys Compd.* **2015**, *645*, 118.

(50) Grosse, C.; Atkins, R.; Kirmse, H.; Mogilatenko, A.; Neumann, W.; Johnson, D. C. *J. Alloys Compd.* **2013**, *579*, 507.

(51) Falmbigl, M.; Putzky, D.; Ditto, J.; Esters, M.; Bauers, S. R.; Ronning, F.; Johnson, D. C. *ACS Nano* **2015**, *9* (8), 8440.

(52) Atkins, R.; Moore, D. B.; Johnson, D. C. *Chem. Mater.* **2013**, *25*, 1744.

(53) Fang, W.; Zhang, L.-C.; Qin, G.; Yan, Q.-B.; Zheng, Q.-R.; Su, G. Layer Dependence of Geometric, Electronic and Piezoelectric Properties of SnSe. **2016**, arXiv:1603.01791v1. arXiv.org e-Print archive. https://arxiv.org/abs/1603.01791 (accessed Oct 15, 2017).

(54) Falmbigl, M.; Alemayehu, M. B.; Merrill, D. R.; Beekman, M.; Johnson, D. C. *Cryst. Res. Technol.* **2015**, *50*, 464.

(55) Mariano, A. N.; Chopra, K. L. *Appl. Phys. Lett.* **1967**, *10* (10), 282.

(56) Alemayehu, M. B.; Ta, K.; Falmbigl, M.; Johnson, D. C. *J. Am. Chem. Soc.* **2015**, *137*, 4831.

(57) Imada, M.; Fujimori, A.; Tokura, Y. *Rev. Mod. Phys.* **1998**, *70* (4), 1039.

(58) Di Salvo, F. J.; Moncton, D. E.; Waszczak, J. V. *Phys. Rev. B* **1976**, *14* (10), 4321.

(59) Altshuler, B. L.; Khmel'nitzkii, D.; Larkin, A. I.; Lee, P. A. *Phys. Rev. B* **1980**, *22* (11), 5142.

(60) Bauers, S. R.; Ditto, J.; Moore, D. B.; Johnson, D. C. *Nanoscale* **2016**, *8* (30), 14665.

(61) Wiegers, G. A. *Prog. Solid St. Chem* **1996**, *24*, 1.

(62) Wan, C.; Wang, Y.; Wang, N.; Koumoto, K. *Materials (Basel).* **2010**, *3* (4), 2606.

(63) Giang, N.; Xu, Q.; Hor, Y.; Williams, A.; Dutton, S.; Zandbergen, H.; Cava, R. *Phys. Rev. B* **2010**, *82* (2), 1.

(64) Wiegers, G.; Haange, R. *Eur. J. solid state Inorg. Chem.* **1991**, *28*, 1071.

## CHAPTER XI

(1) Geim, A. K.; Grigorieva, I. V. *Nature* **2013**, *499* (7459), 419.

(2) Fang, H.; Battaglia, C.; Carraro, C.; Nemsak, S.; Ozdol, B.; Kang, J. S.; Bechtel, H. a; Desai, S. B.; Kronast, F.; Unal, A. a; Conti, G.; Conlon, C.; Palsson, G. K.; Martin, M. C.; Minor, A. M.; Fadley, C. S.; Yablonovitch, E.; Maboudian, R.; Javey, A. *Proc. Natl. Acad. Sci. U. S. A.* **2014**, *111* (17), 6198.

(3) Geim, A. K.; Novoselov, K. S. *Nat. Mater.* **2007**, 183.

(4) Levendorf, M. P.; Kim, C.-J.; Brown, L.; Huang, P. Y.; Havener, R. W.; Muller, D. a.; Park, J. *Nature* **2012**, *488* (7413), 627.

(5) Sutter, P.; Cortes, R.; Lahiri, J.; Sutter, E. *Nano Lett.* **2012**, *12* (9), 4869.

(6) Chhowalla, M.; Shin, H. S.; Eda, G.; Li, L.-J.; Loh, K. P.; Zhang, H. *Nat. Chem.* **2013**, *5* (4), 263.

(7) Kou, L.; Frauenheim, T.; Chen, C. *J. Phys. Chem. Lett.* **2013**, *4* (10), 1730.

(8) Komsa, H.-P.; Krasheninnikov, A. V. *Phys. Rev. B* **2013**, *88* (8), 085318.

(9) Novoselov, K. S.; Castro Neto, a H. *Phys. Scr.* **2012**, *T146*, 014006.

(10) Decker, R.; Wang, Y.; Brar, V. W.; Regan, W.; Tsai, H. Z.; Wu, Q.; Gannett, W.; Zettl, A.; Crommie, M. F. *Nano Lett.* **2011**, *11* (6), 2291.

(11) Wirtz, L.; Marini, A.; Rubio, A. *Phys. Rev. Lett.* **2006**, *96* (12), 1.

(12) Jariwala, D.; Sangwan, V. K.; Lauhon, L. J.; Marks, T. J.; Hersam, M. C. *ACS Nano* **2014**, *8* (2), 1102.

(13) Esters, M.; Alemayehu, M. B.; Jones, Z.; Nguyen, N. T.; Anderson, M. D.; Grosse, C.; Fischer, S. F.; Johnson, D. C. *Angew. Chemie - Int. Ed.* **2015**, *54* (4), 1130.

(14) Noh, M.; Johnson, C. D.; Hornbostel, M. D.; Thiel, J.; Johnson, D. C. *Chem. Mater.* **1996**, *8* (8), 1625.

(15) Beekman, M.; Heideman, C. L.; Johnson, D. C. *Semicond. Sci. Technol.* **2014**, *29* (6), 064012.

(16) Alemayehu, M. B.; Falmbigl, M.; Ta, K.; Ditto, J.; Medlin, D. L.; Johnson, D. C. *Angew. Chemie* **2015**, *127*, 15688.

(17) Mitchson, G.; Falmbigl, M.; Ditto, J.; Johnson, D. C. *Inorg. Chem.* **2015**, *54*, 10309.

(18) Gotoh, Y.; Onoda, M.; Akimoto, J.; Goto, M.; Oosawa, Y. *Jpn. J. Appl. Phys.* **1992**, *31*, 3946.

(19) Petříček, V.; Cisarova, I.; de Boer, J. L.; Zhou, W.; Meetsma, A.; Wiegers, G. A.; van Smaalen, S. *Acta Crystallogr. Sect. B Struct. Sci.* **1993**, *49* (2), 258.

(20) Wiegers, G. A. *Prog. Solid St. Chem.* **1996**, *24*, 1.

(21) Gotoh, Y.; Akimoto, J.; Goto, M.; Oosawa, Y.; Onoda, M. *J. Solid State Chem.* **1995**, *116*, 61.

(22) Wulff, J.; Meetsma, A.; Haange, R. J.; de Boer, J. L.; Wiegers, G. A. *Synth. Met.* **1990**, *39*, 1.

(23) Wiegers, G. A. *J. Alloys Compd.* **1995**, *219* (1-2), 152.

(24) Pervov, V. S.; Makhonina, E. V. *Russ. Chem. Rev.* **2000**, *69* (6), 481.

(25) Westover, R.; Atkins, R. A.; Falmbigl, M.; Ditto, J. J.; Johnson, D. C. *J. Solid State Chem.* **2015**, *236*, 173.

(26) Roisnel, T.; Rodriguez-Carvajal, J. *Mater. Sci. Forum* **2001**, *378-381*, 118.

(27) Akselrud, L. G.; Grin, Y. *J. Appl. Crystallogr.* **2014**, *47* (2), 803.

(28) Phung, T. M.; Jensen, J. M.; Johnson, D. C.; Donovan, J. J.; Mcburnett, B. G. *X-Ray Spectrom.* **2008**, *37*, 608.

(29) Schaffer, M.; Schaffer, B.; Ramasse, Q. *Ultramicroscopy* **2012**, *114*, 62.

(30) van der Pauw, L. J. *Philips Tech. Rev.* **1958**, *20*, 220.

(31) Kresse, G.; Hafner, J. *Phys. Rev. B* **1993**, *47* (1), 558.

(32) Kresse, G.; Hafner, J. *Phys. Rev. B* **1994**, *49* (20), 14251.

(33) Kresse, G.; Furthmuller, J. *Comput. Mater. Sci.* **1996**, *6*, 15.

(34) Kresse, G.; Furthmüller, J. *Phys. Rev. B* **1996**, *54* (16), 11169.

(35) Blöchl, P. E. *Phys. Rev. B* **1994**, *50* (24), 17953.

(36) Kresse, G.; Joubert, D. *Phys. Rev. B* **1999**, *59* (3), 1758.

(37) Perdew, J. P.; Zunger, A. *Phys. Rev. B* **1981**, *23* (10), 5048.

(38) Perdew, J. P.; Burke, K.; Ernzerhof, M. *Phys. Rev. Lett.* **1996**, *77* (18), 3865.

(39) Monkhorst, H. J.; Pack, J. D. *Phys. Rev. B* **1977**, *16* (4), 1748.

(40) Kadijk, F.; Jellinek, F. *J. Less-common Met.* **1971**, *23*, 437.

(41) Alemayehu, M. B.; Falmbigl, M.; Ta, K.; Johnson, D. C. *Chem. Mater.* **2015**, *27*, 2158.

(42) Falmbigl, M.; Alemayehu, M. B.; Merrill, D. R.; Beekman, M.; Johnson, D. C. *Cryst. Res. Technol.* **2015**, *50*, 464.

(43) Lind, H.; Lidin, S. *Solid State Sci.* **2003**, *5* (1), 47.

(44) Trump, B. a.; Livi, K. J. T.; McQueen, T. M. *J. Solid State Chem.* **2014**, *209*, 6.

(45) Zhou, W.; Meetsma, A.; de Boer, J. L.; Wiegers, G. A. *Mater. Res. Bull.* **1992**, *27*, 563.

(46) Oosawa, Y.; Gotoh, Y.; Akimoto, J. *J. Alloys Compd.* **1991**, *176* (2), 319.

(47) Otero-Diaz, L. C.; Withers, R. L.; Gomez-Herrero, A.; Welberry, T. R.; Schmid, S. *J. Solid State Chem.* **1995**, *115*, 274.

(48) Merrill, D. R.; Moore, D. B.; Coffey, M. N.; Jansons, A. W.; Falmbigl, M.; Johnson, D. C. *Semicond. Sci. Technol.* **2014**, *29* (6), 064004.

(49) Wood, S. R.; Merrill, D. R.; Falmbigl, M.; Moore, D. B.; Ditto, J.; Esters, M.; Johnson, D. C. *Chem. Mater.* **2015**, *27* (17), 6067.

(50) Grosse, C.; Atkins, R.; Kirmse, H.; Mogilatenko, A.; Neumann, W.; Johnson, D. C. *J. Alloys Compd.* **2013**, *579*, 507.

(51) Falmbigl, M.; Putzky, D.; Ditto, J.; Esters, M.; Bauers, S. R.; Ronning, F.; Johnson, D. C. *ACS Nano* **2015**, *9* (8), 8440.

(52) Wiegers, G. A. *Prog. Solid State Chem.* **1996**, *24*, 1.

(53) Marezio, M.; Dernier, P.; Menth, A.; Jr, G. H. *J. Solid State Chem.* **1972**, *4* (3), 425.

(54) Auriel, C.; Meerschaut, A.; Roesky, R.; Rouxel, J. *Eur. J. Solid State Inorg. Chem.* **1992**, *29*, 1079.

(55) Atkins, R.; Moore, D. B.; Johnson, D. C. *Chem. Mater.* **2013**, *25* (9), 1744.

(56) Gibson, Q. D.; Schoop, L. M.; Weber, A. P.; Ji, H.; Nadj-Perge, S.; Drozdov, I. K.; Beidenkopf, H.; Sadowski, J. T.; Fedorov, A.; Yazdani, A.; Valla, T.; Cava, R. J. *Phys. Rev. B* **2013**, *88* (8), 1.

(57) Bauers, S. R.; Merrill, D. R.; Moore, D. B.; Johnson, D. C. *J. Mater. Chem. C* **2015**, *3* (40), 10451.

(58) Alemayehu, M. B.; Falmbigl, M.; Ta, K.; Grosse, C.; Westover, R. D.; Bauers, S. R.; Fischer, S. F.; Johnson, D. C. *Chem. Mater.* **2015**, *27* (3), 867.

(59) Calandra, M; Mazin, I.I.; Mauri, F. *Phys. Rev. B* **2009**, *80* (24), 241108

(60) Alemayehu, M. B.; Ta, K.; Falmbigl, M.; Johnson, D. C. *Nanoscale* **2015**, *7* (16), 7378–7385.

(61) Lee, H. N. S.; McKinzie, H.; Tannhauser, D. S.; Wold, A. *J. Appl. Phys.* **1969**, *40* (2), 602.

(62) Zhang, M.; Lv, L.; Wei, Z.; Guo, C.; Yang, X.; Zhao, Y. *Mater. Lett.* **2014**, *123*, 87.

(63) Brom, J. E.; Ke, Y.; Du, R.; Won, D.; Weng, X.; Andre, K.; Gagnon, J. C.; Mohney, S. E.; Li, Q.; Chen, K.; Xi, X. X.; Redwing, J. M. *Appl. Phys. Lett.* **2012**, *100*, 162110.

(64) Zhang, J.; Huang, G. *Solid State Commun.* **2014**, *197*, 34.

(65) Wang, M.-X.; Li, P.; Xu, J.-P.; Liu, Z.-L.; Ge, J.-F.; Wang, G.-Y.; Yang, X.; Xu, Z.-A.; Ji, S.-H.; Gao, C. L.; Qian, D.; Luo, W.; Liu, C.; Jia, J.-F. *New J. Phys.* **2014**, *16* (12), 123043.

**CHAPTER XII**

(1) Hsieh, D.; Qian, D.; Wray, L.; Xia, Y.; Hor, Y. S.; Cava, R. J.; Hasan, M. Z. *Nat. Lett.* **2008**, *452*, 970.

(2) Hsieh, D.; Xia, Y.; Wray, L.; Qian, D.; Pal, A.; Dil, J. H.; Osterwalder, J.; Meier, F.; Bihlmayer, G.; Kane, C. L.; Hor, Y. S.; Cava, R. J.; Hasan, M. Z. *Science (80-. ).* **2009**, *323* (5916), 919.

(3) Moore, J. E. *Nature* **2010**, *464* (7286), 194.

(4) Hasan, M. Z.; Kane, C. L. *Rev. Mod. Phys.* **2010**, *82* (4), 3045.

(5) Qi, X. L.; Zhang, S. C. *Rev. Mod. Phys.* **2011**, *83* (4), 1057.

(6) Zhang, H.; Liu, C.-X.; Qi, X.-L.; Dai, X.; Fang, Z.; Zhang, S.-C. *Nat. Phys.* **2009**, *5* (6), 438.

(7) Chen, Y. L.; Analytis, J. G.; Chu, J.-H.; Liu, Z. K.; Mo, S.-K.; Qi, X. L.; Zhang, H. J.; Lu, D. H.; Dai, X.; Fang, Z.; Zhang, S. C.; Fisher, I. R.; Hussain, Z.; Shen, Z.-X. *Science (80-. ).* **2009**, *325*, 178.

(8) Okamoto, H. In *ASM Alloy Phase Diagrams Database*; Villars, P., Okamoto, H., Cenzual, K., Eds.; Materials Park, OH, 2016.

(9) Lind, H.; Lidin, S. *Solid State Sci.* **2003**, *5* (1), 47.

(10) Lind, H.; Lidin, S.; Häussermann, U. *Phys. Rev. B* **2005**, *72* (18), 184101.

(11) Gaudin, E.; Jobic, S.; Evain, M.; Brec, R.; Rouxel, J. *Mater. Res. Bull.* **1995**, *30* (5), 549.

(12) Murakami, S. *Phys. Rev. Lett.* **2006**, *97* (23), 236805.

(13) Liu, Z.; Liu, C. X.; Wu, Y. S.; Duan, W. H.; Liu, F.; Wu, J. *Phys. Rev. Lett.* **2011**, *107* (13), 136805.

(14) Yang, F.; Miao, L.; Wang, Z. F.; Yao, M. Y.; Zhu, F.; Song, Y. R.; Wang, M. X.; Xu, J. P.; Fedorov, A. V.; Sun, Z.; Zhang, G. B.; Liu, C.; Liu, F.; Qian, D.; Gao, C. L.; Jia, J. F. *Phys. Rev. Lett.* **2012**, *109* (1), 16801.

(15) Drozdov, I. K.; Alexandradinata, A.; Jeon, S.; Nadj-Perge, S.; Ji, H.; Cava, R. J.; Andrei Bernevig, B.; Yazdani, A. *Nat. Phys.* **2014**, *10* (9), 664.

(16) Kou, L.; Tan, X.; Ma, Y.; Tahini, H.; Zhou, L.; Sun, Z.; Aijun, D.; Chen, C.; Smith, S. C. *2D Mater.* **2015**, *2* (4), 45010.

(17) Jin, K.-H.; Jhi, S.-H. *Sci. Rep.* **2015**, *5*, 8426.

(18) Valla, T.; Ji, H.; Schoop, L. M.; Weber, A. P.; Pan, Z. H.; Sadowski, J. T.; Vescovo, E.; Fedorov, A. V.; Caruso, A. N.; Gibson, Q. D.; Müchler, L.; Felser, C.; Cava, R. J. *Phys. Rev. B* **2012**, *86* (24), 3.

(19) Majhi, K.; Pal, K.; Lohani, H.; Banerjee, A.; Mishra, P.; Yadav, A. K.; Ganesan, R.; Sekhar, B.; Waghmare, U. V; Kumar, P. A. *Appl. Phys. Lett.* **2017**, *110*, 162102.

(20) Zhou, W. Y.; Meetsma, A.; Boer, J. L. De; Wiegers, G. A. *Mater. Res. Bull.* **1992**, *27*, 563.

(21) Petříček, V.; Cisarova, I.; de Boer, J. L.; Zhou, W.; Meetsma, A.; Wiegers, G. a.; van Smaalen, S. *Acta Crystallographica Section B*. 1993, pp 258–266.

(22) Rouxel, J.; Meerschaut, A.; Wiegers, G. A. *J. Alloys Compd.* **1995**, *229*, 144.

(23) Trump, B. a.; Livi, K. J. T.; McQueen, T. M. *J. Solid State Chem.* **2014**, *209*, 6.

(24) Clarke, S. M.; Freedman, D. E. *Inorg. Chem.* **2015**, *54* (6), 2765.

(25) Wulff, J.; Meetsma, A.; Haange, R. J.; de Boer, J. L.; Wiegers, G. A. *Synth. Met.* **1990**, *39*, 1.

(26) Oosawa, Y.; Gotoh, Y.; Akimoto, J.; Onoda, M. *J. Alloys Compd.* **1991**, *176*, 319.

(27) Gotoh, Y.; Onoda, M.; Akimoto, J.; Goto, M.; Oosawa, Y. *J. Appl. Phys.* **1992**, *31*, 3946.

(28) Lafond, A.; Fragnaud, P.; Evain, M.; Meerschaut, A. *Mater. Res. Bull.* **1992**, *27*, 705.

(29) Yarmoshenko, Y. M.; Trofimova, V. A.; Shamin, S. N.; Solovyev, I. V.; Kurmaev, E. Z.; Ettema, A. R. H. F.; Haas, C. *J. Phys. Condens. Matter* **1994**, *6* (21), 3993.

(30) Otero-Diaz, L. C.; Withers, R. L.; Gomez-Herrero, A.; Welberry, T. R.; Schmid, S. *J. Solid State Chem.* **1995**, *115*, 274.

(31) Wan, C.; Wang, Y.; Wang, N.; Koumoto, K. *Materials (Basel).* **2010**, *3* (4), 2606.

(32) Falmbigl, M.; Alemayehu, M. B.; Merrill, D. R.; Beekman, M.; Johnson, D. C. *Cryst. Res. Technol.* **2015**, *472* (6), 464.

(33) Merrill, D. R.; Moore, D. B.; Coffey, M. N.; Jansons, A. W.; Falmbigl, M.; Johnson, D. C. *Semicond. Sci. Technol.* **2014**, *29* (6), 64004.

(34) Mitchson, G.; Falmbigl, M.; Ditto, J.; Johnson, D. C. *Inorg. Chem.* **2015**, *54* (21), 10309.

(35) Wood, S. R.; Merrill, D. R.; Falmbigl, M.; Moore, D. B.; Ditto, J.; Esters, M.; Johnson, D. C. *Chem. Mater.* **2015**, *27* (17), 6067.

(36) Hite, O. K.; Nellist, M.; Ditto, J.; Falmbigl, M.; Johnson, D. C. *J. Mater. Res.* **2015**, *8* (7), 886.

(37) Mitchson, G.; Hadland, E.; Göhler, F.; Wanke, M.; Esters, M.; Ditto, J.; Bigwood, E.; Ta, K.; Hennig, R. G.; Seyller, T.; Johnson, D. C. *ACS Nano* **2016**, *10* (10), 9489.

(38) Heideman, C.; Nyugen, N.; Hanni, J.; Lin, Q.; Duncombe, S.; Johnson, D. C.; Zschack, P. *J. Solid State Chem.* **2008**, *181* (7), 1701.

(39) Wiegers, G. A. *J. Alloys Compd.* **1995**, *219* (1–2), 152.

(40) Mitchson, G.; Bauers, S. R.; Schädlich, P.; Ditto, J. J.; Johnson, D. C. *Eur. J. Inorg. Chem.* **2016**.

(41) Wood, S. R.; Merrill, D. R.; Mitchson, G.; Lygo, A. C.; Bauers, S. R.; Hamann, D. M.; Sutherland, D. R.; Ditto, J.; Johnson, D. C. *Chem. Mater.* **2017**, *29*, 773.

(42) Kresse, G.; Hafner, J. *Phys. Rev. B* **1994**, *49* (20), 14251.

(43) Kresse, G.; Furthmüller, J. *Comput. Mat. Sci.* **1996**, *6* (1), 15.

(44) Kresse, G.; Furthmüller, J. *Phys. Rev. B* **1996**, *54* (16), 11169.

(45) Perdew, J. P.; Burke, K.; Ernzerhof, M. *Phys. Rev. Lett.* **1996**, *77* (18), 3865.

(46) Monkhorst, H. J.; Pack, J. D. *Phys. Rev. B* **1976**, *13* (12), 5188.

(47) Blöchl, P. E. *Phys. Rev. B* **1994**, *50* (24), 17953.

(48) Kresse, G.; Joubert, D. *Phys. Rev. B* **1999**, *59* (3), 1758.

(49) Heyd, J.; Scuseria, G. E.; Ernzerhof, M. *J. Chem. Phys.* **2003**, *118* (18), 8207.

(50) Dronskowski, R.; Blöchl, P. E. *J. Phys. Chem.* **1993**, *97* (33), 8617.

(51) Andersen, O. K. *Phys. Rev. B* **1975**, *12* (8), 3060.

(52) Andersen, O. K.; Jepsen, O. *Phys. Rev. Lett.* **1984**, *53* (27), 2571.

(53) Deringer, V. L.; Tchougréeff, A. L.; Dronskowski, R. *J. Phys. Chem. A* **2011**, *115*, 5461.

(54) Maintz, S.; Deringer, V. L.; Tchougréeff, A. L.; Dronskowski, R. *J. Comput. Chem.* **2013**, *34* (29), 2557.

(55) Maintz, S.; Deringer, V. L.; Tchougréeff, A. L.; Dronskowski, R. *J. Comput. Chem.* **2016**, *37* (11), 1030.

(56) Maintz, S.; Esser, M.; Dronskowski, R. *Acta Phys. Pol. B* **2016**, *47* (4), 1165.

(57) Ong, S. P.; Richards, W. D.; Jain, A.; Hautier, G.; Kocher, M.; Cholia, S.; Gunter, D.; Chevrier, V. L.; Persson, K. A.; Ceder, G. *Comput. Mater. Sci.* **2013**, *68*, 314.

(58) Grimme, S. *J. Comput. Chem.* **2006**, *27* (15), 1787.

(59) Grimme, S.; Antony, J.; Ehrlich, S.; Krieg, H. *J. Chem. Phys.* **2010**, *132* (15), 154104.

(60) Grimme, S.; Ehrlich, S.; Goerigk, L. *J. Comput. Chem.* **2010**, *32* (7), 1456.

(61) Tkatchenko, A.; Scheffler, M. *Phys. Rev. Lett.* **2009**, *102* (7), 73005.

(62) Tkatchenko, A.; DiStasio, R. A.; Car, R.; Scheffler, M. *Phys. Rev. Lett.* **2012**, *108* (23), 236402.

(63) Perdew, J. P.; Ruzsinszky, A.; Csonka, G. I.; Vydrov, O. A.; Scuseria, G. E.; Constantin, L. A.; Zhou, X.; Burke, K. *Phys. Rev. Lett.* **2008**, *100*, 136406.

(64) Perdew, J. P.; Zunger, A. *Phys. Rev. B* **1981**, *23* (10), 5048.

(65) Semiletov, S. A. *Tr. Instituta Krist. Akad. Nauk SSSR* **1954**, *10*, 76.

(66) Anderson, M. D.; Heideman, C. L.; Lin, Q.; Smeller, M.; Kokenyesi, R.; Herzing, A. A.; Anderson, I. M.; Keszler, D. A.; Zschack, P.; Johnson, D. C. *Angew. Chemie Int. Ed.* **2013**, *52* (7), 1982.

(67) Köhler, L.; Kresse, G. *Phys. Rev. B* **2004**, *70* (16), 165405.

(68) Henkelman, G.; Arnaldsson, A.; Jónsson, H. *Comput. Mater. Sci.* **2006**, *36* (3), 354.

(69) Tang, W.; Sanville, E.; Henkelman, G. *J. Phys. Condens. Matter* **2009**, *21* (8), 84204.

(70) Yu, M.; Trinkle, D. R. *J. Chem. Phys.* **2011**, *134* (6), 1.

(71) Allred, A. L. *J. Inorg. Nucl. Chem.* **1961**, *17* (3–4), 215.

**APPENDIX B**


(1) Kresse, G.; Hafner, J. *Phys. Rev. B* **1994**, *49*, 14251.

(2) Kresse, G.; Furthmüller, J. *Comput. Mat. Sci.* **1996**, *6*, 15.

(3) Kresse, G.; Furthmüller, J. *Phys. Rev. B* **1996**, *54*, 11169.

(4) Blöchl, P. E. *Phys. Rev. B* **1994**, *50*, 17953.

(5) Kresse, G.; Joubert, D. *Phys. Rev. B* **1999**, *59*, 1758.

(6) Perdew, J. P.; Zunger, A. *Phys. Rev. B* **1981**, *23*, 5048.

(7) Perdew, J. P.; Burke, K.; Ernzerhof, M. *Phys. Rev. Lett.* **1996**, *77*, 3865.

(8) Heyd, J.; Scuseria, G. E.; Ernzerhof, M. *J. Chem. Phys.* **2003**, *118*, 8207.

(9) Dudarev, S. L.; Botton, G. A.; Savrasov, S. Y.; Humphreys, C. J.; Sutton, A. P. *Phys. Rev. B* **1998**, *57*, 1505.

(10) Tkatchenko, A.; Scheffler, M. *Phys. Rev. Lett.* **2009**, *102*, 073005.

(11) Tkatchenko, A.; DiStasio, R. A.; Car, R.; Scheffler, M. *Phys. Rev. Lett.* **2012**, *108*, 236402.

(12) Grimme, S. *J. Comput. Chem.* **2006**, *27*, 1787.

(13) Bučko, T.; Hafner, J.; Lebègue, S.; Ángyán, J. G. *J. Phys. Chem. A* **2010**, *114*, 11814.

(14) Dion, M.; Rydberg, H.; Schröder, E.; Langreth, D. C.; Lundqvist, B. I. *Phys. Rev. Lett.* **2004**, *92*, 246401.

(15) Román-Pérez, G.; Soler, J. M. *Phys. Rev. Lett.* **2009**, *103*, 096102.

(16) Klimeš, J.; Bowler, D. R.; Michaelides, A. *J. Phys. Condens. Matter* **2010**, *22*, 022201.

(17) Klimeš, J.; Bowler, D. R.; Michaelides, A. *Phys. Rev. B* **2011**, *83*, 195131.

(18) Monkhorst, H. J.; Pack, J. D. *Phys. Rev. B* **1976**, *13*, 5188.

(19) Ong, S. P.; Richards, W. D.; Jain, A.; Hautier, G.; Kocher, M.; Cholia, S.; Gunter, D.; Chevrier, V. L.; Persson, K. A.; Ceder, G. *Comput. Mater. Sci.* **2013**, *68*, 314.

(20) Mathew, K.; Singh, A. K.; Gabriel, J. J.; Choudhary, K.; Sinnott, S. B.; Davydov, A. V.; Tavazza, F.; Hennig, R. G. *Comput. Mater. Sci.* **2016**, *122*, 183.

(21) Momma, K.; Izumi, F. *J. Appl. Crystallogr.* **2011**, *44*, 1272.

(22) Mostofi, A. A.; Yates, J. R.; Pizzi, G.; Lee, Y.-S.; Souza, I.; Vanderbilt, D.; Marzari, N. *Comp. Phys. Commun.* **2014**, *185*, 2309.

(23) Kokalj, A. *Comp. Mater. Sci.* **2003**, *28*, 155.

(24) Atkins, R.; Disch, S.; Jones, Z.; Häusler, I.; Grosse, C.; Fischer, S. F.; Neumann, W.; Zschack, P.; Johnson, D. C. *J. Solid State Chem.* **2013**, *202*, 128.

(25) Atkins, R.; Dolgos, M.; Fiedler, A.; Grosse, C.; Fischer, S. F.; Rudin, S. P.; Johnson, D. C. *Chem. Mater.* **2014**, *26*, 2862.

(26) Alemayehu, M. B.; Falmbigl, M.; Ta, K.; Ditto, J.; Medlin, D. L.; Johnson, D. C.; *Angew. Chemie Int. Ed.* **2015**, *54*, 15468.

(27) Falmbigl, M.; Putzky, D.; Ditto, J.; Esters, M.; Bauers, S. R.; Ronning, F.; Johnson, D. C. *ACS Nano* **2015**, *9*, 8440.

(28) Falmbigl, M.; Fiedler, A.; Atkins, R. E.; Fischer, S. F.; Johnson, D. C. Nano Lett. **2015**, *15*, 943.

(29) Hite, O. K.; Falmbigl, M.; Alemayehu, M. B.; Esters, M.; Wood, S. R.; Johnson, D. C. *Chem. Mater.* **2017**, *29*, 5646.

(30) Bayard, M.; Sienko, M. J. *J. Solid State Chem.* **1976**, *19*, 325.

(31) van Bruggen, C. F.; Haas, C. *Solid State Commun.* **1976**, *20*, 251.

(32) Thompson, A. H.; Silbernagel, B. G. *J. Appl. Phys.* **1978**, *49*, 1477.

(33) Thompson A. H.; Silbernagel, B. G. *Phys. Rev. B* **1979**, *19*, 3420.

(34) Schneemeyer, L. F.; Stacy, A.; Sienko, M. *J. Inorg. Chem.* **1980**, *19*, 2659.

(35) Giambattista, B.; Slough, C. G.; McNairy, W.W.; Coleman, R. V. *Phys. Rev. B* **1990**, 41, 10082.

(36) Kamarchuk, G. V.; Khotkevich, A. V.; Bagatsky, V. M.; Ivanov, V. G.; Molinié, P.; Leblanc, A.; Faulques, E. *Phys. Rev. B* **2011**, *63*, 073107.

(37) Gospodarev, I. A.; Eremenko, A. V.; Ignatova, T. V.; Kamarchuk, G. V.; Kolobov, I. G.; Minaev, P. A.; Syrkin, E. S.; Feodosyev, S. B.; Fil, V. D.; Soreau-Leblanc, A.; Molinie, P.; Faulques, E. C. *Low Temp. Phys.* **2003**, *29*, 151.

(38) Horiba, K.; Ono, K.; Oh, J. H.; Kihara, T.; Nakazono, S.; Oshima, M.; Shiino, O.; Yeom, H. W.; Kakizaki, A.; Y. Aiura, *Phys. Rev. B* **2003**, *68*, 155108.

(39) Eaglesham, D. J.; Withers, R. L.; Bird, D. M. J. Phys. C: Solid State Phys. **1986**, *19*, 359.

(40) Togo, A.; Tanaka, I. *Scr. Mater.* **2015**, *108*, 1.

(41) Hughes, H. P.; Webb, C.; Williams, P. M. *J. Phys. C: Solid State Phys.* **1980**, *13*, 1125.

(42) Kim, J.-J.; Park, C.; Olin, H. *J. Korean Phys. Soc.* **1997**, *31*, 713.

(43) Terashima, K.; Sato, H.; Komatsu, H.; Takahashi, T.; Maeda, N.; Hayashi, K. *Phys. Rev. B* **2003**, *60*, 155108

(44) Strocov, V. N.; Shi, M.; Kobayashi, M.; Monney, C.; Wang, X.; Krempasky, J.; Schmitt, T.; Patthey, L.; Berger, H.; Blaha, P. *Phys. Rev. Lett.* **2012**, *109*, 086401.

(45) Zhang, D.; Ha, J.; Baek, H.; Chan, Y.-H.; Natterer, F. D.; Myers, A. F.; Schumacher, J. D.; Cullen, W. G.; Davydov, A. V.; Kuk, Y.; Chou, M. Y.; Zhitenev, N. B.; Stroscio, J. A. *Phys. Rev. Materials* **2017**, *1*, 024005.